

# Nanostructured indium-tin-oxide electrodes for organic photovoltaics

Abeed Lalany

A thesis submitted in partial fulfillment of the requirements for the degree of

Doctor of Philosophy

in

Micro-Electromechanical Systems

&

Nanosystems

Department of Electrical and Computer Engineering

University of Alberta

© Abeed Lalany, 2017

# Abstract

The use of organic, semiconducting polymers provides an attractive option to advance commercial solar photovoltaic technologies. These devices have the potential to be spray-coated on flexible, light-weight substrates and produced cheaply in high volumes; however, performance remains limited in practice. Interpenetrating, transparent nanostructures with near metallic conductivity improve charge extraction while also serving as a 3-D structural support for the photo-absorbing polymer region—extending device power conversion efficiency and lifetime.

For tin-doped, indium-oxide nanostructures there is trade-off between high conductivity, transparency, and the desired highly-branched 3-D ‘nanotree’ morphology; when fabricating highly conductive nanotree films, wires with high conductivity are achievable through deposition at elevated rates; however, increasing the deposition rate results in a reduction of the number of branches. Further, reliable characterization and optimization of the electrical properties of the nanotree arrays is a challenge due to the laterally disconnected architecture, and requires the adaptation of a typically planar device architecture to accommodate the 3-D structures.

In this work, the fabrication of a four-terminal device architecture paired with ohmic contacts removes the contribution from the measurement leads and minimizes the contribution for the lead-nanostructure interface, allowing for the exploration of the electronic interfaces internal to the nanostructure arrays. These electrical test structures are then utilized to explore post-processing anneals to optimize the NW conductivity, while maintaining the highly-branched structures suitable for integration within OPV devices. Device resistance is correlated to the observed electric field dependence, relatable through the electronic modes supported under test. It was found that the oxygen vacancy distribution within individual structures can be affected, measurable through analysis of the shifts in the observable electrical properties of the four-terminal characterization devices. These observations extend the technological feasibility of these nanostructures and present areas of potential improvement in future applications.

# Preface

Contributions to this work include the collection of data, assembly of the necessary apparatus and the performance of experiments outlined within this work.

I performed all experimental fabrication and data collection under the guidance of M.J. Brett and M.T. Taschuk. Support was sought from M.D. Fleischauer and K. Harris for interpretation of datasets.

Characterization of samples and further analysis was done in conjunction with A.L. Beaudry, R.T. Tucker, J.M. LaForge, R. Shewchuk, as well as the previously listed individuals and various staff at the University of Alberta NanoFAB and National Institute of Nanotechnology.

Publications relevant to this thesis are:

1. D. A. Rider et al., “Stable Inverted Polymer/Fullerene Solar Cells Using a Cationic Polythiophene Modified PEDOT:PSS Cathodic Interface,” *Adv. Funct. Mater.*, 2010 (**Chapter 1**).
2. D. A. Rider et al., “Indium tin oxide nanopillar electrodes in polymer/fullerene solar cells,” *Nanotechnology*, 2011 (**Chapter 1**).
3. A. Lalany et al., “Axial resistivity measurement of a nanopillar ensemble using a cross-bridge Kelvin architecture,” *J. Vac. Sci. Technol. A*, 2013 (**Chapter 4**).

For the publications undertaken with D.A. Rider, I was responsible for device fabrication and testing. Publishing of the content in **chapter 5** and **chapter 6** is an ongoing effort.

# Contents

List of tables .....	vii
List of figures .....	viii
Symbols and nomenclature .....	xvii
1 Solar cell .....	1
1.1 Solar industry – brief history and context .....	3
1.1.1 Current wafer-based and commercial thin-film PV .....	4
1.1.2 Emerging thin-film PV .....	5
1.2 Conventional and excitonic solar cells .....	8
1.2.1 Components of an OPV Device.....	9
1.2.2 TCE selection .....	12
Graphene.....	13
Doped metal-oxide materials: ITO .....	14
Previous study: Low dimensional OPV.....	17
1.3 Chapter summary .....	18
1.4 Thesis outline.....	19
1.4.1 Research goals and objectives .....	19
1.4.2 Outline and approach.....	20
2 DC electrical characterization of nanostructured thin films.....	23
2.1 Electrical characterization of nanostructured thin films .....	25
2.1.1 2-wire and 4-wire measurement of nanostructures.....	25
2.1.2 Micron-scaled electrical test structures .....	27
Previous study: CBKR in operation.....	28
2.2 Candidate material systems.....	31
2.3 Our methodology.....	32
2.4 Ohmic junctions.....	34
2.5 ITO material system details .....	38
2.5.1 Further electrical properties of ITO.....	39
Previous study: Shifting plasma edge with carrier concentration.....	40
2.5.2 GLAD structured ITO.....	41
Previous study: Low temperature deposition of structured ITO.....	42
2.5.3 VLS-GLAD structured ITO .....	43
Previous study: Growth of highly conductive branched nanotrees.....	46
2.5.4 Degeneracy in ITO .....	48



Previous study: Sn and oxygen vacancy doping in VLS-ITO NWs .....	51
Previous study: Scattering mechanisms .....	52
2.6 Chapter summary .....	53
<b>3 Experimental details .....</b>	<b>55</b>
3.1 Thin film deposition .....	56
3.1.1 Electron beam evaporation .....	56
3.1.2 Sputtering .....	57
3.2 Summary of experimental process .....	58
3.3 CBKR design rules .....	60
3.3.1 Lithographically defined contacts .....	61
3.3.2 Testing protocol .....	63
3.4 Thin film characterization .....	65
3.4.1 SEM .....	66
3.4.2 XRD analysis .....	67
3.4.3 EELS-enabled TEM .....	67
3.4.4 Surface characterization .....	68
3.5 Chapter summary .....	69
<b>4 Electrical characterisation of GLAD-ITO nanopillars .....</b>	<b>71</b>
4.1 Post capping and wet etch of top contact .....	72
4.2 Device fabrication .....	76
4.3 Completed devices .....	76
4.4 Attempted shaping of Nanostructure dimensions .....	81
4.5 Defect-free contacts .....	82
4.6 Chapter summary .....	83
<b>5 Measurement of VLS-GLAD-ITO nanowires .....</b>	<b>85</b>
5.1 NW capping and tip exposure .....	86
5.2 Device fabrication .....	87
5.3 Completed devices .....	89
5.4 Device error analysis .....	90
5.4.1 Mean NW dimensions .....	90
5.4.2 Determined number of NWs per device .....	92
5.4.3 Measured linear device characteristics .....	95
5.5 As-deposited results .....	96
5.6 Chapter summary .....	98

6 Optimization of ITO nanotree arrays via post-deposition anneals .....	99
6.1 Effect of annealing on nanotree films .....	101
6.2 NW film, bulk and surface characterization.....	106
6.2.1 XRD-determined crystallite evolution with annealing.....	106
6.2.2 Surface compositional analysis.....	109
6.2.3 NW film transmission .....	110
6.2.4 3D-CBKR device resistance shifts with processing.....	115
6.2.5 EELS axial characterization.....	116
6.3 Chapter Summary .....	118
7 Experimental conclusions .....	121
7.1 Current OPV work .....	123
7.2 A future nanotree array—hall mobility measurement.....	125
7.3 Reflection .....	126
Bibliography.....	127
A Case-study: GLAD-OPV .....	152
B 2-wire measurement of GLAD-ITO .....	156
C Film deposition details .....	158
Film level defects.....	158
C.1 GLAD-ITO deposition details.....	160
C.2 VLS-GLAD-ITO deposition details .....	161
D Determination of $N_p$ .....	162
D.1 Device-level defects: Undercutting of Ag contact.....	163
E Crystallographic details .....	165
F EELS sample preparation and processing.....	166
G K-cluster analysis.....	169

# List of tables

Table 1-1 Emerging consumer PV technologies [35] .....	5
Table 2-1 GLAD modulation schemes.....	43
Table 3-1 Growth and processing details. Summarized processing parameters (including process temperature, ambient and process time) for the study of various reduction gas flow rates to optimize nanostructured thin films (see Appendix C).....	60
Table 3-2 Line width measured at the center of millimeter-scale traces.....	63
Table 3-3 Device testing protocol. ....	64
Table 3-4 Characterization technique — region of interest.....	66
Table 5-1 Line-width measured at the center for 375 °C sccm sweep. Note that 2 $\mu$ m line traces are omitted due to our photo-mask layout. Also provided are the average ITO <sub>SP</sub> dimensions (here uncertainty is presented as standard error of the mean for all devices of the indicated nominal dimension).....	93
Table 5-2 Linear as-deposited device results. For device resistance, the standard error of the mean is reported, as well as the corresponding Pearson product-moment correlation coefficient ( $r$ ) and p-value. ....	95
Table 5-3 Summary of ITO deposited under various conditions. Determined as-deposited resistivity for our structured thin films, planar EBE, as well as $\alpha = 50^\circ$ VLS controls and sputtered witness samples (determined via 4PP and hall-probe). ....	97
Table 6-1 Effect of annealing on witness samples (sheet resistance measurements were determined via 4PP). Note, for select conditions, we are missing sample measurements — a small batch of control samples were disrupted and inter-mixed before measurement.....	100
Table 6-2 Summary of device data and K-means clustering analysis. For ITO <sub>VLS</sub> 85 devices, 94 of 128 fabricated devices yield ohmic characteristics. The unadjusted resistivity (i.e., uncorrected for the core-shell architecture increases with processing (irrespective of clustering). Initially, we use the median to split the dataset for each processing condition. Also outlined, a K-means Cluster analysis [197] was undertaken for classification of the data into two (user selected) clusters for each processing condition; this statistical analysis technique was utilized to validate the interpretation of a bi- or multi-modal distribution. Clustering is attributed to an electric-field dependence for all cases except the 175 °C, 10 sccm processing condition (here the number of posts is the distinguishing variable, and arguably there is no clustering—see Appendix G).....	105
Table 6-3 Summary table of crystallite dimensions for $\alpha = 85^\circ$ ITO <sub>VLS</sub> films. Error bars for grain size are based on a Gaussian peak fit for spectra. Lattice constants are determined for the (400) peak. For reference, commercial ITO (t = 125 nm), (222): (21 $\pm$ 0.2) nm, (400): (23.3 $\pm$ 0.3). Samples (*) anneal 1 = 24 hr. oxidation anneal. ....	108
Table D-1 Manual/minimum imageJ threshold routine. ....	162
Table E-2 Process legend.....	165

# List of figures

- Figure 1-1 Ensemble nanoarrays in industry, research and this work. (a) Schematic of an industrial-scale execution of a memory module available in the coming years from Intel<sup>®</sup>–Micron. Copyright Intel Corporation 2016. (b) research state-of-the-art for the idealized gate contact, the all-around wrap gate Figure credit: [8]; (c) our nanotechnology (this work), configurable nanotree thin films (single nanowire (NW) shown), achieved by adjusting the deposition angle ( $\alpha$ ) and azimuthal angle ( $\phi$ ). Figure credit: [9]..... 2
- Figure 1-2 NREL solar efficiency maps. Best research-cell efficiencies for a variety of material systems and configurations. [<http://www.nrel.gov/ncpv/>; accessed Jan. 2015] Note: First commercial microprocessor (Intel 4004, 1971); first bulk polymer/ $C_{60}$  heterojunction PV (Yu, 1994 – see H. Spanggaard (2004), ref: [35] for a detailed review..... 7
- Figure 1-3 Typical BHJ and nanostructure-enhanced OPV. (a) schematic band-diagram depicting the photo-generation process within an excitonic OPV device, adapted from [32]; (b) BHJ with donor (green) and acceptor (purple) regions without (left) and with (right) interpenetrated with a  $\sim 1 \mu\text{m}$  thick film of branched nanotrees; (c) engineering of critical dimensions [11];  $S_{\text{NS}}$  ( $\sim 150 \text{ nm}$ ) and  $S_{\text{Branch}}$  ( $\sim 50 \text{ nm}$ ) to match the size scale of the polymerization domains ( $\sim 10 \text{ nm}$ ) and excitonic diffusion length of a prototypical poly(3-hexylthiophene) (P3HT)/[6,6]-phenyl  $C_{61}$ -butyric acid methyl ester (PCBM) device..... 10
- Figure 1-4 GLAD enhanced VLS. (a) Edge-view SEM of ITO thin-film evolution with deposition angle ( $\alpha$ ) and substrate temperature ( $T_s$ ); (b) edge-view schematic of ‘nanotree’ deposition parameters. Figure credit: [11]..... 16
- Figure 2-1 3D-CBKR and critical dimensions. Schematics of (a) 4PP NW testing configuration; (b) Greek cross architecture in testing configuration, inset: 2L configuration shown, with 2I resulting with straight contacts; (c) a modified CBKR with  $2 \mu\text{m}$  critical dimension; and (d) Oblique schematic view of the contact window where nanostructures are incorporated into an idealized test structure with metallic top and bottom contacts. Contacts are typically numbered from the top, moving counter-clockwise. Current is typically injected up through the diffusion layer (i.e., here, the bottom ITO contact and the NW array) into the metal top contact..... 27
- Figure 2-2 Candidate material systems explored. (a) A variety of metal and metal-oxide materials compatible with GLAD were investigated for integration into the device form presented previously; (b) ITO was selected for due to its ability to form well defined nanostructure and (c) tunable branching during VLS growth. Also explored were (d)  $\text{TiO}_2$  films (e) and Cr films; device-scale defects prevented the use of the latter (f)..... 31
- Figure 2-3 Integration schematic for the nanostructures. (a) Schematic of our 4-wire testing configuration; (b) schematic model depicting an array of parallel resistive

elements in series with a contact resistance; (c) nanotree films are integrated within devices fabricated on (d) p-type Si wafers, with sputtered ITO acting as the growth surface and bottom electrode. ....	32
Figure 2-4 Current injection and voltage characteristics of 3D-CBKR. (a) Top-down schematic of current injection where difference in trace width and contact window ( $\delta$ ) introduces a non-uniform current distribution. For out VLS-GLAD devices the current path is through: the top contact (Ag), interface 1 (Ag/ITO <sub>VLS</sub> ), the array under test, interface 2 (ITO <sub>VLS</sub> /ITO <sub>SP</sub> ), and through the bottom contact (ITO <sub>SP</sub> ); inset: edge view of same. (b) Schematic band diagram depicting an n <sup>+</sup> region between ideal ohmic contacts with uniform current distribution resulting in a linear i-v relation; adapted from ref: [125], [126]. ....	35
Figure 2-5 NW-metal interface. (a) elemental mapping determined with electron-energy-loss spectroscopy (EELS) of an as-deposited NW grown at moderate rate (1.0 nm s <sup>-1</sup> , $\alpha = 85^\circ$ ); (b) edge-view schematic for overlap region between conformal Ag top contact and ITO NWs (the purple region is the insulating polymer used for isolation); (c) metal contact to a degenerate semiconductor band diagram for an ohmic contact; (d) contact between a metal and a metallic nanostructure results in the presence of a tunnel barrier whose profile is determined by the work-function offset of the metal and metallic nanostructure ( $\phi_{Ag}$ and $\phi_{ITO}$ ); adapted from ref: [124]. ....	37
Figure 2-6 Representative metal-oxide behaviour. (a) Near-normal transmission spectra for a doped tin oxide thin film outlining the Burstein-Moss blue-shift of the band edge with increasing carrier concentration determined by Granqvist et al. [151], calculated using the shown values of electron density and film thickness. Figure credit: [151]. ....	41
Figure 2-7 GLAD deposition apparatus and film nucleation. (a) Control over the vapor flux angle relative to the substrate and rotation about the substrate normal is achieved using a programmable substrate holder equipped with two stepper motors; (b) substrate profile depicting atomic shadowing of the incident flux; (c) auxiliary view of same. Figure credit: GLAD image database, accessed Jan. 2016. ....	42
Figure 2-8 GLAD ITO parameter-sweep. (a) no rotation, fixed deposition angle ( $\alpha = 60^\circ$ ); (b) no rotation, fixed deposition angle ( $\alpha = 85^\circ$ ); (c) slow rotation; (d) alternating 180° deposition intervals; (e) vertical uniaxial and; (f) vertical biaxial films. Figure credit: [90]. ....	44
Figure 2-9 Transition to kinetic growth regime. (a) schematic of surface trapping mechanism. Figure credit: [155]; (b) increasing $T_s / T_M$ to a value $\sim 0.3$ promotes adatom mobility, 'blurring' features, adapted from Patzig et al. [156]; (c) schematic of the precipitation of fully extended NWs; (d) top-down SEMs of our polymer infilled VLS-ITO films; (e) partially extended NWs; (f) schematic of catalyst droplet. Figure credit: [158]. ....	47
Figure 2-10 Demonstrated range of the VLS-GLAD-ITO material system. Films grown at $\alpha = 50^\circ$ and $\alpha = 85^\circ$ and various rates (500 nm scale bars). Pairing of VLS	

growth with GLAD yields a film composed of single crystal nanotrees, with control over trunk diameter, branch placement, and the density of NW features in a film. Figure credit: [9], [11].	49
Figure 2-11 ITO crystal schematics from literature: ITO unit cell for (a) fully crystalline (b) fully amorphous unit cell. Figure credit: [133]. The oxygen partial pressure during deposition has been shown to select between different orientations, with oxygen deficient growth resulting in (c) [400] textured films and oxygen rich growth in (d) [222] textured films. Figure credit: [142]. From ref [9]: A schematic illustrating the crystal structure and facets of a single-crystal ITO nanotree trunk growing in the [100] direction, shown from (e) auxiliary and (f) top-down perspectives. Figure credit: [9].	50
Figure 2-12 Resistivity varying with Sn [at. %] and deposition rate. The dashed line is the 'commercial grade' threshold (Delta Tech., 0.16 mΩ·cm). Inset: Precipitation of a metallic core at 3.0 nm s <sup>-1</sup> . Transmission Electron Microscopy images of NWs deposited at elevated rates.	52
Figure 3-1 Experimental process flow and relation to equation 2-6. An initial calibration study had a yield of 25% (AL4-007A). Processes were further tuned and yield improved for subsequent process groupings (50–94% yield for AL4-007B). Key parameters are highlighted (left) with the process flow for device fabrication and electrical testing discussed primarily in this chapter, and subsequent thin film characterization discussed further in chapter 6.	59
Figure 3-2 Determination of device dimensions and photomask design. (a) Dependence of R <sub>D</sub> on device area, and (b) Dependence of R <sub>p</sub> on post-base diameter; (c) 4 × 4 array of device chips; (d) housing 36 devices each (6 × 6 array). Device areas range from 4 μm <sup>2</sup> to 100 μm <sup>2</sup> , and allow for the systematic determination of intrinsic electrical properties of the nanostructures between lithographically defined electrodes; (e) final device configuration.	62
Figure 3-3 Characterization scheme of ITO thin films and controls. Via equation 1.1 and 1.2 we can observe shifts in the degree of doping within NW arrays and thin film controls; various characterization techniques allow us to probe the macroscopic, (a) film level properties as well as the (b) bulk and near surface regions of the nanostructures.	66
Figure 4-1 Device fabrication over-view. (a) A typical device-chip is shown with the region of uniform fabrication highlighted (dashed region); (b) the transition from nanostructure to planar top contact is a challenge overcome through grading of the top contact (discussed later). Shown above is a delaminated top contact from a cleaved sample — for this reason samples were freeze-fractured during SEM sample preparation (note the tapering of nanostructures discussed in chapter 3).	72
Figure 4-2 ITO <sub>GLAD 83</sub> device wet-etch. Plan and edge-view SEMs of: (a, b) ITO films prepared on Au contacts using GLAD with deposition angle (α = 83°), (c, d) α = 83° ITO film on Au, 'capped' with 250 nm graded (α = 83° → 30°) + 100 nm	

planar Ag, and (e, f) $\alpha = 83^\circ$ ITO ‘capped’ film after etching non-device areas (i.e., no Au bottom contact). .....	73
Figure 4-3 ITO <sub>GLAD 83</sub> device optimal wet etch. (a) Porosity of uncapped films (triangles); reducing porosity with increasing thickness ('variable cap') of Ag (circles); 250 nm Ag cap + 100 nm planar ('cap/planar') Ag; (b) increasing top-contact resistivity and surface void fraction with increasing etch-time in non-device areas, etch times longer than 25 s resulted in device failure; (c) plan-view SEM of partially etched Ag top contact; (d) ImageJ threshold image of same. ....	74
Figure 4-4 ITO <sub>GLAD 83</sub> device schematic and process flow. (a) 3D-CBKR in the “2I” configuration; intersecting line widths of 2–10 $\mu\text{m}$ corresponding to contact areas of 4–100 $\mu\text{m}^2$ . (b) 3-D CBKR Device intersection (Au / ITO / Ag). (c,d) photomask pattern is transferred to Si wafer coated with 100 nm layer of Au (e,f) GLAD ITO structures are deposited on lithographically defined Au traces (g,h) structures are capped with graded Ag top contact. $w = (33 \pm 7) + (0.28 \pm 0.2)h$ [nm] for ITO <sub>GLAD 83</sub> structures. ....	75
Figure 4-5 GLAD-ITO completed device. (a) Edge view SEM of active region and (b) sample i-v curve for completed CBKR device ( $\sim 83 \mu\text{m}^2$ $\alpha = 83^\circ$ ITO). ....	77
Figure 4-6 ITO <sub>GLAD 83</sub> device defects. (a) Edge view and (b) Plan view of defect region resembling dense-bulk film resulting from step-height differential between the Si substrate and Au contact; (c) large scale device with lower defect density. ....	78
Figure 4-7 ITO <sub>GLAD 83</sub> device area independent scaling. (a) Device resistance as a function of device area. The solid line is a best fit to devices above 7.5 $\mu\text{m}^2$ showing the expected $(A_D)^{-1}$ scaling. The dashed line is a best fit described in the text, including the effect of the defect region. The fit shows device resistance scales approximately with $(A_D)^{-1/2}$ below 25 $\mu\text{m}^2$ and $(A_D)^{-1}$ above 25 $\mu\text{m}^2$ ; (b) distribution of device $\rho_i$ for all devices. ....	79
Figure 4-8 ITO <sub>GLAD 83</sub> ion-milling. Edge view and plan view SEMs of (a), (b) as-deposited ITO <sub>GLAD 83</sub> films; after ion milling (c), (d) 1 min. Adapted from ref: [188]. ....	81
Figure 4-9 Embedded contacts. (a) Edge view and (b) Plan view of embedded Au electrode, eliminating the step-height differential between the Si substrate and Au contact. ....	82
Figure 5-1 Graded cap, polymer infill and NW tip exposure for ITO <sub>VLS 85</sub> structures. (a) Edge-view SEM of structures with $\sim 200$ nm of Ag capping; (b) top-down view of same; (c) edge-view SEM of films in-filled with HPR 504 and NW tips exposed with a progressive low-power O <sub>2</sub> plasma ash; (d) top-down SEM of exposed tips prior to top-contact deposition. ....	86
Figure 5-2 Summary of device fabrication. (a) Schematic oblique-view of intersecting device area with NWs modelled as an array of parallel resistors; (b) oblique-view SEM of same, inset: 500 $\mu\text{m}$ scale bar. Schematic and edge-view SEM micrographs	

of: (c, d) embedded ITO <sub>SP</sub> bottom contact prior to lift-off; (e, f) ITO <sub>VLS</sub> structures in-filled with an insulating polymer (labelled as PR), exposed with low-power plasma ashing process; (g, h) graded Ag top contact.....	88
Figure 5-3 Completed device. (a) Edge-view SEM of completed device; (b) Representative device i-v characteristic demonstrating ohmic behaviour within our measurement window.....	89
Figure 5-4 NW diameter and column tilt. (a) NW diameter histogram (n = 1678) determined by top-down SEM image analysis, right skew is believed to be branch contribution, inset: plan-view SEM of exposed NWs, 200 nm scale bar; (b) column tilt histograms (n = 282) determined by edge-view SEM image analysis for structures > 850 nm, 200 nm scale bar. Plan-view SEM micrographs of: (c) ideally exposed (d) moderately over-exposed, and (e) severely over-exposed device regions. ....	91
Figure 5-5 Summary of N <sub>P</sub> determination procedure. (a) Plan-view SEM of polymer-infilled, plasma exposed NWs. The trench region results in the further isolation of structures; (b) edge-view SEM of same; (c) top down SEMs at multiple regions along the bottom ITO contact to determine the local post density; (d) each frame undergoes a threshold routine (see Appendix D for details) to determine the number of exposed NWs, inset: dashed boxes are samplings of dispersed presumably core-shell structures (10 nm scale bar), solid boxes are illustrative; (e) the number of posts (i.e. n = 192) is averaged over 3 frames to yield the local post density (i.e. $11.2 \pm 0.4$ posts / $\mu\text{m}^2$ for this frame); (f) undercut of the Ag trace is assessed with optical microscope (plan view); (g) severe undercut of a nominally 10 $\mu\text{m}$ wide Ag trace.....	94
Figure 5-6 Surface depletion layer and as-deposited resistivity results. (a) schematic representation of the upwards band bending of the Fermi level induced from gap surface states that cause carrier depletion in a thin surface region; (b) as-deposited estimates (n = 10) for the NW intrinsic resistivity and an observed violation of normality for the device distribution. Assuming $\delta^* \sim 1$ nm, there is an alignment of the lower mode with our as-deposited controls (see Table 5-3). ....	96
Figure 6-1 Reduction of ITO thin film (EBE) controls. Electrical characteristics (hall-probe / 4PP) for 200 nm dense planar thin film. Open symbols are indicative of values after the air anneal. ....	100
Figure 6-2 Contribution of varying NW metallic core cross-sectional area. (a) Normalized resistivity vs. the cross-sectional area of a supposedly metallic core NW . Curves of constant resistance (for fixed NW length) demonstrate that a decreasing cross-sectional area can account for the observed trend of increasing device resistance with increasing reduction intensity, e.g., when $A_{NW} \sim A_{core} (\approx 30 \text{ nm})$ . Further, there is an underlying non-normal distribution of device results (see inset, normal curves added for a guide to the eye); (b) cluster A (triangles) and cluster B (circles) and controls (diamonds) for all processing conditions (see also Appendix G). Here, $\rho_i$ is estimated using $D_{NW} = 32.2 \pm 0.6$ nm, less the estimated $\delta^* \sim 1$ nm. Included for reference are the electrical characteristics for ITO <sub>TF</sub>	



- samples (diamonds). Open symbols are indicative of values after the air anneal. Inset: schematic band diagram depicting the chemical depletion mechanism, adapted from: [161]. Here,  $\delta^*$  is suggested to extend far into the bulk of the NW(s). .... 102
- Figure 6-3 Estimated chemical depletion vs. reduction flow rate. (a) Estimated chemical depletion layer ( $\delta^*$ ) for indicated processing conditions (initially,  $\delta^*$  estimated to be  $\sim 1$  nm for the as-deposited condition), inset: EELS oxygen compositional map for representative NW processed at 100 sccm, 375 °C with dimensions  $\sim$  matching estimates of  $\delta^*$ ; (b) complementary metal distribution for same NW; inset: schematic depicting  $\delta^*$  extending into the bulk of the NW due to oxygen vacancy filling) ..... 103
- Figure 6-4 Tapered metallic core for sample AB2096. (a) Dark field TEM of sample AB2096 ( $0.5 \text{ nm s}^{-1}$ ,  $t = 10 \text{ }\mu\text{m}$ ) with the region of interest highlighted for EELS compositional analysis; (b) EELS compositional temperature map of the trunk region showing areas of maximum and minimum In concentrations, adjoined frame showing same for tip region (10 nm scale bar); (c) same for temperature map of the complimentary ITO concentration. This is an unpublished observation, noted by LaForge. .... 104
- Figure 6-5 XRD spectra. X-ray diffraction line profiles for the  $\text{ITO}_{\text{GLAD } 83}$  and crystalline VLS nanotree structures (with as-deposited, air-only, and ‘sccm sweep’ conditions ordered first).  $\text{ITO}_{\text{VLS } 85}$  films indexed to  $(\text{In}_{1.94}\text{Sn}_{0.06})\text{O}_3$  ICSD 01-089-4596 (dashed lines)..... 107
- Figure 6-6 Surface composition and shifts with reduction of NWs. (a) Relative atomic surface concentration of In and O (determined by AES,  $\sim 1\text{-}2$  nm probe depth) and  $\phi_s$  (determined by UPS,  $\sim 3\text{-}5$  nm probe depth) varying with processing (average of three measurements across three sites of interest); inset: relative atomic surface concentration of Sn varying with processing and probe depth. Open symbols are indicative of values post air anneal. .... 109
- Figure 6-7 Transmission spectra for as-deposited and air-annealed VLS films. As-deposited films ( $0.2 \text{ nm s}^{-1}$  and indicated  $\alpha$ ); (a) films post air anneal; (b) and post air + 375 °C, 100 sccm reduction anneal. Note: major feature at 2700 nm, as well as minor features at 1400 nm and 2250 nm, are due to absorption by the UV-grade, fused silica substrate; inset: transmission curve of a blank substrate from [202]. The dashed line provided as a guide to the eye for the shifting plasma edge (compare with transmission spectra for reduced films). Spectra were collected by M.T. Taschuk. A version of this dataset was published within the supplemental information of [11]. .... 111
- Figure 6-8 Transmission spectra. (a) Schematic depicting the local reduction environment for various reduction gas flow rates; (b) As-deposited films ( $0.2 \text{ nm s}^{-1}$  and indicated  $\alpha$ ) — post air + 375 °C, 100 sccm reduction anneal. Dashed line provided as a guide to the eye for the shifting plasma edge (see previous as-deposited and air annealed transmission spectra). .... 112

Figure 6-9 Metallic Transition of films deposited at elevated rates. Transmission spectra for films, deposited at 0.1, 0.5 and 2.0 nm s <sup>-1</sup> , as-deposited films (solid line) and films post air + 375°C, 100 sccm reduction anneal (dashed lined): (a) ITO <sub>VLS 85</sub> films; (b) ITO <sub>VLS 50</sub> films.....	114
Figure 6-10 EELS core-loss temperature map for oxygen and metal spectra. (a) top-down EELS spectrum map (device 4d244); (b) oxygen core-loss temperature map for same—processed at 100 sccm, 375 °C; (c) normalized metal (In + Sn) core-loss of the same NW depicting complementary distribution of metal within the NW.	116
Figure 6-11 Aperiodic cores as observed by EELS and TEM analysis. Oxygen core-loss RGB (a,b,c) channels, where the scale matches that of previous EELS maps (see Fig. 6-12 a). Core-loss data presented using the ImageJ plugin Image5D (used to handle the time series of 3D-multichannel data stored in the .dm3 file). Edge view SEM of structures deposited at 3.0 nm s <sup>-1</sup> (50 nm scale bar) for: (d) continuous core, (e) concentric core, and (f) rippled core; inset: schematic for various core-shell models. ....	117
Figure 6-12 EELS phase mapping of a side-contacted NW. (a) High-angle annular dark-field (HAADF) image; isolated elemental phase map for (b) In, (c) ITO, and (d) the surface plasmon. ....	118
Figure 7-1 Experimental schematic process flow. Nanostructures processed under the indicated conditions are deposited between metallic contacts (outlined in chapter 4 and 5). Further characterization reveals an induced, aperiodic, core-shell structure (see the discussion of chapter 6). Inset: EELS mixed phase map (for ITO NW of Fig. 6-14) including In catalyst droplet, ITO and surface plasmon. ....	122
Figure 7-2 Nanostructured OPV. Explored by our collaborators in the Chemistry department, the (a) functionalization of the NW surface prepares it for (b) integration into a nano-enhanced OPV device; (c) A line scan elemental analysis indicates that strong indium signal from the inner the ‘trunk’, while the zinc signal is mainly from the outer skin, indicating that ZnO ‘skin’ surrounds the inner ITO ‘core’. Figure credit: [212].....	124
Figure 7-3 Multi-gate CBKR architecture. (a) Substrate-level layout; (b) Device-level layout; and (c) a schematic NW interconnect (deposition processes on the left and fabrication processes on the right).....	125
Figure A-1 GLAD-ITO OPV. (a) GLAD-ITO ( $\alpha = 83^\circ$ ) structures integrated into a P3HT : PCBM BHJ; (b) capped with $\sim 80$ nm of Al. (c) The resulting illuminated current density-voltage plots fabricated with commercial ITO (orange diamonds), GLAD ITO (black triangles) and silica-capped GLAD ITO (magenta squares) anodes. (500 nm scale bar); (d) Scanning electron micrograph of 150 nm GLAD ITO capped with 50 nm silica to prevent electrical shorts between electrode and cathode (200 nm scale bar). Figure credit: [51]. ....	152
Figure A-2 Polymer pore confinement. (a) edge tilt (10°) SEM images of GLAD-SBD TiO <sub>2</sub> film, with 3 nm growth intervals, 1 nm transition period, inset: top-down view of same (1 $\mu$ m scale bar) (b) 11 nm growth interval, 1 nm transition period. (c)	

absorption spectra for annealed GLAD-SBD TiO <sub>2</sub> devices (175 °C, 20–80 mins) (d) R <sub>s</sub> measurements for same. ....	154
Figure B-1 $\alpha$ sweep and 2-wire measurement. (a) 2-wire measure of the axial resistance revealed a factor of $\sim 2$ increase in R <sub>D</sub> for high- $\alpha$ films (relative to our planar Ag control), inset: evolving laterally-isolated ITO <sub>GLAD</sub> films; (b) schematic device architecture of nanostructures isolated between sculpted Ag cap and commercial ITO substrates. ....	156
Figure B-2 Equivalent circuit model and schematic. (a) The series contribution from the electrodes is removed with 4-wire measurement; included are the interface contributions and the geometrical contribution due to the parallel plate contribution of the electrodes. A series inductance was supposed during these initial experiments; (b) schematic of same. ....	157
Figure C-1 Film-level defects. (a) Top-down SEM showing NWs that are ideally plasma-ashed, those with exposed branches, and large film level defects; (b) schematic illustration depicting the latter. ....	158
Figure C-2 Device-scale defects. Isolated defects observed during (a) Ag deposition; (b) Ag + VLS-GLAD-ITO deposition; and (c) VLS-GLAD-ITO deposition. ....	159
Figure D-1 Estimated Ag trace dimensions. (a) Top-down SEM of a device with PR overhang; inset: ‘terracing’ at the edge of PR photo-mask (1 $\mu$ m scale bar); (b) Top-down optical microscopy of the same; (c) Top-down threshold image of optical frame, depicting estimated error region ( $\delta W_{Ag}$ ) and Ag linewidth ( $W_{Ag}$ ). ....	163
Figure D-2 Determination of $W_{Ag}$ and device damage. (a) oblique SEM, and (b) optical micrograph view of cleaved top contact section allowing us to observed the PR coated Ag contact directly; (c) edge-view SEM of device 2b111 and (d) top-view optical micrograph of same. Undercutting is believed to be responsible for contact degradation and deviation of device performance. Note: device 2b111 failed open circuit and therefore is not included in the final dataset. ....	164
Figure E-1 Peak width, centre and width for (400) and (222) peaks of interest. Error bars represent instrument error (calibrated against LaB6 standard ( $I_{111}/I_{110}$ ), and with varying goniometer angle). Maximum intensity ratio between $I_{400}/I_{222} \sim 88\text{--}92^\circ$ for (400), and $118\text{--}122^\circ$ for (222). An alternative Cauchy fit gives, (400): $(75 \pm 16)$ nm, (222): $(30 \pm 5)$ nm. Here, the uncertainty represents the standard deviation of the range of observed grain sizes for the given orientation (across all processing conditions). For a detailed consideration of the progression of film texture with rate see ref: [94] and [9]. ....	165
Figure F-1 EELS sample preparation and data collection. (a) Oblique-view SEM of a 100 sccm device being excavated using a FIB; (b) plan-view SEM of sample after being thinned from top and bottom with the FIB; (c) top-down TEM of branched NW film suspended within the polymer in-fill region; (d) isolated NW; inset: corresponding core-loss EELS spectrum map. ....	166

Figure F-2 EELS spectrum collection process. (a) During EELS characterization, an incident transmission beam ( $\sim 1.1$  eV) scans the cross-section of an isolated NW mid-section ( $\sim 150$  nm thick), and the resulting elemental peaks are resolved using principle component analysis (PCA). PCA is a statistical technique that considers the variance in contrast of a spectrum image; inset: the data set is then reconstructed using only those principal components, eliminating those that represent noise [180]; (b) this analysis produces a dataset (.dm3 file) that can be manipulated and analyzed digitally. The resulting dataset can be considered as a three-dimensional data cube whose x-y dimensions (real-space imaging dimensions) and z dimension (energy loss in the spectra) contain spectroscopic information related to the local bonding environment. Energy filtering allows us to select the metal components and (c) oxygen component in the collected spectrum image, by isolating the associated energy range characteristic of In, Sn, and O; from this analysis we can generate the core-loss temperature map for metal spectra and oxygen (d and e, respectively).167

Figure F-3 Air-annealed EELS core-loss temperature map. (a) oxygen normalized metal profile for the ‘air-only’ sample (taken along  $\sim 30$  nm dashed line); the relatively uniform/flat elemental profile of the air-annealed NW isolated from device 3c211 (unlike the pronounced metallic core of Fig. 6-10). Inset: the RGB channels are separated using the ImageJ plugin Image5D (used to handle the time series of 3D-multichannel data stored in the .dm3 file). Compare with Fig. 6-12 a–c. ....168

Figure G-1 K-means cluster assignment for all conditions. SPSS output for 2 cluster, ‘K-means clustering’ analysis. Results from the analysis of normalized variance (ANOVA), reveal that relative to the electric-field [ $F(1,92) = 165.57, p < 0.05$ ], the number of posts [ $F(1,92) = 0.987, p = 0.323$ ] and processing condition [ $F(1,92) = 0.990, p = 0.322$ ] are not the dominant variables that explain the clustering of our device data; a notable exception is samples processed at 10 sccm and 175 °C for which the number of posts is the dominant variable need to explain the multi-modal clustering. ....169

# Symbols and nomenclature

$A$	Deposition angle, angle of flux relative to substrate normal
$\phi$	Azimuthal angle of the substrate chuck during deposition
$\Gamma$	Deposition flux rate
$T$	Temperature
$t$	Film thickness
$A_{\text{NW}}$	Cross-sectional area of full nanowire
$A_{\text{core}}$	Cross-sectional area of supposedly metallic core nanowire
$\tau$	Average time between scattering events
$\sigma_i(\rho_i)$	Intrinsic conductivity (resistivity)
$\mu_e$	Majority carrier mobility (n-type)
$n_e$	Majority carrier density (n-type)
$m_e$	Mass of a free electron
$q$	Charge of a free electron
$\omega_p$	Plasma frequency
$\epsilon$	Material permittivity
$h$	Plank's constant
$a$	Crystal lattice constant
$\theta$	Bragg angle
$D$	Scherrer crystallite size
$d_{\text{hkl}}$	Crystal lattice spacing
$I_{\text{test}}$	Applied test current
$V_M$	Measured device voltage
$\rho_C$	Specific contact resistivity
$\rho_D$	Areal post density

$A_D$	Device cross-sectional area
$A_C$	Contact area
$W_{elec.}$	Width of electrode (i.e., Au, Ag, ITO <sub>SP</sub> )
$\phi_i$	Material work-function
$\delta(^*)$	Deviation in contact window (chemical depletion width)
$R_O$	Inline electrode resistance contribution
$R_C$	Contact resistance
$R_S$	Sheet resistance
$R_D$	Measured device resistance
$V_K$	Kelvin potential
$R_K$	Kelvin resistance
$R_{geom}$	Geometrical resistance contribution
$l_t$	Transfer length (distance needed for 63% of signal to pass)
$l_c$	Contact cross-sectional length
$N_P$	Number of posts in a given device
$J$	Current density
$E$	Electric field (oriented parallel to the material's long axis)
$E_F$	Position of Fermi level, measured from valence band maximum
$E_C$	Position of conduction band edge
$E_V$	Position of valence band edge
$E_{VAC}$	Vacuum level
$E_g$	Material bandgap
$V_O$	Oxygen vacancy density
$L_D$	Exciton diffusion length
$l_o$	Electron elastic mean free path
AES	Auger electron spectroscopy

BHJ	Bulk heterojunction
CBKR	Cross bridge Kelvin resistor
CTM	Crystal thickness monitor
EBE	Electron beam evaporation
EDX	Energy dispersive X-ray spectroscopy
EHP	Electron-hole-pair (exciton)
FIB	Focused ion beam
4PP	Four point probe
GLAD	Glancing angle deposition
ITO <sub>x</sub>	Indium-tin-oxide; subscript indicates deposition parameters
NW	Nanowire
OPV	Organic photovoltaic
PCBM	[6,6]-phenyl C61-butyric acid methyl ester
PCE	Power conversion efficiency
P3HT	Poly(3-hexylthiophene)
PVD	Physical vapor deposition
SBD	Serial bi-deposition
SCCM	Standard cubic centimeters per minute
SEM	Scanning electron microscopy
TCE	Transparent conducting electrode
TCO	Transparent conducting oxide
TEM	Transmission electron microscopy
UPS	Ultraviolet photoelectron spectroscopy
VLS	Vapour-liquid-solid
XRD	X-ray diffraction

# 1 Solar sell

The solar photovoltaic (PV) industry in its present form has been enveloped by the progression of the microelectronics industry, and so is expected to be subject to the similar limitations. The tools and process technologies characteristic of the microelectronics industry have allowed for the unprecedented control/fabrication of crystalline materials and their doping. The development and refinement of its fundamental building block [1], the metal-semiconductor junction, has facilitated the steady miniaturization of integrated circuit elements and a subsequent increase in feature density (manifesting as an exponential increase in computational power, paired with decreasing costs – as mapped by ‘Moore’s Law’) [1]. Our relentless march towards the atomic scale is impeded by the complexity encountered at this size scale [2], and so has catalyzed a reprisal of Moore’s Law; it is currently suggested that application-dependent design now dominates development strategy, and a so called ‘More than Moore’ strategy prevails [3]. For PV applications, this shift in strategy includes the integration of power production, storage and end-use circuitry. This is in comparison to current implementations which separate power production from the ‘balance of systems’



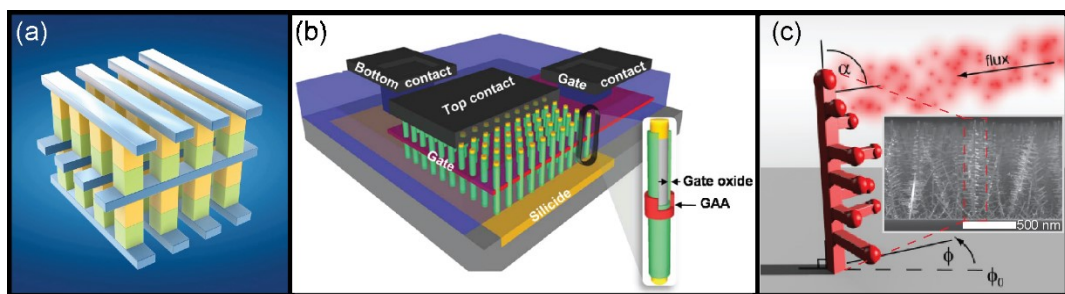


**Figure 1-1 Ensemble nanoarrays in industry, research and this work.** (a) Schematic of an industrial-scale execution of a memory module available in the coming years from Intel<sup>®</sup>–Micron. Copyright Intel Corporation 2016. (b) research state-of-the-art for the idealized gate contact, the all-around wrap gate Figure credit: [8]; (c) our nanotechnology (this work), configurable nanotree thin films (single nanowire (NW) shown), achieved by adjusting the deposition angle ( $\alpha$ ) and azimuthal angle ( $\phi$ ). Figure credit: [9]. (including battery banks and inverters). The key requisite to achieve this new strategy is the use of flexible fabrication techniques and advanced material systems. Such techniques as coating with nano-composite materials can allow for the novel application of stacked, or ‘tandem’ solar cells with designs integrating directly with battery charging units [4], [5], and fabrication ideally proceeding within a single process line [6], [7]. The further miniaturization and integration of these circuit elements requires the blending of research disciplines and the expansion of current micro- and nano-fabrication techniques, as well as more sophisticated process verification methods.

Current mass manufacturing methodologies utilize planar (2-D) thin film nanostructuring via lithography, enabling high yield, high throughput and ultra large-scale integration technologies<sup>1</sup>. The extension of fabrication methodologies into the third-dimension in the field of microelectronics is currently driving advances in memory storage and display technologies, where research efforts have focused on increasing the addressable feature density at sub-10 nm dimensions (see the ‘3-D XPoint’ memory module schematic in **Fig. 1-1 a**) [10], and improving electrostatic control at reduced dimensions (shown in **Fig. 1-1 b**, a nanowire-based field-effect transistor array utilizing a gate-all-around architecture) [8]. This thesis explores highly branched ensemble nanostructure arrays and their relevance to the field of organic PVs (a schematic of an isolated branched nanostructure, or ‘nanotree’, utilized in this work is shown in **Fig. 1-1 c**) [9]. Engineering nanotree conductors for solar cells has parallels to size scales in ultra large scale integration as it requires dealing with sub-10 nm critical dimensions for

<sup>1</sup>Intel’s<sup>®</sup> Broadwell-EP Xeon processor has 7.2 billion transistors.

polymer/excitonic domains as well as the nanostructure cross-sectional dimensions. Further, if a trunk branch union is considered as an interconnect, then the interconnect density is approximately 170 billion  $\text{cm}^{-2}$  for our deposition conditions [11].

Due to their unique opto-electronic properties and variable morphologies, nanostructured thin films have been identified as candidates for next-generation energy conversion devices [12]. One flexible nanostructure deposition technique is glancing angle deposition (GLAD) which produces highly porous thin films with tunable morphologies [11], [13]–[15]. GLAD films have been used for sensors [16]–[18], catalyst supports or electrochemical electrodes [19]–[24], and solar cells [25]–[28], where the easily accessible surface area improves response time, electrochemical activity, and charge extraction (respectively), but increases the complexity in desired film requirements. The identifying feature of GLAD is physical vapor deposition (PVD) proceeding at oblique angles ( $\alpha$ ) with modulation of the azimuthal angle ( $\phi$ ) allowing for control of the apparent position of the source; together, these conditions enable an unprecedented degree of control over an individual nanostructure’s morphology. The performance of devices utilizing GLAD nanostructures remains limited by insufficient control of the film’s surface and ‘bulk’ material properties. As a result, focus has recently shifted to more advanced control of an individual nanostructure’s material properties, including control of phase, crystallographic orientation, and dopant level; however, reliable diagnostics for nanostructure arrays have not yet been developed<sup>2</sup>.

## 1.1 Solar industry – brief history and context

A viable solar technology is considered on the basis of power conversion efficiency (PCE)<sup>3</sup>, material usage, and manufacturing complexity and cost [2]. PV devices directly convert sunlight into electricity, absorbing light (photons) of sufficient energy to promote electrons into the conduction band, where they become free charge carriers and are available to do electrical work. Organic PV devices (OPVs) accomplish this

---

<sup>2</sup>Discussed further in **chapter 2** for the material system of interest: indium-tin-oxide (ITO).

<sup>3</sup>PCE is given by the ratio of output power to input power, where the former is typically measured under the global AM 1.5 spectrum (1000  $\text{W}/\text{cm}^2$  at 25 °C), and the latter is determined by the device characteristics [218].

through the use of organic small molecules and polymers, which are compatible with low-temperature, solution processing, and integration with flexible, plastic substrates [2], [29], [30]. Of these technologies, polymer-based photo-absorbers have garnered much attention due to their extreme flexibility in synthesis; ideal for design and fabrication of OPVs, but not for long-term stability and therefore lifetime of the final product.

The use of organic, semiconducting polymers provides an attractive option to advance commercial solar technologies due to their potential for low-cost, and wide-scale adoption; however, they have yet to reach the requisite PCE and lifetime thresholds of traditional wafer-based and commercial thin film technologies [2]. Nanostructures are expected to enhance the performance of OPVs through improved long-range order, and increased surface area interaction within the otherwise disordered photo-absorbing matrix, extending the PCE and lifetime (discussed later) [12], [31], [32].

### 1.1.1 Current wafer-based and commercial thin-film PV

Wafer-based PV is epitomized by single- and poly-crystalline Si devices, which can be highly efficient and stable, but expensive [2]. Commercial thin films and amorphous Si technologies have incrementally improved key metrics such as specific power and have continued the cost-reduction trend of PV technologies, contributing to grid parity in many markets [33]. These early-generation, inorganic-semiconductor technologies currently dominate the global PV market. However, the cost of production, thick active layers, and energy-intensive processing are impeding further progress with wafer-based and current commercial thin film PV technologies [2]. An overview of the various research-grade PV technologies is summarized in **Fig. 1-2**, outlining the historical progress made in the fields of single-crystal Si, polymeric, as well as other PV technologies. The PV market has experienced a compound annual growth rate of 40 % between 2010 to 2016, with Si-wafer based PV technology accounting for ~ 94 % of total production (77.3 GW worldwide) in 2016, with the remainder being comprised of inorganic thin film technologies [34].

### 1.1.2 Emerging thin film PV

The energy-intensive and costly production of inorganic, multijunction devices has made room in the market for emerging thin film technologies — including perovskite, dye-sensitized, and OPV architectures — which offer the prospect of a new generation of solar cells that are flexible, light-weight and efficient. Efforts to further these technologies include fundamental physical studies, as well as applied research wherein new materials, device architectures, and characterization tools are being developed, with a focus on nano-scale engineering.

The current market dominance of inorganic-semiconductor -based PV technologies can be attributed to the well-known and studied Si material systems [1], heavily leveraged by the knowledge-base of the microelectronics industry—while, for example many of the polymers utilized in the OPV industry were spawned out of the later study of organic light emitting diodes. See Spanggaard et al. for a detailed review of the early progression of OPV technologies; namely, the progression from single-layer and bi-layer junctions to the now common bulk-heterojunction (BHJ) [35]. **Table 1-1** outlines PCEs for emerging PV technologies. The gains made for OPVs over the course of this project— i.e.,  $\eta_{\text{PCE}} \approx 5\%$  in 2010 [36],  $\eta_{\text{PCE}} \approx 11\%$  in 2017 [37].

**Table 1-1 Emerging consumer PV technologies [37]**

PV technology	PCE [%]	Organization:
Perovskite	$23.6 \pm 0.6$	Stanford
DSSC	$11.9 \pm 0.4$	Sharp
OPV	$11.2 \pm 0.3$	Toshiba

The low-cost potential of OPVs resides in the low-temperature, solution-based processing allowing for spray-coating or ‘printing’ of solar cells, not typically possible with current wafer and thin film PV technologies utilizing inorganic-semiconductors. Spray-coating enables efficient manufacturing through direct printing and encapsulation of OPV modules on high throughput, so-called roll-to-roll production lines [38]–[41]. However, OPVs currently remain limited by relatively low PCE and sub-par device lifetime [39], [42], [43], preventing their commercialization.

Recent research efforts to improve OPV PCE and lifetime include, but are not limited to, the synthesis of low-bandgap polymers for improved irradiance spectral match and absorption [44]–[46], controllable domain morphology (through annealing and the use of different solvents) [47]–[50], and the long-term stability of polymeric solar cells with interfacial modifiers/stabilizers [51]–[54]. Further, OPVs benefit in all facets of their quantum efficiency from nanostructure enhancement; what remains is assessing the cost and complexity associated with production and incorporation of suitable structures (discussed later). Interpenetration of the photo-absorbing matrix with low-dimensional nanostructures is expected to yield improvements in photo-absorption and photo-generation of free charge carriers by **i.** enabling thicker photo-absorbing layers, and **ii.** introducing long-range order and increased interaction between the electrode and the photo-absorbing matrix [31], [55], [56]. Commercial OPV devices have yet to be established on a meaningful scale, with few companies producing consumer products to date [34]. Of note, InfinityPV (founded in 2014 by Frederik C. Krebs of the Technical University of Denmark) produce a small-scale, retractable OPV charger for phones complete with built-in lithium ion battery [57]. In addition, InfinityPV fabricates OPV cells and modules for educational use, testing and manufacturing analysis, demonstrating their large-scale roll-to-roll printing capabilities. At the commercial scale, this coming year (2018), Heliatek (Dresden, Germany) aims to produce the first mass-produced OPV product, with a focus on building integration [58].

Establishing a market for OPV devices will require developing new characterization techniques to further iterate on pursuits such as the enhancement of a BHJ with nanostructures. A recent example of this is the work by Banerji, demonstrating the ability to optically probe the charge transfer characteristics at nano-scale interfaces intrinsic to the photo-absorbing matrix within an OPV device [59]. In this work, we investigate the interfaces within individual nanostructures suitable to be embedded within an OPV device. Here, the challenge is that the interfaces are nano-scaled, often disordered, and buried within the nanostructures. Further challenges include deconvoluting the growth dynamics and effects of high-temperature processing for the complex nanostructures observed.

## Best Research-Cell Efficiencies

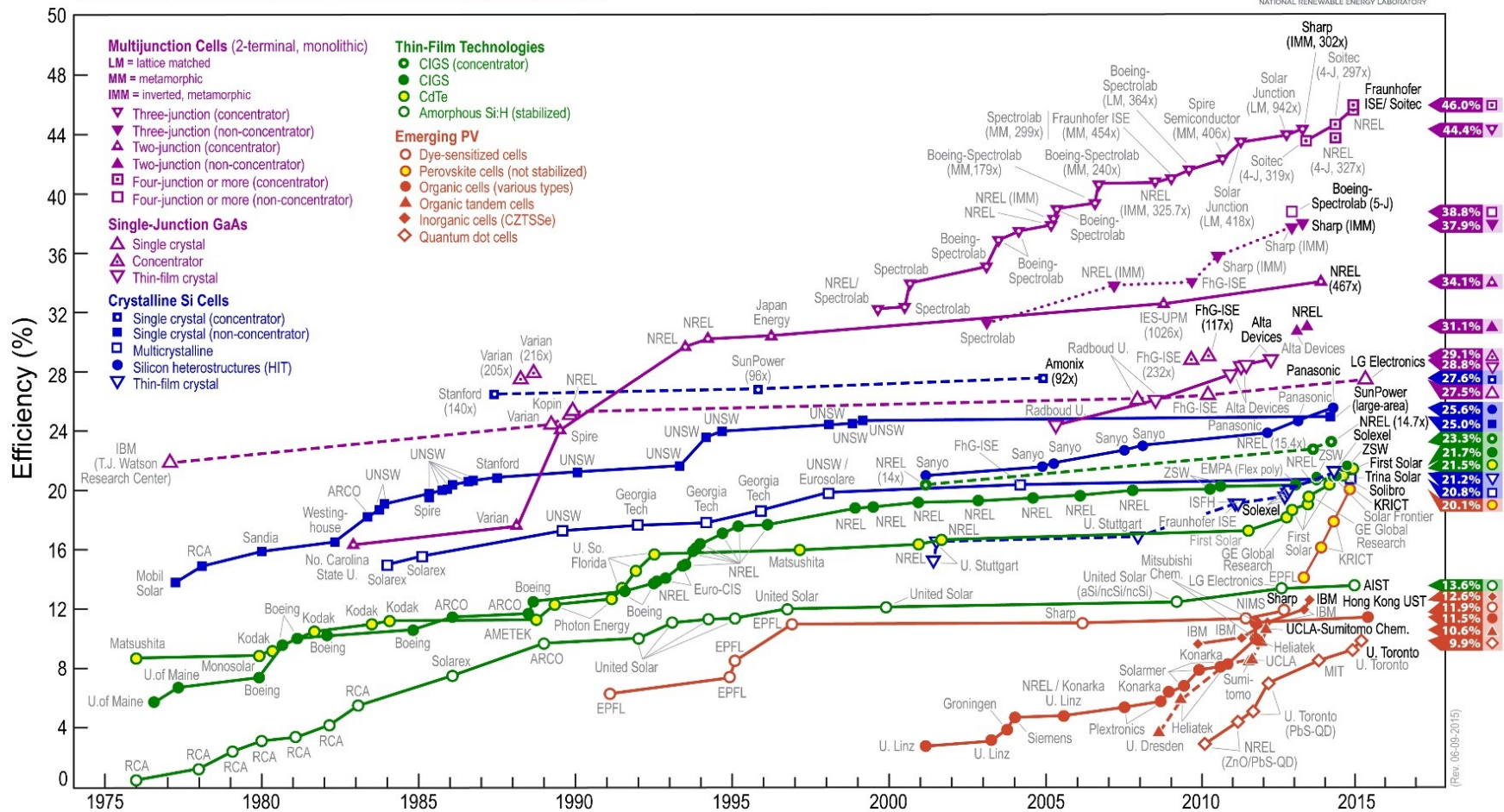


**Figure 1-2 NREL solar efficiency maps.** Best research-cell efficiencies for a variety of material systems and configurations. [http://www.nrel.gov/ncpv/; accessed Jan. 2015] Note: First commercial microprocessor (Intel 4004, 1971); first bulk polymer/C<sub>60</sub> heterojunction PV (Yu, 1994 – see H. Spanggaard (2004), ref: [35] for a detailed review.

Semiconducting, low-dimensional nanowires (NWs) that exhibit unique opto-electronic properties offer advantages of light concentrating, light trapping, and the possibility to decouple light absorption and carrier collection into orthogonal directions, all of which are highly dependent on the NW dimensions, void fill-fraction and intrinsic material properties. Tuning the feature size and density of nanostructured, metallic thin films is active area of research, and constitutes the field of plasmonics [60], [61]; this approach can help to improve absorption, while permitting a reduction in the physical thickness of thin film PV device. Although tuning of the plasmonic response of our films is outside the scope of this work, the distribution of metallic content is relevant to determine the dominant conductive paths within our devices (discussed in later chapters).

This doctoral thesis work explores the isolation of ensemble nanostructure arrays for electrical characterization and proceeds with their optimization to explore their relevance to the field of OPVs. By improving the conductivity of the nanostructures, we hope to minimize internal resistances and enable the tuning of the opto-electronic response to affect the charge transfer characteristics within the OPV device. Future challenges include the requirement that films must be concurrently optimized for light absorption and electronically coupled to the nanostructure/polymer interface for efficient charge extraction [54], [62], [63]. As this is an exploratory study, future work will likely benefit from angle-dependent optical characterization and modelling of the plasmonic response, as recently demonstrated by others for nanostructures similar to those utilized in this work [64].

## 1.2 Conventional and excitonic solar cells

To understand our material selection and configuration of the subsequent nanostructured thin film, it is useful to consider the underlying photo-conversion mechanism in OPVs and how it differs from *conventional* solar cells. Within an OPV device, light absorption results in electrostatically bound charge carriers (an electron-hole pair, EHP, or ‘exciton’), characteristic of *excitonic* solar cells, as opposed to free charge carriers (electrons and holes) in inorganic-semiconductor-derived *conventional*

solar cells [65]. The delayed charge separation characteristic of *excitonic* solar cells is due to the associated attractive coulomb potential-well of the EHP extending over a greater volume [65]. Further, the characteristically poor carrier mobility in organic polymers can be attributed to the low dielectric constant of polymers (compared to inorganic-semiconductors) resulting in the polymer intermolecular forces being too weak to form a coherent 3-D crystal lattice [35], [65]. For these reasons, charge transport must proceed by hopping between localized states [66], and the resulting carrier mobility is typically low and imbalanced within OPVs [65].

Within *excitonic* solar cells, the resulting exciton must diffuse to the donor/acceptor interface for dissociation [39], [45]. Here, the energy difference in the lowest unoccupied molecular orbital of the acceptor and the highest occupied molecular orbital of the donor provides a region of sufficient electric field to facilitate dissociation and subsequent charge collection and transport. Ideal phase segregation within a bulk-heterojunction (BHJ) would maximize the interfacial interaction between donor and acceptor phases, while providing a clear path for *exciton dissociation* and eventual charge extraction of free carriers at the respective electrodes. The overall process is characterized as the system's internal quantum efficiency (i.e., the number of electrons produced by an incident photon, shown schematically in **Fig. 1-3 a**) [32]. See Gregg et al. for a detailed review on the subject [65].

### 1.2.1 Components of an OPV Device

OPVs require a transparent conductive electrode (TCE), a metal top contact, interfacial modifying/transport layers, and the photo-absorbing heterojunction<sup>1</sup> consisting of electron-donor and -acceptor layers (see **Fig. 1-3 b**). In a 2008 review of photocurrent generation in nanostructured OPVs, Yang et al. found that a 'chessboard' morphology (inter-digitated donor and acceptor pillars) presented an ideally nanostructured OPV. The nanostructured junction improves charge collection and increases the likelihood that a photo-generated exciton will be formed within exciton diffusion length ( $L_D$ ), and diffuse to the dissociation interface [31].

---

<sup>1</sup>A blend of polymer (donor) and fullerene (acceptor) — or bulk-heterojunction (BHJ) as it is often termed—can be evolved through use of solvents, annealing, and layer-by-layer deposition [47], [48], [219].



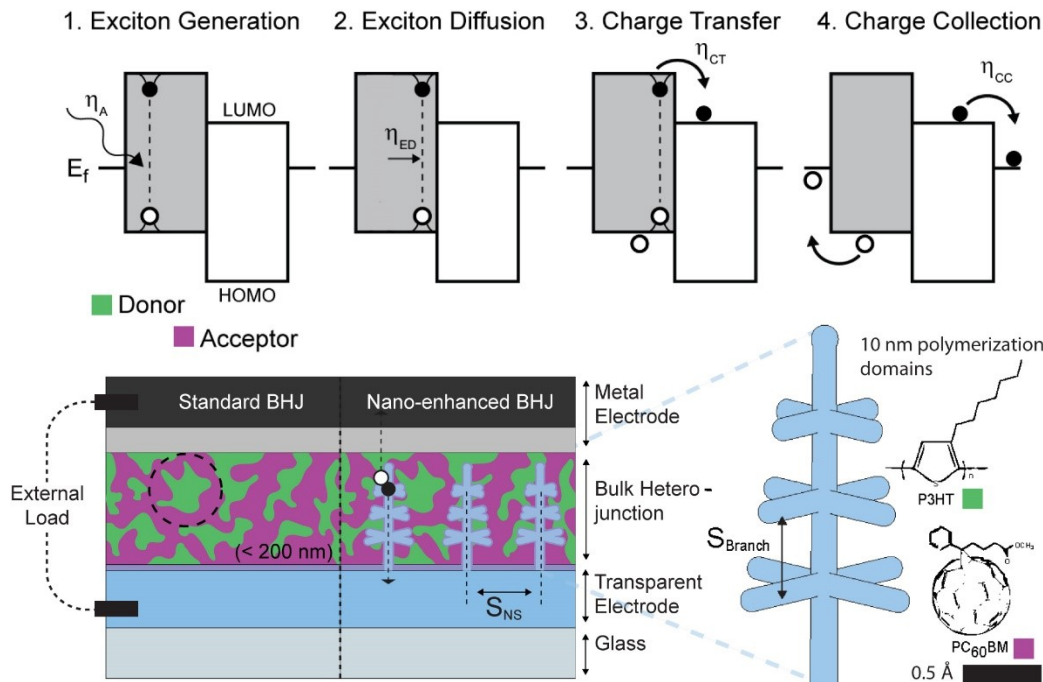


**Figure 1-3 Typical BHJ and nanostructure-enhanced OPV.** (a) schematic band-diagram depicting the photo-generation process within an excitonic OPV device, adapted from [32]; (b) BHJ with donor (green) and acceptor (purple) regions without (left) and with (right) interpenetrated with a  $\sim 1 \mu\text{m}$  thick film of branched nanotrees; (c) engineering of critical dimensions [11];  $S_{NS}$  ( $\sim 150 \text{ nm}$ ) and  $S_{Branch}$  ( $\sim 50 \text{ nm}$ ) to match the size scale of the polymerization domains ( $\sim 10 \text{ nm}$ ) and excitonic diffusion length<sup>2</sup> of a prototypical poly(3-hexylthiophene) (P3HT)/[6,6]-phenyl C<sub>61</sub>-butyric acid methyl ester (PCBM) device.

A performance limitation in OPV devices is that polymers cannot efficiently transport charges in excess of  $L_D$ , which limits the maximum thickness of the photoactive layer typically to  $< 200 \text{ nm}$  [67]. Thick active layers ( $> 200 \text{ nm}$ ) yield isolated polymer regions that do not contribute to device performance (so called ‘dead space’, see **Fig. 1-3 b, left frame**). Light absorption and charge generation are restricted to this thin photoactive layer, making it difficult to achieve commercially relevant device efficiencies. Achieving a greater thickness for commercial applications requires a chemically stable, conducting, and transparent scaffolding, with features on the size scale relevant to polymer folding within OPV devices [31], [32], [55], [56], [68]. In the spirit of the bi-continuous architecture suggested by Yang et al., the critical dimensions of a nanostructured film can be engineered in 3-D to match those of the nano-scale morphology of the photoactive matrix (shown schematically in **Fig. 1-3 c**) [56], [69], [70]. Further, interpenetration of the photo-absorbing matrix with nanostructures can

<sup>2</sup>Critical dimensions are of the order 10–30 nm (the estimated diffusion length of a photo-excited state,  $L_D$ ) [31], [32], but values as low as 3 nm appear in literature [67].

bridge those regions not within a  $L_D$  from the charge collection interface. In this manner, nanostructured TCEs provide a path towards an ordered photo-junction through the engineering of critical dimensions that match those of the photo-absorbing matrix.

When specifying the desired morphology of nanostructures for our application, we must balance geometric considerations by limiting nanostructure spacing ( $S_{NS}$ ) and branch spacing ( $S_{Branch}$ ) to the scale of  $L_D$  [31], [55], while maximizing the packing density of the photo-absorbing layer. This requires that we maximize  $S_{NS}$ , thereby introducing the concept of an optimally configured film (**Fig. 1-3 b, right frame**) [55]. For this work, from a wide-range of nanostructured thin films, we select films that are considered near-ideal for integration with an OPV device. We then attempt to optimize the conductivity of these films with post-deposition anneals.

Of note, an initial attempt by our group to structure a transparent conducting oxide (TCO), reported in 2011, utilized nanostructured indium tin oxide (ITO) transparent electrodes with critical dimensions of the same order as the domains found within OPVs. This study succeeded with modest gains in key electrical metrics scaling with surface area enhancement, but optimization attempts were not successful [71]. The shortcomings of this preliminary study were mainly due to limitations of the device electrical characterization, and an incomplete understanding of polymer alignment within nanostructure pores. At the time, only an indirect measure of electrical characteristics was available to optimize the structured ITO thin films. Since then, internal efforts have included structuring of the acceptor phase [72] and donor phase [73]. For the former, Thomas et al. structured acceptor nano-columns with inter-column spacing tuned to better match the expected dimensions encountered within an OPV, while simultaneously increasing the hetero-interface area. For the latter, van Dijken et al. utilized periodically seeded substrates to deposit donor nanostructures, to the same ends. Additionally, several researchers have attempted to structure the TCO electrode using single-crystal ITO NWs [28], [74]; however, it has remained difficult to achieve commercially relevant device efficiencies with this technique. For further details for the above studies, including some initial experiments that guided our nanostructure selection, see **Appendix A**.

### 1.2.2 TCE selection

TCEs typically fall into the categories of graphene and graphene derivatives, conductive polymers (e.g., PEDOT: PSS), TCOs (e.g., In<sub>2</sub>O<sub>3</sub>, ZnO, SnO<sub>2</sub>), and various hybrid stacks [75]–[77]. **Table 1-2** gives a summary of select material systems from the above review [75], and complimentary references.

**Table 1-2 Select bulk TCE material systems**

Material system	$\rho_{i,min}$ [ $\mu\Omega\text{ cm}$ ]	$n_{e,max}$ [ $10^{21}\text{ cm}^{-3}$ ]	$\mu_e$ [ $\text{cm}^2\text{ V}^{-1}\text{ s}^{-1}$ ]	Notes:
Graphene	5	0.3	< 5000	3
ZnO : Al	200	1	~1–65	4 [78], [79]
SnO <sub>2</sub> : F	500	1	~15–50	
In <sub>2</sub> O <sub>3</sub> : Sn	100	3	~10–150	5 [80], [81]
PEDOT:PSS	700	10	< 1	6

For an n-type TCE, where electrons are the majority carriers, the opto-electronic performance is often characterized by the pairing of high conductance and transmission to the material and deposition dependence of its observable conductivity<sup>7</sup> ( $\sigma_i$ ), or its reciprocal, resistivity ( $\rho_i$ ), and plasma frequency ( $\omega_p$ ) through measurement of the carrier concentration ( $n_e$ ):

$$\sigma_i = \frac{1}{\rho_i} = qn_e\mu_e = \frac{n_e q^2 \tau}{m_e^*} \quad (1-1)$$

$$\omega_p = \sqrt{\frac{n_e q^2}{m_e^* \epsilon_r \epsilon_0}} \quad (1-2)$$

<sup>3</sup>Ellmer estimates graphene values by areal carrier density of  $10^{13}\text{ cm}^{-2}$  and  $t = 0.34\text{ nm}$  [75]. Mobility values as high as  $200,000\text{ cm}^2\text{ V}^{-1}\text{ s}^{-1}$  have been reported for samples with modified geometries [220].

<sup>4</sup>Competing wide-bandgap transparent conducting metal-oxide material systems (i.e., the doped ZnO and SnO<sub>2</sub> material systems) currently lack the degree of branched structural control characteristic of GLAD-enhanced single-crystal growth of ITO, but process developments suggest that they too hold promise for high surface-area electrodes [54], [221].

<sup>5</sup>There are reports of single-crystal ITO NWs with  $\rho_i \sim 10^{-5}\text{ }\Omega\text{ cm}$  [117], [176], although the findings of our study suggest that these are in fact metallic NWs.

<sup>6</sup>Polymer mobility and carrier density values estimated by Ellmer et al.

<sup>7</sup>The right-hand relation of equation 1-1 is often referred to as the Drude conductivity [222].

where  $q$  is the elementary charge,  $\mu_e$  is the carrier mobility,  $m_e^*$  is the effective mass of carriers,  $\epsilon = \epsilon_r \epsilon_0$  is the permittivity of the material, and  $\tau$  the average time between collisions (the various scattering mechanisms are discussed further in **chapter 2**). Within this study, we utilize the Sn-doped  $\text{In}_2\text{O}_3$  (ITO) material system, an inorganic-semiconductor, and ubiquitous TCO [75], [80], [82], [83]. ITO films retain the highest overall figure-of-merit for TCEs, although many replacement material systems are being pursued due to sourcing issues with In [41], [75], [77], [84], [85]. For a detailed summary of the various n-type TCE technologies, see the review by Ellmer et al.<sup>8</sup> [86]. Below, a brief overview is provided for graphene and doped metal-oxide systems.

## Graphene

Graphene is the thinnest-known 2-D material, where carbon atoms form a honeycomb lattice structure. Graphene possesses ultra-high conductivity, optical transparency, exceptional structural strength, and mechanical flexibility [76]. The use of graphene to replace semiconductor material systems is one of the great challenges of modern research. Of note, the prototypical P3HT/PCBM OPV devices discussed in this work utilize the closed graphitic structure, or ‘fullerene’, (i.e., the solubilized ‘bucky-ball’, PCBM) as the electron acceptor in OPV devices due to its high electron affinity ( $\chi$ ) [29], [31], [87].

Within a graphitic sheet, each carbon atom possesses three valence electrons chemically binding it with its neighbours, and a fourth delocalized electron that contributes to electrical conduction at the sheet level. Where metals have partially full energy bands, insulator energy bands are empty or are separated by an energy gap. Within graphene, the energy bands form ‘Dirac cones’ connected at their extremities, with no gap or partially-filled bands. Consequently, graphene exhibits electronic properties for a 2-D gas of charged particles described by the relativistic Dirac equation, rather than the non-relativistic Schrodinger equation, with an effective mass [76] and exotic physical manifestations including the engineering of singularities in the density of

---

<sup>8</sup>This review asserts that the field of n-type TCOs has nearly reached maturity, the exception being ionic amorphous mixed oxides with an electron mobility  $\sim 10 \text{ cm}^2 \text{ V}^{-1} \text{ s}^{-1}$  despite large degrees of structural disorder; for comparison, hydrogen passivated amorphous Si (a-Si:H) has  $0.1 \text{ cm}^2 \text{ V}^{-1} \text{ s}^{-1}$  [75], [171].

states [88] and ballistic conduction<sup>9</sup> [89]. Currently, graphene does not possess the structural hierarchy and corresponding high surface area on the size scale that we desire, and so is suggested to be used in conjunction with low-dimensional NWs (see **chapter 7**, current and future work).

## Doped metal-oxide materials: ITO

TCOs are ubiquitous within the PV field, as they are easily vacuum deposited, combine high transparency in the visible and near-infrared with near-metallic electrical conductivity (typically in the range of  $10^{-4} \Omega \text{ cm} < \rho_i < 10^{-3} \Omega \text{ cm}$ ). TCO thin films can be further optimized through high temperature anneals and are highly tuneable. Features such as the onset of absorption and the position of the plasma edge are adjustable through the introduction and control of an electron degeneracy in this class of wide bandgap semiconductors (discussed further in terms of Sn and oxygen vacancy doping in **chapter 2** specific to ITO NWs).

ITO is the doped-metal oxide of relevance to this work. High aspect ratio ITO nanostructures can be fabricated via anisotropic etching [71], GLAD [90], kinetic vapor-liquid-solid (VLS) growth [11], [91], [92], and novel chemical synthesis techniques [93]. Each nanostructuring technique induces additional variations in structure geometry, which further extend the range of electrical properties that can be expressed by individual nanostructures. GLAD and VLS are the techniques primarily utilized in this work, and represent the current state of the art in the structuring of ITO. These inherent single-crystal NWs often possess high aspect ratios, branched morphologies with enhanced electrical conductivity, high transmissivity, and relatively low defect density [11], [92], [94], [95]. The available enhancements to growth control within this material system involves flux engineering (including deposition rate and  $\alpha$  modulation) [11], branch placement and shadowing [9], and the ordering of NW arrays through the use of lattice matched substrates [96]. Of specific interest to us is the capability of the ITO material system to produce highly branched ‘nanotrees’ (term coined in relation to their appearance) through a low temperature, self-catalyzed VLS growth process [11],

---

<sup>9</sup>In this regime, resistance no longer scales with the length of wire (as is classically the case) but becomes quantized, depending on the ratio between the width of the wire and the Fermi wavelength ( $\lambda_F$ ) of electrons (discussed further in **chapter 2** in terms of the kinetics of growth for sub-micron NWs).

[92]. Recent advances by the Brett research group have allowed for the refinement of these nanostructures, which together with the GLAD technique affords us the ability to tune structure features on the size scale relevant to OPV devices [11], [12], [31], [55].

GLAD is an advanced physical vapor deposition (PVD) technique that involves the engineering of thin film columnar structures on the micro and nanoscale. The pairing of dynamic substrate rotation and highly oblique collimated vapor flux allows us to precisely modify the apparent incoming direction and angle of flux incident upon the substrate and the subsequent evolving nanostructured film (typically  $\alpha > 70^\circ$ ). When paired with a threshold substrate heating ( $T_s = 240^\circ\text{C}$  for our experimental system), a hybrid VLS-GLAD growth regime is enabled, which further extends the library of nanostructures possible (see **Fig. 1-4 a**). Further details of the growth process specific to the ITO material system are discussed in **chapter 2**, including the use of various azimuthal angle modulation schemes explored by our lab (degrees of freedom shown schematically in **Fig. 1-4 b**).

In the present study, GLAD films containing amorphous nanopillar structures are deposited at low temperatures and oblique angle ( $\alpha = 83^\circ$ ). The film is integrated between a bottom, Au contact, and a sculpted, Ag top contact. The resulting devices are utilized as a proof-of-concept for our proposed measurement methodology (**chapter 4**). Subsequent process and fabrication procedures are applied to VLS-GLAD NW films deposited at moderate rates ( $0.5\text{ nm s}^{-1}$ ) and oblique angle ( $\alpha = 85^\circ$ ). As films deposited at low  $\alpha$  (i.e.,  $< 70^\circ$ ) result in dense films that have significant lateral conductivity, these films can be studied with traditional thin film electrical characterization techniques, and serve as experimental controls. My key contribution has been the fabrication and testing of nanostructure arrays, and the exploration of post-processing anneals to optimize the NW conductivity, while maintaining the highly-branched structures suitable for integration within OPV devices<sup>10</sup>. The primary challenge of this work was to design, fabricate and test the four-terminal nanotree ensemble arrays, while our collaborators in the chemistry department focused on integrating shorter structures into OPV devices (discussed in **chapter 7**).

---

<sup>10</sup>Selected for study as film morphological degradation (i.e., loss of branches) is observed for higher rate films, discussed further in **chapter 2**.

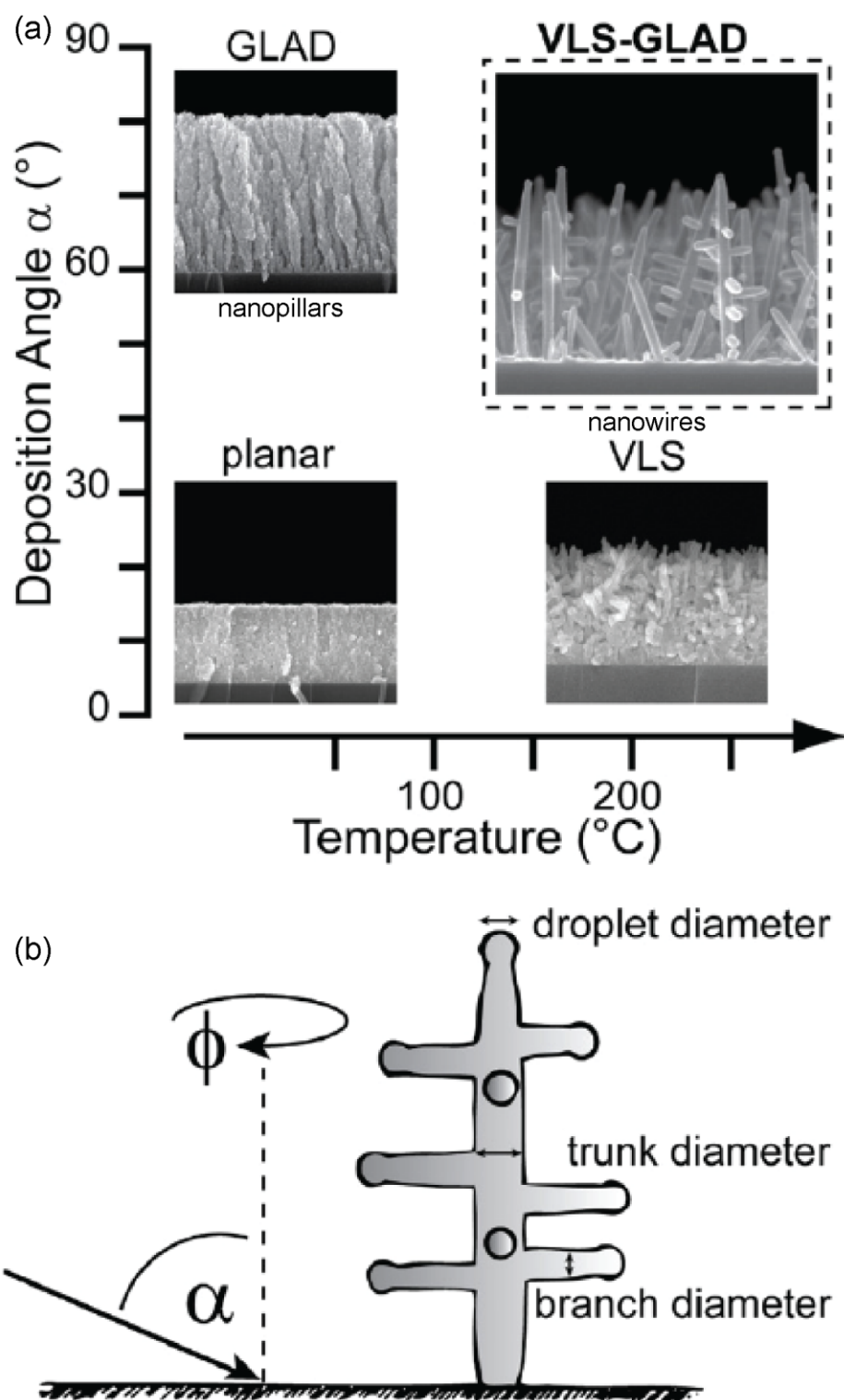


**Figure 1-4 GLAD enhanced VLS.** (a) Edge-view SEM of ITO thin-film evolution with deposition angle ( $\alpha$ ) and substrate temperature ( $T_s$ ); (b) edge-view schematic of 'nanotree' deposition parameters. Figure credit: [11].

The use of ITO is justified, despite scarcity issues with In, for three practical reasons: **i.** the exploratory nature of this work, **ii.** validating the micro-fabricated test structures utilized in this work through experimentation with such a well-known and well characterized material system, and **iii.** academically by the study of the growth mechanisms of this unique material system.

### Previous study: Low dimensional OPV

For OPV applications, our NW specification criteria requires that we maximize the NW packing density, selecting structures with features on the order of  $L_D$ , while ensuring optimal electronic alignment with the photo-absorbing polymer. Combining the above two constraints allows us to further improve the internal quantum efficiency ( $\eta_{IQE}$ )<sup>11</sup> of the OPV device by extending the allowable absorption region, while ensuring that all regions are within a distance  $L_D$  from the electrodes. To further improve the absorption efficiency ( $\eta_A$ ) of a NW-enhanced photo-junction, see discussion of: NW–NW spacing and organization [55], [97], branch configuration [64], [70], [96], and the metallic nanoparticle distribution [60]. The latter is instrumental in determining the plasmonic response of a given metallic thin film and can be used to improve  $\eta_A$ , while permitting a reduction in the physical thickness of thin film PV device [60].

Typically, exciton diffusion ( $\eta_{ED}$ ) in a polymer consists of both intra-chain transport and inter-chain hopping, and each of these two processes have their respective characteristic length scales. Kannan et al., considered a situation within the organic phase of a NW-enhanced OPV where, under the condition of quantum confinement, one encounters only single chains between NWs, thereby eliminating inter-chain hopping [55]. Further, confinement in the NWs was also suggested to increase  $\mu_e$  due to reduced phonon scattering [55]. Transport in this regime can be traced to the transmission probability from polymer to NW in the limit of overlapping exciton

---

<sup>11</sup>Ideal phase segregation within a BHJ maximizes the interfacial interaction between donor and acceptor phases, and upon absorption of a suitably energetic photon (measured by the absorption efficiency,  $\eta_A$ ) provides a clear path for *exciton dissociation* ( $\eta_{ED}$ ), and eventual charge transfer ( $\eta_{CT}$ ) and collection ( $\eta_{CC}$ ) of free carriers at the respective electrodes. This process is collectively defined by a system's internal quantum efficiency ( $\eta_{IQE}$ ) (shown schematically in **Fig. 1-3 a**) [32].



domains<sup>12</sup>. In this case, carrier transport within the NW-enhanced OPV may be completely determined by its chemical potential ( $\mu$ ). Similarly, within dye-sensitized solar cells (DSSC), Gregg et al. have shown that changing the equilibrium electrical potential across the device has little or no effect on the device behaviour, suggesting that the device is governed entirely by the chemical potential gradient ( $\nabla\mu$ ) [65].

The optimal transfer of charge carriers into the NW requires modification of the work function ( $\phi_i$ ), modified through carrier doping and modification of the surface dipole (discussed further in **section 2.5.1**) [98]. The former is considered a bulk effect (i.e., through the shifting Fermi level) and the latter a near surface effect for our system (relevant to the energy alignment at the hetero-interfaces). The requirements of electronic coupling and charge injection between polymer and NW are captured by the charge transfer ( $\eta_{CT}$ ) and charge collection ( $\eta_{CC}$ ) efficiencies, respectively. For a NW in the side-contacted configuration, a region of sufficient band-bending is required for the former, and a minimized NW  $\rho_i$  is required for the latter<sup>13</sup>. Towards maximizing  $\eta_{CC}$ , there is a compromise when fabricating highly conductive ITO<sub>VLS</sub> films: NWs with high conductivity are achievable through deposition at elevated rates [94], however increasing the deposition rate ( $\Gamma$ ) results in a reduction of the number of branches (and an increase in trunk diameter) [11]. In this elevated rate regime branches decrease to nearly zero (discussed in **chapter 2**). In this work, we explore high temperature anneals to pair the desired branched-NWs with tuneable NW conductivity, measurable with a 4 terminal, cross-bridge Kelvin resistor (CBKR) device architecture.

## 1.3 Chapter summary

Structuring the photo-active matrix in 3-D allows us to improve upon the idealized chessboard morphology suggested by Yang et al., decoupling the photo-active layer thickness from exciton diffusion-limited photo-current generation. As the resulting

---

<sup>12</sup>This is a simplified picture of a dissociation interface implemented at the NW-polymer interface (e.g., through immobilization of C<sub>60</sub> [223], [224]); this architecture requires modification to work in practice to account for the inhomogeneities in the NW surface potential (see **chapter 7**, for further discussion).

<sup>13</sup>Typically, such a junction is characterized by charge transfer into the semiconductor, and a commensurate image force in the metal. In such a case, a charge neutral level which does not necessarily align with the Fermi level, results in band-bending (i.e., junction is ‘pinned’ at this interface). Control of the width of this region is necessary to minimize the charge injection barrier from polymer to NW.

photocurrent is equal to the external quantum efficiency of the device integrated over the solar spectrum, by improving charge generation the nanostructures contribute an enhancement factor to its PCE. This allows us to challenge the current limits of light absorption and charge generation in the nanostructure/polymer matrix. This morphology represents a further step to limit recombination losses associated with polymer regions not within the  $L_D$  (i.e., the isolated regions between nanostructured domains). Thus, to advance OPV technology towards an idealized photo-absorbing junction, we use interpenetrating, nanostructured TCEs, which provide an expedited track for charge extraction in OPVs while also serving as a structural support for the photo-active matrix.

Although GLAD-structured ITO is capable of achieving a near-idealized OPV device architecture [27], [31], initial experimental results have not achieved the expected improvements. The difficulties described share a general origin: the internal structure and composition of GLAD films are poorly understood, leading to complex factors that limit device performance. As a result, focus has recently shifted to more advanced control of an individual nanostructure’s material properties including phase, crystallographic orientation, and dopant level [11], [94], [99]. With these new capabilities, it is increasingly important to electrically characterize GLAD-ITO structures, with the aim of evaluating the GLAD film’s unique opto-electronic properties for OPV device applications.

## 1.4 Thesis outline

### 1.4.1 Research goals and objectives

Fabricating the CBKR devices utilized in this work has been an exercise in bridging the morphological and electronic domains while dealing with sub-10 nm dimensions. The overarching goal is to validate the through-post (i.e., axial) conductivity measurements using direct and indirect experimental approaches, and relate the results to deposition parameters (i.e., deposition angle, rate, substrate temperature etc.) suitable for forming GLAD films of desirable conductivity.

### Primary objectives:

1. Validate electrical test structures fabricated within this work, understanding and eliminating defects to isolate an intrinsic measure of our nanostructures;

- This required the adaptation of a typically planar CBKR device architecture to accommodate our 3-D structures.

2. Use the above test structures to modify the electrical properties of our material system through post-deposition anneals (investigated to increase the requisite charged carrier density through oxygen vacancy doping of these branched nanowires).

- This required the exploration of an upwards band-bending region, oxygen vacancy neutralization upon cooling of samples, and a shifting Fermi level.

### Secondary objective:

3. Interpret our results within the current understanding of GLAD and VLS growth mechanisms.

- This required pairing recent literature and experimental observations to address the multiple paths towards metallic core-shell NWs.

My key contribution has been the fabrication and testing of laterally isolated nanostructure arrays (of the type outlined in **Fig. 1-4 a**)<sup>14</sup>, and the exploration of post-processing anneals to optimize their conductivity, while maintaining the highly-branched structures suitable for integration within OPV devices.

### 1.4.2 Outline and approach

The remainder of the thesis is organized as follows: background information is provided on the electrical test structures, thin film growth and the ITO material system (**chapter 2**). Then the experimental and characterization tools are discussed (**chapter 3**). Experimental details for the integration of different types of nanostructures follow

---

<sup>14</sup>Films deposited at low  $\alpha$  (i.e.,  $< 70^\circ$ ) result in dense films that have significant lateral conductivity. In this work, these films are studied with traditional thin film electrical characterization techniques, and serve as experimental controls.

(**chapters 4 and 5**). The main result of this thesis, outlining the optimization of our thin films, conclude the experimental work (**chapter 6**). Finally, our observations are summarized, and guide suggestions for future work (**chapter 7**).



## 2 DC electrical characterization of nanostructured thin films

For our purposes, high electrical conductivity along the length of GLAD structures — normal to the substrate plane — is necessary to exploit the high surface area of GLAD films for potential use in optoelectronic devices; however, the internal structure and composition of GLAD films are poorly understood. This leads to complex factors that limit device performance and necessitates a measure of the intrinsic properties of a thin film. To measure nanostructure conductivity along its long axis, good electrical contact to both ends of the structure is required. This has been experimentally demonstrated by others with 2-wire measurement of individual nanostructures isolated between nanoprobe and substrate; in this configuration, measurement is limited by probe dimensions and feature density, as well as low current density [100]. Techniques using a probe paired with a metallic droplet large enough to contact an array of nanostructures extends the observable test current through the ensemble array to  $\sim 1$  A [101], [102].

However, from 2-wire measurements only an indirect measure<sup>1</sup> of the evolving film's electrical properties can be determined as this measure includes the in-line contribution from top and bottom electrodes ( $R_O$ ) and the contact junctions ( $R_C$ ).  $R_C$  contributions result from the interface formed between measurement probes and a given sample; in the case of sensitive measurements  $\ll 1 \Omega$  (i.e., that of a nanostructured thin film) these contributions can occlude the desired measurements, and as such must be minimized. An absolute measure necessitates the implementation of a 4-wire measurement, which isolates our desired intrinsic measure from the above contributions.

By minimizing the contact resistivity ( $\rho_c = R_C A_C$ , where  $A_C$  is the area of the contact) at the two interfaces of interest (i.e., where electrodes contact the top and bottom of nanostructures), and integrating NWs within a four-terminal device, we attempt to obtain an intrinsic measure of resistivity ( $\rho_i$ ) for our nanostructures. The former minimizes the contributions of  $R_C$  and the latter enables a 4-wire measurement and the removal of the contributions from  $R_O$ . The design and fabrication of such a device allows us to apply Ohm's law and a simple parallel resistor model (outlined later). Application of this model to our nanostructure arrays allows us to learn more about the intrinsic electrical characteristics of our nanostructures as they shift with different processing conditions (namely, high temperature oxidation and reduction anneals). The key points of consideration for the electrical test device are:

1. 2-wire vs. 4-wire measurements.
2. Design and fabrication of a 4-terminal, micron-scaled electrical test structures including the fabrication of ohmic junctions.
3. Integration of a narrowly distributed sub-population of nanostructures into the above device (discussed further in **chapter 5**).

---

<sup>1</sup>Initially 2-wire measurements were performed to study the application of a sculpted Ag cap to bridge and interconnect our nanostructured films. See **Appendix B** for an outline of initial 2-wire measurements of GLAD-ITO films.

## 2.1 Electrical characterization of nanostructured thin films

### 2.1.1 2-wire and 4-wire measurement of nanostructures

The DC electrical characterization of an isotropic, dense planar thin film is typically determined via one of two methods, depending on sample geometry: **i.** a linear probe for infinite and semi-infinite 2-D samples, or **ii.** a van der Pauw configuration for 2-D samples of arbitrary geometry. The linear probe technique is often utilized in an in-line four-point-probe (4PP) configuration<sup>2</sup>, and is a robust technique with standardized equipment and a well-developed analytical toolkit [103]–[105]. The van der Pauw configuration has been utilized to consider samples fabricated on the micron-scale. Both methods are 4-wire measurements that utilize four, ideally point contacts that are used to mitigate resistances associated with contact contributions typical of 2-wire measurements. For a standard measurement on a thin film, where film thickness,  $t$  is much smaller than the probe spacing, the equation for  $\rho_i$  is [103]–[105]:

$$\rho_i = \frac{\pi t}{\ln(2)} \frac{\Delta V}{I_{\text{test}}} \approx 4.532 \cdot t \frac{\Delta V}{I_{\text{test}}} \quad (2-1)$$

Where  $I_{\text{test}}$  is the applied test current, and  $\Delta V$  the voltage drop across the sample. If the doping profile of the thin film is known (i.e., it is uniform across  $t$ ), then  $\rho_i$  can be found directly, otherwise sheet resistance ( $R_S = \rho_i/t$ ) is presented on an  $[\Omega/\square]$  basis. Moving from the  $\mu\text{m}$ -scale to nano-scale samples requires correction factors accounting for non-idealities stemming from **i.** reduced film thicknesses, **ii.** finite lateral dimensions, and **iii.** probing near the edge of a sample [103]–[105]. For a detailed outline of the determination of  $R_S$ , the evolution of van der Pauw structures and the available electrical line-width test structures for semiconductor process characterization, see the thesis by S. Smith [106].

---

<sup>2</sup>For a 4-wire measurement, the four probes are separated into outer force (i.e., current-carrying) and inner voltage-sensing pairs, with a negligible current (and therefore voltage drop) at the sense-probe/film interface. In the case of an inline 4PP measurement, we are limited to the lateral resistance along the current path between the inner two probes of interest, which does not account for anisotropies in nanostructured thin films. Electrical anisotropy has been observed in nanostructured ITO thin films, with in-plane resistivity depending on the azimuthal angle between nanostructure orientation and electrical conduction direction [111].



When applying the 4PP technique to GLAD films, it has been observed that as  $\alpha$  increases, the in-plane resistivity increases from near-bulk values to many orders of magnitude greater [90], [107]–[111]. Films deposited at increasingly oblique angles also have increased porosity and nanostructure separation; our own 2-wire measure of the resistance across the thickness of the film revealed a steep increase for  $\alpha > 70^\circ$  (in **chapter 4** we observe  $\sim 5$ -fold increase, see also **Appendix B**). For this reason, there exists a threshold deposition angle for each material system above which the standard 4PP characterization techniques yield ambiguous results [90], [108]–[110], that are likely a measure of the morphological evolution of the thin film rather than an accurate measure of  $\rho_i$ . This relationship has been attributed to a decrease in film density, which **i.** results in diminished and preferential conductive pathways (i.e., electrical anisotropy) and **ii.** leads to laterally isolated structures in the extreme (as observed in **Appendix B**). Reliable characterization and optimization of the electrical properties of nanostructure arrays is a challenge due to this laterally disconnected architecture. The extensive boundaries that exist in GLAD structures, as well as the statistical fluctuations in the microstructural properties (e.g., statistical distributions in column diameter, crystallite size, dopants etc.), are also expected to affect electrical behaviour [112]–[115].

Efforts to achieve isolated measurements of single ITO NWs have involved the 4-wire electrical characterization, conducted across lithographically defined contacts (shown schematically in **Fig. 2-1 a**) [115]–[119]. These studies have been limited by relatively low through put (typically  $< 40$  NWs for a given study). Complementary to these isolated measurements, it is desirable to develop a measurement technique that integrates and characterizes the nanostructure ensemble behaviour normal to the substrate (i.e., axial)—a configuration common in typical device applications. Test structures must be fabricated on the size scale relevant to microelectronic devices, as for large arrays, the contribution of the junctions is on the same scale as the device resistance ( $R_D$ ), preventing a direct measurement of the resistance contribution of an individual nanostructure ( $R_P$ ). In **chapter 3**, an initial sensitivity study outlines the relationship between the dimensions of our test structures, the number of nanostructures contained and our sensing limits according to available equipment.

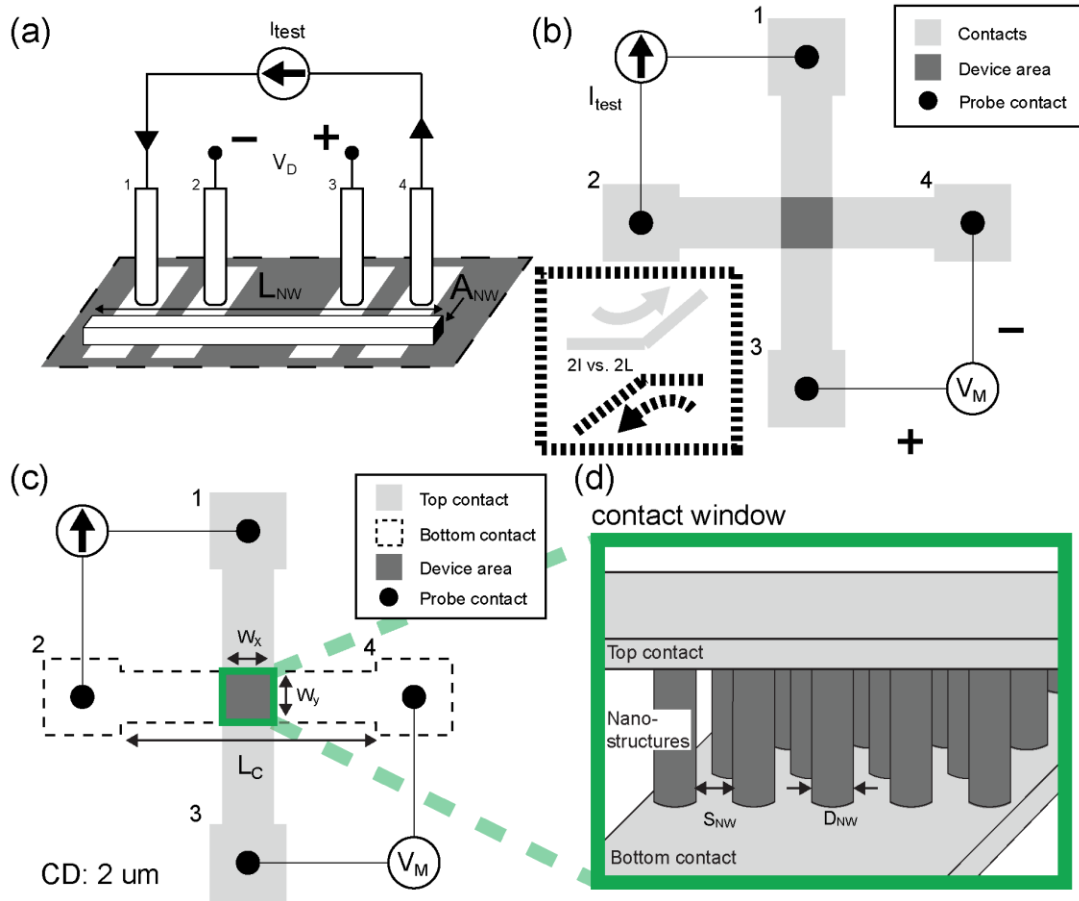


**Figure 2-1 3D-CBKR and critical dimensions.** Schematics of (a) 4PP NW testing configuration; (b) Greek cross architecture in testing configuration, inset: 2L configuration shown, with 2I resulting with straight contacts; (c) a modified CBKR with 2 μm critical dimension; and (d) Oblique schematic view of the contact window where nanostructures are incorporated into an idealized test structure with metallic top and bottom contacts. Contacts are typically numbered from the top, moving counter-clockwise. Current is typically injected up through the diffusion layer (i.e., here, the bottom ITO contact and the NW array) into the metal top contact.

## 2.1.2 Micron-scaled electrical test structures

To measure a homogenous thin film on the size scale relevant to microelectronic devices, a Greek Cross is often utilized (see **Fig. 2-1 b**) [106], [120]. To study the junction between two dissimilar materials, a cross-bridge Kelvin resistor (CBKR) is used to determine the specific contact resistivity ( $\rho_C$ ), which controls the contact interface resistance,  $R_C$  [121]–[125]. In a commercial production-line, monitoring the variability of  $\rho_C$  between a metal and a diffusion region (i.e., a semiconductor thin film) is critical to the fabrication process, as too large a  $\rho_C$  results in the majority of the device voltage being dropped across the interface and introduces an inefficiency in operation (discussed later in terms of an ohmic junction). Therefore monitoring  $\rho_C$  is typically

undertaken with a CBKR fabricated on the same wafer or die as conventional devices to monitor the process, and is highly sensitive to fabrication parameters<sup>3</sup>.

Towards an intrinsic measure of our ITO nanostructures, we must adapt the CBKR test structure to incorporate our nanostructures (shown schematically in **Fig. 2-1 c, d**). The now-termed ‘three-dimensional CBKR’ (3D-CBKR) has critical dimensions that are determined by our practical lithographic limits (line width = 2  $\mu\text{m}$ ), and for our size scale allows for measured  $R_D \ll 1 \Omega$ .

### Previous study: CBKR in operation

With our general specifications and fabrication challenges outlined above, we first considered a typical CBKR device and the basic assumptions originally presented by Loh et al. [125]:

1. Neglect the minority carrier contribution (as the metal-semiconductor interfaces inject far more majority carriers). This allows us to solve the majority carrier continuity equation in the semiconductor region immediately beneath the metal contact (elsewhere, in the charge free region,  $\nabla^2 V = 0$  holds). Under bias, a current  $I_{\text{test}}$  is injected into the contact through the horizontal arm and a constant Kelvin potential ( $V_K = I_{\text{test}} R_K$ ) is measured in the perpendicular arm, far away from the contact<sup>4</sup>.
2. By assuming  $R_{S,\text{metal}} \ll R_{S,\text{diffusion}}$ , the contact-diffusion system can be described entirely by the surface potential  $V$  in the diffusion region. This relationship is governed by the Helmholtz equation which applies in the diffusion region directly underneath the metal contact<sup>5</sup>:

$$\frac{\partial^2 V}{\partial x^2} + \frac{\partial^2 V}{\partial y^2} = \frac{R_S}{\rho_C} V = \frac{V}{(l_t)^2} \quad (2-2)$$

---

<sup>3</sup>Discussed in **section 2.3** is the tuning of  $\rho_C$  and its relevance to the 3D-CBKR.

<sup>4</sup> $V_K$ , which does not depend on its point of measurement:  $V_K = V_K(R_S, \rho_C, w, l)$  and therefore includes geometric contributions resulting from asymmetries in the test current path. Spurious contributions cause deviations from extracted and actual  $\rho_C$  values [126].

<sup>5</sup>In this 2-D model, conductivity is assumed independent of the  $x$  and  $y$  spatial variables (i.e., all effects of the  $z$ -axis are lumped into the one parameter,  $R_S$ ) [125], [126]. Deviations in device resistance with processing then give some indication of the changing channel dimensions. For an isolated nanostructure, this can apply to oxygen rich, assumed insulating device regions (the surface depletion region in **chapter 5** and chemical depletion layer observed in **chapter 6**, discussed later).

The last term of the Helmholtz equation represents the current flow in a direction perpendicular to the diffusion level into the metal level (which is referenced as zero potential—i.e., the metal layer is assumed to be an ideal ground plane). The potential  $V$ , depends on the material parameters ( $R_S$ ,  $\rho_C$ ) and the physical dimensions ( $w$ ,  $l$ ) as well as the two spatial variables ( $x$ ,  $y$ ). Under special circumstances, namely when the contact size ( $l_C$ ), is smaller than the transfer length  $l_t (= \sqrt{\rho_C/R_S})$  — the distance at which 63% of the current has transferred to the sample —  $R_C = \rho_C/A_C$  (that is the, ‘one-lump’ model holds) [125], [126]. This 0-dimensional model assumes that the potential is constant in the semiconductor layer and the current density entering the contact window is uniform<sup>6</sup>.

Of importance to achieve an isolated measure of  $R_C$  for a CBKR is the mitigation of ‘current-crowding’ effects, resulting where device topography results in regions of varying electric field density and spurious contributions to our measured Kelvin resistance (i.e.,  $R_K = R_C + R_{\text{geom}}$ ). Investigated in detail by Schreyer et al., as  $\rho_C$  approaches zero,  $R_K$  approaches  $R_{\text{geom}}$  (i.e., for small  $\rho_C$  the measured resistance approaches a constant value which is a function of the contract geometry). Other notable geometric considerations include: **i.** joule heating at sharp corners; and **ii.** current bending where right angles in the current path result in additional contributions to  $V_K$  (discussed further in **chapter 3** in terms of the applicable design rules).

The CBKR can be fabricated in either a ‘2I’ or ‘2L’ configuration. In the former, the angle between top and bottom contact arms is  $90^\circ$  (i.e., there a right angle in the current path), which can result in joule heating and ‘current bending’. The ‘2L’ configuration can correct these contributions by aligning the injection and extraction points. Although the 2I configuration is known to exhibit a geometric contribution to resistance measurements [127], our electrode resistivity values and test currents are low enough to mitigate any current crowding issues (outside of edge defect contributions), and we do not expect current bending due to our 3-D architecture (discussed further in **section 2.3** in terms of the electrostatics at the metal/nanostructure interface). The

---

<sup>6</sup>This model applies for cases in which  $l_C < l_t$ , where the latter is set by the channel dimensions. See **figure 2-4** (discussed further in terms of an ohmic junction). Within this model, the  $R_C$  of a contact will approach  $\rho_C/A_C$  as the contact size decrease below the transfer length.

pairing of our 3-D geometry and ohmic junctions<sup>7</sup>, is believed to negate the above geometric contributions, as such we utilized a CBKR in the 2I configuration vs. the 2L configuration for ease of alignment and fabrication (see **Fig. 2-1 b**, inset for schematic) [121], [128], [129]. Also of note, non-linear behaviour has been reported with increasing  $I_{\text{test}}$  [122], but was not observed within the test window for our devices.

For a typical planar CBKR,  $R_S$  is given by [125], [126], [130]:

$$R_S = \left( \int_0^t \sigma_i(z) dz \right)^{-1} = \frac{\rho_i}{t} \quad (2-3)$$

By minimizing the contact resistivity ( $\rho_c$ ) at the two interfaces of interest (i.e., where electrodes contact the top and bottom of nanostructures), and integrating NWs within a four-terminal device, we are limited in this device by a single interface<sup>8</sup>. In this case,  $R_S$  can be replaced by the resistance of a parallel array of resistors representing an NW of mean dimensions ( $R_P$ )—here the modified Kelvin potential is dependent only on the resistance of an element  $R_P$  and the number of elements,  $N_P$  within a given device (see the device error analysis of **chapter 5**). Applying a similar 2-D model (above) to our NW arrays, we assume that the NWs are uniform in the x and y dimensions, with variations assumed only in the z-dimension (i.e., along the length of the NWs). The design and fabrication of such a device allows us to apply Ohm's law and a simple parallel resistor model. Reducing this discussion required that we address multiple scattering mechanisms (discussed later). Application of this model to our nanostructure arrays allows us to learn more about the intrinsic electrical characteristics of our nanostructures as they shift with different processing conditions (namely, high temperature oxidation and reduction anneals). Deviations in  $R_D$  with processing then give some indication of any change in the channel cross-sectional dimensions. For an isolated nanostructure, this can apply to oxygen rich, assumed insulating device regions (the surface depletion region in **chapter 5** and chemical depletion layer observed in **chapter 6**).

---

<sup>7</sup>Made possible by establishing a homojunction at the bottom interface and minimizing the work-function offset at the top interface.

<sup>8</sup>For nano-scale structures, particularly in the end-bonded configuration metal-induced gap states are secondary to dominant electrostatics at reduced dimensions. At low current densities, it is therefore expected that the electrostatics owing to our NW dimensions dominate the current flow (discussed later).

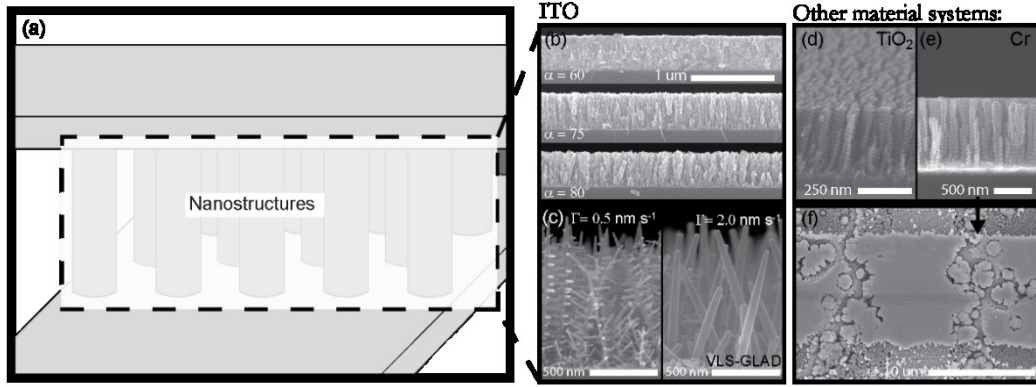


**Figure 2-2 Candidate material systems explored.** (a) A variety of metal and metal-oxide materials compatible with GLAD were investigated for integration into the device form presented previously; (b) ITO was selected for due to its ability to form well defined nanostructure and (c) tunable branching during VLS growth. Also explored were (d)  $\text{TiO}_2$  films (e) and Cr films; device-scale defects prevented the use of the latter (f).

## 2.2 Candidate material systems

The initial search for a candidate material system required that we consider the ease of deposition and integration into final device form as previously discussed (**Fig. 2-2 a**), as well as the stability of the thin film during post-deposition anneals. Ultimately ITO was selected due to the well understood and characterized deposition parameters as well as the flexibility in the tuning of the nanostructures (see **Fig. 2-2 b, c**) [9], [11], [90], [131]. These structures are discussed in detail in the proceeding section. Also investigated were  $\text{TiO}_2$  structures deposited at  $\alpha = 86^\circ$  (see **Fig. 2-2 d**, these structures were also used in the SBD-polymer pore-confinement experiments outlined in **Appendix A**) and Cr deposited at  $\alpha = 86^\circ$  (see **Fig. 2-2 e**). The latter material system proved to be incompatible with our microfabrication processing window, likely due to the high density of defects in the electrode over-lap region (see **Fig. 2-2 f**). ITO films were also found to have significant film- and device-level defects, which precluded the use of narrow traces for the bottom electrode in many cases (see later chapters, and **Appendices C** and **D**). Defects dictated nominal device areas ( $A_D$ ) of  $> 25 \mu\text{m}^2$  for GLAD-ITO and VLS-GLAD-ITO devices in order to achieve an unobstructed measure of the electrical characteristics. Also investigated were Ag nanostructured films deposited at oblique angles; however, due to the relatively low melting point of Ag [132], films did not maintain their nanostructured form during post-deposition annealing (not shown).

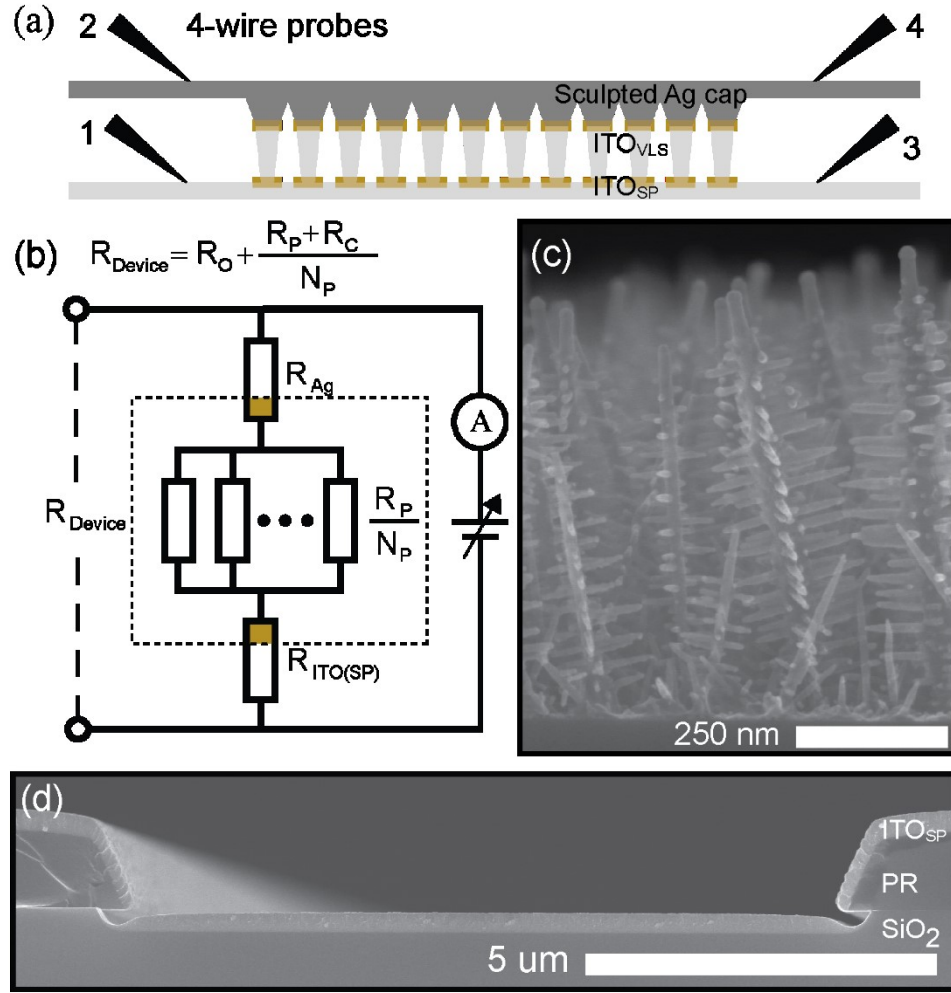


**Figure 2-3 Integration schematic for the nanostructures.** (a) Schematic of our 4-wire testing configuration; (b) schematic model depicting an array of parallel resistive elements in series with a contact resistance; (c) nanotree films are integrated within devices fabricated on (d) p-type Si wafers, with sputtered ITO acting as the growth surface and bottom electrode.

## 2.3 Our methodology

Shown schematically in **Figure 2-3 a** is device in final 4-wire testing configuration. We utilize an idealized parallel resistor model, where **Figure 2-3 b** is a schematic depiction of a circuit model containing an array ( $N_p$ ) of parallel resistive elements ( $R_p$ ) in series with a contact resistance ( $R_C$ ). Further, tuning  $\rho_C$  is dependent on the barrier height (governed by the pairing of metal and semiconductor, and the quality of contact) and the doping density (measured by the position of the Fermi level,  $E_F$ ) and effective mass ( $m_e^*$ ) of carriers within the nanostructure(s) [95], [133], [134]. **Figure 2-3 c** is an example of processed NWs integrated within our devices. Devices are fabricated on p-type Si

wafers, with sputtered ITO (ITO<sub>SP</sub>) acting as the VLS growth surface and bottom electrode (**Fig. 2-3 d**). Our parallel circuit model begins with Ohm's Law:

$$\mathbf{J} = \sigma_i \mathbf{E} \quad (2-4)$$

Where the  $\sigma_i$  is the proportionality constant empirically determined between current density ( $\mathbf{J}$ ) and an applied electric field ( $\mathbf{E}$ ), for a homogeneous sample with dimensions of length  $L$  and cross section  $A$  in a uniform electric field<sup>9</sup>. Assuming the applied electric field is oriented parallel to the material's long axis,  $J = I A^{-1}$  and the potential difference between its two ends is  $V = EL$ . The deposition of uniaxial films (introducing radial symmetry) and the fabrication of ohmic contacts (ensuring that the majority of voltage is dropped across the bulk of the NWs) allows us to combine the above relations and solve  $R_P$  for the parallel array:

$$R_P = \rho_i L / A \quad (2-5)$$

Here,  $R_P$  is determined from the device resistance ( $R_D$ ) in the 4-wire configuration applying Ohm's law ( $V_M = I_{\text{test}} R_D$ ). Utilizing a simple parallel resistor model (assumes a uniform current distribution):

$$R_D = \frac{\prod_{i,j} R_{ij}}{\sum_{i,j} R_{ij}} = \frac{R_P}{N_P} \quad (2-6)$$

Here  $R_{ij}$  is a typical resistive element (i.e., a single post of mean dimensions) and  $N_P$  is the number of elements within a device. Assuming uniform posts numbering  $N_P$ , and that the applied field is uniform across a given electrode (i.e.,  $R_{S,\text{metal}} \ll R_{S,\text{diffusion}}$ ), we can combine equations (2-4) and (2-5):

$$\rho_i = N_P \cdot R_D \frac{A}{L} = N_P \frac{E}{J} \quad (2-7)$$

Substituting the previous relationships for current density and device voltage yields the right-hand relation; and assumes a uniform current density and ohmic junctions (schematically shown in **Fig. 2-4 a** for a non-uniform current distribution arising from a

---

<sup>9</sup>Here  $L$  is the length of a NW ( $L_{\text{NW}} = t$ ). In **chapter 4**, a cylindrical model is used for GLAD-ITO nanostructure to account for the observed broadening of nanostructures (discussed later).



device-scale defect—a similar situation is encountered in **chapter 4** due to the edge defects caused by the step height difference introduced by the bottom electrode) [126].

Deviations in device resistance with processing give some indication of the changing channel dimensions through the effect on the supported transverse modes. Of note, the channel dimensions of the core configurations observed in this work are on the order of the elastic mean free path ( $l_0$ ) observed by others for similar ITO NWs [119], [135], [136], requiring that we consider the mesoscopic character of our parallel arrays (beyond the scope of this work, see **chapter 7** – Future work). Here, the conductance of the sample is given by the sum of all the transmission possibilities an electron has when propagating with energy equal to the chemical potential ( $\mu$ )<sup>10</sup> [137]. (This is believed to be facilitated in our ITO NWs by the ionic contribution introduced by oxygen vacancies ( $V_{\text{O}}$ ) and  $\text{O}^{2-}$  ions<sup>11</sup>).

Through the microfabrication techniques described in the coming chapters, we are able to adapt a planar four-terminal CBKR device architecture to measure the axial resistivity of nanostructured arrays, and obtain a measure of  $R_p$ . This required that we **i.** fabricate high-quality electronic junctions, **ii.** select suitable nanostructures to be grown upon lithographically defined contacts, and **iii.** test devices within a specified tolerance range, so as to avoid damage. The assumption here is that we are operating at sufficiently low current densities, and where conduction modes do not mix (the latter is discussed in **chapter 3**).

## 2.4 Ohmic junctions

In the present study, the ohmic behaviour of devices is a critical requisite for an intrinsic measure of our nanostructures (see **chapter 4** for GLAD-ITO devices and **chapter 5** for VLS-GLAD-ITO devices). For an ideally ohmic junction, there is an unimpeded

---

<sup>10</sup>In a mesoscopic system, the electron motion is quantum mechanically coherent in the entire sample; the transport is therefore analyzed as a wave scattering problem; a measured system is said to be mesoscopic if the length scales characteristic of the device fulfill the relationship outlined by:  $a_0 \ll \lambda_F \lesssim \ell_0 \lesssim \mathcal{L} < \ell_\phi \lesssim \ell_{\text{in}}$  (here, we have, in ascending size, the atomic Bohr radius, the Fermi wavelength of the electron, the elastic mean free path, the sample size, the coherence length, and the energy relaxation length) [137].

<sup>11</sup>Within ITO thin film samples, the presence of a mobile electrolyte has been shown to eliminate all equilibrium or induced electric fields with a screening length of  $\sim 1$  nm [225].

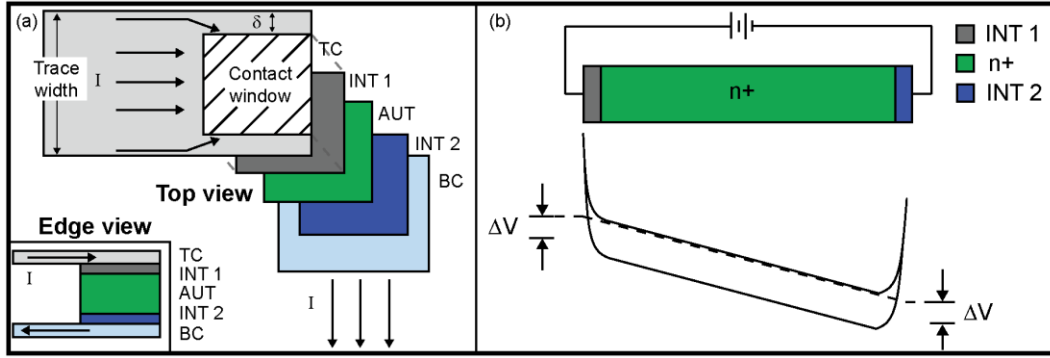


**Figure 2-4 Current injection and voltage characteristics of 3D-CBKR.** (a) Top-down schematic of current injection where difference in trace width and contact window ( $\delta$ ) introduces a non-uniform current distribution. For out VLS-GLAD devices the current path is through: the top contact (Ag), interface 1 (Ag/ITO<sub>VLS</sub>), the array under test, interface 2 (ITO<sub>VLS</sub>/ITO<sub>SP</sub>), and through the bottom contact (ITO<sub>SP</sub>); inset: edge view of same. (b) Schematic band diagram depicting an n+ region between ideal ohmic contacts with uniform current distribution resulting in a linear  $i$ - $v$  relation; adapted from ref: [125], [126].

transfer of majority carriers from one material to another (shown schematically in **Fig. 2-4 b**). The fabrication of high quality contacts that pass a uniform current density can be extremely challenging. Fabrication requires geometric considerations, particularly the configuration of the region between top contact and the array under test (ideally overlapping with the ‘contact window’) as well as the electronic band alignment at the metal-semiconductor interface. The former requires consideration of the overlap region of the metal top contact and nanostructures, while the latter requires alignment between the energy levels in the conduction band ( $E_C$ ) and valence band ( $E_V$ ) in the semiconductor and the Fermi level ( $E_F$ ) in the metal. Linear current-voltage ( $i$ - $v$ ) characteristics are indicative that under test the majority of the voltage is dropped across the bulk of the NW(s) (i.e., there is a negligibly small voltage drop across the junctions), providing an isolated measure of the array under test.

The fabrication of an electronic-grade (ohmic) junctions requires detailed consideration of the metal top contact as well as the individual nanostructures. For example, a typical VLS-grown ITO NW contains a metal catalyst nanoparticle, and so influences the local carrier concentration and therefore alignment at the electronic junction (**Fig. 2-5 a** shows an elemental map of a typical ITO NW containing an In catalyst nanoparticle — the particular characterization technique utilized here is discussed further in **chapter 3**). An estimate for the relative position of the Fermi Level

(defined with respect to the metal top contact chemical potential),  $(\mu - E_C) \approx 11 \text{ meV}$  (estimated using typical values for metallic ITO,  $n_e = 5 \times 10^{20} \text{ cm}^{-3}$ )<sup>12</sup>.

For VLS-GLAD-ITO devices the interfaces of interest are:

1. **Interface 1:** between the top contact (Ag) and individual ITO NWs (ITO<sub>VLS</sub>) under test. An Ag top contact selected for its thin film stability [132] and its similar work function and mobility to ITO ( $\sim 4.6 \text{ eV}$ ,  $\sim 40 \text{ cm}^2 \text{ V}^{-1} \text{ s}^{-1}$ ) [138], shown schematically in **Fig. 2-5 b**; and
2. **Interface 2:** between NWs and the bottom contact, considered as a n-n+ homojunction, with a gradient of carriers from ITO<sub>VLS</sub> to ITO<sub>SP</sub><sup>13</sup>.

The influence of the respective junctions must be assessed in conjunction with the device *i-v* characteristics, which to the first-order demonstrate a negligible contribution from the interfaces (discussed in later chapters, see **Fig. 2-5 c** for schematic band-diagram of an ideal ohmic junction with an unimpeded transmission pathway).

For an end-bonded metallic nanostructure forming atomic contact with a metal electrode, it is expected that a tunnel junction is formed between the metallic contact and our metallic nanostructures. During the study of metal contacts to degenerate semiconducting NWs, Stern et al. demonstrated similar behavior to bulk interfaces, and found that they can be treated with the same tunneling model used for the bulk material<sup>14</sup> [123]. Considering then the region near the metal catalyst droplet, here the barrier to conduction is estimated as the work-function offset between Ag and ITO (shown schematically in **Fig. 2-5 d**). This offset is dependent on the crystal orientation of Ag [138], and the local surface conditions and metallic contributions of the

---

<sup>12</sup>Estimated using  $m^* = 0.3m_e$ . Of note, Reunchan et al. found that the introduction of  $V_O$  to an ITO unit cell begs the consideration of an evolving band structure with an indirect transition becoming energetically favorable (the  $V_O$  transition was estimated to be  $\sim 200 \text{ meV}$  below the CBM) [134].

<sup>13</sup>As the NWs and bottom contacts are both subject to post-processing anneals, we must consider the difference in oxygen diffusion between them; however, by current continuity the direction of the band-bending at the bottom interface is expected to be secondary to the dominant electrostatics [124].

<sup>14</sup>Carrier transport across an ohmic junction is characterized by 3 primary mechanisms [1]: **1.** Thermionic emission, where carriers have sufficient energy to overcome the barrier; **2.** Thermionic field emission, where ‘hot carriers’ tunneling through the top of the barrier; and **3.** Field emission, where carriers can tunnel through the entire barrier. For the latter, the depletion layer is sufficiently narrow — a result of high doping density in the metallic semiconductor [1].

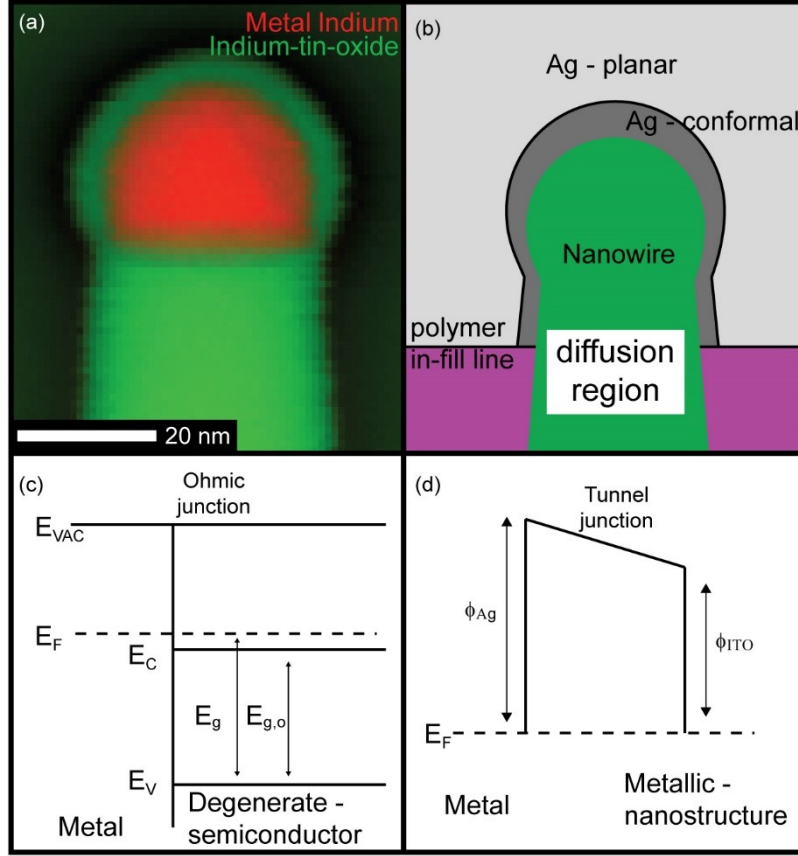


**Figure 2-5 NW-metal interface.** (a) elemental mapping determined with electron-energy-loss spectroscopy (EELS) of an as-deposited NW grown at moderate rate ( $1.0 \text{ nm s}^{-1}$ ,  $\alpha = 85^\circ$ ); (b) edge-view schematic for overlap region between conformal Ag top contact and ITO NWs (the purple region is the insulating polymer used for isolation); (c) metal contact to a degenerate semiconductor band diagram for an ohmic contact; (d) contact between a metal and a metallic nanostructure results in the presence of a tunnel barrier whose profile is determined by the work-function offset of the metal and metallic nanostructure ( $\phi_{\text{Ag}}$  and  $\phi_{\text{ITO}}$ ); adapted from ref: [124].

nanostructure, all of which vary with deposition conditions (discussed further with respect to ITO in **section 2.5**). An estimate then of the barrier height in this region is  $\phi_b \lesssim 100 \text{ meV}$ .

For nano-scale structures, particularly in the end-bonded configuration metal-induced gap states are expected to be secondary to dominant electrostatics at reduced dimensions. At low current densities it is therefore expected that the electrostatics owing to our NW dimensions will dominate the current flow [124]. Discussion of this situation is necessary due to unique structures encountered with post-processing, and is expected to be the cause of the anomalous distribution of our devices (discussed further in **chapter 6**).

## 2.5 ITO material system details

The key metrics when considering the performance of a TCO is the opto-electronic response of the structures (related to the carrier generation level, i.e., through the introduction of  $V_0$ ) which involves balancing **equations 1-1** and **1-2** to tune the pass band for incident light as well as tuning of the charge transfer characteristics within an OPV and modification of the charge injection barrier through tuning  $\phi_i$ . A system's  $\phi_i$  is modified through [98]:

1. Carrier doping ( $\phi_i$  decreases as Fermi level increases for fix ionization potential); and
2. Modification of the surface dipole ( $\phi_i$  increases as ionization potential increases for fixed Fermi level).

The former is considered a bulk effect (relevant to the film's opto-electronic response i.e., through the shifting bandgap and Fermi level) and the latter a near surface effect for our system (relevant to the energy alignment at the hetero-interfaces within an OPV device). See **chapter 3** for an outline of the characterization methods.

ITO is a well-known, wide bandgap, degenerately doped n-type semiconductor — a standard TCE used in many organic light emitting diodes and OPVs [75], [80], [82]. ITO has an intricate cubic bixbyite crystal structure with a unit cell comprised of 80 atoms [133], [134], and an evolving band structure, highly dependent on phase, crystallinity and doping [80], [81], [133], [134], [139], [140]. For example, an ITO thin film is often defined as oxygen rich or metallic, with the (222) lattice plane associated with a high density of interstitial oxygen sites, affecting the incorporation of Sn dopants during film growth [141], [142]. Heavy degenerate doping has been shown to add up to 0.5–0.8 eV to the fundamental bandgap ( $E_{g,o}$ ) of  $\text{In}_2\text{O}_3$  (see **Fig. 2-4 c**), with resulting values of  $E_g = 3.5\text{--}4.1$  eV being reported (a typically cited value is 3.75 eV) [143], [144]. The work-function of ITO varies depending on growth and annealing conditions. Typically, a value of 4.7 eV is used for the work-function of ITO [112], but this can vary by up to 0.6 eV depending on processing conditions [145]. See Bel Hadj Tahar et al. for a detailed review on the optoelectronic properties of ITO, including variations with post-processing [81].

Of note, Ishida et al. explored the post-deposition annealing of films deposited at normal incidence and  $\alpha = 45^\circ$ , in air and hydrogen atmospheres [112], [146]. Within these studies, it was demonstrated that the surface dipole and phase of the thin films could be affected by the annealing process, decreasing with the amounts of metal In and Sn, and amounts of crystalline ITO phase. It was further noted that annealing also introduced complicated surface effects — an issue that is exacerbated with increasing deposition angle, and the resulting increase in surface area to volume ratios. We are further interested in the interior structure of the NW as well as the critical electronic dimensions.

The near-surface region is defined by a thin amorphous surface layer and epitaxially matched branches [96]. After the formation of a trunk-branch pair, continued deposition with incomplete incorporation, results in an amorphous side-wall, which is believed to contribute to the local ordering during annealing. During the study of the dependence of  $R_s$  on the volume fraction of amorphous and crystalline phases, Paine et al. noted that through structural relaxation and crystallization, local ordering increases the local  $V_O$  concentration [147]. Further, for ITO thin films (50 nm, sputtered) Wulff et al. found that in situations of elevated deposition rate the crystal growth rate is critically defined by the **i.** diffusion of oxygen into the metallic structure, and **ii.** the fast crystallization of amorphous ITO phases [148]. The above outlines a metallic core, surrounded by an amorphous shell, with the skin similarly defined by the pairing of an ordered region and a region of disorder (see the later asymmetrical crystal grain dimensions as well as elemental composition maps—**chapter 6**).

### 2.5.1 Further electrical properties of ITO

For ITO, an effective mass value of  $m_e^* = 0.3m_e$  is typically used [94], [149]. In the case of bulk ITO,  $n_e$  is generally accepted as being the range  $10^{19}$ – $10^{21}$   $\text{cm}^{-3}$ , where the lower bound was determined by Gupta et al., relating to the degeneracy limit<sup>15</sup> of ITO [150], and the upper bound is an observed limit relating to the Sn doping limits and disorder tolerance due to lattice defects [81], [82]. During 4PP electrical transport measurements

---

<sup>15</sup>Occurring when the doping density exceeds a critical carrier density ( $n_{\text{critical}} = 2.3 \times 10^{19} \text{cm}^{-3}$ , determined by Gupta et al.), and the impurity band merges with the conduction band, i.e., Mott critical density [226].

on single ITO NWs, Chiu et al. estimated the electron elastic mean-free-path ( $l_0$ ) from the measured Drude resistivity to be  $\sim 5\text{--}10$  nm ( $D_{\text{NW}} = 110\text{--}220$  nm) [119]. Similar values have been noted for sputtered thin film ITO samples ( $t = 125\text{--}240$  nm,  $l_{\text{mfp}} = 5\text{--}7$  nm) [135]. In the case of a complete degeneracy, mobility and carrier concentration are no longer independent, with a carrier density dependence introduced for mobility ( $\mu_e \propto n_e^{-2/3}$ ) [81], highlighting the self-limiting nature of carrier doping in ITO due to ionized impurities (other relevant scattering mechanisms within our system are discussed later).

Previous study: Shifting plasma edge with carrier concentration

**Figure 2-6** depicts a typical ITO transmission spectra, produced by Granqvist et al. for 200 nm ITO thin films [151]. Here, with reference to the  $3 \times 10^{21} \text{ cm}^{-3}$  curve: region A is associated with the strongly allowed absorption due to electron inter-band transitions; region B is the high transmission passband in the visible spectrum region; and region C is associated with free carrier absorption. The work by Granqvist et al. demonstrates a progressive blue-shift in the plasma edge and the on-set of transmission with increasing carrier concentration ( $10^{20} < n_e < 3 \times 10^{21} \text{ cm}^{-3}$ ), with the former being related to the previously outlined relationship (**equation 1-2**) defining  $\omega_p$ , and the shifted bandgap attributed to the Burstein-Moss effect [151], [152]. In this case, the Mott critical density is exceeded and electrons occupy the conduction band in the form of an electron gas. The energy gap is shifted as a result of the doping and the magnitude is determined by two competing mechanisms [82]:

- i. Bandgap narrowing as the donor level merges with the conduction band (the so-called Mott critical density); and
- ii. Narrowing counteracted by the Burstein-Moss effect (due to blocking of the lowest states in the conduction band).

For the degenerately doped  $\text{In}_2\text{O}_3$  material system, the net effect is a widened bandgap. Of importance to us is that an increase in a film's carrier concentration can be observed directly through the shifting plasma edge. This allows is an indirect observation as UV-vis spectra include interactions between the incident beam with branches and film undergrowth. Compare with the 3D-CBKR device measurement, where we isolate a

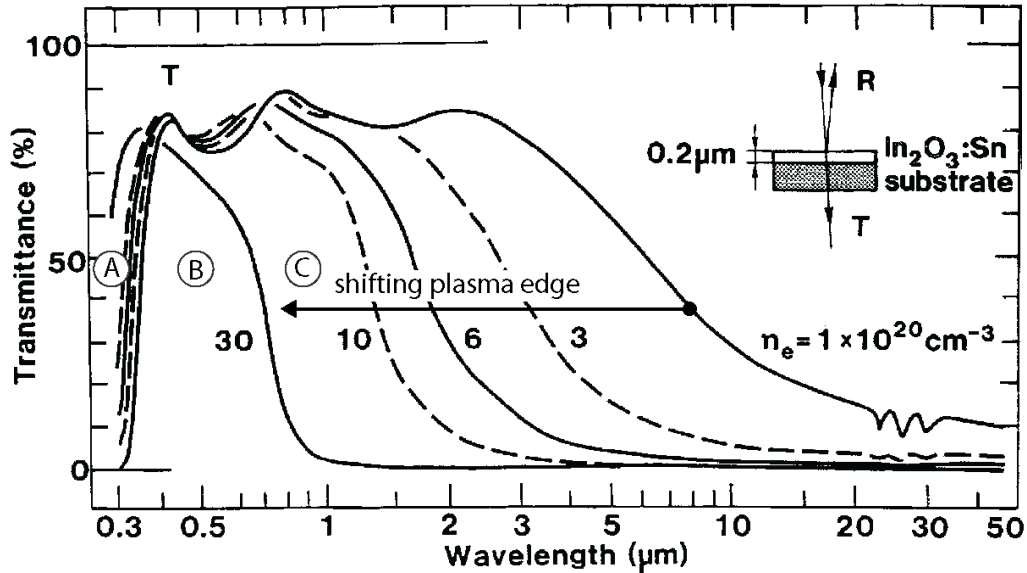


**Figure 2-6 Representative metal-oxide behaviour.** (a) Near-normal transmission spectra for a doped tin oxide thin film outlining the Burstein-Moss blue-shift of the band edge with increasing carrier concentration determined by Granqvist et al. [151], calculated using the shown values of electron density and film thickness. Figure credit: [151].

subset of the film (i.e., the top  $\sim 5\%$  of structures within the thin film samples—see **chapter 5** for further discussion). Doping of ITO is further discussed in **section 2.5.3** in the context of studies pertaining to single crystal ITO NWs.

## 2.5.2 GLAD structured ITO

A GLAD deposition assembly utilizes 2 stepper motors; one modifies the azimuthal position of the flux and the other changes the substrate tilt with respect to the source (see **Fig. 2-7 a**). These two degrees of freedom act in concert and, when varied in time, yield complex structures that evolve in 3-D according to predefined deposition programs and feedback control. GLAD functions primarily on the basis of atomic shadowing and limited adatom mobility (see **Fig. 2-7 b, c**) [13], [153]. During the GLAD structuring of thin films, substrate rotation is computer controlled, and monitored using a crystal thickness monitor (CTM) for feedback control to account for variability in the PVD rate. Substrate rotation alters the apparent location of the vapour source, and therefore alters the shadowing dynamics, allowing for films to be sculpted according to variations in the azimuthal angle of the substrate chuck during deposition ( $\phi$ ) [13]. Once nuclei form, they shadow regions immediately next to them, capturing subsequent flux on the initial nucleation sites, forming the GLAD structure. With increasing substrate



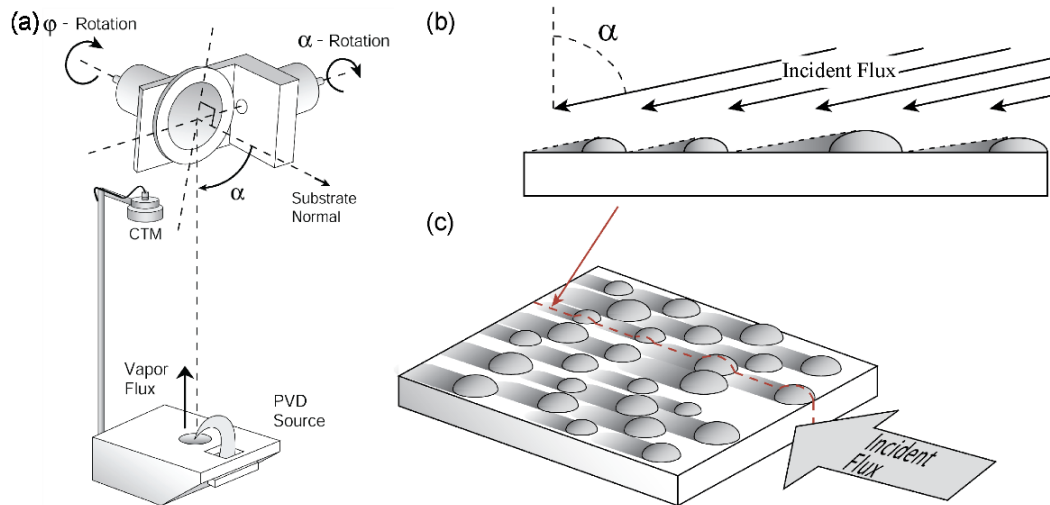


**Figure 2-7 GLAD deposition apparatus and film nucleation.** (a) Control over the vapor flux angle relative to the substrate and rotation about the substrate normal is achieved using a programmable substrate holder equipped with two stepper motors; (b) substrate profile depicting atomic shadowing of the incident flux; (c) auxiliary view of same. Figure credit: GLAD image database, accessed Jan. 2016.

temperature ( $T_s$ ), the number density of nucleation centers decrease while their size increases due to the Ostwald Ripening mechanism [154].

### Previous study: Low temperature deposition of structured ITO

Harris et al. conducted a detailed study with GLAD-ITO deposited under various conditions [90]. With fixed  $\phi$ , tilted columns resulted (**Fig. 2-8 a, b**), but with slow and continuous motion, helical structures are fabricated (**Fig. 2-8 c**). By rotating the substrate  $180^\circ$  at fixed intervals, a stack of columns with alternating directions, or zigzags, is formed (**Fig. 2-8 d**). The pitch of the resulting structures is defined as the amount of vertical growth during a  $360^\circ$  rotation in  $\phi$ . As the angular velocity is increased the pitch approaches the column diameter and helical geometry is lost, and uniaxial structures resembling dense vertical columns or posts are observed (**Fig. 2-8 e**). Films deposited with biaxial symmetry can be engineered with features on the order of a few nanometers by adjusting growth and transition intervals (**Fig. 2-8 f**). This process refinement, utilizing the  $\phi$ -sweep technique to mitigate column-broadening, enables fabrication of uniform columnar films. The  $\phi$ -sweep technique involves periodically and discretely rotating the substrate back and forth about the substrate normal as the film grows (as opposed to the continuous rotation in  $\phi$  used to create vertical post). The

GLAD modulation schemes are summarized in **Table 2-1**. This technique was utilized in the previously referenced work by van Dijken et al. as well as in the preliminary polymer pore-confinement experiments outlined in **Appendix A** [72].

**Table 2-1 GLAD modulation schemes**

<b>Pitch</b>	<i><math>\phi</math> rotation</i>	
	<b>Stepped</b>	<b>Continuous</b>
Large	Zig-zag	Helix
Small	SBD	Vertical post

Of further importance is the local shadowing environment and the incorporation of distinct defects— particularly the ionize oxygen vacancy defect ( $V_{\text{O}}$ ), where the defining features of GLAD are then [155]:

1. The angular broadening of the incident vapor flux, and
2. The surface trapping probability (see **Fig. 2-9 a** for schematic).

### 2.5.3 VLS-GLAD structured ITO

Typically GLAD operates in a regime where surface diffusion is limited to allow shadowing at the nanostructure-level to define film morphology [13], [153]. Increasing the ratio of  $T_{\text{S}}$  (film growth surface/substrate temperature), to source (or material melt) temperature ( $T_{\text{M}}$ ) to  $> 0.3$ , promotes adatom mobility and can result in the 'blurring' of features (**Fig. 2-9 b**) [156]. When  $T_{\text{S}}$  becomes a significant fraction of  $T_{\text{M}}$ , and a catalyst is present, VLS growth can occur (e.g., the Sn-In eutectic in the case of ITO [92]).

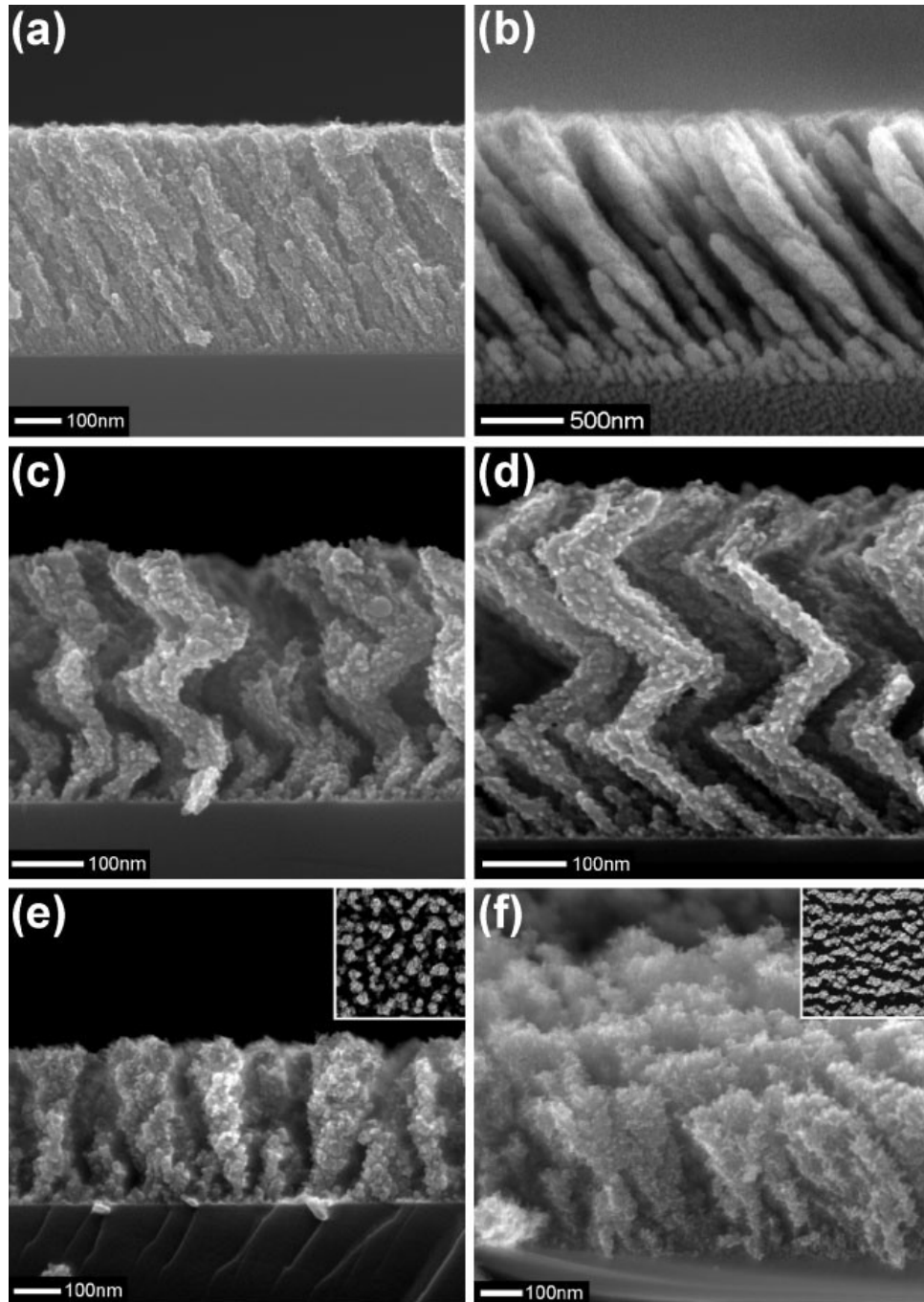


**Figure 2-8 GLAD ITO parameter-sweep.** (a) no rotation, fixed deposition angle ( $\alpha = 60^\circ$ ); (b) no rotation, fixed deposition angle ( $\alpha = 85^\circ$ ); (c) slow rotation; (d) alternating  $180^\circ$  deposition intervals; (e) vertical uniaxial and; (f) vertical biaxial films. Figure credit: [90].

Reported by Wagner and Ellis in 1964, the first demonstration of VLS growth was for Si whiskers using Au as a catalyst material [157]. The VLS growth of Si NWs can also be mediated by other metal catalysts, such as In [158]. Similarly, ITO NW growth has been demonstrated with Au; however, higher temperatures are required to form catalyst droplets (pulsed laser deposition, 750 °C) [117]. For self-catalyzed VLS growth in ITO occurs at a comparatively low temperature [92]. Here, In-Sn serves as the metal catalyst when it is heated above its eutectic melting point. Increasing this ratio beyond a critical threshold temperature ( $T_S \sim 165\text{--}240\text{ }^\circ\text{C}$ ) results in self-catalyzed ITO<sub>VLS</sub> nanotrees and the precipitation of fully extended NWs (shown schematically in **Fig. 2-9 c and d** from the top down in **d**). See **figure 2-9 e** for insufficient  $T_S$ . The resulting structures grow in a regime where growth is determined by the rate of impinging flux upon a metal catalyst droplet (see **Fig. 2-9 f** for schematic, as well as later discussion).

The growth mechanism proceeds as follows: the In-Sn metal catalyst is heated above its eutectic melting point and forms liquid alloy catalyst droplets on the substrate [92]. These droplets form at relatively low temperatures ( $\sim 150\text{ }^\circ\text{C}$ ) and collect growth material, catalyzing the VLS growth of crystalline ITO NWs. This also includes the epitaxial growth of NW branches on the sidewall of the NW trunk. Subsequent direct impingement of evaporant results in a super-saturated alloy, exploiting the solubility of one material in the other above the mixture's eutectic point. Through volume diffusion to the liquid-solid interface, evaporant atoms are incorporated into the available adsorption sites of the lattice, resulting in the vertical growth [159].

The key element in the VLS growth process is that the resulting structures grow in a regime where the crystallization rate exceeds the nucleation rate, resulting in 'whisker' growth [156]. These inherent single crystal NWs often possess high aspect ratios, enhanced electrical conductivity, high transmissivity, and low defect density [11], [92]. The combination of GLAD with the VLS process to produce single-crystal 'nanotree' structures presents an improvement over 'nanopillars' for opto-electronic applications [11]. Additionally, adjusting deposition conditions can increase the complexity of their resulting structures [159], [160].

A defining feature of VLS growth at the nanometre scale, are the chemical potential oscillations of the catalyst droplet, recently reported by Wang et al. for VLS growth in Si NWs [158]. Through analysis of the kinetics of the axial and radial growth, Wang discovered that oscillations between fast and halted growth can manifest as leapfrog changes in length and quantization in the kinetics of growth<sup>16</sup> [158]. This behaviour stems from the fact that as  $1/R$  (where  $R$  is the radius of the catalyst droplet) approaches an equilibrium value, it follows an oscillatory instead of a monotonic path (see previous schematic **Fig. 2-9 f**). Owing to this nanometre size effect, the authors produced ultra-long single crystal Si NWs ( $> 1.5$  cm,  $D_{\text{NW}} = 240$  nm) [158].

Previous study: Growth of highly conductive branched nanotrees

**Figure 2-10** outlines that as the deposition angle is increased ( $\alpha = 50^\circ \rightarrow 85^\circ$ ) and rate decreased ( $\Gamma = 2.0 \text{ nm s}^{-1} \rightarrow 0.5 \text{ nm s}^{-1}$ ) finer, more densely branched structures, with limited undergrowth result. Explained by Beaudry et al. [11]:

1. With increasing  $\alpha$ , the combination of decreasing trunk diameter and increasing trunk-to-trunk spacing results in decreasing shadowing from neighbouring whiskers. The resulting number of branches per unit trunk length increases rapidly with increasing  $\alpha$ , as this dominant geometric effect increases flux incident on trunk sides.
2. Increasing the flux rate results in a reduction of the number of branches and an increase in trunk, and branch diameter, as the increased  $\Gamma$  will proportionally increase the rate of material crossing the vapour-to-liquid interface. The liquid droplet will increase in volume until the rate of liquid-to-solid transition has increased proportionally. In this elevated rate regime, branches decrease to nearly zero as increases in trunk diameter, and a relatively unchanged nearest neighbour distance, result in dominant geometrical shadowing effects.

---

<sup>16</sup>In **section 2.5.4** we discussed briefly the effects of elevated growth enabled through these nanometer size-effects [158]; the depletion of the local growth environment of oxygen is suggested to lead to the precipitation of a metallic core.

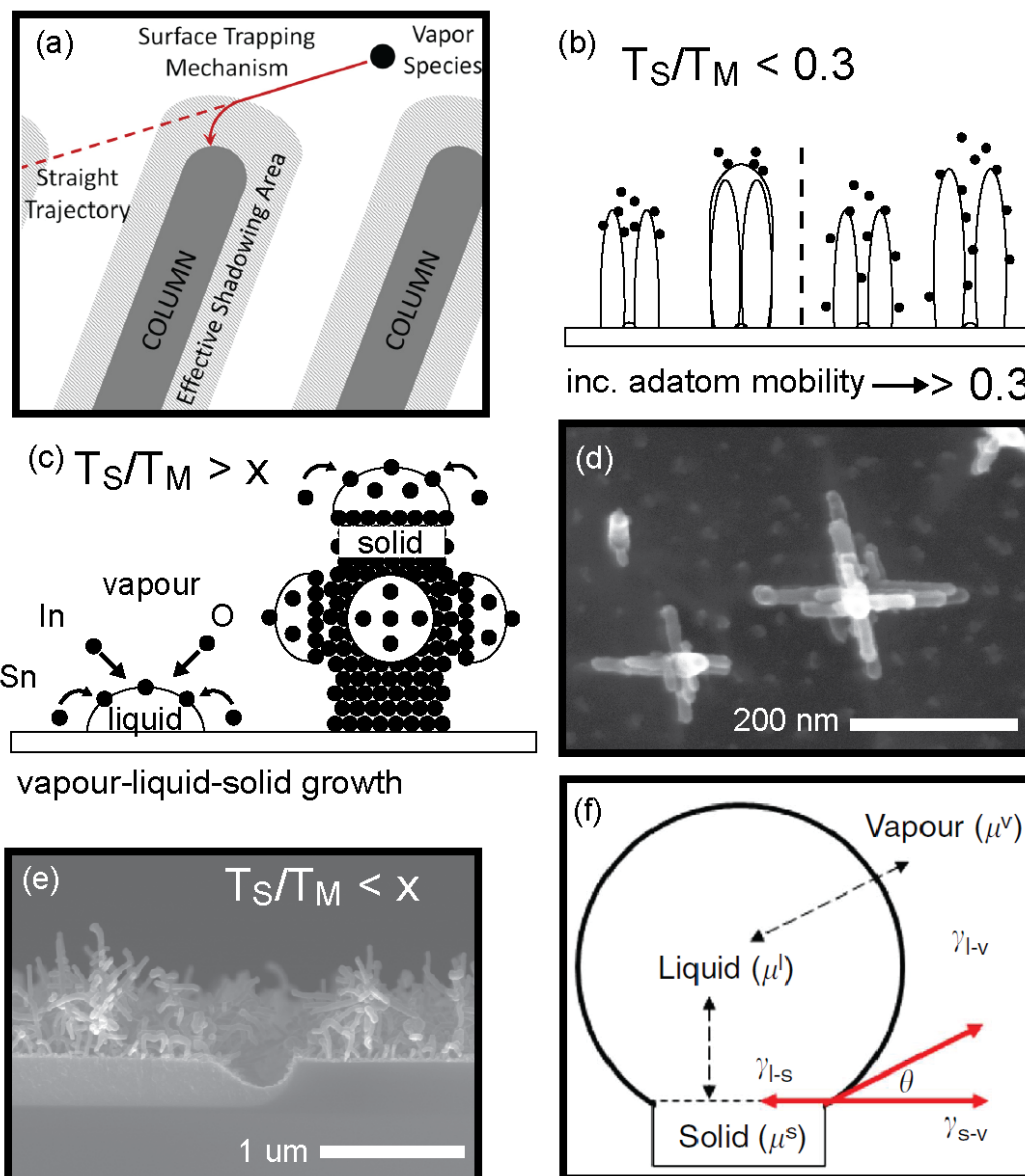


**Figure 2-9 Transition to kinetic growth regime.** (a) schematic of surface trapping mechanism. Figure credit: [155]; (b) increasing  $T_s/T_M$  to a value  $\sim 0.3$  promotes adatom mobility, 'blurring' features, adapted from Patzig et al. [156]; (c) schematic of the precipitation of fully extended NWs; (d) top-down SEMs of our polymer infilled VLS-ITO films; (e) partially extended NWs; (f) schematic of catalyst droplet. Figure credit: [158].

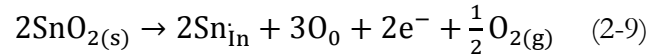
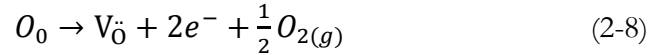
In the present study, structures are selected with near ideal morphology (i.e., feature spacing on the order of  $L_D$ ), requiring growth at moderate rates ( $0.5 \text{ nm s}^{-1}$ ) and high deposition angle ( $\alpha = 85^\circ$ ) to maintain branched morphology (**Fig. 2-10**, middle row, right). However, deposition at moderate rates results in structures with limited carrier concentrations (discussed later) [94]. The exploration of post-processing anneals

is meant to optimize the NW conductivity, while maintaining the highly-branched structures suitable for integration into OPV devices. For this experiment we utilize:

1. An air anneal, we can correct structural disorder; followed by
2. A reduction anneal, which increases the free carrier concentration through introduction of doubly ionized oxygen vacancies ( $V_{\text{O}}$ ).

## 2.5.4 Degeneracy in ITO

The substitutional incorporation of Sn in the  $\text{In}_2\text{O}_3$  cubic bixbyite crystal lattice contributes one conduction electron, while a  $V_{\text{O}}$  contributes two [81]. These sources of  $n_{\text{e}}$  have a subsequent influence on the overall structural, electrical and optical characteristics of the TCO film. Below are the equations governing the incorporation of the above dopants into the lattice [81]:



However, the process of incorporating these dopants is highly sensitive to various defect complexes; see [161] and references therein for a more thorough treatment of the defect chemistry of ITO. The resulting material system has a lattice parameter close to that of  $\text{In}_2\text{O}_3$  (for ITO  $a = 10.12\text{--}10.31\text{\AA}$ ) [162] and the resulting film characteristics are a convolution of deposition parameters — namely, oxygen partial pressure,  $\Gamma$  and  $\alpha$ , as well as  $T_{\text{s}}$  and Sn (at. %) [81], [141], [162]. The above two sources of  $n_{\text{e}}$  must be carefully adjusted to maintain film crystallinity, as excess can introduce local disorder and a corresponding reduction in  $\mu_{\text{e}}$  and optical transmittance [94], [117], [151]. These doping variations contribute to observed mobility values between  $\sim 10\text{--}150\text{ cm}^2\text{ V}^{-1}\text{ s}^{-1}$  [80], [81], where mobility can vary significantly within samples of similar  $n_{\text{e}}$ .

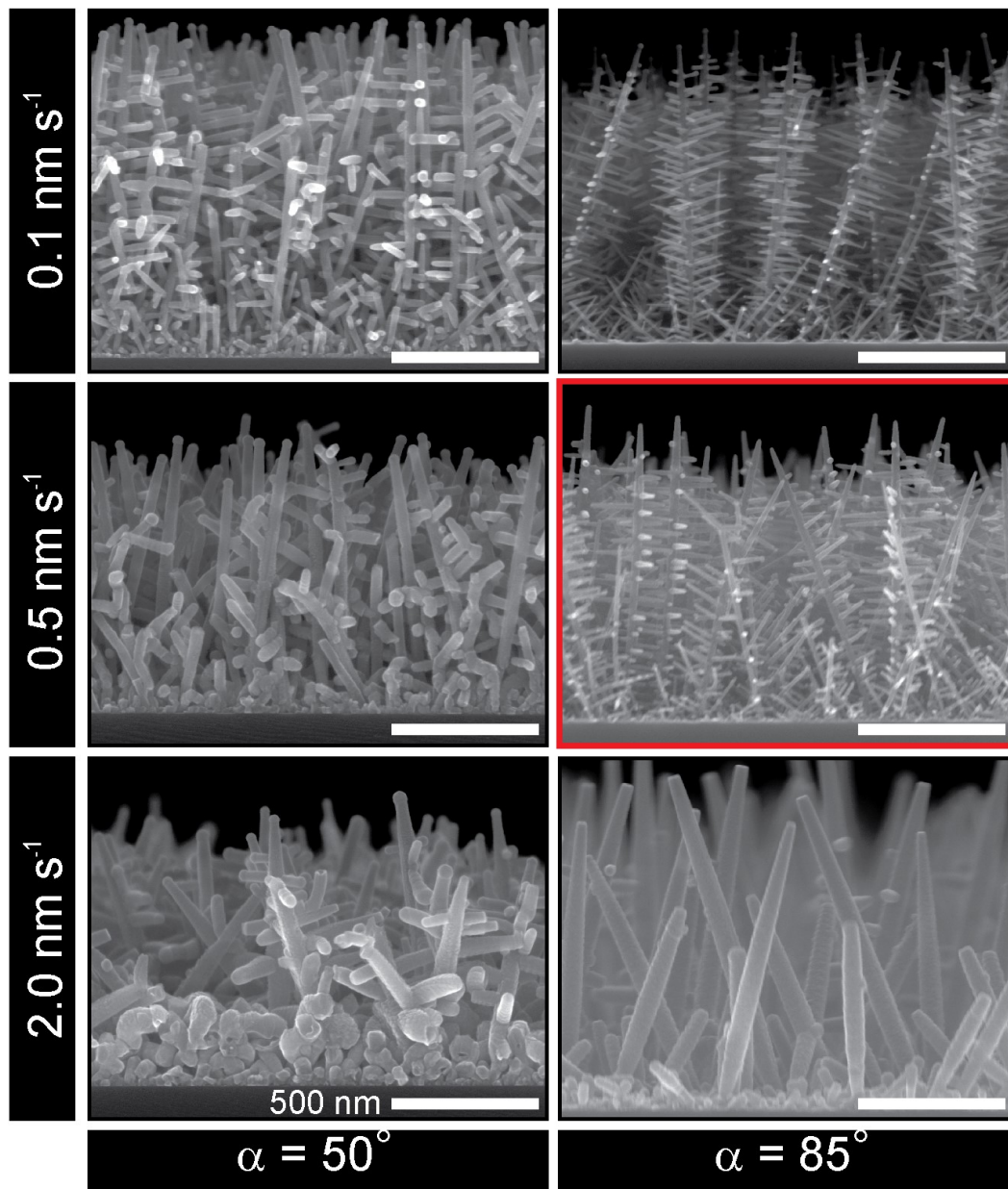


**Figure 2-10 Demonstrated range of the VLS-Glad-ITO material system.** Films grown at  $\alpha = 50^\circ$  and  $\alpha = 85^\circ$  and various rates (500 nm scale bars). Pairing of VLS growth with GLAD yields a film composed of single crystal nanotrees, with control over trunk diameter, branch placement, and the density of NW features in a film. Figure credit: [9], [11].



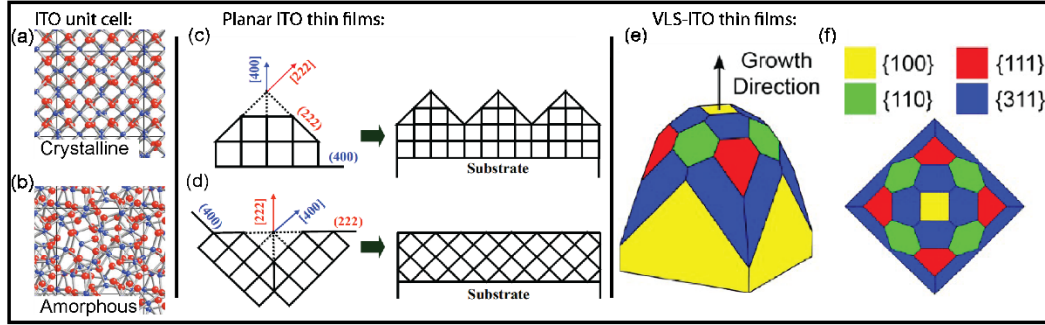


**Figure 2-11 ITO crystal schematics from literature:** ITO unit cell for (a) fully crystalline (b) fully amorphous unit cell. Figure credit: [133]. The oxygen partial pressure during deposition has been shown to select between different orientations, with oxygen deficient growth resulting in (c) [400] textured films and oxygen rich growth in (d) [222] textured films. Figure credit: [142]. From ref [9]: A schematic illustrating the crystal structure and facets of a single-crystal ITO nanotree trunk growing in the [100] direction, shown from (e) auxiliary and (f) top-down perspectives. Figure credit: [9].

Further pertinent literature observations include the effect of crystalline order (or lack thereof) and preferential growth orientation. Towards an understanding of the relationship between different crystalline phases and electrical conduction, Rosen et al. simulated the quenching of a molten ITO source, and investigated the precipitation of unit-cells with varying degrees of crystallinity. When quenching times were varied, it was found that it is possible for  $E_F$  to extend beyond the conduction band minimum in a fully amorphous crystal [133], demonstrating that a degeneracy can be introduced in a highly disordered sample (see **Fig. 2-11 a** and **b** for crystalline and amorphous ITO unit cells, respectively). Kim et al. noted distinct geometric relations for preferentially (400) and (222) oriented sputtered ITO thin-films; the authors explained their observations in terms of the relative surface energy of a given crystal plane, with (222) oriented films favored with the presence of oxygen in the sputtering ambient [142] (refer to **Fig. 2-11 c** and **d** for crystallographic orientation schematic). From LaForge et al., a schematic illustrating the crystal structure and facets of a single-crystal ITO nanotree trunk growing in the [100] direction (see **Fig. 2-11 e** and **f** for auxiliary and top-down perspectives, respectively) [9]. Note, branch growth occurs in the four {100} direction normal to the trunk [9].

Previous study: Sn and oxygen vacancy doping in VLS-ITO NWs

In the pursuit of highly conductive ITO NWs, Sn and  $V_O$  doping have been pursued by several researchers in the field [81], [82]. Meng et al. demonstrated that they could improve the average resistivity of NWs by four orders of magnitude through in situ Sn doping (0 to 19 at. %), with an observed incorporation limit preventing further doping in the NW (**Fig. 2-12**, open triangles,  $\rho_i \sim 0.2 \text{ m}\Omega\cdot\text{cm}$ ) [117]. However, there is a steep degradation in transmission between 10–20 at. % of Sn [163], limiting the amount of Sn doping suitable for TCO applications.

LaForge et al. demonstrated an approximately four-fold increase in  $n_e$  in highly branched, laterally connected nanotree networks ( $t \sim 16\text{--}20 \text{ }\mu\text{m}$ ) by increasing the deposition rate from  $0.5 \text{ nm s}^{-1}$  to  $3.0 \text{ nm s}^{-1}$  (**Fig. 2-12**, open diamonds,  $\rho_i = 0.3 \pm 0.1 \text{ m}\Omega\cdot\text{cm}$ ) [94]. For the observed increases in  $n_e$ , it was suggested that the increased growth rate resulted in a lower oxygen incorporation rate and therefore an increased  $V_O$  (inferred as the Sn concentration was constant at 6 at. % in the film) [94]. This gain in electrical performance can be at the expense of the ideal morphology, and introduction of a complex metallic core-shell architecture (see **Fig. 2-12**, inset). In this work, it is suggested that metallic cores are precipitated under conditions of elevated rates where oxygen incorporation is limited; this includes oxygen deficient conditions introduced through competitive growth dynamics (i.e., flux starvation as branches are buried into the film) [99]. The point of interest here is that the formation of such structures at elevated rates is consistent with the ‘leap-frog’ growth mechanism outlined previously. Similar chemical-vapour-deposited structures have been reported by Kim et al., with Au-embedded ITO NWs [164], and Li et al., with In-filled [165]  $\text{In}_2\text{O}_3$  NWs, indicating that there are multiple paths towards metallic NWs.

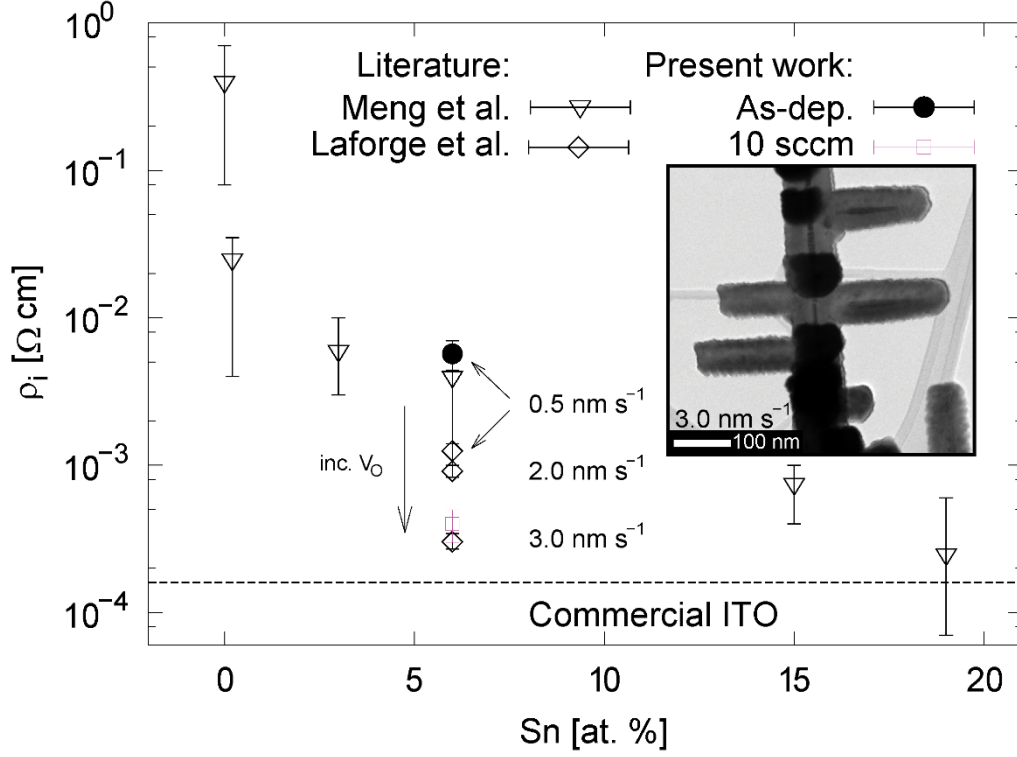


**Figure 2-12 Resistivity varying with Sn [at. %] and deposition rate.** The dashed line is the 'commercial grade' threshold (Delta Tech., 0.16 mΩ·cm). Inset: Precipitation of a metallic core at 3.0 nm s<sup>-1</sup>. Transmission Electron Microscopy images of NWs deposited at elevated rates.

### Previous study: Scattering mechanisms

Key parameters when considering the intrinsic resistivity of a structured thin film are the sources of scattering. Electron mobility in a bulk TCO is limited by ionized impurity scattering, which is considered the dominant scattering process for carrier concentrations above 10<sup>19</sup> cm<sup>-3</sup>. The maximum carrier concentration is limited by dopant solubility in the host material, and larger impurity densities can form clusters (~2×10<sup>21</sup> cm<sup>-3</sup> for ITO) [75]. At reduced dimensions, other factors need also be considered. These include the dimensions of the nanostructure as they contribute to the surface scattering [166], [167] and the size of the crystallites as they contribute to the grain boundary scattering [168], both of which have been found to contribute to the electrical resistivity of NWs on the size scale observed within this work [113]. Considered by Fuchs and Sondheimer, when the film thickness decreases below the bulk electronic MFP, resistivity increases due to diffuse scattering at the film boundaries [166], [167]. Considered by Mayadas and Shatzkes, as thin films proceed to a thickness less than the mean grain size, the increased contribution from grain boundaries also

contribute to increases in resistivity [168]. Durken et al. found that both effects may be needed to explain electrical performance, incorporating the variation of mean grain size on wire dimensions during the study of polycrystalline Au NWs (10–70 nm) [113].

Factors concerning the dominant scattering mechanisms that need further consideration, and that will be explored in later chapters are:

1. For our nanotree arrays,  $l_c < l_t$ , and at low current densities it is expected that the electrostatics owing to our NW dimensions will dominate the current flow [124], [161], [169].
2. For sufficiently large crystal grain sizes ( $D > 20$  nm) it has been observed that grain-boundary scattering is not the dominant scattering mechanism [113], [170]–[172].
3. Weak disorder arising from the random potential at the NW surface act to screen electrons towards the core of the NW [95].

## 2.6 Chapter summary

In-plane resistivity measurements of metals and conductive oxide GLAD films have been previously performed [90], [107]–[111], revealing the increasing in-plane resistivity with increasing oblique deposition angle. Electrical anisotropy has also been observed, with differing in-plane resistivity for different nanocolumn orientations [111]. A thorough study of both in-plane and through-post, axial conductivity as a function of film composition, morphology, porosity, and crystallinity/phase is required to understand the complex interplay between film morphology and corresponding electrical properties.

Quantifying differences between vertical and lateral-plane characteristics of GLAD films requires expanding on established techniques for in-plane measurements (which largely neglect morphological effects) and tailoring techniques to apply directly to GLAD films. In the coming chapters we outline the design and fabrication of a ‘3D-CB’, where the region of interest is intrinsic to our nanostructure arrays.

This research builds from the electrical characterization of ITO films by LaForge, which revealed structural confinement on the scale of a few nanometres [94] and motivated the air annealing treatment to correct this disorder (discussed further in **chapter 6**). To further these findings, the data point determined from our work for as-deposited resistivity for  $\alpha = 85^\circ$ ,  $0.5 \text{ nm s}^{-1}$  film (**Fig. 2-12**, closed circle) and 10 sccm processed sample (**Fig. 2-12**, purple square)<sup>17</sup>. These data points require some context, and in later chapters, the following considerations are important:

- The fabrication of defect free contacts;
- Limiting uncertainty in **equation 2-7** to propagated counting error; and
- The precipitation of core-shell structures (including spontaneously, at growth).

---

<sup>17</sup>These values were determined using an estimated surface-depletion layer of  $\sim 1 \text{ nm}$  (discussed later).

### 3 Experimental details

This chapter contains a brief overview of the experimental methods used in this work, including an outline of the fabrication methodology, the assessment and characterization of as-deposited and processed films, as well as the testing of completed devices. The experimental process flow used to fabricate and test the devices is briefly outlined here. First, films are deposited at moderate rates upon bottom contacts and, in the case of VLS-grown NWs, processed and encapsulated in an insulating polymer. The encapsulation is required to prevent Ag side-wall deposition, which can result in contacting of top and bottom electrodes, and short circuiting of the device. As discussed in the previous chapter, the selection of Ag and its conformal application to our nanostructures yields ohmic characteristics (determined for each device under study). Via equation 1-1 and 1-2 we can observe shifts in the degree of doping within NW arrays and thin film witness samples. Various characterization techniques allow us to probe the macroscopic, film-level properties as well as the bulk and near surface regions of the nanostructures. Deconstructed devices are used for EELS characterization, while witness samples were used for UPS, AES, XRD and UV-VIS characterization.

## 3.1 Thin film deposition

The vacuum deposition of structured thin films requires control over the substrate position relative to a fixed source and a directional particle flux from source to substrate. Dynamic control over substrate rotation is set by the motion of two stepper motors that are computer-controlled with custom software. Advanced control incorporates feedback from the CTM to allow the motion of the substrate to be triggered by predetermined stages, specified as functions of accumulated thickness during growth. For our GLAD depositions, CTM-monitored growth was employed, whereas VLS depositions were timed with constant, continuous rotation (see previous **Fig. 2-7 a** for schematic of deposition apparatus).

To reduce the angular distribution of flux material (evaporant) arriving at the substrate, long throw-distances ( $L$ ) and low vacuum are required to minimize collisions within the gas during transit ( $L \sim 42$  cm,  $< 100$  mPa, effective source diameter  $\sim 1$  cm) [154]. There are several techniques to generate a particle flux in a PVD system. The two main methods used in this thesis are electron beam (EBE, used for nanostructure deposition) and sputtering (used for the deposition of smooth, planar bottom contacts), both are described briefly below.

### 3.1.1 Electron beam evaporation

Within an EBE system, electrons are generated by thermionic emission, accelerated through a high-voltage field (5.6 kV), and directed to the source with electromagnetic sweep coils. A tailored sweep of the electron beam (circular in our case) distributes heating, and is adjusted to avoid uneven deposition rates (requiring  $\sim 10$  min conditioning, pre-warming the source before deposition).

A highly collimated vapour flux is necessary to achieve dynamic control of an evolving structured thin film. This flux is produced by heating a crucible full of source material with a 10–100 mA electron beam. Upon sufficient heating, the vapour pressure of the source material will exceed the hydrostatic pressure within the chamber and produce a highly collimated (low divergence) vapour flux of low energy particles ( $E \sim 100$  meV)—with radiative heating from the vapour source being a secondary

consideration for low-temperature depositions [154]. During deposition, an impinging vapour atom is adsorbed at the nanostructure surface, and is incorporated or re-evaporated. In the former case, the adatom has excess energy, and transfers it to the film surface until it is in thermal equilibrium; the general trend for thin film deposition is an increase in crystallization due to increased adatom mobility with increasing substrate heating ( $T_s$ ) [154].

In the present research, ITO chunks (Materion Inc., Milwaukee, WI, 91:9  $\text{In}_2\text{O}_3\text{:SnO}_2$ , 99.99% pure) were used as source material in a custom GLAD deposition chamber (AXXIS, Kurt J. Lesker, base pressure  $2 \times 10^{-4}$  Pa). The GLAD-ITO was deposited by EBE ( $L = 42$  cm,  $\alpha = 83^\circ$ ) and nominal deposition rate of  $\sim 0.2$  nm  $\text{s}^{-1}$ , and was conditioned for  $\sim 10$  min with a circular sweep of the beam. All VLS-GLAD ITO structures investigated during the conductivity study were deposited in a single deposition ( $\Gamma = 0.5$  nm  $\text{s}^{-1}$ ,  $\alpha = 85^\circ$ ), with varying process parameters administered post-deposition (see **Appendix C** for the motion files of the present study, used to set the growth steps and material CTM tooling factors).

For heated depositions,  $T_s$  was monitored using a type-T thermocouple mounted approximately 1 cm above the center of the deposition chuck (see [11] for calibration details). The deposition chuck was thermally isolated from the substrate motion drive shaft by a Macor headpiece. Dense planar ( $\Gamma = 0.2$  nm  $\text{s}^{-1}$ ,  $\alpha = 30^\circ$ ,  $t = 200$  nm), and  $\alpha = 50^\circ$  VLS-GLAD films ( $\Gamma = 0.5$  nm  $\text{s}^{-1}$ ,  $\alpha = 50^\circ$ ,  $\text{ITO}_{\text{VLS } 50}$ ), were processed in parallel to serve as controls for our  $\alpha = 85^\circ$  VLS-GLAD films ( $\text{ITO}_{\text{VLS } 85}$ ). Ag top contacts were also deposited within the above deposition chamber, with details provided in **section 3.4**. In addition to films grown for CBKR characterization, multiple films were grown by A.L. Beaudry; these films are used to supplement the current work, particularly those films utilized for the  $\Gamma$ - and  $\alpha$ -sweep detailed in **chapter 6**.

### 3.1.2 Sputtering

By employing sputtering to deposit our dense planar bottom contacts (Au for GLAD devices and ITO within oxide trenches for VLS-GLAD structures), we are able to produce smooth bottom contacts that serve as the growth surface for our subsequently



deposited structured thin films. For this PVD technique, vapour flux is produced by bombardment of solid target with heavy ions ( $\text{Ar}^+$  in our system). During this process a plasma is ignited and accelerates the positively charged ions towards the negatively biased target. This results in momentum transfer events and results in the ejection of target atoms forming the flux. In an ideal case, sputtering has the benefits of maintaining the stoichiometry of the target due to the physicality of the transfer process (i.e., sputter yield can vary with material, but is typically better than with evaporation). A reactive gas can also be added (i.e., oxygen in the case of ITO depositions) to further tune the properties of the deposited film. This is a relatively high pressure process ( $>10$  Pa) that results in increased scattering, improving step coverage in wafers with topography, particularly within our oxide trenches (outlined in **chapter 5**). Compared to EBE, this is a higher energy process ( $E \sim 10$  eV) and results in significant substrate heating [154].

## 3.2 Summary of experimental process

Outlined in **figure 3-1** is the experimental process flow utilized to populate equation 2-6 in order to yield  $\rho_i$ . A similar procedure was followed to determine  $\rho_i$  for ITO<sub>GLAD</sub> devices (discussed in **chapter 4**). Initial study of the optimization anneals was conducted on planar samples, and for this reason, we proceed with two approaches to assess the effects of the reduction anneals on our nanostructured thin films:

1. 375 °C, reduction flow sweep (reduction at 10 sccm, 30 sccm, 100 sccm)
2. 10 sccm temperature sweep (175°C\*, 275°C, 375°C, 425°C\*)<sup>1</sup>

Nanotree films were subject to a two-stage anneal used in previous work (summarized in **Table 3-1**) [27]: anneal 1 (atmosphere, 1 hr, 500°C linear ramp, passively cooled), and anneal 2 (three-zone tube furnace, 375°C, 5%  $\text{H}_2$  – 95% balanced Ar, 10–100 sccm). During anneal 2, samples were ramped linearly to  $T_s$ , held for 60 min, and passively cooled to  $< 90^\circ\text{C}$  before removal. Reported in-plane sheet resistance of planar films and ITO<sub>VLS 50</sub> films was verified using both 4PP (Signatone, 1.6 mm) and

---

<sup>1</sup>The latter study is complicated as the indicated (\*) samples were oxygen annealed for 24 hrs (as opposed to 1.5 hrs) due to a set-point malfunction with the oven controller. As the results of both studies cannot be directly compared, device-level trends are presented where applicable.

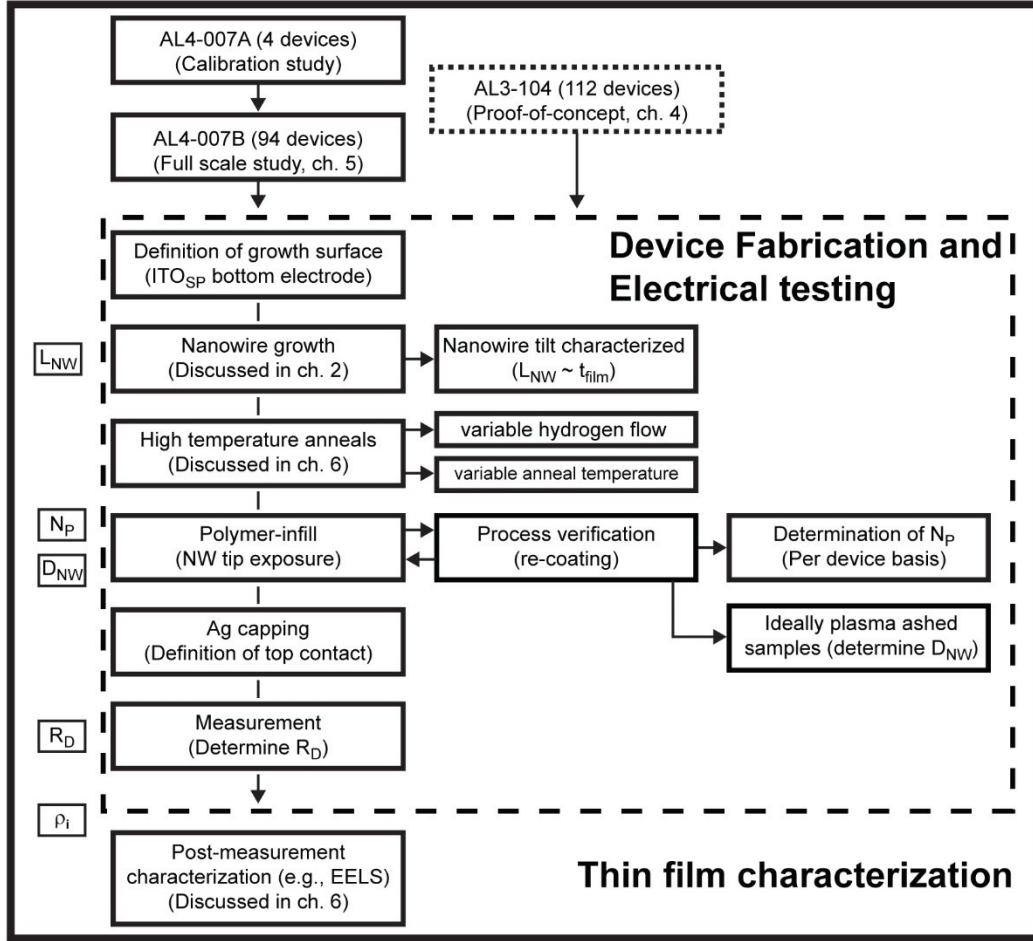


**Figure 3-1 Experimental process flow and relation to equation 2-6.** An initial calibration study had a yield of 25% (AL4-007A). Processes were further tuned and yield improved for subsequent process groupings (50–94% yield for AL4-007B). Key parameters are highlighted (left) with the process flow for device fabrication and electrical testing discussed primarily in this chapter, and subsequent thin film characterization discussed further in **chapter 6**.

Hall probe (Accent HL5500PC); these two techniques yielded measurements that were within 5% of each other for a given sample and were found to follow trends noted in literature [173], [174].

Samples were prepared using standard freeze-fracture cleaving techniques, and images were obtained with a scanning electron microscope (SEM, Hitachi FE S-4800, 15 kV, 22  $\mu$ A) and analyzed using ImageJ image analysis software [175]. Transmission spectra (185–3300 nm, Perkin-Elmer NIR-UV) were taken of films on UV-grade, fused silica substrates, before and after anneals. X-ray diffraction patterns (XRD, Bruker D8 Discover, HiStar area detector, Cu K $\alpha$ , 15 mm WD), Auger electron spectroscopy measurements (AES, JAMP-9500F, probe diameter 3–8 nm at the sample, 24 mm WD), ultra-violet photoelectron spectra (UPS, Kratos Ultra, 21.2 eV He I source, 10 V bias),

and transmission electron micrographs (TEM, JEOL 2200 FS, 200 kV) were taken of films deposited on Si substrates. Within the following sections further details are provided for the specifics of our thin film depositions, device testing protocol and thin film characterization.

**Table 3-1 Growth and processing details.** Summarized processing parameters (including process temperature, ambient and process time) for the study of various reduction gas flow rates to optimize nanostructured thin films (see **Appendix C**).

<b>Process:</b>	<b>Process Temperature [°C]:</b>	<b>Ambient:</b>	<b>Process time [min]:</b>
Growth (AL4-007b)	240	Vacuum	5 min
Anneal 1	500	Atmosphere	90 min
Anneal 2	375	5 % H <sub>2</sub> / 95 % Ar	60 min

### 3.3 CBKR design rules

The definition of our measurement window requires consideration of our device specifications and the allowable current density. The former is a combination of the interface band-engineering described in **chapter 2**, as well as the device layout described below. The latter is estimated from the study of the current density failure limits in Au NWs, previous 4-wire testing by others of single ITO NWs, as well as from the NW diameter and planar density observed for the films under study in this, and previous work.

Reported systematic contributions to the electrical characteristics of the planar CBKR architecture include:

1. Contributions from edge defects (introducing the factor  $\delta$  in **Fig. 2-3**)<sup>2</sup> [122], [125], [126];
2. Contacting metallic trace thickness to contact width ratios (typical range is 0.03–0.2, similar to the range utilized in this work); as well as the
3. 2I vs. 2L configuration (discussed previously, see **Fig. 2-1 b**) [121].

---

<sup>2</sup>Ideally the test current flows directly into the contact window; non-ideal structures have an extra contribution from near planar material around the contact window (shown schematically in **Fig. 2-3 a**) [121].

The observed linear  $i$ - $v$  characteristics, as well as deviations due to defects unique to our 3-D architecture and GLAD films, allow us to separate systematic contributions from our device. Further, device characteristics are judged against the response of our thin film controls (discussed further in **chapter 5** and **chapter 6**). By comparing deviations in the expected response of our thin films, and observed device- and film-level defects, we can address the effect of various systematic contributions.

### 3.3.1 Lithographically defined contacts

To define the critical dimensions of our test structures, the dependence of  $R_D$  on device area necessitated device areas ranging from  $4\text{ }\mu\text{m}^2$  to  $100\text{ }\mu\text{m}^2$ . An initial sensitivity study was conducted in preparation for the integration of GLAD-ITO nanopillars deposited at  $\alpha = 83^\circ$  (ITO<sub>GLAD 83</sub>). We found that focusing on larger linewidths was preferable to combat device area variation, as there is a diminishing effect of over-etching with increased linewidth.

Using the relationship for  $R_P (= \rho_i L/A)$  and a simple parallel-post model, the dependence of  $R_D$  on device area and post-base diameter ( $w$ ) is shown in **Fig. 3-2 a** and **b**, respectively. The large body of prior work on GLAD has shown that typical post dimensions near  $\sim 30\text{ nm}$  result for our deposition conditions (e.g., see [11], [90]), this leads to likely upper and low bounds for numbers of posts per unit area, and of interest in our case, the number of nanostructures in a test structure. Holding  $w_2$  constant and varying  $w_1$ , the corresponding  $R_D$  values for a nominal  $100\text{ }\mu\text{m}^2$  device demonstrate that post-base dimensions can have potentially large contributions in our experimental range (i.e., for  $< 30\text{ nm}$  there is a notable increase in resistance). Considering our practical lithographic limits ( $\sim 2\text{ }\mu\text{m}$ , resulting in  $N_P > 30$  in the case of VLS-GLAD ITO devices), and situations requiring the highest instrument sensitivity (e.g., cases for which we are potentially measuring metallic NWs), the range of tested NWs was  $30 \lesssim N_P \lesssim 1000$  (where the lower bound is a fabrication limit, and the upper bound an observed limit for our size-scale, paired with further isolation due to the polymer in-fill set outlined in **chapter 5**).

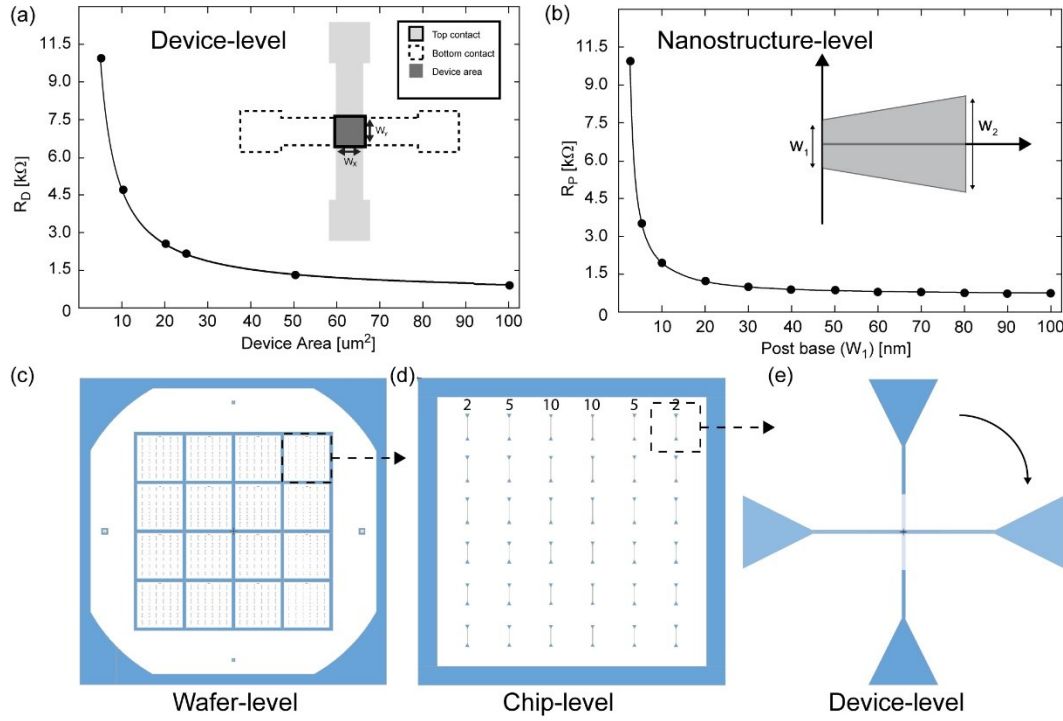


**Figure 3-2 Determination of device dimensions and photomask design.** (a) Dependence of  $R_D$  on device area, and (b) Dependence of  $R_P$  on post-base diameter; (c) 4 × 4 array of device chips; (d) housing 36 devices each (6 × 6 array). Device areas range from 4  $\mu\text{m}^2$  to 100  $\mu\text{m}^2$ , and allow for the systematic determination of intrinsic electrical properties of the nanostructures between lithographically defined electrodes; (e) final device configuration.

To isolate any unwanted systematic resistance contributions, a photo-mask was designed with trace lengths varied (0.5 mm, 0.75 mm, and 1 mm) and with triangular contact pads (height – 200  $\mu\text{m}$ , base – 200  $\mu\text{m}$ ). Line-widths were 2  $\mu\text{m}$  (our practical lithographic limit), 5  $\mu\text{m}$ , and 10  $\mu\text{m}$ ; the areal intersection/overlap of the top and bottom electrodes define the resulting device area. Devices were spaced generously at the photo-mask level (2 mm, center-to-center) to allow for sufficient tolerances during mask alignments, as well as ease of device isolation during post-processing and characterization (**Fig. 3-1 a, b**). Devices were fabricated in a CBKR configuration (shown schematically in **Fig. 3-1 c**) on p-type  $\langle 100 \rangle$  silicon wafers (University Wafer, 4 inch, nominally 100  $\Omega$  cm). Devices were fabricated in 6 × 6 arrays, with one mask used for both top and bottom contacts (i.e., mask rotated 90° for the second round of lithography). For the fabrication of GLAD-ITO devices we updated our procedures to incorporate process refinements implemented after the study of these proof-of-concept devices (discussed further in **chapter 4** and **5**). Wafers were cleaned with a 3:1 v : v

mixture of sulphuric acid (96%) and hydrogen peroxide (30%) at 130 °C for 20 min. A 30 nm Cr adhesion layer (Kurt J. Lesker, 99.95% pure) was sputter-deposited at a rate of  $\sim 0.38 \text{ nm s}^{-1}$  (0.933 Pa Ar, 33 cm throw distance,  $2 \text{ W cm}^{-2}$ ). Au (Materion Microelectronics Inc., Milwaukee, WI, 99.999% pure) was chosen for the bottom electrode for its air stability, low resistivity, and relatively high melting point. A 180 nm thick Au layer was sputter deposited at a rate of  $\sim 0.24 \text{ nm s}^{-1}$  (0.933 Pa Ar, 33 cm throw distance,  $0.5 \text{ W cm}^{-2}$ ).

Following each respective layer's deposition, the Au/Cr electrode geometry was defined by standard contact photolithography techniques; HPR 504 photoresist was exposed at  $140 \text{ mJ cm}^{-2}$  at wavelengths of 365 nm and 400 nm. Photoresist was developed using a NaOH-based developer (Shipley Microposit 354) with the endpoint being determined via visual inspection (after  $\sim 25 \text{ s}$ ). Au/Cr electrodes were subsequently wet-etched to yield the final contact geometry (Au etchant: Fisher Scientific, 200 g  $\text{KIO}_3$ /75g  $\text{I}_2$ /2L deionized water; Cr etchant: 882367, Fujifilm Electronic Materials, North Kingstown, RI).

Ag top contacts (Materion Inc., Milwaukee, WI, 99.99% pure) were deposited via EBE in the same GLAD deposition chamber as our nanostructures, at  $\sim 0.25 \text{ nm s}^{-1}$ . Ag contacts were defined by photolithographic techniques outlined previously, using a 4:1 dilute solution of Cr etchant : deionized water (see **Table 3-2**). Further details regarding the deposition parameters of the Ag top contact are provided in **chapter 4** and **5** for GLAD-ITO devices and VLS-GLAD ITO devices, respectively.

**Table 3-2 Line width measured at the center of millimeter-scale traces.**

	$W_{\text{Au}} [\mu\text{m}]$ :			$W_{\text{Ag}} [\mu\text{m}]$ :		
Nominal	2	5	10	2	5	10
Experimental	$1.1 \pm 0.1$	$4.2 \pm 0.1$	$9.3 \pm 0.1$	$1.3 \pm 0.1$	$4.2 \pm 0.1$	$8.9 \pm 0.3$

### 3.3.2 Testing protocol

While highly metallic ITO NWs with diameters of  $\sim 125 \text{ nm}$  have been shown to be extremely resilient to joule heating [176], Karim et al. have observed diameter dependent failure ( $\sim 0.5 \times 10^{12} \text{ A m}^{-2}$ ) in Au NWs with diameters  $< 100 \text{ nm}$  [177]. Based on our

values for NW diameter and planar density [11], we imposed a test current limit of  $\leq 30 \mu\text{A}$  to limit current densities to  $< 10^9 \text{ A m}^{-2}$ , minimizing joule heating [113]. Depending on the number of structures contained within a device, this results in the current per device ranging from 0.03–0.3  $\mu\text{A}$ , which is expected to be well below the expected diameter-dependant failure limit when considering a single NW within an array under test. Further, only devices with stable, linear  $i$ - $v$  characteristics were studied further.

Device resistance was measured with 10 m $\Omega$  precision with collection intervals spaced while limiting joule heating. Four-wire resistance measurements were collected using a digital multimeter (Aligent 34401A). Device  $i$ - $v$  characteristics were obtained using a power supply (Agilent U8001A) and digital multimeter in a 4-wire configuration, limited by the 10 m $\Omega$  resolution and the 100 M $\Omega$  maximum input resistance of our digital multimeter (this process corresponds to a resistivity range that extends from  $10^{-6} \Omega \text{ cm}$  to  $10^{11} \Omega \text{ cm}$ , respectively). We note that device defects (i.e., shorts) may result in a lower practical upper limit.

In-plane sheet resistance of planar films was measured with a standard 4PP (Signatone, 1.6 mm probe spacing). The following testing protocol was used to characterize and verify the measurement apparatus (step 1 and 2), top and bottom electrodes (step 3 and 4), as well as the multiple probe configurations (step 5), outlined below (see **Table 3-3**). Data analysis was then conducted using a fixed probe configuration (i.e., in **chapter 6** we fix  $I_{\text{test}} = 30 \mu\text{A}$ ).

**Table 3-3 Device testing protocol.**

Step:	Probe configuration:	Notes:
1	1-3 / 2-4	Measure $R_C$ : record contact resistance (short probes together, record 2-wire multi-meter reading)
2	4-wire	Verify apparatus in 4-wire configuration: resistance of 180 m $\Omega$ (nominal) resistor determined in force / sense configuration
3	1-3	Measure $R_{\text{Au/ITO}}$ : record 2-wire resistance
4	2-4	Measure $R_{\text{Ag}}$ : record 2-wire resistance
5	4-wire, multiple configurations	Measure the allowed probe configurations (to mitigate issue of measurement offset, check for Schottky barrier and / or current-crowding effects).
6	-	Reject devices that display unstable characteristics.

Of interest to us is the frequency response of the nanostructure arrays—here, a variation in thickness or composition of the dielectric layer is believed to be the root cause of the resultant impedance spectrum closely approximates a constant phase element (see **Fig. 2-5** for composition and schematic of the NW-metal interface). This behaviour is thought to arise from inhomogeneities in the electrode-material system that can be described in terms of a (non-normalizable) distribution of relaxation times due to frequency dispersion of the capacitance at the interface (see reference [178], and references therein for further discussion). The above outlines a threshold where a device is characterized by either a continuous metallic core or a broken shell. Here, we are bounded by the range  $10^{-6} \Omega \text{ cm} \lesssim \rho_i \lesssim 10^{-3} \Omega \text{ cm}$ , where the lower bound is the resistivity of In and the upper bound ITO. As the variance within a given array increases, fewer loops ( $\lesssim 10$ ) are required to saturate the observed resistance (for our devices  $30 \lesssim N_p \lesssim 1000$ ) [179]. From this, we can only observe relative shifts in this behaviour with high temperature processing (see **chapter 7**, future work for suggestions how to extend beyond this limit). Further, due to the exploratory nature of this work, linear  $i$ - $v$  characteristics were considered sufficient and we avoid depletion of the junction with larger biases and higher probing frequencies, for risk of damaging contacts<sup>3</sup>.

### 3.4 Thin film characterization

Toward a deeper consideration of the phase, crystallographic orientation, and doping profile within our samples, we use: **i.** SEM to determine the mean NW dimensions as well as the local feature density; **ii.** XRD to determine the mean crystallite size and orientation; **iii.** EELS-enabled TEM to determine the radial chemical composition; and **iv.** AES/UPS to determine the surface composition and work-function, respectively. These techniques are briefly introduced below (see **Table 3-4** and **Fig. 3-3**).

---

<sup>3</sup>An initial attempt was made on GLAD-ITO devices to probe into the MHz range, but yielded purely resistive samples. Initial estimates indicate that a power supply with GHz probing frequencies and/or the inclusion of a blocking layer is required for measure — the latter was explored in earlier study of ITO<sub>GLAD</sub> structures by our group (see **Appendix A**) [27].



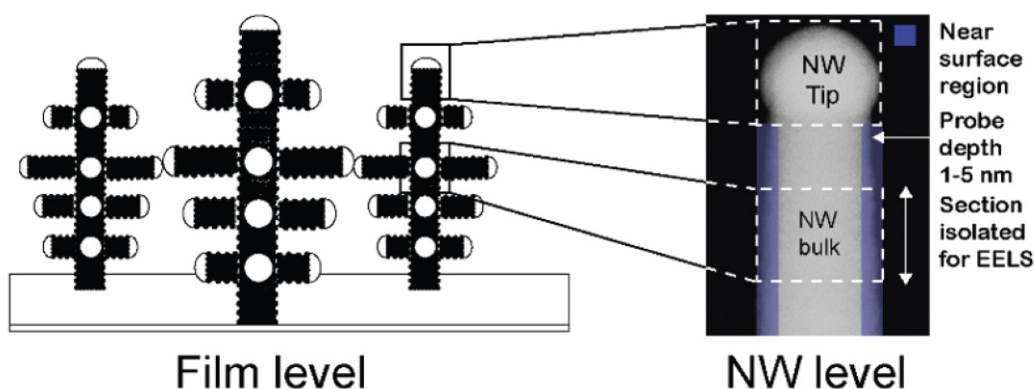


**Figure 3-3 Characterization scheme of ITO thin films and controls.** Via equation 1.1 and 1.2 we can observe shifts in the degree of doping within NW arrays and thin film controls; various characterization techniques allow us to probe the macroscopic, (a) film level properties as well as the (b) bulk and near surface regions of the nanostructures.

**Table 3-4 Characterization technique — region of interest.**

	Near-surface region	Bulk
Film-level	UPS	XRD, UV-VIS
NW-level	AES	3D-CBKR, EELS

### 3.4.1 SEM

SEM is used extensively throughout this work to determine the morphological evolution of films (with  $\Gamma$  and  $\alpha$ ), nanostructure dimensions ( $D_{NW}$  and  $L_{NW}$ ), and the local post-density (used to determine  $N_p$ , see **Appendix D** for further details). We can determine the number of exposed NWs, in part, as they extend above the plane of the polymer in-fill; the catalyst droplets and exposed section of the NW trunk provide a large interaction volume and therefore operate as a large secondary electron source for the SEM detector. In our case, the primary electron beams are produced by field-emission (15 kV accelerating voltage). When impinging on the specimen, the beam is decelerated and its energy transferred inelastically to atomic electrons in the sample. The result is a distribution of electrons that manage to leave the specimen in the form of low-energy secondary electrons, or higher-energy back-scattered electrons. Secondary electrons are emitted from the core of atoms and, due to their low energy, they originate from the surface of the sample, providing information about the topography and morphology of the film. The output signal is captured by a detector consisting of a scintillator/photomultiplier pair and serves to modulate the intensity of a CRT-rastered synchronously with the primary beam, forming the SEM image [154].

### 3.4.2 XRD analysis

XRD analysis is used to observe how processing causes changes in our film's crystallinity, as well as changes in crystallite size and orientation. Crystalline materials are typically defined as polycrystalline (with random or textured crystallite orientation) or single crystal. Non-crystalline materials are termed amorphous, and have no long-range order. This measurement technique involves the coherent, elastic scattering of hard x-ray light ( $\hbar\omega > 10$  keV or  $\lambda < 0.2$  nm) to obtain information about the spatial positions of atoms in a crystal lattice. The Bragg angle ( $\theta$ ) is related to the crystal spacing ( $d_{hkl}$ ) by:

$$2d_{hkl}\sin(\theta) = n\lambda \quad (3-1)$$

The diffraction profiles are obtained by rotating the x-ray source<sup>4</sup> through all  $\theta$  positions, and recording the intensity of diffracted light  $I(2\theta)$ . This analysis provides a 'finger print' of the material phases within the sample. In **chapter 6**, the lattice constant ( $a$ ) is calculated using equation 3-1, grain size ( $D$ ) was determined using the Scherrer equation (with  $K = 0.9$ ,  $\lambda = 0.154$  nm) [154]:

$$I(2\theta) = \frac{K\lambda}{D \cos\theta} \quad (3-2)$$

### 3.4.3 EELS-enabled TEM

Transmission electron microscopy (TEM) is used to study an individual nanostructure's morphology, composition, and local crystallinity (as compared to the film-level characterization of XRD measurements). Pairing this technique with electron energy loss spectroscopy (EELS), the elemental composition and distribution within our processed NWs can be ascertained. To enable the transmission of an energetic beam through the long axis of our NWs, a mid-body plan section of several devices were isolated using a Focused Ion Beam (FIB). Applying this methodology to a given device provides many candidate structures for study (discussed further in **chapter 6**). All EELS characterization within this study was conducted by Kai Cui from the National Institute of Nanotechnology (NINT), Edmonton, AB.

---

<sup>4</sup>In a symmetric  $\theta/2\theta$  scan the angle of incidence of the incoming x-ray beam and the position of the diffractometer/goniometer can be varied independently to access regions of interest in reciprocal space.

During EELS characterization, an incident transmission beam ( $\sim 1.1$  eV) scans the cross-section of an isolated NW mid-section ( $\sim 150$  nm thick, see **Fig. 3-3**), and the resulting elemental peaks are resolved using principle component analysis (PCA)<sup>5</sup> [180]. Electrons are transmitted through a thin sample and are either **i.** unscattered, **ii.** elastically scattered or **iii.** inelastically scattered. A spectrum image is composed of the number of incident-transmitted electrons inelastically scattered as a function of energy-loss.

Spectra can be recorded from highly spatially localized regions of the sample ( $\sim 1$  nm). From 50 eV ( $\sim$ low-loss limit) up to several thousand eV of energy loss, the inelastic excitations involve electrons in the localized core orbitals on atom sites (edges arise from excitations from the core orbitals to just above the Fermi level of the material). Once collected, specific energy losses corresponding to the characteristic core edges of the atomic species present in the sample can be selected, allowing for elemental mapping [181]. This analysis produces a .dm3 file that can be considered as a three-dimensional data cube whose x-y dimensions (real-space imaging dimensions) and z dimension (energy loss in the spectra) contain spectroscopic information related to the local bonding environment. (for the spectrum collection process, see **Appendix F**).

#### 3.4.4 Surface characterization

As discussed in **chapter 2**, the work-function and phase of the ITO thin films can be affected by annealing in oxidizing and reducing environments. For this reason, the complementary techniques of AES and UPS are used to yield insight into the surface composition and work-function (respectively), as the surface properties of our NWs shift with post-processing anneals. Determination of the surface work-function and surface composition is critical for device performance because they affect the energy barrier height at a given hetero-interface (i.e., within an OPV device) [11, 12]. These techniques are used in conjunction with shifts in  $R_D$  as it varies with processing, to better understand how the array and device architecture pair. Surface characterization of

---

<sup>5</sup>PCA is a statistical technique that uses the variance of the contrast in different dimensions, the data set is then reconstructed using only those principal components, eliminating those that represent noise [180].

our NWs was carried out at the Alberta Centre for Surface Engineering and Science, University of Alberta, by Shihong Xu.

Photoelectron spectroscopy consists of a primary beam of UV photons incident upon a sample, and using an inelastic secondary electron cut-off of the energy distribution curve, we can directly measure the ITO work function [145]. AES yields a quantitative compositional analysis of the surface region. Here, auger electrons have a short mean free path; therefore, we are limited to scanning 5–30 Å of sample surface. An auger electron is equivalent to the relaxation energy released in the form of an ejected electron upon sufficient excitation, and proceeds as: **i.** a probe beam excites an inner shell electron, ionizing the atom and producing a core hole; **ii.** an upper level electron decays into the core, transferring its energy to another upper-level electron that is ejected (resulting in a doubly ionized atom). AES analysis therefore allows us to observe relative shifts in surface chemistry with our processing anneals.

### 3.5 Chapter summary

Throughout the device fabrication process we utilized the thin film characterization techniques outline within this chapter, specifically SEM is used extensively to determine the mean dimensions of our nanostructured thin films (particularly to populate our simple parallel resistor model, equation 2-6). We conduct XRD analysis to gain further insight into our mean crystallite dimensions, and to ensure crystal stability with high temperature processing. The pairing of EELS and the techniques of AES and UPS are used to observe bulk and surface compositional shifts, respectively. The application of the above techniques are described in the coming chapters, and are used in conjunction with UV-vis characterization (described in **chapter 2**) to relate the opto-electronic performance of films to the electro-chemical shifts in our nanostructures.



## 4 Electrical characterisation of GLAD-ITO nanopillars

This chapter outlines the incorporation of amorphous GLAD-ITO nanostructures into the 3D-CB device architecture. These devices demonstrate proof-of-concept of our capability to achieve an isolated measure of the electrical performance of the nanostructure arrays. A key point of consideration is the region of uniformity across the device chip (nominally  $1.5\text{ cm} \times 1.5\text{ cm}$  area containing the  $6 \times 6$  device array). Due to non-idealities encountered during wet-etching, our region of uniformity was limited to the inner  $4 \times 4$  device array (or  $\sim 1\text{ cm}^2$  central region), significantly lowering our device yield per chip from 36 to 16. The total number of GLAD-ITO devices fabricated was 112, with edge defects further limiting us to  $\sim 40$  devices used to determine a reasonably unbiased measure of  $\rho_i$  (see **Fig. 4-1** for device chip level uniformity, discussed later in this chapter are device-level defects).

---

ections of this chapter are taken from: Lalany et al., *Axial resistivity measurement of a nanopillar ensemble using a cross-bridge Kelvin architecture*, JVST:A, 31, 3, (2013) [227].

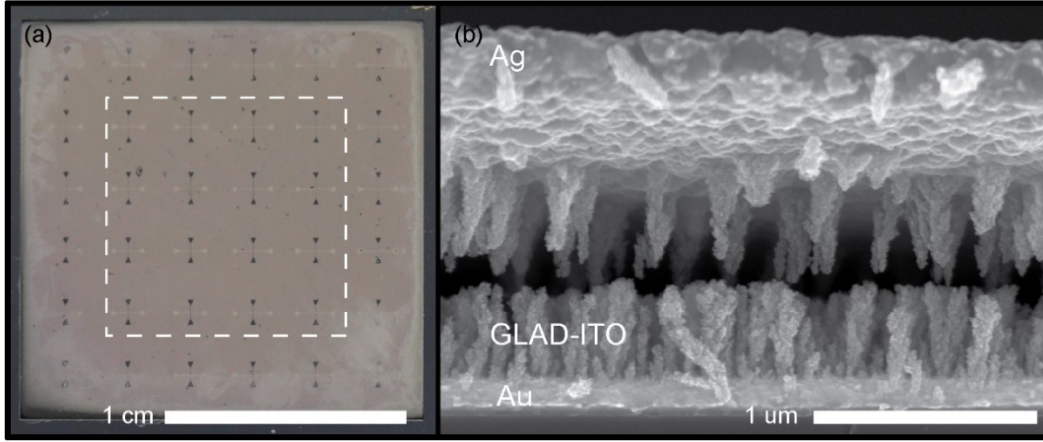


**Figure 4-1 Device fabrication over-view.** (a) A typical device-chip is shown with the region of uniform fabrication highlighted (dashed region); (b) the transition from nanostructure to planar top contact is a challenge overcome through grading of the top contact (discussed later). Shown above is a delaminated top contact from a cleaved sample — for this reason samples were freeze-fractured during SEM sample preparation (note the tapering of nanostructures discussed in **chapter 3**).

To investigate any alteration in the performance of the structured top contacts, Ag contacts were deposited on laterally isolated GLAD structures ( $\text{TiO}_2$ ,  $\alpha = 86^\circ$ ). The measured  $\rho_i$  was found to be within  $\sim 5\%$  of planar EBE-deposited Ag samples (determined via standard 4PP) indicating that the overlap region with the nanostructures does not appreciably degrade the conductivity of the top contact. The Au bottom electrode provides a flat and chemically stable growth surface, further selected for its ease of fabrication. **Figure 4-1 a** is an image of a typical device chip with an inner region of uniformity (dashed square — the Ag traces of devices outside of this region demonstrated significant under-cutting during wet etching and typically registered as open circuits during device testing). Further, a key challenge is the transition of our graded Ag top contact from conformal structured thin film, to a planar layer within a thickness range, tuned to mitigate issues of film stress (see **Fig. 4-1 b** for an example of a delaminated top contact for a cleaved sample). Significant effort was expended to ensure the quality of this interface, with the associated fabrication details outlined below.

## 4.1 Post capping and wet etch of top contact

**Figure 4-2** outlines top and edge-view SEMs of as-deposited GLAD-ITO devices, as well as Ag-capped ITO films, with and without wet etching (**Fig. 4-2 a-f**). To bridge the morphological difference between a vertical post array and the desired planar electrode

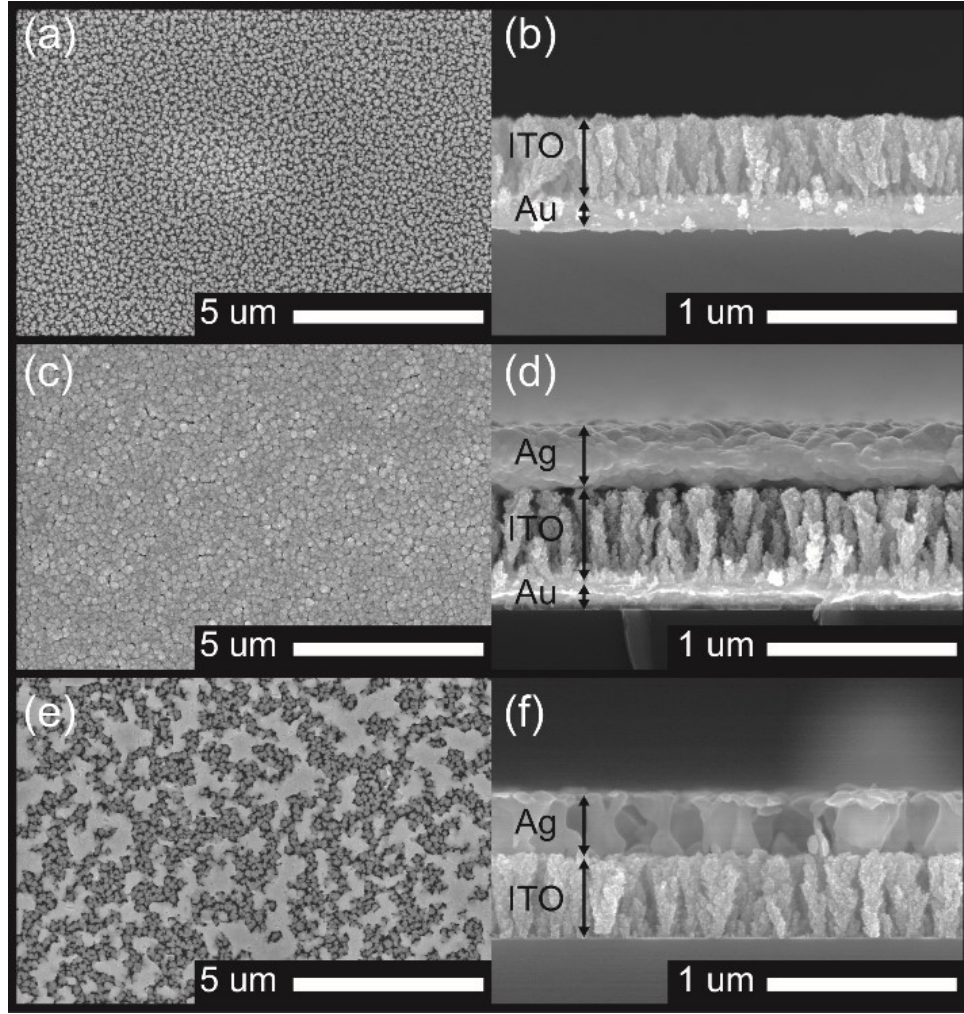


**Figure 4-2 ITO<sub>GLAD 83</sub> device wet-etch.** Plan and edge-view SEMs of: (a, b) ITO films prepared on Au contacts using GLAD with deposition angle ( $\alpha = 83^\circ$ ), (c, d)  $\alpha = 83^\circ$  ITO film on Au, ‘capped’ with 250 nm graded ( $\alpha = 83^\circ \rightarrow 30^\circ$ ) + 100 nm planar Ag, and (e, f)  $\alpha = 83^\circ$  ITO ‘capped’ film after etching non-device areas (i.e., no Au bottom contact).

layer, we used a capping layer with the deposition angle varying linearly with thickness from  $83^\circ$  to  $30^\circ$ , as per previous study [182]. An initial oblique deposition angle during the capping layer deposition is used to minimize the chance of introducing short circuits between the top and bottom contacts and minimize film stress (**Fig. 4-2 c, d**). Various Ag cap thickness of 200 nm, 225 nm, and 250 nm, and etching times were investigated (shown after wet-etching **Fig. 4-2 e, f**). **Figs. 4-3 a and b** shows the change in surface void fraction as a function of cap thickness and etching time (see **section 3.3.1** for the details of the etchants used), determined from plan view SEM images using ImageJ, with areal void fractions  $< 1\%$  (see **Fig. 4-3 c** for a representative area). Our 250 nm graded Ag film was then followed by a 100 nm thick planar Ag layer deposited at  $\alpha = 30^\circ$ .



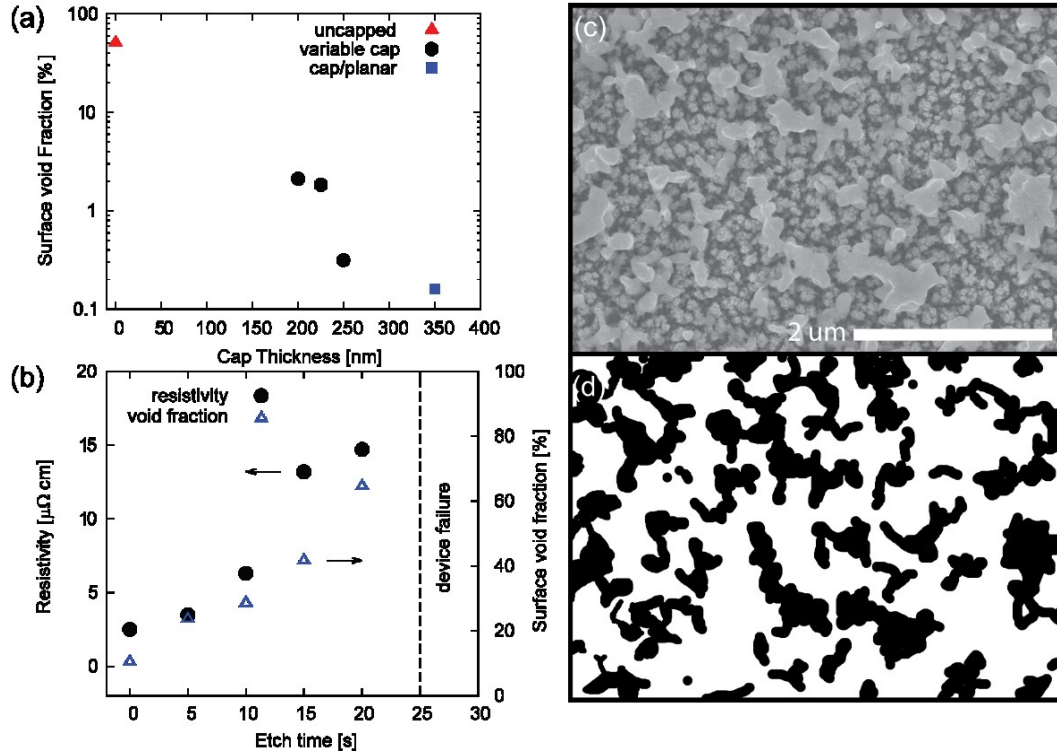


**Figure 4-3** ITO<sub>GLAD 83</sub> device optimal wet etch. (a) Porosity of uncapped films (triangles); reducing porosity with increasing thickness ('variable cap') of Ag (circles); 250 nm Ag cap + 100 nm planar ('cap/planar') Ag; (b) increasing top-contact resistivity and surface void fraction with increasing etch-time in non-device areas, etch times longer than 25 s resulted in device failure; (c) plan-view SEM of partially etched Ag top contact; (d) ImageJ threshold image of same.

Wet-etch characteristics were adjusted to balance device definition and isolation, as excessive etching resulted in the complete lift-off of electrode traces. A variety of etch times and their effects on the top contact were investigated to allow for well-defined, laterally electrically-isolated contacts while not undermining device areas. Smaller devices were observed to be especially sensitive to over-etching (expectedly, due to perimeter scaling). **Fig. 4-3 c** illustrates the effects of “optimized” etching, disrupting lateral conductivity in non-device areas to an extent that device areas are fully isolated (**Fig. 4-3 d** — void fraction mask determined via the image’s binary threshold map). An etch time between 20 s and 25 s was found to be optimal for our conditions, ranging from  $\sim 1.5 \times 10^{-5} \Omega \text{ cm}$  to open circuit. We note that the effect of etch time on our devices is highly sensitive to fabrication parameters, and will require optimization for each deposition angle or porosity. Towards a measure of  $\rho_i$ , these nanostructures were incorporated structures into the idealized four-terminal device (shown schematically in **Fig. 4-4 a, b**).

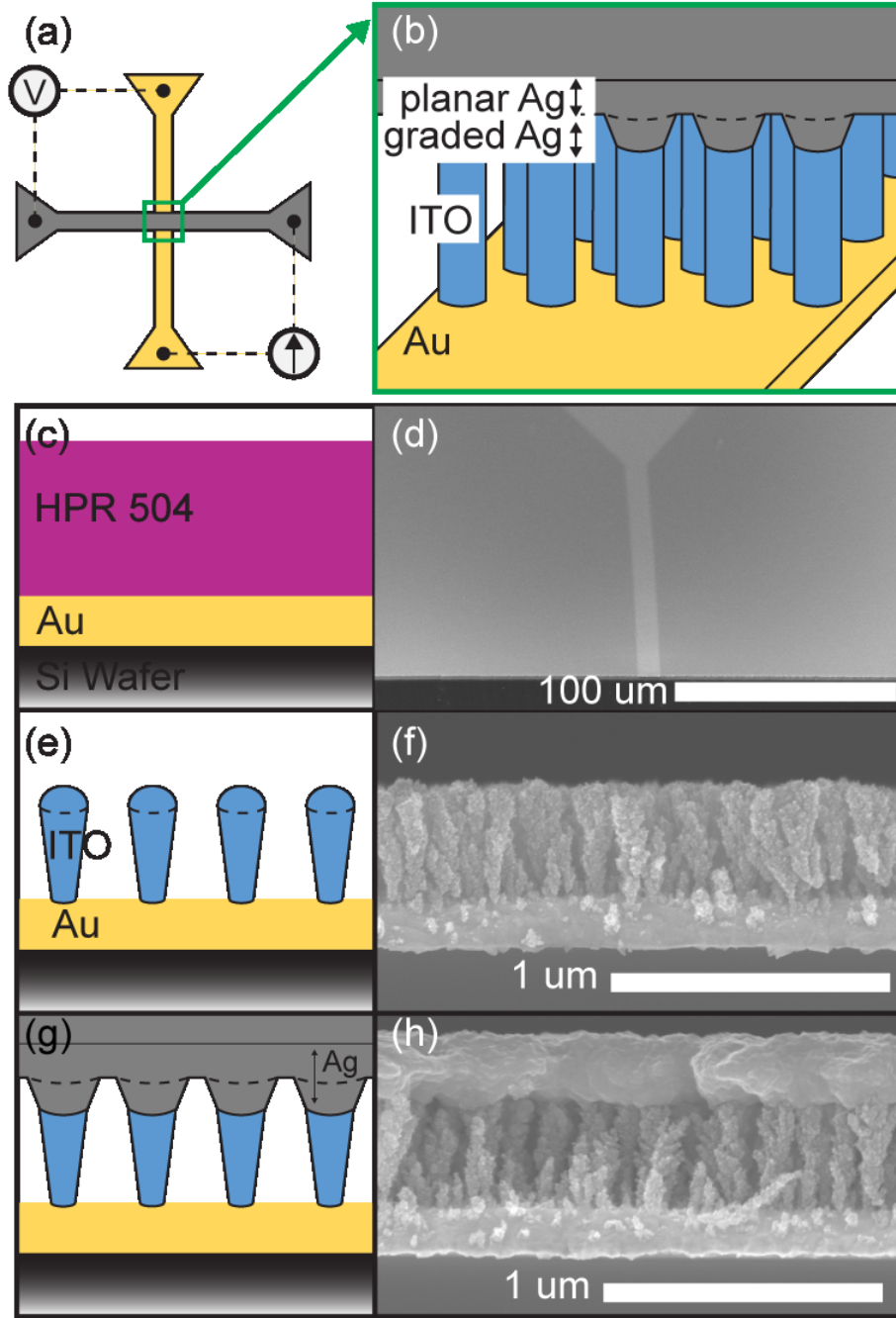


**Figure 4-4 ITO<sub>GLAD 83</sub> device schematic and process flow.** (a) 3D-CBKR in the “2I” configuration; intersecting line widths of 2–10 μm corresponding to contact areas of 4–100 μm<sup>2</sup>. (b) 3-D CBKR Device intersection (Au / ITO / Ag). (c,d) photomask pattern is transferred to Si wafer coated with 100 nm layer of Au (e,f) GLAD ITO structures are deposited on lithographically defined Au traces (g,h) structures are capped with graded Ag top contact.  $w = (33 \pm 7) + (0.28 \pm 0.2)h$  [nm] for ITO<sub>GLAD 83</sub> structures

## 4.2 Device fabrication

Nanostructured ITO films (400 nm nominal thickness) were deposited on Au electrodes (see **Fig. 4-4 c, d**), at an oblique incident flux angle of  $\alpha = 83^\circ$ , with the growth rate (25 nm per substrate rotation) tuned to obtain dense vertical structures (see **Fig. 4-4 e, f**). These deposition parameters produced tapered frustums, spaced approximately 50 nm apart, and are similar to ITO nanostructures fabricated in our initial GLAD-OPV study [183]. Nanostructure spacing and morphology can be further adjusted by varying the deposition angle and pitch, respectively [184], [185]. Post width and density were determined via analysis of cross-sectional and top-view SEM images with ImageJ software. Image analysis treatment was consistent for all films and was conducted over an  $\sim 80 \mu\text{m}^2$  sample region (top-down analysis) for post density, and an  $\sim 1.8 \mu\text{m}$  range for post width (edge-view analysis), with post width measurements taken at different heights above the substrate surface (a procedure outlined in ref: [186]). The  $\text{ITO}_{\text{GLAD } 83}$  nanostructure diameter was found to fit the form  $w = (33 \pm 7) + (0.28 \pm 0.2)h$  [nm], varying with height due to nanostructure broadening. While a power-law is commonly used to describe post growth, the ITO vertical posts studied here are not consistent with power law scaling at small thicknesses. This is attributed to a critical threshold not surpassed, within which the effects of the initial nucleation dynamics dominate.

## 4.3 Completed devices

**Figure 4-5 a** shows a cross sectional SEM of a completed device, cleaved through the device intersection region (shown schematically in **Fig. 4-4 g**, and in an isolate region in **Fig. 4-4 h**). To check for ohmic behaviour in our devices, sense and force probe polarity were varied (**Fig. 4-5 b**). We note that test currents in excess of  $\sim 5$  mA resulted in unreliable measurements, possibly due to excessive joule heating and subsequently damaged test structures [187]. Device area is nominally defined as the plan view overlap between the bottom (Au) and top (Ag) electrodes. SEM characterization of completed devices shows a defect region along the boundaries of the Au electrode, where an intermediate morphology of near dense planar was found (visible in **Fig. 4-5 a**, and magnified in **Fig. 4-6 a, b**).

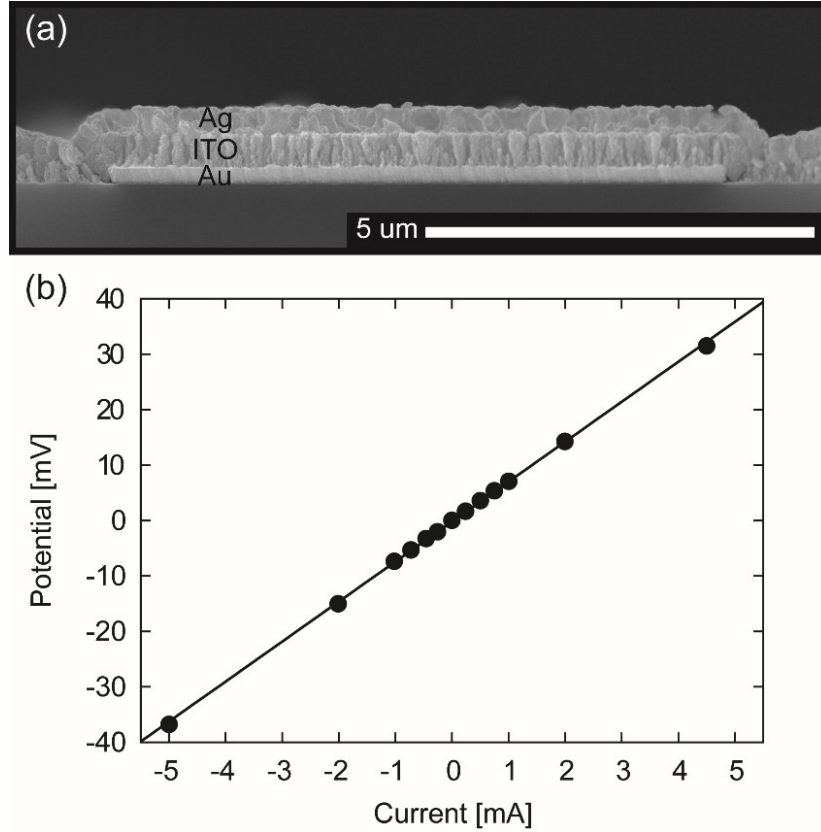


**Figure 4-5** GLAD-ITO **completed device**. (a) Edge view SEM of active region and (b) sample  $i$ - $v$  curve for completed CBKR device ( $\sim 83 \mu\text{m}^2$   $\alpha = 83^\circ$  ITO).

The above edge effects can be attributed to growth of the ITO film at the step-edge between the Au electrode and Si substrate ( $\sim 200 \text{ nm}$ ). At large deposition angles, ITO deposits on the side of the Au step at near normal incidence, resulting in a defect region along both long edges of the Au electrode, similar to previous reports [182]. If the edge defects dominate device performance, resistance is expected to scale roughly with edge length, scaling with the overlap between the silver electrode and the gold electrode. As a first order approximation, we can write the expected length scaling as  $1/\sqrt{A_D}$ , where  $A_D$  is the nominal device area<sup>2</sup>. If, on the other hand, the edge defects do not contribute significantly, resistance should scale as  $1/A_D$  (as is the case for larger devices, see **Fig. 4-6 c**).

Device area was calculated from Ag and Au widths after the etching procedures; etching produced a slight decrease in device areas below the nominal values due to pattern transfer issues during lithography. **Figure 4-7 a** shows resistance data from the

<sup>2</sup>As linewidths vary as  $2 \mu\text{m}$ ,  $5 \mu\text{m}$ , and  $10 \mu\text{m}$ , a scale factor of approximately two results.

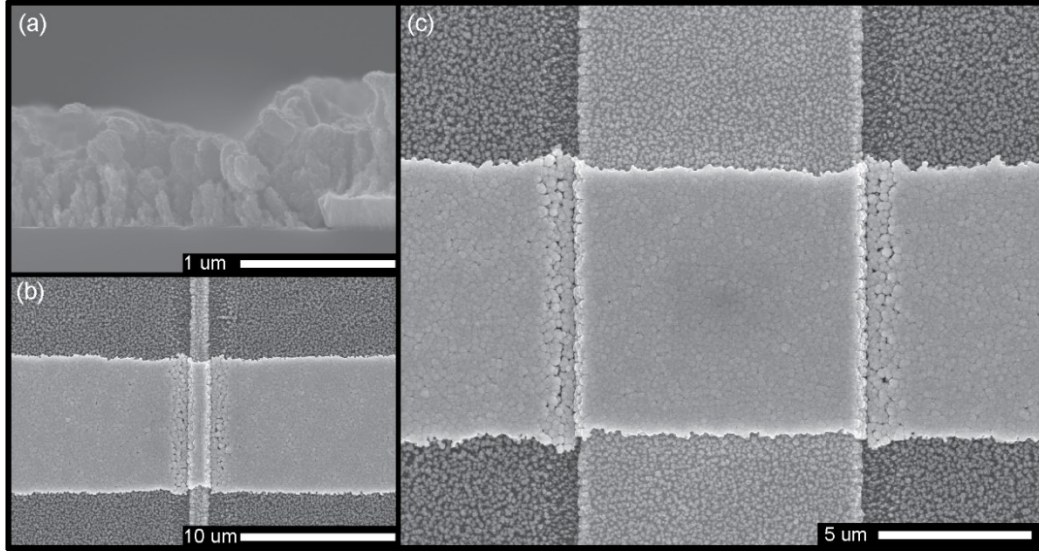


**Figure 4-6 ITO<sub>GLAD 83</sub> device defects.** (a) Edge view and (b) Plan view of defect region resembling dense-bulk film resulting from step-height differential between the Si substrate and Au contact; (c) large scale device with lower defect density.

112 devices (averaged for each nominal device area), ranging in area from  $1.4 \mu\text{m}^2$  to  $83 \mu\text{m}^2$ . **Figure 4-7 b** spans the defect-limited and post-limited regimes discussed. To verify that the larger devices provide an unbiased measurement, we combined the expected device resistance scaling behaviours below:

$$\log(R_D) = \frac{1}{2} \log(R_D) - u(A_D, A_0) \log(A_D - A_0) + R_0 \quad (4-1)$$

where  $R_D$  is device resistance,  $A_0$  represents the crossover between defect-limited and area-limited regimes, and  $R_0$  represents area-independent factors such as contact resistance. Adding the  $A_0$  fit variable for the crossover region between regimes allows us to evaluate the impact of the defects on our measurements. The transition between regimes is sigmoidal, defined by:

$$u(A_D, A_0) = \frac{1}{2} \left[ 1 - \frac{1}{1 + \exp\left(\frac{A_D - A_0}{c}\right)} \right] \quad (4-2)$$

where  $c$  represents the sharpness of the transition between regimes. Equation 4-2 was fit to the data in **Fig. 4-7 a**, using  $A_0$ ,  $R_0$  and  $c$  as fit parameters. The least-squares fit yields a cross-over point between regimes at approximately  $25 \mu\text{m}^2$ , such that our  $83 \mu\text{m}^2$  device is more than a factor of three above the defect-limited regime, and thus offers a reasonably unbiased measurement of  $R_D$ .

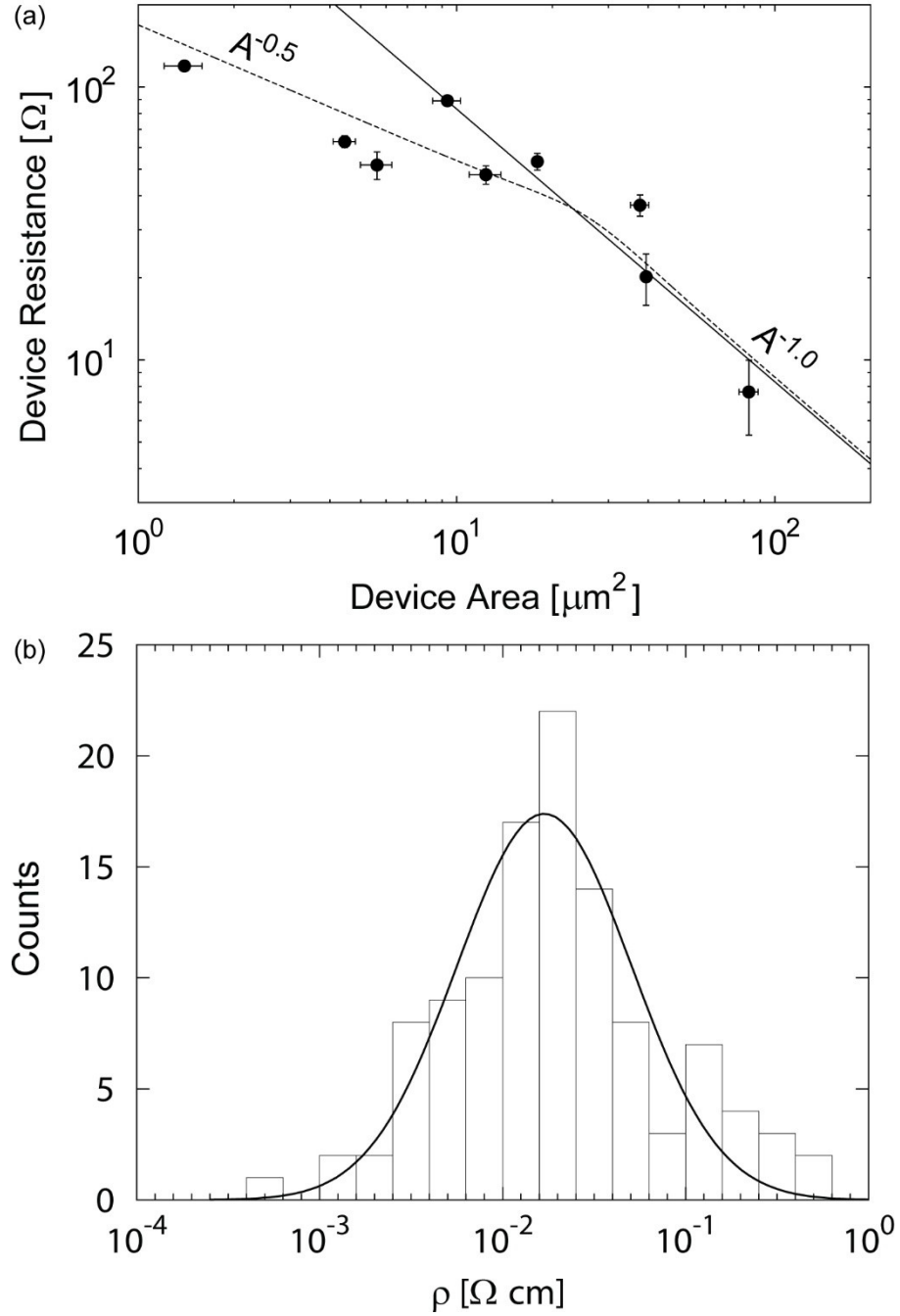


**Figure 4-7 ITO<sub>GLAD 83</sub> device area independent scaling.** (a) Device resistance as a function of device area. The solid line is a best fit to devices above  $7.5 \mu\text{m}^2$  showing the expected  $(A_D)^{-1}$  scaling. The dashed line is a best fit described in the text, including the effect of the defect region. The fit shows device resistance scales approximately with  $(A_D)^{-1/2}$  below  $25 \mu\text{m}^2$  and  $(A_D)^{-1}$  above  $25 \mu\text{m}^2$ ; (b) distribution of device  $\rho_i$  for all devices.

A pronounced illustration of the effect of defects is the difference in scaling behaviour between nominal  $20 \mu\text{m}^2$  devices, where for devices with  $W_{\text{Au}} = 2 \mu\text{m}$ ,  $W_{\text{Ag}} = 10 \mu\text{m}$ , devices scale with perimeter (i.e., defects dominate). This is in comparison to devices with  $W_{\text{Au}} = 10 \mu\text{m}$ ,  $W_{\text{Ag}} = 2 \mu\text{m}$ , where devices scale with area (as expected). For this reason, the former was excluded in the final devices distribution used to estimate  $\rho_i$  (see discussion below). To calculate our material's resistivity, we modelled our ITO devices as a parallel network of frustums. We begin with the resistance ( $R$ ) of an infinitesimal element of length  $dx$ ,

$$dR_p = \frac{\rho_i}{\pi \cdot r(x)^2} dx \quad (4-3)$$

where  $\rho$  is the material's resistivity, and  $r(x)$  defines post radius as a function of height. Based on the post morphology observed, and the sensitivity analysis from **chapter 3**, we approximate the post radius by

$$r(x) = r_1 + \left(\frac{r_1 - r_2}{h}\right) x \quad (4-4)$$

where  $r_1$  and  $r_2$  are the radii of the frustum base and top, respectively, and  $h$  is film thickness. Using the device resistance ( $R_D$ ) of a parallel network with  $N_p$  elements (**equation 2-7**), and integrating across film height, we obtain:

$$\rho_i = N_p \cdot R_D \cdot \pi \cdot \left(\frac{r_1 \cdot r_2}{h}\right) \quad (4-5)$$

Where, as previously outlined,  $N_p$  is the number of contacted posts, and  $h$  is the average nanostructure height, respectively. All devices were individually assessed between sequential fabrication and processing steps using optical micrography, SEM, and 4-wire characterization. Applying our model for ITO<sub>GLAD83</sub> films, an intrinsic material resistivity of  $(11 \pm 3) \text{ m}\Omega \text{ cm}$  is calculated, compared to  $(5.7 \pm 0.3) \text{ m}\Omega \text{ cm}$  for our ITO<sub>TF</sub> control (see **Fig. 4-7 b** for a histogram of the device data) which includes all devices ( $n = 112$ ). As defects dominate,  $A_D$  tends to  $A_{\text{defect}}$ , and in the limit of a small device the measurement is that of a dense, bulk planar thin film. The above estimate includes all devices, however isolating those devices that fall within the unobstructed scaling regime,  $\rho_i = (28 \pm 5) \text{ m}\Omega \text{ cm}$  ( $n = 44$ ).



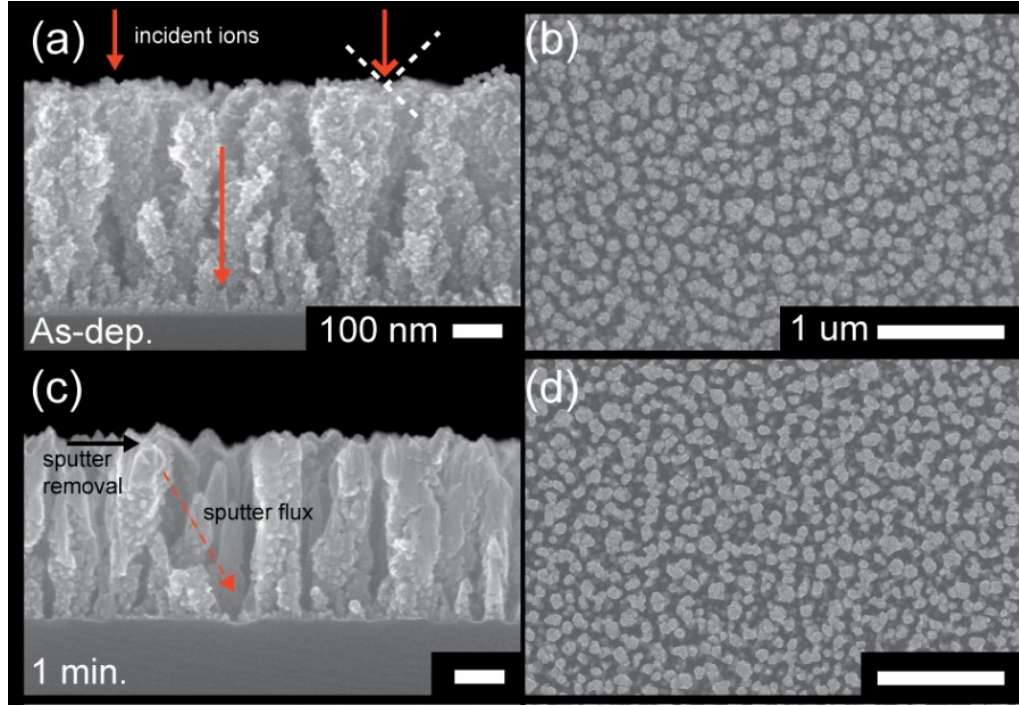


**Figure 4-8 ITO<sub>GLAD 83</sub> ion-milling.** Edge view and plan view SEMs of (a), (b) as-deposited ITO<sub>GLAD 83</sub> films; after ion milling (c), (d) 1 min. Adapted from ref: [188].

A limitation of the initial 3D-CB architecture was the edge defects introduced at the step height of the bottom contact and substrate, as well as the statistical fluctuations in the microstructural properties inherent to the growth of GLAD films (i.e., assessing the critical dimensions of ITO<sub>GLAD 83</sub> structures, as discussed above, there exists a current bottleneck due to post tapering). Electrical characterization of the subsequent thin films is hampered by the requirement of the fabrication of defect-free contacts, and the need for improved uniformity of nanostructures.

## 4.4 Attempted shaping of Nanostructure dimensions

The injected test current is limited by scattering at the frustum base, limiting current transfer in the nanostructure array devices. To address the ‘bottleneck’ or broadening induced asymmetries between  $w_1$  and  $w_2$  (refer to **Fig. 3-2 b**), ion-milling has been explored by other as a post-deposition tool to condition the limiting dimensions and sources of scattering at the interface between nanostructure and electrode [189]. On the film level, ion-milling affects pillar spacing and cross-sectional geometry, increasing



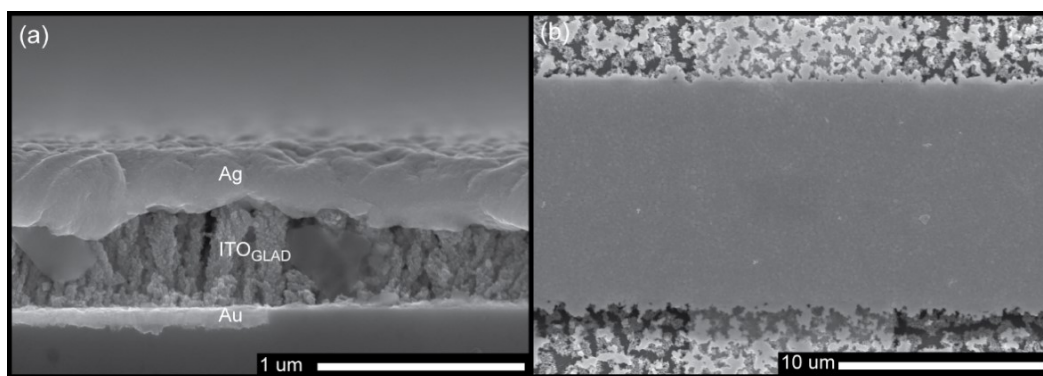


**Figure 4-9 Embedded contacts.** (a) Edge view and (b) Plan view of embedded Au electrode, eliminating the step-height differential between the Si substrate and Au contact.

packing density and inducing birefringence, respectively [188]. In an attempt to reduce the effects of column tapering and further affect the associated scattering at the nanostructure-electrode interface (discussed in **chapter 2** in terms of diffuse scattering at the film boundaries), ion-milling of structures was explored. With ion-milling, ion-induced mass ejection and redistribution consumes the underlying nucleation layer, resulting in more uniform, columnar structures (**Fig. 4-8** illustrates the progressive nature of this process). Milling times  $> 2$  min resulted in the vertical thinning of films, as material sputtered at normal incidence is ejected away from structures, and ultimately escapes causing the overall thinning of films [189]. Along the pillar edge, sputtered materials are primarily ejected towards, and ultimately redeposit onto, the substrate and the base of neighbouring pillars, with only indirect control of lateral thinning resulting. Huang et al., noted that sputter yield increases with ion angle of incidence, reaching a maximum at a material-dependent angle ( $\sim 60^\circ$ ). Of concern to this study, Huang also showed that ion bombardment tends to alter the stoichiometry and diminish the crystallographic structure of the nanostructure array materials. For these reasons, alternative structuring tools were investigated, particularly substrate heating to induce highly ordered, single crystal structure with the edge defects addressed through refinements in the fabrication procedure.

## 4.5 Defect-free contacts

To address the fabrication of defect-free contacts, embedded bottom contacts were fabricated using a similar process to that given by Steele et al., wherein electrodes are counter-sunk to avoid the defect-causing step-edge (see **Fig. 4-9**) [190]. This

fabrication-enhancement was successful in correcting the step-height defect, but uniformity at the wafer-level proved to be an issue with the prescribed reactive ion etch process. For this reason, an alternative method involving a uniform thermal-oxide mask and a HF wet-etch was utilized and, with uniform, crystalline ITO structures, form the focus for the remainder of the thesis.

## 4.6 Chapter summary

The observed deviations in the scaling behaviour of our devices allows us to identify a threshold area beyond which the resistivity of our nanostructures can be determined. The difference in resistivity of a factor of approximately 5 between structured and unstructured films may be attributed to composition, crystallinity and morphological differences, and is suggestive that post-processing annealing will be required to explore and improve film electrical and optical characteristics of nanopillar films. The challenge with these structures is the ambiguity surrounding the definition of the conductive channel for a given amorphous structure<sup>3</sup> [191], [192]. This is particularly difficult with respect to the internal structure and nano-scale porosity common to GLAD nanostructures [193], and must be considered in conjunction with the contribution of a surface depletion region characteristic of ITO thin films [98], [161]. This causes deviations between physical dimensions and electronic dimensions, and begs the need for further study to gauge the relative contributions from each of the above sources of uncertainty.

---

<sup>3</sup>XRD analysis reveals that ITO<sub>GLAD 83</sub> films are fully amorphous compared to the polycrystalline dense planar control, and VLS-ITO NWs (shown later in **Fig. 6-5**).



## 5 Measurement of VLS-GLAD-ITO nanowires

From **chapter 1**, our primary objective is to validate the 3D-CB test structures, and use them to optimize the electrical properties of our material system through post-deposition anneals. The former required that we understand and eliminate device-scale defects to facilitate an unbiased measure of  $\rho_i$ ; the latter is investigated to tune the NW conductivity while maintaining the highly-branched structures suitable for integration into OPV devices<sup>1</sup>. The procedure undertaken to accomplish the above involved the fabrication of VLS-GLAD-ITO devices and their measurement, as well as the thin film characterization of witness samples and deconstructed devices. The former required the determination of  $N_P$ ,  $R_D$ ,  $A_{NW}$ , and  $L_{NW}$  (see **Fig. 3-1** for the process-flow); the latter involved the use of thin film characterization techniques outlined in **chapter 3** to track

---

<sup>1</sup>Structures can be deposited at elevated rates to increase  $n_e$ , as demonstrated by LaForge et al. [94], however film morphological degradation (i.e., loss of branches) is observed for higher rate films, as was seen in **chapter 2, Fig. 2-10**.

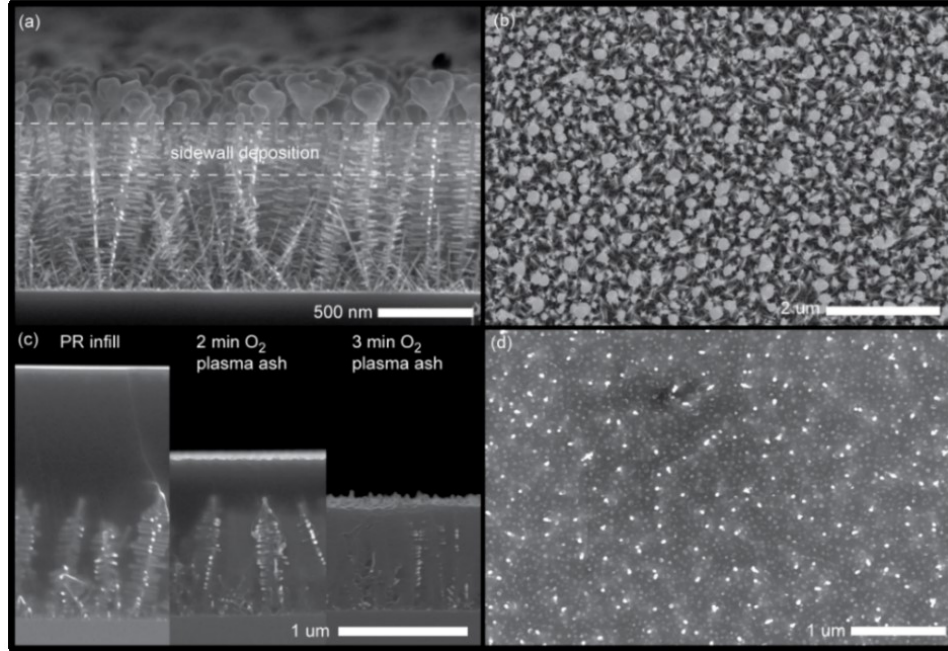


**Figure 5-1 Graded cap, polymer infill and NW tip exposure for ITO<sub>VLS85</sub> structures.** (a) Edge-view SEM of structures with  $\sim 200$  nm of Ag capping; (b) top-down view of same; (c) edge-view SEM of films in-filled with HPR 504 and NW tips exposed with a progressive low-power O<sub>2</sub> plasma ash; (d) top-down SEM of exposed tips prior to top-contact deposition.

relative shifts in chemical and crystallographic properties, as well as the intrinsic NW doping profiles. The results of this study are best understood through the evolution of films and device performance with high temperature anneals and are discussed further in **chapter 6**. This chapter outlines the fabrication routine undertaken to remove all contributing sources of defects to our measurements (i.e.,  $R_{\text{geom}} = 0$ )<sup>2</sup>.

## 5.1 NW capping and tip exposure

The direct capping technique used in the study of ITO<sub>GLAD83</sub> films was attempted on the ITO<sub>VLS85</sub> structures. Due to the differing dimensions and spacing of the nanostructures, direct capping resulted in sidewall deposition—a potential for shorting during measurement (see **Fig. 5-1 a** for edge-view SEM, and **b** for a top-down view). As cap layer stress increases with thickness [194], there is a finite thickness within which to transition from a porous, conformal layer, to dense planar layer with sufficient lateral conductivity required for the definition of contact terminals (see **Fig. 2-4 b** for schematic). To bridge the spacing between structures directly would require a thick top-

<sup>2</sup>From **section 2.2**, as per our outline methodology, as  $R_C \rightarrow 0$ , and  $R_{\text{geom}} = 0$ ,  $R_K \rightarrow R_P$  (here  $N_P$  is the limiting source of uncertainty).

contact capping layer, introducing film stresses that may be detrimental to fabrication and testing (as was seen in **Fig. 4-1 b**). To facilitate the direct capping of the nanotree films, HPR 504 (2400 rpm, 10 s spread, 50 s spin) was used to in-fill the films (**Fig. 5-1 c**)<sup>3</sup>, and a low-power plasma ( $\sim 30$ s steps, 400 mTorr,  $1 \text{ W cm}^{-2}$ ) was then employed to expose the tips of the NWs (**Fig. 5-1 d**).

## 5.2 Device fabrication

The use of counter-sunk bottom electrodes are key to avoid measurement-limiting edge-defects (see **Fig. 5-2 a, b** for schematic and SEM image of a completed device). To this end, Si wafers were thermally oxidized (Thermco Minibrute,  $950^\circ\text{C}$ , 70 min), resulting in a 350 nm thermal oxide layer, with electrode trenches defined with a wet etch (HF,  $\sim 55 \text{ nm/min}$  etch rate)<sup>4</sup>. The wet etch resulted in uniform trenches defined over the four-inch device wafer. A 350 nm layer of ITO was then sputter-deposited into the trenches at  $0.2 \text{ nm s}^{-1}$  (5 mTorr Ar, 33 cm throw distance,  $2 \text{ W cm}^{-2}$ ), and serves as both bottom contact and VLS growth surface. Schematic and SEM images outline the process-flow used to embed the ITO<sub>SP</sub> contacts into a thermal oxide layer; here bottom contacts were isolated laterally through a sonication-enhanced lift-off of the underlying photoresist and ITO<sub>SP</sub> between trenches using an acetone bath (shown prior to lift-off in **Fig. 5-2 c, d**).

A key difference from the fabrication procedure outlined in **chapter 4** is the use of a polymer in-fill step to allow for the direct capping of NWs<sup>5</sup>. Once in-filled, a low-power plasma ash was used to expose the tips of the NWs. After NW tip exposure, but before metal capping, it was required to determine the number of posts per device ( $N_p$ ) — a key parameter to populate our parallel post model. First, we confirm an adequate degree of exposure (through SEM imaging); then, if samples were over-exposed (discussed later), they were re-filled and re-exposed. Ideally plasma-ashed samples were used to determine the mean cross-section of the NWs (see **Fig. 5-2 e, f**). The polymer in-fill facilitates the subsequent direct capping (**Fig. 5-2 g, h**).

---

<sup>3</sup>Through experimentation it appears that spin speeds  $< 2000 \text{ rpm}$  yield incomplete coverage, and clumping occurs at spin speeds  $> 3000 \text{ rpm}$ .

<sup>4</sup>The use of a wet etch here ensures the uniformity of bottom electrodes across the four-inch device wafer (for comparison the reactive ion etch process used in **chapter 4** has a region of uniformity  $\sim 1 \text{ in}^2$ ).

<sup>5</sup>Note, high temperature processing anneals were applied prior to this step.

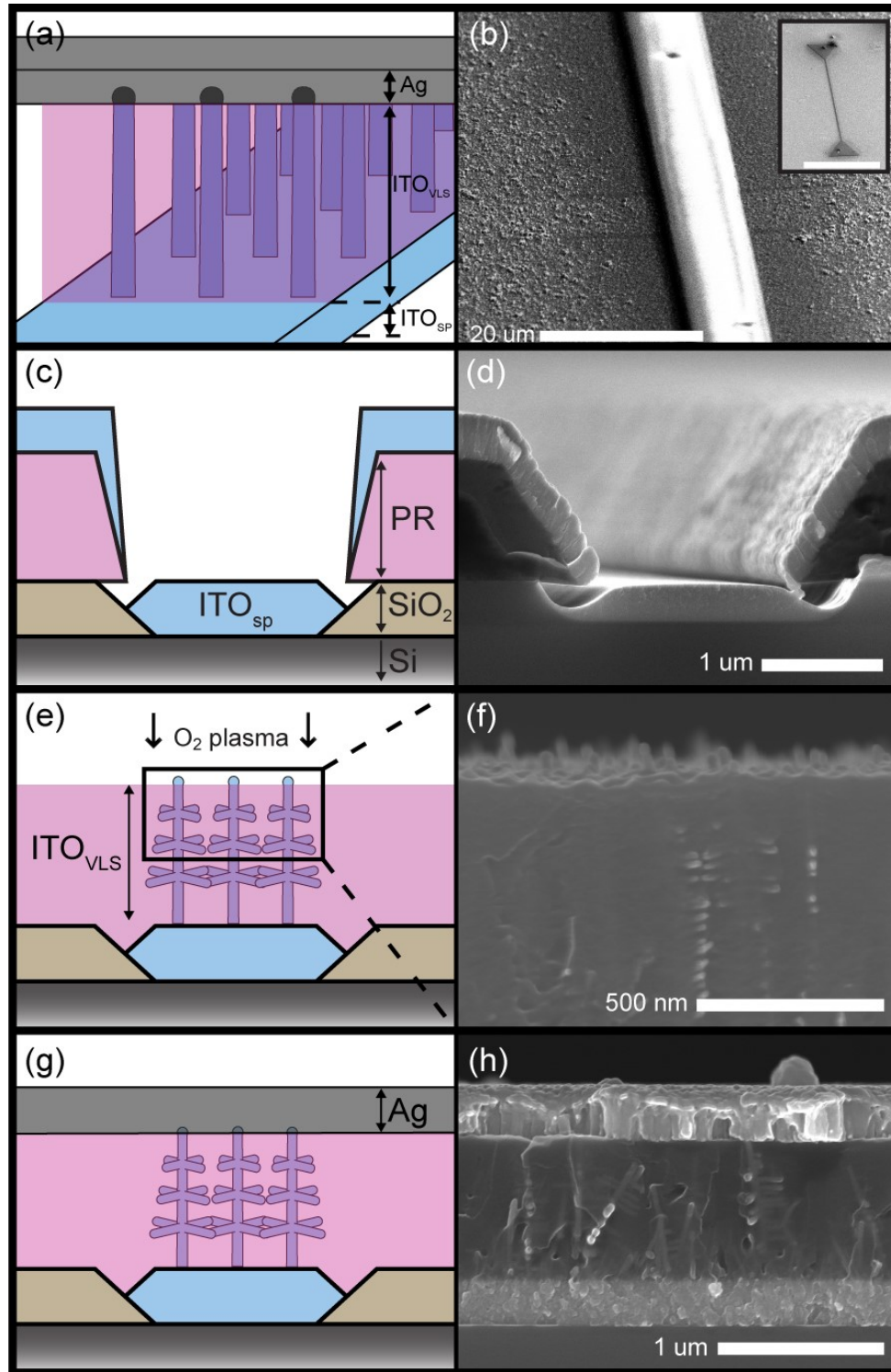


**Figure 5-2 Summary of device fabrication.** (a) Schematic oblique-view of intersecting device area with NWs modelled as an array of parallel resistors; (b) oblique-view SEM of same, inset: 500 μm scale bar. Schematic and edge-view SEM micrographs of: (c, d) embedded ITO<sub>SP</sub> bottom contact prior to lift-off; (e, f) ITO<sub>VLS</sub> structures in-filled with an insulating polymer (labelled as PR), exposed with low-power plasma ashing process; (g, h) graded Ag top contact.

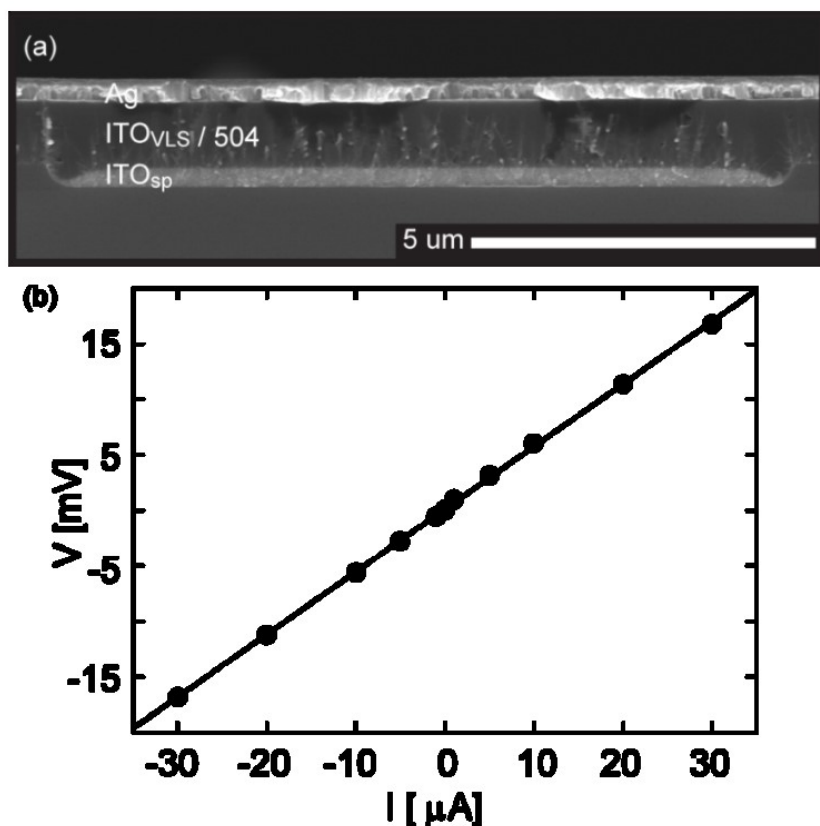


**Figure 5-3 Completed device.** (a) Edge-view SEM of completed device; (b) Representative device  $i$ - $v$  characteristic demonstrating ohmic behaviour within our measurement window.

### 5.3 Completed devices

To determine  $R_D$ , the measurement procedure outlined in **Table 3-3** was followed. The key outcome from the testing of completed devices (**Fig. 5-3 a**) was the collection and verification of linear  $i$ - $v$  characteristics determined for each device (see **Fig. 5-3 b** for a representative characteristic). All ITO<sub>VLS</sub> 85 structures investigated were deposited in a single deposition ( $\alpha = 85^\circ$ ,  $0.5 \text{ nm s}^{-1}$ , see **Appendix C** for further deposition details), with varying process parameters administered post-deposition. Planar and  $\alpha = 50$ – $87^\circ$  ITO<sub>VLS</sub> films are used as controls to observe the contributions of morphological evolution with  $\alpha$ -scaling. Witness samples were processed in parallel to enable post-measurement thin film characterization (discussed further in **chapter 6**). The subsequent processing details are presented in terms of their contribution to the proceeding error analysis, with the effects of defects and device-level trends discussed.



## 5.4 Device error analysis

The device resistivity determination procedure simplifies to:

1. Determine the mean NW dimensions (i.e.,  $A_{NW}$  and  $L_{NW}$ );
2. Determine  $N_p$  for each device;
3. Measure  $R_D$ ; and
4. Estimate  $\rho_i$  using the above determined values to fit **equation 2-6**.

The following sub-sections provide further details for each of these steps.

### 5.4.1 Mean NW dimensions

We can determine the number of exposed NWs, in part, as they extend above the plane of the polymer in-fill; the catalyst droplets and exposed section of the NW trunk provide a large interaction volume and therefore operate as a large secondary electron source for the SEM detector.  $D_{NW}$  was determined from top-down SEMs, and  $L_{NW}$  from edge-view SEMs ( $L_{NW} = 957 \text{ nm} \pm 7 \text{ nm}$ , where the uncertainty is represented by the standard error of the mean — see **Fig. 5-4 a**). The estimated mean droplet-diameter of structures (see **Fig. 5-4 b**) above the polymer infill line was found to be  $32.2 \pm 0.6 \text{ nm}$ , determined after polymer infill, and prior to plasma ashing ( $34 \pm 6 \text{ nm}$  from edge-view SEM analysis<sup>6</sup>). Here, the extended tail of the diameter distribution may be attributed to exposed branches interfering with top-down image analysis. Note, the NW trunk diameter was determined from the analysis of droplet size from ideally plasma-ashed samples, and assumed representative for all devices<sup>7</sup> (**Fig. 5-4 c**).

---

<sup>6</sup>Determination of  $D_{NW}$  from edge view SEM is limited by a situation where we are imaging the diagonal dimension, for NWs randomly oriented (i.e., not necessarily with a cubic face aligned with respect to the sample during edge-view analysis), this results in a larger determined value and associated broader distribution.

<sup>7</sup>For our initial calibration devices (AL4-007A):  $L_{NW} = 725 \pm 20 \text{ nm}$  and  $D_{Droplet} = 24.6 \pm 0.5 \text{ nm}$ ; for the ‘full-scale’ study (AL4-007B):  $L_{NW} = 957 \pm 7 \text{ nm}$  and  $D_{Droplet} = 32.2 \pm 0.6 \text{ nm}$ ; giving an indication of the variance in film properties between depositions.

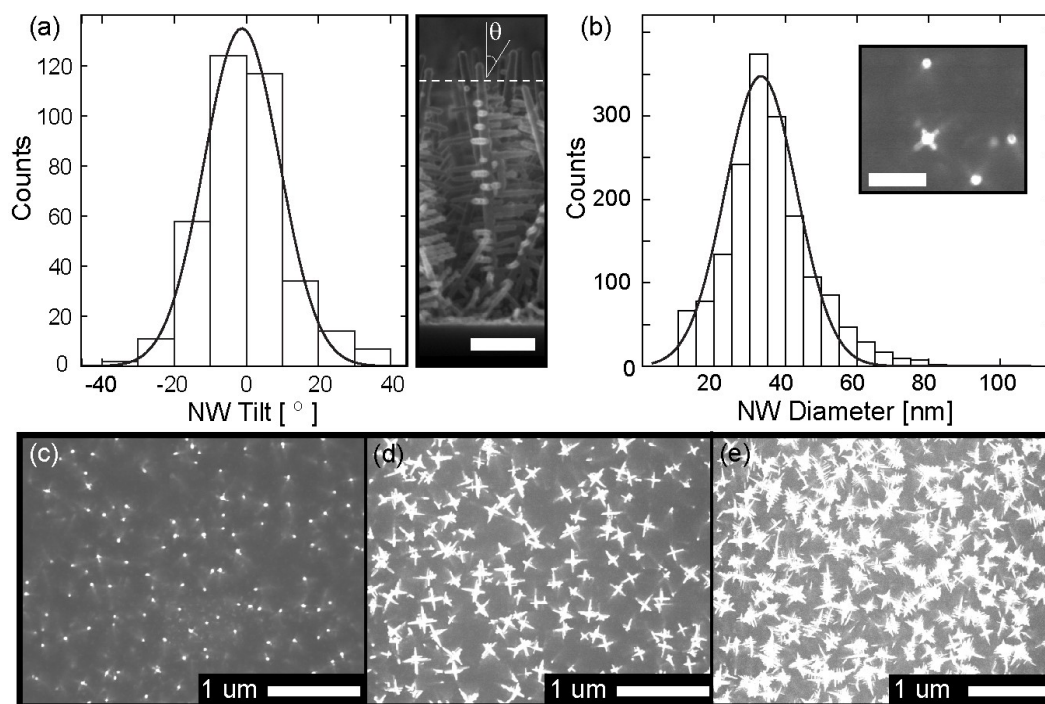


**Figure 5-4 NW diameter and column tilt.** (a) NW diameter histogram ( $n = 1678$ ) determined by top-down SEM image analysis, right skew is believed to be branch contribution, inset: plan-view SEM of exposed NWs, 200 nm scale bar; (b) column tilt histograms ( $n = 282$ ) determined by edge-view SEM image analysis for structures  $> 850$  nm, 200 nm scale bar. Plan-view SEM micrographs of: (c) ideally exposed (d) moderately over-exposed, and (e) severely over-exposed device regions.

With progressively over-exposed samples (**Fig. 5-4 d, e**), it becomes more challenging to separate the branches and catalyst droplets. **Figure 5-4 d** is near the limit of our ability to discern individual NWs using the outlined image analysis techniques (for this reason further investigation was required to gauge the suitability of the available image analysis routines to find a fair means of determining  $N_P$ —see **Appendix D**). Determination of  $N_P$  for severely over-ashed samples is particularly challenging due to the increased contribution from the film undergrowth, as features merge due to charging of samples during SEM analysis<sup>8</sup>. Within our methodology, we are selecting those NWs that have grown above the threshold of the polymer infill line, and are therefore ignoring the contribution of extinct NW growth (resulting from competitive growth dynamics) and the branches of the structures isolated between our bottom electrode and polymer infill line.

<sup>8</sup>Significant enhancements to resolution have been demonstrated with the use of scanning helium ion microscopy (SHIM), utilized to overcome charging effects that typically obscure SEM images [96], and represents a likely solution to the above issues.

The contribution from NW tilt to the device conduction length ( $L_{NW}$ ) was also explored at the calibration stage (completed on AL4-007A films). Column tilt as an isolated variable was found to be a secondary consideration when determining  $\rho_i$  for structures above the polymer infill line (**Fig. 5-4 a inset**, dashed line); this is in comparison to the observed 10-fold variation in  $R_D$  observed within each processing condition (see **Appendix G**)<sup>9</sup>.

### 5.4.2 Determined number of NWs per device

The NWs are isolated on the  $ITO_{SP}$  bottom contact, as there is a physical barrier between devices and structures in non-device regions.  $W_{ITO}$  is the width of the bottom ( $ITO_{SP}$ ) contact, and  $W_{Trench}$  is the width of the region below the deposition plane, bordering the bottom contact, and results in further isolation of structures. The region  $W_{Trench}$  results from the isotropic HF wet etch and subsequent sputter-infilling through the photoresist mask; growth in this region does not result as it is below the deposition plane (see **Fig. 5-5 a, b**). Due to local variations in exposed NWs, as well as uncertainty in Ag trace alignment, the local post density ( $\rho_D$ ) was used, and determined on a per-device basis from the average of three frames per device (discussed further below, see **Fig. 5-5 c, d**)<sup>10</sup>. See **Appendix D** for further details. The number of NWs was determined as:

$$N_P = A_D \cdot \rho_D \quad (5-1)$$

where  $A_D$  is defined as the region of overlap between the electrodes. This approach allowed us to limit uncertainty in  $\rho_D$  to propagated counting error on a per-frame basis and we are limited by an underlying Poisson distribution (e.g., see **Fig. 5-5 e** for post count). **Figure 5-5 f** is an example of an optimal etch, while **figure 5-5 g** illustrates the degree of potential undercut of the top electrode. **Table 5-1** outlines deviations from nominal line-width dimensions due to undercutting of the Ag trace.

---

<sup>9</sup>With respect to column tilt angle, Taschuk et al. similarly found that the angle trunks made with the substrate normal tend to be less than 45° [196]. Taschuk explained this observation by proposing a 2-D growth model in which the largest exposed face of a nucleation layer of randomly orientated cubic crystallites is within 45° of the substrate normal (the other faces are partially buried in the initial 2-D layer, reducing growth in that direction—see also the discussions of **section 2.5.3**) [196].

<sup>10</sup>As previously discussed, there are hints of the spontaneous formation of core-shell structures (see **Fig. 5-5 d, inset** for zoomed in threshold images of such individual NWs). Discussed further in **chapter 6**.

**Table 5-1 Line-width measured at the center for 375 °C sccm sweep.** Note that 2  $\mu\text{m}$  line traces are omitted due to our photo-mask layout<sup>11</sup>. Also provided are the average ITO<sub>SP</sub> dimensions (here uncertainty is presented as standard error of the mean for all devices of the indicated nominal dimension).

	<b>W<sub>ITO</sub> [<math>\mu\text{m}</math>]:</b>			<b>W<sub>Ag</sub> [<math>\mu\text{m}</math>]:</b>		
Nominal	2	5	10	2	5	10
Experimental	-	$3.85 \pm 0.04$	$8.78 \pm 0.03$	-	$3.5 \pm 0.2$	$9.1 \pm 0.1$

The determined  $N_p$  for a device is bounded by a deposited film’s feature density and the associated error in the determined local post density ( $\delta\rho_D \leq \rho_D \leq \sim 19 \text{ NWs } \mu\text{m}^{-2}$ ), as well as  $A_D$  — discussed in the following section. Here, the upper bound is the observed feature density of an as-deposited film for our given deposition parameters [11], and the lower bound can be reduced by including multiple frames of the device intersection region — effectively mapping the local post density in the vicinity of the center of the ITO<sub>SP</sub> bottom contact (i.e., the region likely to be capped with Ag). We are then limited by our ability to correctly identify an exposed NW and therefore our ability to assess  $\rho_D$ .

The capping with Ag and wet etching of this layer resulted in flat, seemingly defect-free contacts (see **Fig. 5-3 a**, compare with **Fig. 4-5 a**) with similar device-chip etch characteristics as **Fig. 4-1 a**, and an observed yield between 50–94% (see **Table 6-2** for a summary of device yield per process condition). At the device-level, further uncertainty results from the severe under-cutting of Ag contacts during wet-etching (shown in **Fig. 5-5 f** and **g**). However, an estimate of  $W_{Ag}$  was made possible, in part, due to the optical transparency of the PR and high reflectivity of our metal top contact (see **Appendix D**, and later sections) allowing us to observe the underlying trace dimensions<sup>12</sup>.

<sup>11</sup>As before, devices on the perimeter of the 6 × 6 array were sacrificed for an optimal etch of the center region (i.e., the inner 4 × 4 array), and yield was therefore limited to < 16 devices per chip—this results in no viable 2  $\mu\text{m}$  traces due to the photo-mask layout (see previous **Fig. 3-2 d**).

<sup>12</sup>In extreme cases of under-cutting (potentially through the width of a trace), contact degradation results in the formation of ‘micro-channels’. The formation of these channels severely undermines our confidence in the determined  $N_p$ ; however in the limited cases where this class of defect was observed, devices failed open circuit and were therefore not included in the dataset (see **Appendix D** for further information).

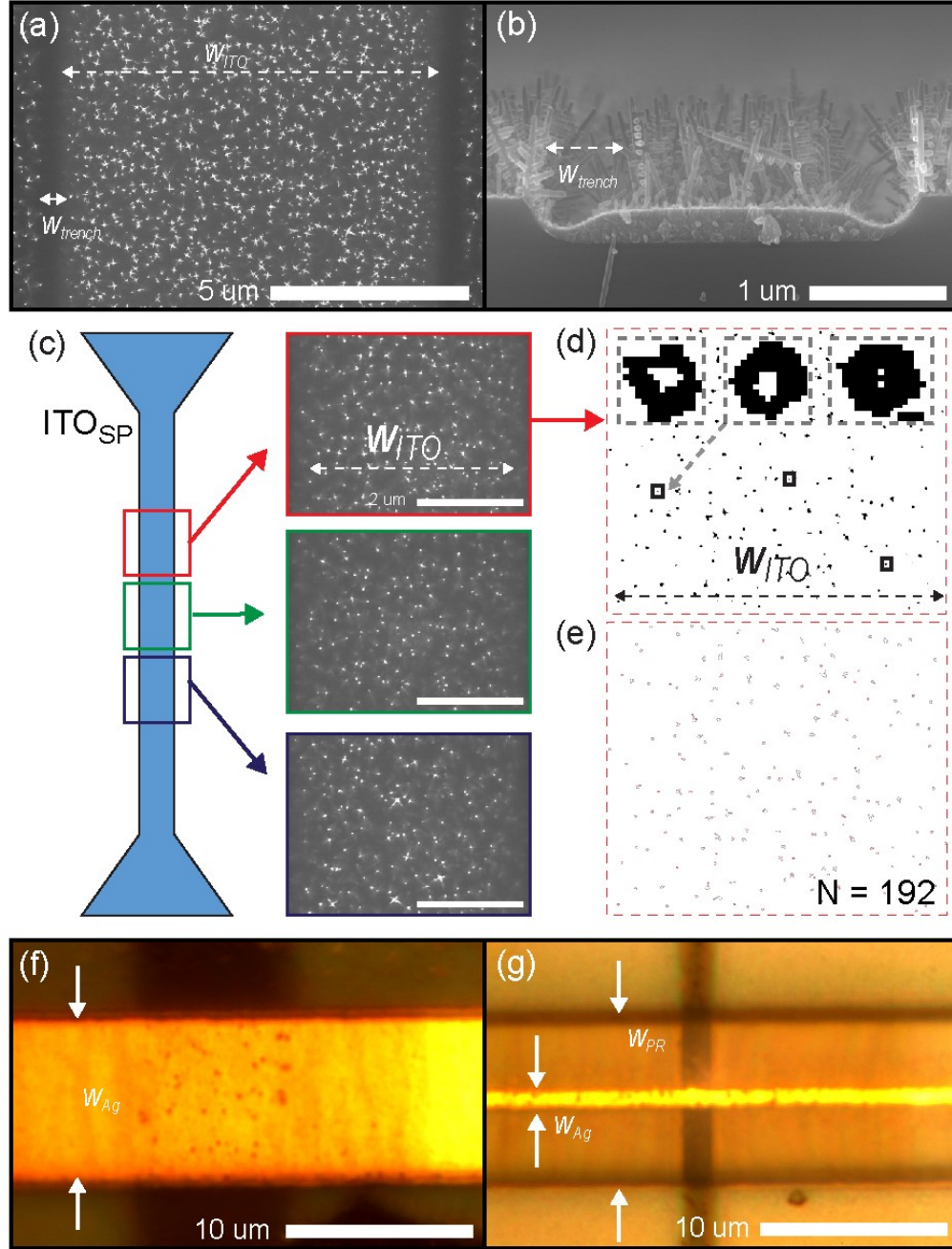


**Figure 5-5 Summary of  $N_p$  determination procedure.** (a) Plan-view SEM of polymer-infilled, plasma exposed NWs. The trench region results in the further isolation of structures; (b) edge-view SEM of same; (c) top down SEMs at multiple regions along the bottom ITO contact to determine the local post density; (d) each frame undergoes a threshold routine (see **Appendix D** for details) to determine the number of exposed NWs, inset: dashed boxes are samplings of dispersed presumably core-shell structures (10 nm scale bar), solid boxes are illustrative; (e) the number of posts (i.e.  $n = 192$ ) is averaged over 3 frames to yield the local post density (i.e.  $11.2 \pm 0.4$  posts /  $\mu m^2$  for this frame)<sup>13</sup>; (f) undercut of the Ag trace is assessed with optical microscope (plan view); (g) severe undercut of a nominally 10  $\mu m$  wide Ag trace.

<sup>13</sup>Initially 2 frames per device (as-deposited devices; to further account for non-idealities, 3 frames per device were used. Over-exposure also motivated the separation of the determination of  $N_p$  and  $D_{NW}$ .

**Table 5-2 Linear as-deposited device results.** For device resistance, the standard error of the mean is reported, as well as the corresponding Pearson product-moment correlation coefficient ( $r$ ) and  $p$ -value.

Device code:	$N_P \pm \delta N_P$	$R_D \pm \delta R_D [\Omega]$	$r$	$p$
2c111	$108 \pm 11$	$5539 \pm 19$	0.999997	6.6E-09
3c111	$318 \pm 32$	$4238 \pm 30$	0.999995	1.3E-08
*3e111	$147 \pm 15$	$5804 \pm 411$	0.974964	4.7E-03
4b111	$189 \pm 19$	$392 \pm 10$	0.999968	2.2E-07
4c111	$372 \pm 38$	$404 \pm 19$	0.999926	7.6E-07
4d111	$380 \pm 39$	$229 \pm 2$	0.999924	7.9E-07
4e111	$290 \pm 29$	$231 \pm 5$	0.999988	4.7E-08
5b111	$199 \pm 15$	$280 \pm 16$	0.999960	3.0E-07
5d111	$218 \pm 12$	$8563 \pm 130$	0.999946	4.8E-07
5e111	$88 \pm 7$	$270 \pm 9$	0.999956	3.5E-07

### 5.4.3 Measured linear device characteristics

$R_D$  is measured over the range 1–30  $\mu\text{A}$ ; where the uncertainty is given by the standard error of the mean for the 5 data points collected in this range (see **Table 5-2**, column 3)<sup>14</sup>. During testing, anomalies were noted, where minor variations in  $R_D$  occurred, and were believed to be an effect of increasing test currents causing the ‘burnout’ of shunting paths (for this reason, data collection was conducted manually). A Pearson product-moment correlation coefficient ( $r$ ) was computed to assess the device  $i$ - $v$  characteristics. There is a strong positive correlation between  $I_{\text{test}}$  and  $V_D$  for all devices ( $n = 10$ ):  $r < 0.97$ ,  $p < 0.005$  for the as-deposited process condition, supporting an ohmic conduction model for our devices.

<sup>14</sup>In the table above, the first two digits refer to device position on wafer (see **Fig. 3-2 d**) and last three digits refer to process history (see **Appendix G** for process legend). The device denoted with (\*) had  $n = 4$  instead of  $n = 5$  for the included measurement range.

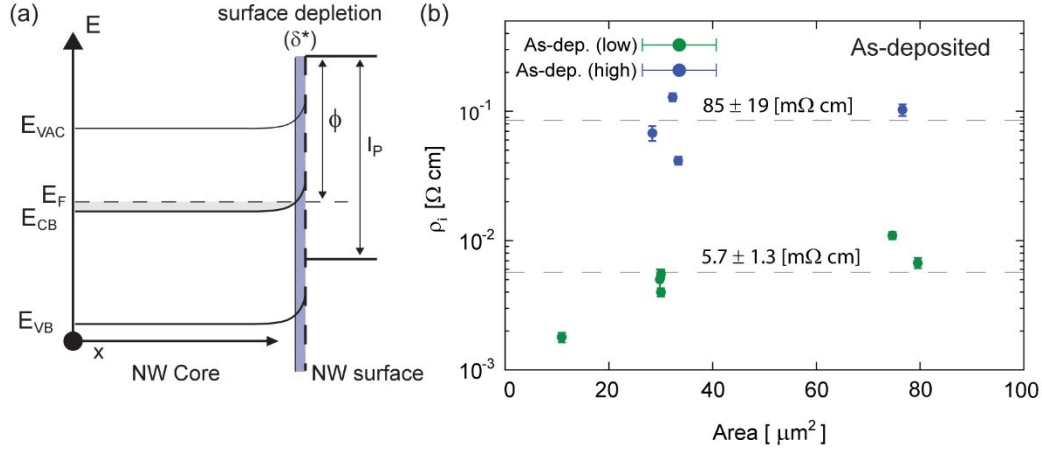


**Figure 5-6 Surface depletion layer and as-deposited resistivity results.** (a) schematic representation of the upwards band bending of the Fermi level induced from gap surface states that cause carrier depletion in a thin surface region; (b) as-deposited estimates ( $n = 10$ ) for the NW intrinsic resistivity and an observed violation of normality for the device distribution. Assuming  $\delta^* \sim 1$  nm, there is an alignment of the lower mode with our as-deposited controls (see **Table 5-3**).

## 5.5 As-deposited results

Of importance to our measurement of  $\rho_i$  is the definition of the NW conductive cross-section, expected to be further reduced due to a surface depletion layer ( $\delta^*$ ) [161], [195]. For ITO thin films, the surface is prone to oxidation, in-diffusion of oxygen and annihilation of oxygen vacancy donors or neutralization of Sn-impurity donors [161]. Typically, donor-compensation limits surface depletion to a few angstroms within ITO thin films; however, deeper chemical depletion layers caused by the filling of  $V_{\text{O}}$  have also be shown to extend this region into what is typically assumed to be the bulk of a given ITO thin film (discussed in further **chapter 6**) [161], [195]. For our as-deposited NWs, we estimated a  $\sim 1$  nm surface depletion layer which includes contributions from amorphous side-wall deposition (i.e., deposition material not incorporated within the crystalline structures during the growth period — see **Fig. 5-6 a** for a schematic band diagram). Applying our parallel resistor model, assuming  $\delta^* \sim 1$  nm and a square cross-section, we determine a value of  $\rho_i = (5.7 \pm 1.3) \text{ m}\Omega \text{ cm}$  from our  $\text{ITO}_{\text{VLS } 85}$  devices (see **Fig. 5-11 b** and **Table 5-3**)<sup>15</sup>.

<sup>15</sup>During experimentation and our initial analysis, the device electrical properties and their distributions were assumed to be distributed log-normal with high resistance devices attributed to the failure of the NW/Ag. junctions to open circuit (e.g., due to joule-heating) resulting in the measurement of fewer NWs

**Table 5-3 Summary of ITO deposited under various conditions.** Determined as-deposited resistivity for our structured thin films, planar EBE, as well as  $\alpha = 50^\circ$  VLS controls and sputtered witness samples (determined via 4PP and hall-probe).

	ITO <sub>SP</sub>	ITO <sub>TF</sub>	ITO <sub>GLAD 83</sub>	ITO <sub>VLS 50</sub>	ITO <sub>VLS 85</sub>
Deposition method	Sputtered	EBE	EBE, GLAD	EBE, VLS	EBE, VLS, GLAD
$\rho_i$ [ $\text{m}\Omega\cdot\text{cm}$ ]	$0.8 \pm 0.1$	$5.7 \pm 0.3$	$28 \pm 5$	$6.4 \pm 4.6$	$5.7 \pm 1.3$
$\alpha$ [°]	Normal	30	83	50	85
$t_{\text{CTM}}$ [nm]	340	200	400	300	300
$R_{\text{CTM}}$ [ $\text{nm s}^{-1}$ ] (nominal)	0.2	0.2	0.2	0.5	0.5
Measurement technique	4PP / Hall	4PP / Hall	3D-CBKR	4PP / Hall	3D-CBKR

The electrical characteristics of dense thin film EBE samples were determined by 4PP and hall probe, yielding  $\rho_i = (5.7 \pm 0.3) \text{ m}\Omega \text{ cm}$ . The as-deposited resistivity of our ITO<sub>VLS 50</sub> controls was able to be estimated by standard 4PP measurement and hall-probe ( $R_s = 138 \text{ }\Omega/\square$ ,  $0.5 \text{ nm s}^{-1}$ ), as these films demonstrate considerable lateral conductivity. The film is treated as a parallel combination of a dense nucleation layer ( $100 \pm 25 \text{ nm}$  from analysis of edge-view SEM) underlying an interconnected branched network, measured from the base of the film to a level where branching, and therefore lateral conduction, ceases ( $\sim 800 \text{ nm}$  from **Fig. 2-10**) [196]. This yields an estimate of  $\rho_i = (6.4 \pm 4.6) \text{ m}\Omega \text{ cm}$ , due to the uncertainty in the exact conduction path/contribution of branches<sup>16</sup>. Also of note are thick samples deposited under similar conditions by LaForge et al. with  $\rho_i \sim 1 \text{ m}\Omega \text{ cm}$  (**Fig. 2-12**, open diamonds) determined by terahertz spectroscopy ( $\alpha = 85^\circ$ ,  $t = 18 \text{ }\mu\text{m}$ ,  $0.5 \text{ nm s}^{-1}$ ) [94]. For this study, films grown in excess of  $10 \text{ }\mu\text{m}$  were required to achieve a sufficient signal-to-noise ratio and resulted in a feathered film of single-crystal structures with significant lateral conductivity. Structural carrier confinement on the scale of a few nanometres was observed by LaForge, and

---

and therefore a larger  $R_D$ . Later, data ‘clustering’ was related to applied electric field (E), with low field and high field performance observed within a given processing condition (see **Appendix G**).

<sup>16</sup>Where  $R_s = \rho_i/t$  and the allowed range of film thickness varies from a minimum set by the dense nucleation layer and the maximum set by the level at which branching, and therefore lateral conduction, ceases ( $\sim 800 \text{ nm}$ ). This results in an allowed range of  $\rho_i = 1.8 - 11 \text{ m}\Omega \text{ cm}$ .



motivated the study of post-deposition annealing treatments to remove the disorder (discussed further in **chapter 6**).

## 5.6 Chapter summary

The optical transparency of the photoresist and high reflectivity of the Ag contact allowed us to determine the dimensions of the top contact (and therefore the cross-sectional area of the device); and represents the likely cause of minor deviations from linear device performance. The determination of the width of the Ag trace was the most error-prone stage, and future efforts utilizing the outlined techniques of this work would benefit from the transition to a compatible dry etch and binary photoresist system for a likely improvement in yield and fidelity in pattern transfer.

Through the course of the fabrication procedure undertaken in this chapter all geometric defects have been removed; this isolation procedure results in the dimensions of the NW, and the intrinsic chemical gradients within, defining the conduction boundaries. We are limited in our analysis in a case where the device current distribution is asymmetric (due to device damage or preferential current paths) — therefore deviations may occur in the case of:

- Large film-level defects (as was the case in **chapter 4**).
- Micro-channel formation, which prevents an accurate measure of device area, and therefore  $N_P$  (see **Appendix D**).
- Preferential metallic paths (discussed further in **chapter 6**).

## 6 Optimization of ITO nanotree arrays via post-deposition anneals

Anneals were performed after thin film growth, but before polymer in-fill (refer to **Fig. 3-1** for the process flow). The first (air) anneal is meant to correct structural disorder, as suggested by LaForge et al. [94]. The expectation is that anneal 1 may improve  $\mu_e$ , but this might also cause  $V_0$  filling and a subsequent lowering of  $n_e$ . Thus, a second (reduction) anneal is required to recover the desired high  $n_e$  within the presumably optimally ordered crystalline structures. The standardized anneal routine used by our lab includes a 90 min, 500 °C air anneal, followed by a 60 min, 100 sccm, 375 °C reduction anneal (see **Table 3-1**)[197]. The primary witness sample utilized is EBE ITO thin films ( $\text{ITO}_{\text{TF}}$ , 200 nm, 0.2 nm s<sup>-1</sup>) deposited from the same source material and within the same deposition system as  $\text{ITO}_{\text{VLS}}$  samples (see **Appendix C**). All dense thin films demonstrated considerable lateral conductivity, and were therefore able to be measured with standard 4PP (and hall probe for planar samples), exhibiting improved conductivity at the 100 sccm, 375 °C processing condition. Within this chapter, a statistical analysis is undertaken to assess the dominant variable describing the observed clustering of  $R_D$  measurements, as they progress with processing and vary with  $N_P$ .

**Table 6-1** Effect of annealing on witness samples (sheet resistance measurements were determined via 4PP). Note, for select conditions, we are missing sample measurements — a small batch of control samples were disrupted and inter-mixed before measurement.

	$R_s [\Omega \square^{-1}]$		
	$(\rho_i [\text{m}\Omega \cdot \text{cm}], \mu_e [\text{cm}^2 \text{V}^{-1} \text{s}^{-1}], n_e [10^{20} \text{cm}^{-3}])$		
Sample	ITO <sub>SP</sub> (t = 340 nm)	ITO <sub>TF</sub> (t = 200 nm)	ITO <sub>VLS 50</sub> (t = 1 $\mu\text{m}$ ) <sup>1</sup>
As-deposited	<b>21.9</b>	<b>285</b>	<b>138</b>
	(0.8, 10.6, 7.7)	(5.7, 1.3, 8.5)	
Air-only	-	<b>150</b>	<b>867</b>
		(3.0, 14.9, 1.4)	
10 sccm – 375 °C	<b>14</b>	<b>85</b>	-
	(0.5, 120, 1.1)	(1.7, 19.8, 1.9)	
30 sccm – 375 °C	<b>17</b>	<b>30</b>	-
	(0.6, 83.9, 1.3)	(0.6, 26, 3.9)	
100 sccm – 375 °C	<b>10.8</b>	<b>25</b>	<b>72</b>
	(0.4, 68, 2.5)	(0.5, 33.1, 3.7)	
Commercial ITO (t = 125 nm)	<b>12.8</b>		
	(0.2, 42.9, 9.1)		
Measurement technique	4PP/Hall probe	4PP/Hall probe	4PP

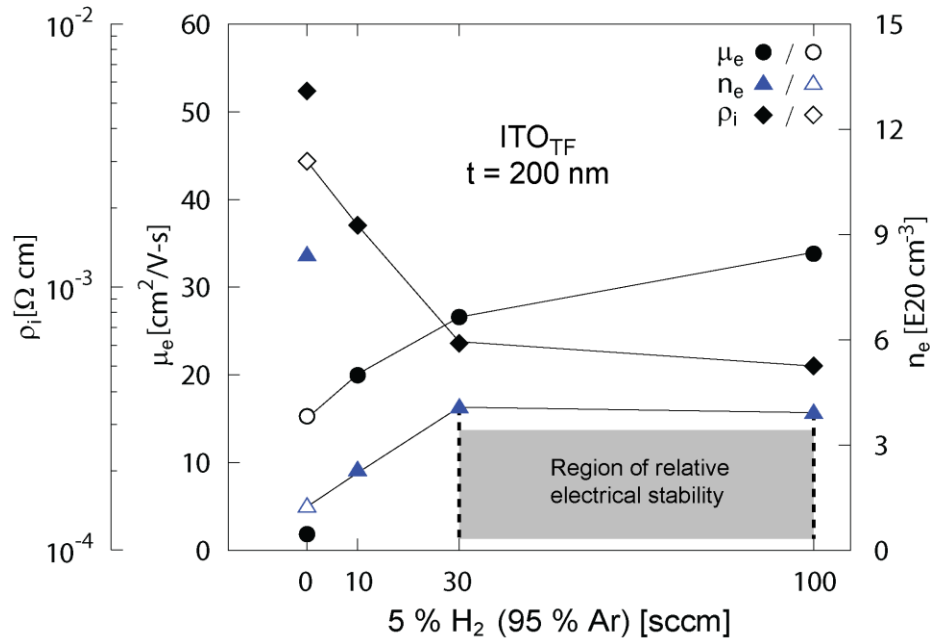


**Figure 6-1 Reduction of ITO thin film (EBE) controls.** Electrical characteristics (hall-probe / 4PP) for 200 nm dense planar thin film. Open symbols are indicative of values after the air anneal.

<sup>1</sup>The deviation in the response to anneal 1 is confounded by **i.** the higher effective deposition rate of low- $\alpha$  films (i.e., at low  $\alpha$ , proportionally more flux passes through the deposition window for a fixed deposition thickness — as read by the CTM — affecting the film morphology); and **ii.** the convoluted conduction path (e.g., is the increase in  $R_s$  due to  $V_0$  filling and/or a disruption of the branched network — see Fig. 2-10 and the previous discussion of section 5.5).

## 6.1 Effect of annealing on nanotree films

Results from the 4PP and hall-probe characterization of the ITO planar controls are shown in **Table 6-1** and summarized for ITO<sub>TF</sub> samples in **Fig. 6-1** (open symbols are indicative of values after the air anneal). For ITO<sub>TF</sub> samples there is significant decrease in  $n_e$ , and increase in  $\mu_e$  after anneal 1. The former is attributed to  $V_0$  filling, and the latter to reduced grain-boundary scattering due to an increase in grain size (discussed later in **section 6.2.1**). After anneal 2, there was a demonstrated improvement in electrical performance ( $\rho_i \sim 0.5 \text{ m}\Omega \text{ cm}$ ) observed for 100 sccm films, with a region of relative electrical stability observed (i.e., 30–100 sccm).

To calculate  $\rho_i$ , a measure of  $A_{NW}$  is required (see **equation 2-7**). Previously,  $A_{NW}$  was determined via top-down SEM (see **section 5.4.1**), however deviations in the internal dimension within the ‘core’ of an individual NW may occur due to the observed compositional shifts explored in this chapter. Here,  $A_{core}$  is the cross-sectional area of a supposedly metallic core within an otherwise homogenous NW. Outlined in **Figure 6-2 a** is the normalized NW  $\rho_i$  vs.  $A_{core}$ . Plotted as well are curves of constant resistance for a fixed NW length (i.e.,  $L_{NW} = t_{film}$ ), and varying cross-section dimensions. This plot demonstrates that a decreasing cross-section dimension could account for the observed trend of increasing  $R_D$  with increasing reduction intensity (e.g., when  $D_{NW} \sim D_{core} (\approx 30 \text{ nm})$ , the as-deposited condition is recovered)<sup>2</sup>.

Within our dataset there is a violation of normality that was statistically significant for each processing condition—including the unprocessed, as-deposited devices (see **Fig. 6-2 a, inset**)<sup>3</sup>. When isolating samples processed at variable reduction intensity (10–100 sccm, 375 °C) the observed  $R_D$  increases in a fashion opposite to our dense planar thin film (see **Fig. 6-2 b** for the estimated  $\rho_i$  vs. reduction gas flow rate).

---

<sup>2</sup> Changes in the electrical properties of our ITO<sub>VLS 85</sub> films are attributed primarily to alterations in  $n_e$ , with film crystallinity and the effects of  $\mu_e$ , being secondary (see **section 6.2.1**)—rationalized in **section 6.2.4** in terms of dopant introduction in the NW core, and dopant neutralization in the NW shell.

<sup>3</sup>This underlying non-normal distribution of the device results was assessed using the Shapiro-Wilk statistical test [217], [228]. For the as-deposited processing condition ( $n = 10$ ):  $W = 0.762$ ,  $p < 0.005$ . Of note, the device data ( $n = 44$ ) for GLAD-ITO devices (**chapter 4**) was also found to be non-normal ( $W = 0.915$ ,  $p < 0.005$ ). For ITO<sub>VLS</sub> devices the dataset appears to be multi-modal or crudely bimodal; no agreeable method in the literature could be found to strictly classify a bimodal distribution, however there is a theoretical frame work that does [229]. Further study is required.

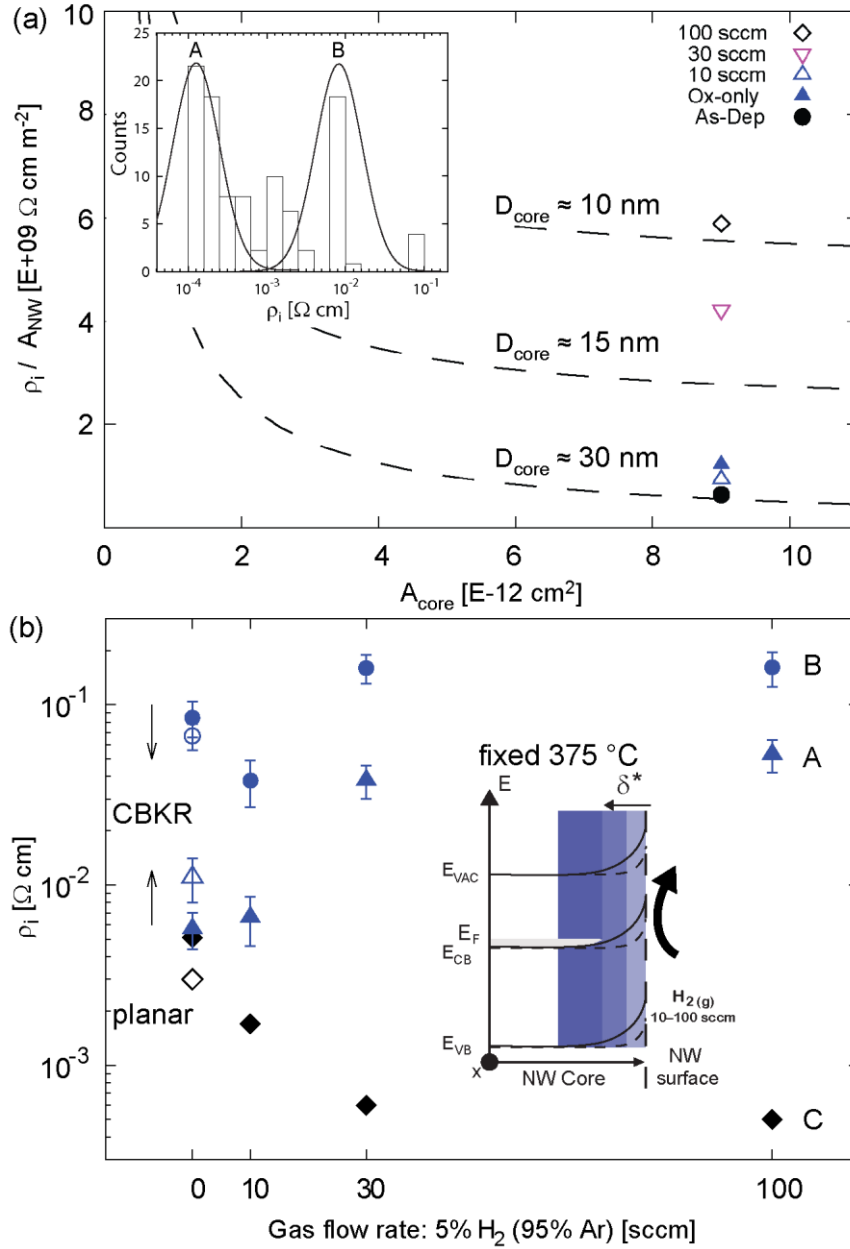


**Figure 6-2 Contribution of varying NW metallic core cross-sectional area.** (a) Normalized resistivity vs. the cross-sectional area of a supposedly metallic core NW. Curves of constant resistance (for fixed NW length) demonstrate that a decreasing cross-sectional area can account for the observed trend of increasing device resistance with increasing reduction intensity, e.g., when  $D_{NW} \sim D_{core} (\approx 30 \text{ nm})$ . Further, there is an underlying non-normal distribution of device results (see inset, normal curves added for a guide to the eye); (b) cluster A (triangles) and cluster B (circles) and controls (diamonds) for all processing conditions (see also **Appendix G**). Here,  $\rho_i$  is estimated using  $D_{NW} = 32.2 \pm 0.6 \text{ nm}$ , less the estimated  $\delta^* \sim 1 \text{ nm}$ . Included for reference are the electrical characteristics for  $\text{ITO}_{TF}$  samples (diamonds). Open symbols are indicative of values after the air anneal. Inset: schematic band diagram depicting the chemical depletion mechanism, adapted from: [161]. Here,  $\delta^*$  is suggested to extend far into the bulk of the NW(s).

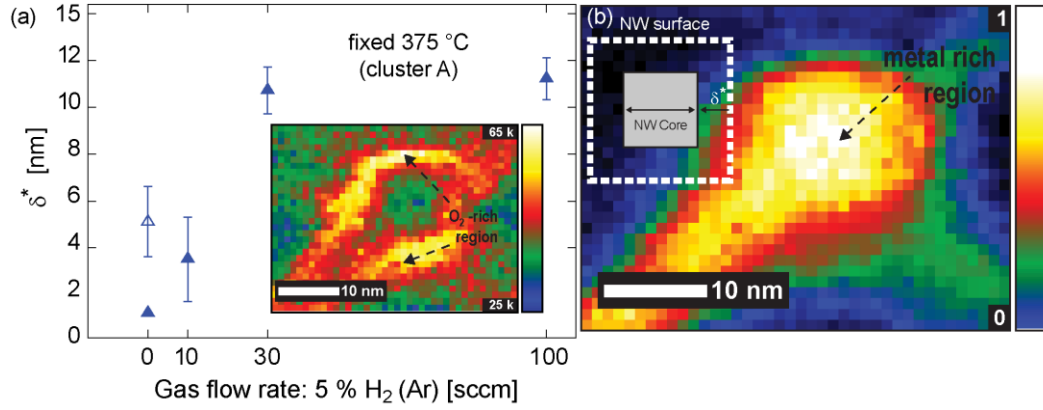


**Figure 6-3 Estimated chemical depletion vs. reduction flow rate.** (a) Estimated chemical depletion layer ( $\delta^*$ ) for indicated processing conditions (initially,  $\delta^*$  estimated to be  $\sim 1$  nm for the as-deposited condition), inset: EELS oxygen compositional map for representative NW processed at 100 sccm, 375 °C with dimensions  $\sim$  matching estimates of  $\delta^*$ ; (b) complementary metal distribution for same NW; inset: schematic depicting  $\delta^*$  extending into the bulk of the NW due to oxygen vacancy filling)

Upon further analysis, it was found that the observed increase in  $R_D$  is attributable to a channel constriction (this statistical analysis is summarized in **Table 6-3**, and further described in **Appendix G**). Note, previously the ‘anomalous mode’ discussed in **chapter 5** was discarded as it was assumed due to a device failure mechanism. Given the implications of this analysis, we move to further assess the observed clustering as well as the increasing  $R_D$  with processing. From **chapter 5**, initially donor compensation limits the upwards band-bending to a near-surface effect this region is estimated to be  $\sim 1$  nm for a typical ITO thin film (**Fig. 6-2 b, inset** — dashed lines) [161], [198]. With processing, reduced doping near the surface is suggested to result in an increased space charge layer ( $\delta^*$ ), caused by the filling of  $V_O$ , extending this region into what is typically considered the bulk of a given ITO thin film (**Fig. 6-3 b, inset** — full lines) [161]. This shift in properties is not associated with a charge, and is therefore said to be a chemical depletion [161], [198], [199]. The determination of the extent of  $\delta^*$  assists in defining the boundaries of the conductive ITO ‘core’ of the NWs.

Given the above, we can assess the initial relationship between the two modes (i.e., as-deposited devices) as well as shifts in the channel dimensions with processing.

For the former, we use  $\frac{\rho_{i,B}}{\rho_{i,A}} = \frac{R_{D,B} \cdot A_{NW,B}}{R_{D,A} \cdot A_{NW,A}}$  and isolate for  $D_{NW,B}$  (the NW cross sectional diameter for cluster B), setting  $t = L_{NW,A} = L_{NW,B}$ . The above ratio results in estimated dimensions of  $D_{NW,B} = (4.7 \pm 1.1)$  nm (assuming a 1 nm surface-depletion layer for the

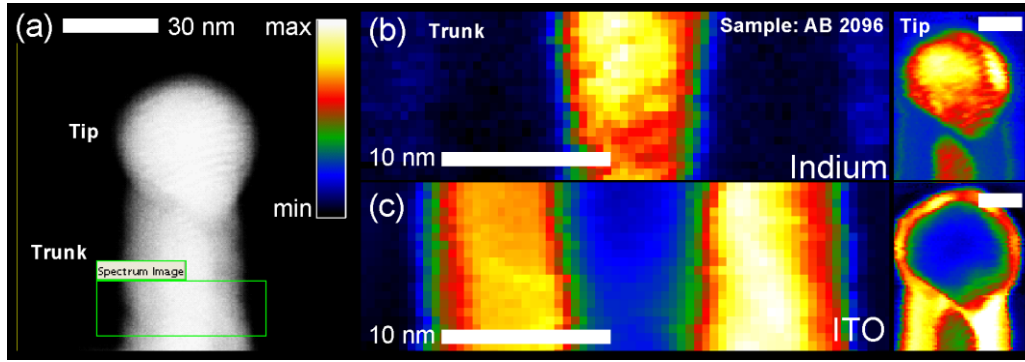


**Figure 6-4 Tapered metallic core for sample AB2096.** (a) Dark field TEM of sample AB2096 ( $0.5 \text{ nm s}^{-1}$ ,  $t = 10 \text{ }\mu\text{m}$ ) with the region of interest highlighted for EELS compositional analysis; (b) EELS compositional temperature map of the trunk region showing areas of maximum and minimum In concentrations, adjoined frame showing same for tip region (10 nm scale bar); (c) same for temperature map of the complimentary ITO concentration. This is an unpublished observation, noted by LaForge.

‘as-deposited’ condition). For the latter, shown in **Figure 6-3 a**, we further isolate cluster A, finding the dimensions of a chemically depleted wire to match those determined by the shifts in the observed CBKR device measurements (estimated by assuming the increase in  $R_D$  is primarily due to a channel constriction). This observation was validated by isolating single NWs within processed devices (100 sccm,  $375 \text{ }^\circ\text{C}$ ), and observing a complementary elemental distribution—noting a metal-rich core and an oxygen rich shell (see **Fig. 6-3 a and b**, described further in **section 6.2.5**). These dimensions are in agreement with the estimates of  $\delta^*$  and are also consistent with the observations of others [119], [135], for the  $l_0$  within ITO. These observations imply an electronic relationship, established at growth, and evolving with processing.

Of relevance to this work, during study of the terahertz conductivity of  $\text{ITO}_{\text{VLS}}$  NWs, LaForge et al. grew films in excess of  $10 \text{ }\mu\text{m}$ , which result in a feathered film of single-crystal structures with significant lateral conductivity [94]. A sample from this study (also deposited at the moderate rate of  $0.5 \text{ nm s}^{-1}$ ,  $t = 10 \text{ }\mu\text{m}$ ) is shown in **figure 6-11**. Here, competitive growth dynamics are expected to be frustrated at increasing film thicknesses, demonstrating that conditions of elevated deposition rates may result locally and can result in a highly metallic core, demonstrating that there are multiple processing paths to metallic NWs<sup>4</sup>.

<sup>4</sup>Oxidation within Si NWs core-shell structures is strongly dependent on the wire curvature and oxidation time; compressive stress increases the activation energy of oxidant diffusivity resulting in a so-called ‘self-limiting’ oxidation regime [230]–[232]. This may explain the similar core dimensions observed in **Fig. 6-3** and **Fig. 6-4** for NWs of similar diameter — implying the core : shell is a defining feature of these NWs.

**Table 6-2 Summary of device data and K-means clustering analysis.** For ITO<sub>VLS</sub> 85 devices, 94 of 128 fabricated devices yield ohmic characteristics. The unadjusted resistivity (i.e., uncorrected for the core-shell architecture increases with processing (irrespective of clustering). Initially, we use the median to split the dataset for each processing condition. Also outlined, a K-means Cluster analysis [200] was undertaken for classification of the data into two (user selected) clusters for each processing condition; this statistical analysis technique was utilized to validate the interpretation of a bi- or multi-modal distribution. Clustering is attributed to an electric-field dependence for all cases except the 175 °C, 10 sccm processing condition (here the number of posts is the distinguishing variable, and arguably there is no clustering—see **Appendix G**).

Processing condition:	Yield (/16)	Median Split:					K-cluster:	
		$\rho_i$ [m $\Omega$ cm]			E [V cm <sup>-1</sup> ]	P-value	E [V cm <sup>-1</sup> ]	P-value
		All	A B	Min.	A B		A B	
As-deposited (111)	63 %	8.9 $\pm$ 1.5	5.7 $\pm$ 1.3 85 $\pm$ 19	1.8 $\pm$ 0.1	99 $\pm$ 10 2041 $\pm$ 292	(p<0.05)	441 1876	E (p<0.05)
Air-only (211)	94 %	30 $\pm$ 10	11 $\pm$ 3 67 $\pm$ 11	4.3 $\pm$ 0.3	139 $\pm$ 36 784 $\pm$ 118		93 1920	
375°C – 10 sccm (242)	50 %	13.4 $\pm$ 7	6.6 $\pm$ 2 38 $\pm$ 11	0.4 $\pm$ 0.1	166 $\pm$ 51 674 $\pm$ 157		267 2101	
375°C – 30 sccm (243)	63 %	58 $\pm$ 26	38 $\pm$ 8 160 $\pm$ 29	6 $\pm$ 0.9	149 $\pm$ 75 672 $\pm$ 105		459 2110	
375°C – 100 sccm (244)	56 %	89 $\pm$ 28	53 $\pm$ 11 161 $\pm$ 35	24 $\pm$ 5	195 $\pm$ 112 1158 $\pm$ 193		322 1188	N <sub>P</sub> (p<0.05)
175°C – 10 sccm (322)	94 %	56.8 $\pm$ 9	23 $\pm$ 7 78 $\pm$ 9	3.5 $\pm$ 0.9	84 $\pm$ 28 1374 $\pm$ 490		57 238	
275°C – 10 sccm (232)	94 %	15.3 $\pm$ 8.7	8.4 $\pm$ 3.2 35 $\pm$ 11	0.6 $\pm$ 0.1	180 $\pm$ 58 918 $\pm$ 106		288 1082	E (p<0.05)
425°C – 10 sccm (352)	94 %	51 $\pm$ 26	25 $\pm$ 6 121 $\pm$ 43	3.5 $\pm$ 0.4	174 $\pm$ 57 1295 $\pm$ 241		721 2504	



## 6.2 NW film, bulk and surface characterization

As outlined in **chapter 3** (see **Fig. 3-3**), our thin film characterization techniques allow us to probe the macroscopic, film-level properties as well as the bulk and near surface regions of the NWs. Deconstructed devices are used for EELS characterization, while witness samples were used for UPS, AES, XRD and UV-VIS characterization. The pairing of EELS and the techniques of AES and UPS are used to observe bulk and surface compositional shifts, respectively. We conduct XRD analysis to gain further insight into crystal stability with high temperature processing to assess the likely contribution of grain-boundary scattering. Via UV-VIS characterization, we can observe shifts in the degree of doping within NW films (as  $\omega_p \propto \sqrt{n_e}$ , according to **equation 1-2**), and the spectral response give some indication of the electrical properties for annealed samples.

### 6.2.1 XRD-determined crystallite evolution with annealing

The ITO<sub>TF</sub> sample has an initial grain size of  $\sim 8$  nm, increasing to  $\sim 20$  nm after anneal 1, and remains stable with subsequent reduction anneals; films showed no initial preferred orientation, and a strong  $\langle 222 \rangle$  preferred orientation after anneal 1 (see **Fig. 2-11** for schematic). Here, it is believed that significant crystal re-ordering results in our crystallite exceeding a critical threshold (discussed previously), and we operate in a regime where grain-boundary scattering is not the dominant scattering mechanism for these sufficiently large crystal grains. In this regime sheet resistance ( $R_s$ ) is stable, compared with increases in  $R_s$  for grain sizes decreasing to near  $\sim 10$  nm [113], [170]–[172]. Further, for planar samples, the  $\rho_i$  of ITO thin films have been shown to be  $\sim$  constant for grain sizes  $> 20$  nm [172], and independent of  $\langle 400 \rangle$  vs.  $\langle 222 \rangle$  orientation ( $0.2 \text{ m}\Omega \text{ cm}$ ;  $40 \text{ cm}^2/\text{V}\cdot\text{s}$ ,  $7.5 \times 10^{20} \text{ cm}^{-3}$ ) [81].

Outlined in **figure 6-5** are the XRD spectra for ITO<sub>GLAD 83</sub> and ITO<sub>VLS 85</sub> samples, with the former being fully amorphous and the latter crystalline. After an initial shift in film texture, crystalline samples are stable with further processing. The crystallite dimensions are estimated using the Scherrer equation (**equation 3-2**) for the indicated peaks of interest.

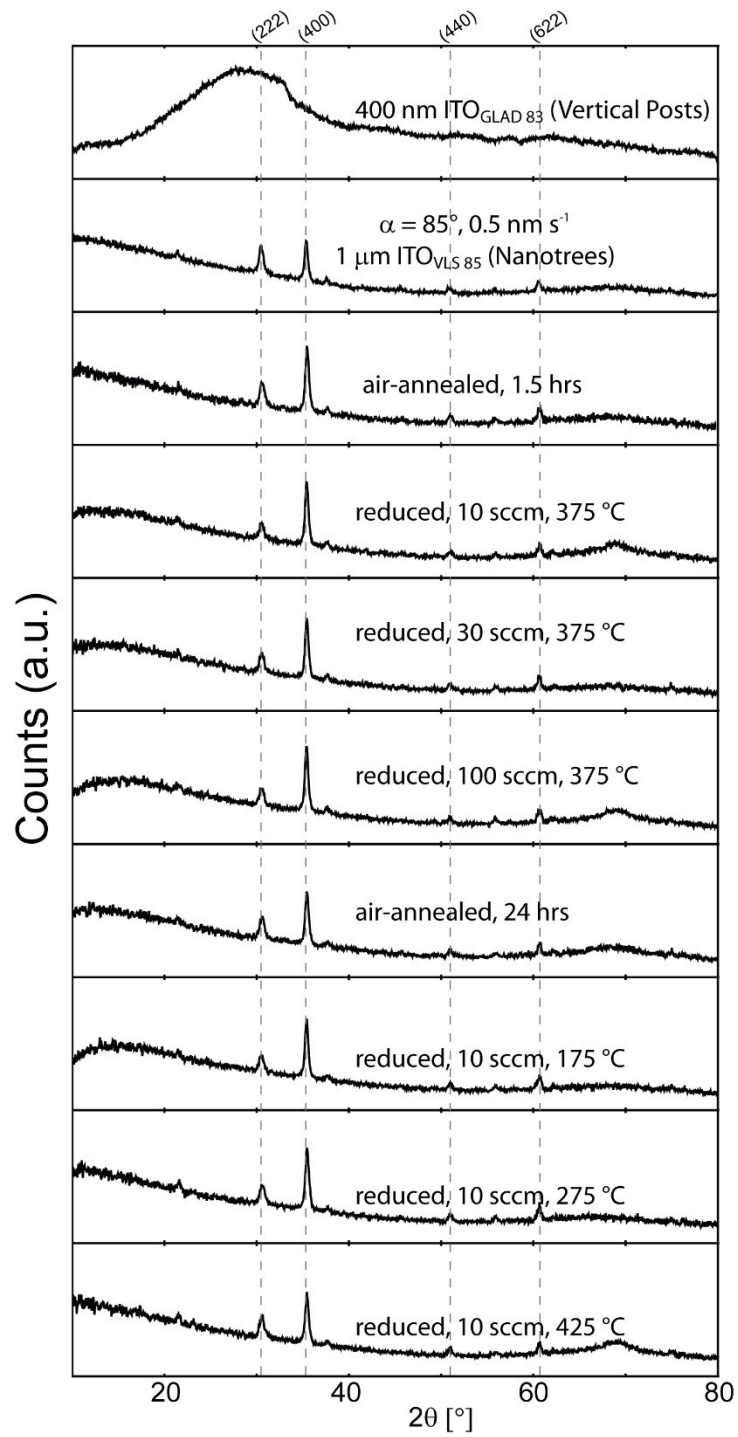


**Figure 6-5 XRD spectra.** X-ray diffraction line profiles for the ITO<sub>GLAD 83</sub> and crystalline VLS nanotree structures (with as-deposited, air-only, and ‘sccm sweep’ conditions ordered first). ITO<sub>VLS 85</sub> films indexed to (In<sub>1.94</sub>Sn<sub>0.06</sub>)O<sub>3</sub> ICSD 01-089-4596 (dashed lines).

**Table 6-3** Summary table of crystallite dimensions for  $\alpha = 85^\circ$  ITO<sub>VLS</sub> films<sup>1</sup>. Error bars for grain size are based on a Gaussian peak fit for spectra. Lattice constants are determined for the (400) peak. For reference, commercial ITO (t = 125 nm), (222): (21 ± 0.2) nm, (400): (23.3 ± 0.3). Samples (\*) anneal 1 = 24 hr. oxidation anneal.

Processing condition	ITO <sub>TF</sub>		ITO <sub>VLS 85</sub>		
	(222)	(400)	(222)	(400)	
	Grain size [nm]	Grain size [nm]	Grain size [nm]	Grain size [nm]	Lattice constant, <i>a</i> (Å)
As-deposited	7.7 ± 0.5	-	18 ± 3	33 ± 1	10.156
Air (1.5 hr)	18.3 ± 0.2	19.2 ± 0.2	17 ± 1	27 ± 6	10.117
(24 hr)	-	-	18 ± 1	29 ± 3	10.127
10 sccm, 375 °C	19 ± 0.2	19.6 ± 0.2	20 ± 2	30 ± 2	10.136
30 sccm, 375 °C	-	-	15 ± 3	29 ± 3	10.134
100 sccm, 375 °C	18.9 ± 0.2	19.3 ± 0.2	18 ± 1	33 ± 2	10.144
*10 sccm, 175 °C	-	-	17 ± 2	34 ± 1	10.145
10 sccm, 275 °C	19.2 ± 0.2	19.6 ± 0.2	17 ± 1	26 ± 5	10.118
*10 sccm, 425 °C	20.9 ± 0.2	21.8 ± 0.3	19 ± 2	29 ± 5	10.129

ITO<sub>VLS 85</sub> films possessed an initial grain size of 33 ± 1 nm as determined from the (400) peak, and 18 ± 3 nm by the (222) peak, and were stable with subsequent reduction anneals. Films initially showed an approximately equal growth orientation, and [400] preferred growth orientation after anneal 1 (similar to trends noted by Beaudry et al. [11]). The <400> texture remained largely unchanged with subsequent reduction anneals. For ITO<sub>VLS 85</sub> samples, two trends were consistent for all processing conditions: **i.** (400) grain size are larger than the 20 nm ‘threshold’; and **ii.** (400) grain size > (222) grain size (see **Table 6-3**). As films are <400> textured, this asymmetry is suggestive that we are either observing an artifact of core-shell structures and/or we are observing a measure of the physical dimensions of the branches (as they hold a geometric relationship with the trunk, i.e., =  $D_{NW}/\sqrt{2} \sim 20$  nm) [11]. See **Appendix E** for further crystallographic details and **figure 2-11** for crystal orientation schematic.

<sup>1</sup>All reduced films were first air annealed. Error bars represent standard error of the mean. Ideally, the grain size should be calculated from all peaks, however preferred orientation makes this difficult. For a detailed consideration of the progression of film texture with rate see ref: [94] and [9]. An alternative

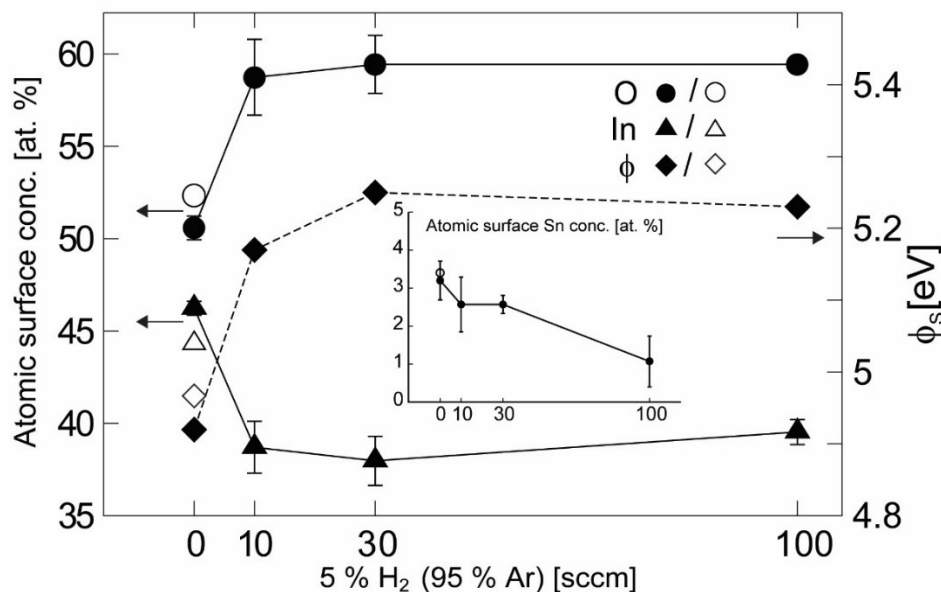


**Figure 6-6 Surface composition and shifts with reduction of NWs.** (a) Relative atomic surface concentration of In and O (determined by AES,  $\sim 1$ -2 nm probe depth) and  $\phi_s$  (determined by UPS,  $\sim 3$ -5 nm probe depth) varying with processing (average of three measurements across three sites of interest); inset: relative atomic surface concentration of Sn varying with processing and probe depth. Open symbols are indicative of values post air anneal.

## 6.2.2 Surface compositional analysis

The relative surface atomic composition was probed via AES, with a  $\sim 1$ -2 nm probe depth (**Fig. 6-6**— open symbols are indicative of values post air anneal). UPS has been demonstrated as a strong tool to measure shifts in  $\phi_i$  (for a brief discussion see **section 2.5**) [98]. An increase in  $\phi_i$  with reduction, and the above observed shifts in surface chemical composition, are consistent with the surface depletion mechanism of metal oxide NWs. This mechanism is typically considered a near-surface effect (i.e., estimated to be  $\sim 1$  nm for as-deposited NWs). Discussed previously, a reduced doping level near the surface results from  $V_O$  filling, and leads to an increased depletion region which extends into what is normally considered the bulk of the NW (see **Fig. 6-2 b, inset** for schematic band diagram)<sup>2</sup> [161], [198]. It is believed that the shift in surface oxygen content is indicative of a shift to neutral  $\text{In}_2\text{O}_3$  [134]. (This may explain the weak trend of the exclusion of Sn impurities in the near surface region, see **Fig. 6-6, inset**).

Cauchy fit (see **Appendix E**) gives, (400):  $(75 \pm 16)$  nm, (222):  $(30 \pm 5)$  nm (here, the uncertainty represents the standard deviation across all processing conditions for the given orientation).

<sup>2</sup>As the probe depth for UPS is  $\sim$ few nm, the challenge becomes characterizing the buried interfaces within the NW. Once  $\delta^*$  extends to a depth exceeding the probe depth, our measurement should be stable/saturate (consistent with observed trends).

Within the crystal, oxygen diffusivity is dominated by the (222) crystal dimensions, which serve as rapid oxygen diffusion paths resulting in annihilation of  $V_{\text{O}}$  [161], [186]. Further, Bielz et al. noted that hydrogen-induced  $V_{\text{O}}$  were found to be easily replenished by traces of water in the feed gas during high temperature processing [201]. It is expected that upon NW cooling,  $V_{\text{O}}$  filling occurs and is therefore a stable phenomenon observable upon testing and characterization. Further, from the diameter distribution data collected in **chapter 5**, observations from literature beg further consideration of **i.** thin wires resulting from elevated growth ( $\sim 20$  nm), and **ii.** larger diameter wires ( $\sim 50$  nm). The former has an increased probability of possessing a continuous core [94], [158], and the latter is expected to facilitate increased  $\text{H}_2$  uptake [201], and so would be more likely to possess a continuous metallic core after the reduction anneal<sup>3</sup>. Identifying the relative contribution from each of the above may explain the previously noted opposite response to the air anneal of the two device clusters. From **equation 5-1**, there then exists a threshold to measure a device characterized by a NW with a continuous metallic core (discussed later in terms of an observed aperiodicity along the z-axis).

### 6.2.3 NW film transmission

Transmission spectra were examined to better understand the observed shifts in electronic properties as  $\omega_{\text{p}} \propto \sqrt{n_{\text{e}}}$  (outlined in **section 2.5.1, Fig. 2-6**). As discussed in **chapter 2**, degenerate doping results in an increase in the effective band gap through a Burstein-Moss shift—observed as a blue-shifting  $\omega_{\text{p}}$ . At ‘too high’ of doping, free carrier absorption will shift the associated  $\omega_{\text{p}}$  into the visible from the near-IR, thereby limiting the optical transparency [98]. Transmission spectra (180–3300 nm) were collected at normal incidence, with a peak visible transmission of  $\sim 93\%$  observed for high- $\alpha$  films (**Fig. 6-7 a**).

---

<sup>3</sup>Bielz et al. attributed this behaviour to the decreased availability of ‘deep states’ within high surface area samples (understood as with a high surface area : volume, a smaller diameter NW will be more coordinated, owing to the increased contribution from surface states) [201].

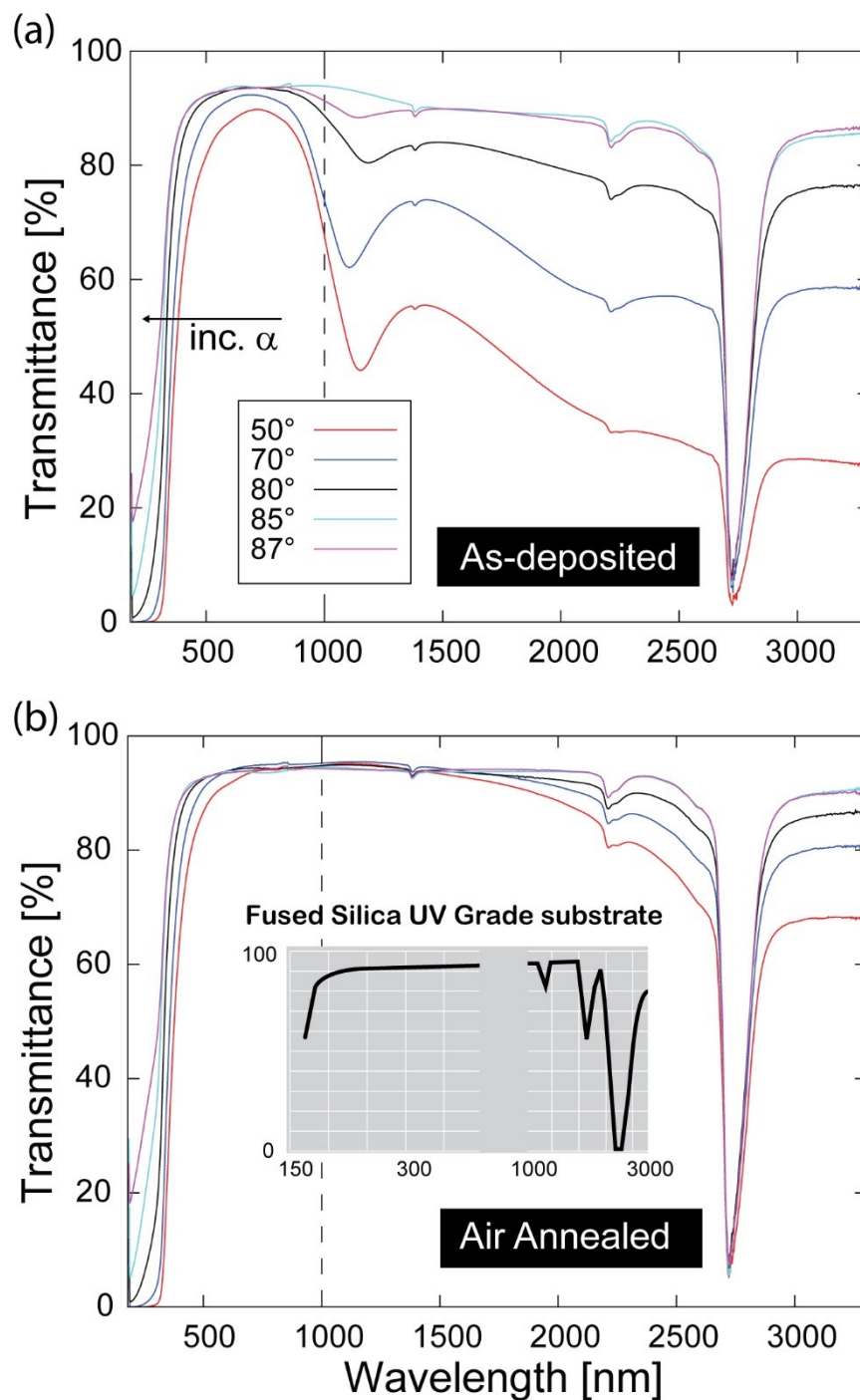


**Figure 6-7 Transmission spectra for as-deposited and air-annealed VLS films.** As-deposited films ( $0.2 \text{ nm s}^{-1}$  and indicated  $\alpha$ ); (a) films post air anneal; (b) and post air +  $375^\circ\text{C}$ , 100 sccm reduction anneal. Note: major feature at 2700 nm, as well as minor features at 1400 nm and 2250 nm, are due to absorption by the UV-grade, fused silica substrate; inset: transmission curve of a blank substrate from [202]. The dashed line provided as a guide to the eye for the shifting plasma edge (compare with transmission spectra for reduced films). Spectra were collected by M.T. Taschuk. A version of this dataset was published within the supplemental information of [11].

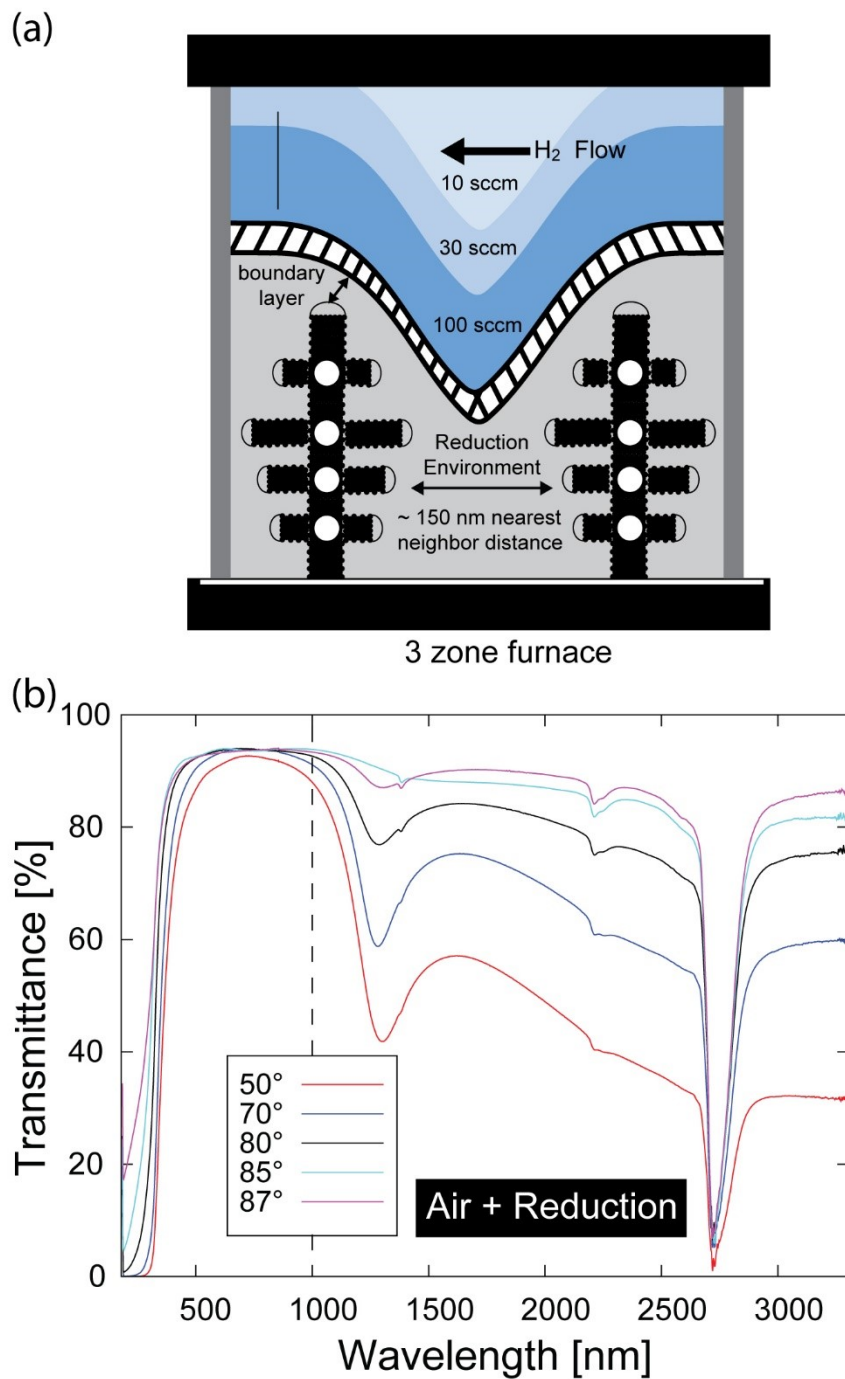


**Figure 6-8 Transmission spectra.** (a) Schematic depicting the local reduction environment for various reduction gas flow rates; (b) As-deposited films ( $0.2 \text{ nm s}^{-1}$  and indicated  $\alpha$ ) — post air +  $375^\circ\text{C}$ , 100 sccm reduction anneal. Dashed line provided as a guide to the eye for the shifting plasma edge (see previous as-deposited and air annealed transmission spectra).

The air anneal prior to reduction is intended to heal crystalline structures improving visible transmission, at the expense of  $n_e$  (see **Fig. 6-7 b** — loss of IR-reflectivity) [81], [173]. Of note, the major feature at 2700 nm, as well as minor features at 1400 nm and 2250 nm, are due to absorption by the UV-grade, fused silica substrate (see **Fig. 6-7 b, inset**). Transmission spectra were collected for the 100 sccm, 375 °C to explore what is assumed to be our peak reduction intensity (see **Fig. 6-8 a** for schematic depicting local reduction environment). After the reduction anneal, IR-reflectivity is recovered less a  $\sim 150$  nm red shift in  $\omega_p$ , and is consistent with the reintroduction of  $V_O$  (**Fig 6-8 b**).

Visible transmission decreased particularly for ITO<sub>VLS</sub> films deposited at  $\alpha = 50^\circ$  and elevated deposition rates, with a change in spectral shape with reduction (see **Fig. 6-9 a** for  $\alpha = 85^\circ$  and, **b** for  $\alpha = 50^\circ$  films). In **section 6.1** we discussed the constriction introduced through a chemically depleted shell for reduced films deposited at moderate rates, and a metallic core deposited at growth, where competitive growth dynamics are expected to be frustrated at increasing film thicknesses. Further, here the decrease in visible transmittance is attributed to an increase in film reflectance due to the precipitation of metallic core at the higher effective deposition rate of low- $\alpha$  films (i.e., at low  $\alpha$ , proportionally more flux passes through the deposition window for a fixed deposition thickness).

Note, the multiple features (‘plasma edges’) of **figure 6-7, 6-8 and 6-9** have been related in the literature to the strong coupling of core and shell for complex nanostructures [203]. Further observations such as the blue-shift of the absorption edge with  $\alpha$  requires further study; a potential angle dependence during UV-VIS characterization introduces complicated dynamics (e.g., the angle-dependent contribution from branches and other film-level features as well as the effective deposition rate). In **Fig. 6-7 a**, there is a notable inversion of the  $\omega_p$  trend for  $\alpha = 87^\circ$  and  $\alpha = 85^\circ$  films at the high, and low energy transition to visible-excitation present, and persists with annealing. Initial estimates based on the branch density per NW, and NW film density suggest that at this threshold branches become the more massive elements of the film [11].



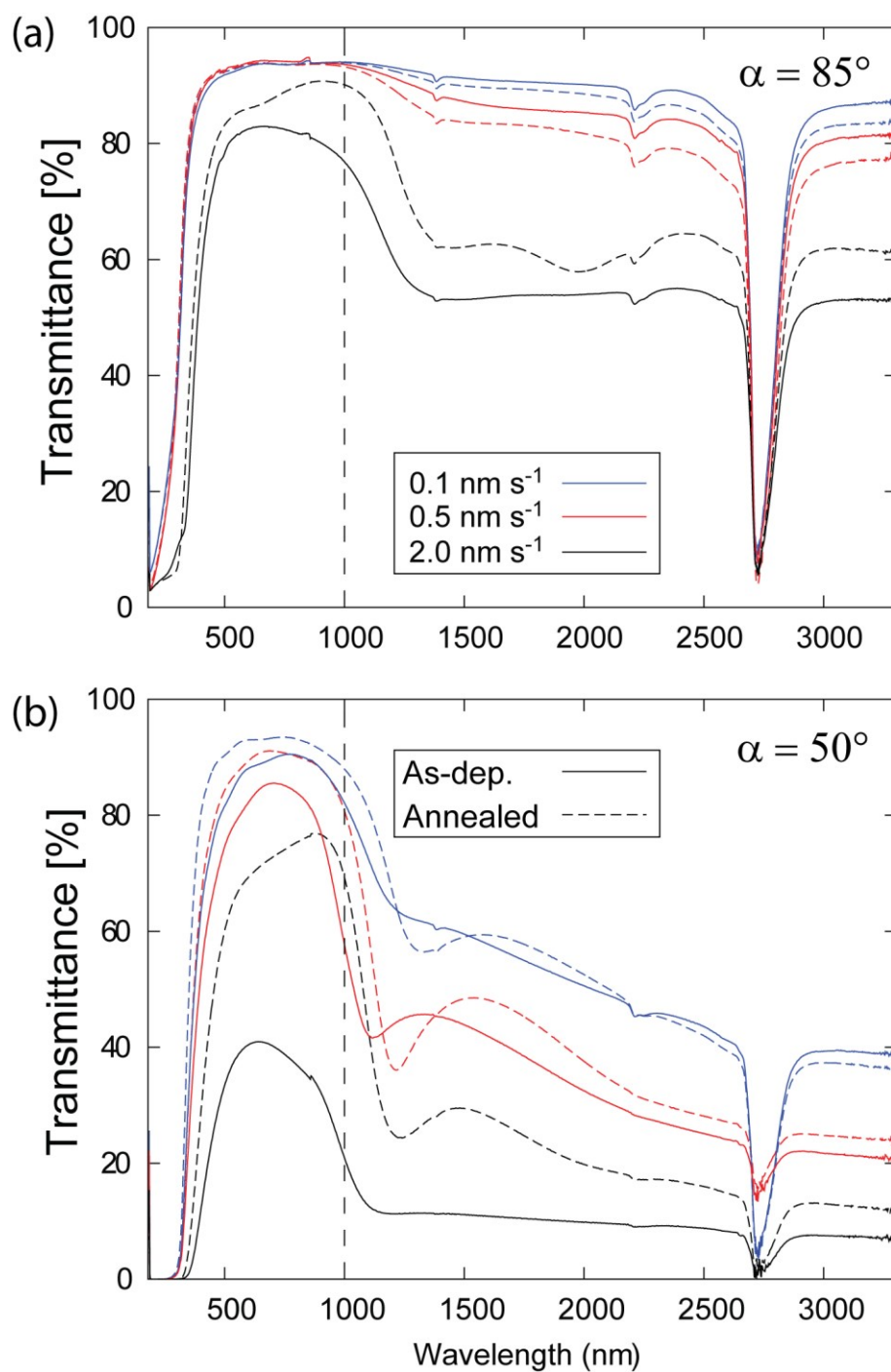


**Figure 6-9 Metallic Transition of films deposited at elevated rates.** Transmission spectra for films, deposited at 0.1, 0.5 and 2.0 nm s<sup>-1</sup>, as-deposited films (solid line) and films post air + 375°C, 100 sccm reduction anneal (dashed lined): (a) ITO<sub>VLS 85</sub> films; (b) ITO<sub>VLS 50</sub> films.

### 6.2.4 3D-CBKR device resistance shifts with processing

In **section 5.5** and **6.1**, we combine the mean dimensions of our NWs to determine  $\rho_i$  for a given device. Discussed previously, the  $V_O$  filling leads to an increased depletion region which extends into what is normally considered the bulk of the NW. This shift in properties is not associated with a charge, and is therefore said to be a chemical depletion [161], [198]. The determination of the extent of  $\delta^*$  assists in defining the boundaries of the NW core; an estimate of the extent of this depletion width calculated using the device data is shown in **figure 6-3 a**. Here, we assume  $\rho_i$  is constant (i.e., of as-deposited electronic quality) and assume the shifts in  $R_D$  (outlined by **Fig. 6-2 b**) are due to constricting channel dimensions through the above describe chemical depletion mechanism (see **Fig. 6-3 a inset** — radial elemental composition of a NW core-shell structure). It is therefore asserted that volume reduction is the dominant mechanism accounting for our observed increase in  $R_D$ . We have estimated  $\delta^*$  assuming:

1. An as-deposited core resistivity ( $\rho_i \sim 5 \text{ m}\Omega \text{ cm}$ );
2. The chemical depleted shell is largely electrically insulating and the increase in  $R_D$  is due primarily to a reduction in the conductive volume of the NW.

**Equation 2-6** is then modified to account for the conductive volume lost to chemical depletion, where now:  $A_{NW} = (D_{NW} - 2\delta^*)^2$ . This simplified calculation ignores the contribution of Sn migration<sup>4</sup>, assuming a core of as-deposited material, with chemical depletion acting to establish a new core boundary (i.e., we are tracing the theoretical curve in **Fig. 3-2 b**). This estimate therefore represents a lower bound on the effects of chemical depletion mechanism, operating to define an electrically conductive core, and a largely insulating shell (subject to the limiting dimension of  $l_0$  within ITO). This introduces deviations between the physical extents of the structures and their internal electronic dimensions, with  $R_D$  further subject to the threshold for metallic NW(s) dominating the measurement.

---

<sup>4</sup>The shift in surface Sn concentration is believed to be a near surface effect (assumed due to the high diffusivity of oxygen and relatively stable crystallite and grain size) and therefore a secondary consideration. The  $\sim 150 \text{ nm}$  shift in the plasma edge in **figure 6-7 a** and **6-8 b** is offered as support for this interpretation, as the shift may be related to those Sn dopants ‘stranded’, and rendered electrically neutral due to oxidation of the oxygen-rich shell region [161], [198].

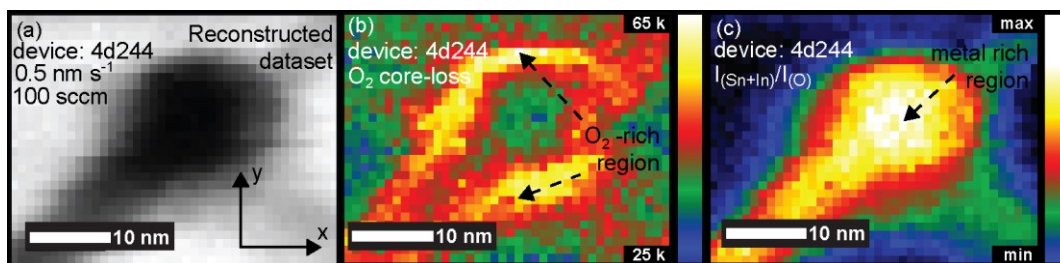


**Figure 6-10 EELS core-loss temperature map for oxygen and metal spectra.** (a) top-down EELS spectrum map (device 4d244); (b) oxygen core-loss temperature map for same—processed at 100 sccm, 375 °C; (c) normalized metal (In + Sn) core-loss of the same NW depicting complementary distribution of metal within the NW.

### 6.2.5 EELS axial characterization

To further explore the effects of the reduction anneals on our devices, and the NWs within, we deconstructed an air-annealed device (device code: 3c211) and a 100 sccm, 375 °C annealed device (device code: 4d244) for EELS characterization. This analysis allows us to study the elemental composition and distribution within processed NWs. Shown for device 4d244, a mid-body plan section of the device NW array was isolated using a Focused Ion Beam (FIB), providing many candidate ‘torsos’ for EELS study (see **Appendix F** for the FIB NW isolation procedure).

Energy filtering allows us to select the metal components and oxygen component in the collected spectrum image, by isolating the associated energy range characteristic of In, Sn, and O (see **Appendix F** for an outline of the spectrum collection process). Isolation of the oxygen spectral components allow us to observe the chemical gradients within samples of processed ITO NWs. We are therefore able to observe the radial oxygen-concentration gradients believed to be induced through the reduction anneal of the fabricated NW arrays. In total, for the 100 sccm device, 9 NWs were queried with line scans across their cross-sectional dimension, all demonstrating an oxygen rich shell to varying extents. For the NW showing the most pronounced gradients a full EELS map was collected. Shown in **figure 6-10 a** is an isolated NW from device 4d244 for which a full (40 pixel × 40 pixel) EELS spectrum map was collected. Within this isolated NW we find highly metallic and oxygen rich regions, whose ‘contours’ are illustrated using a temperature map (see **Fig. 6-10 b** for elemental oxygen distribution and **Fig. 6-10 c** for complementary elemental metal distribution).

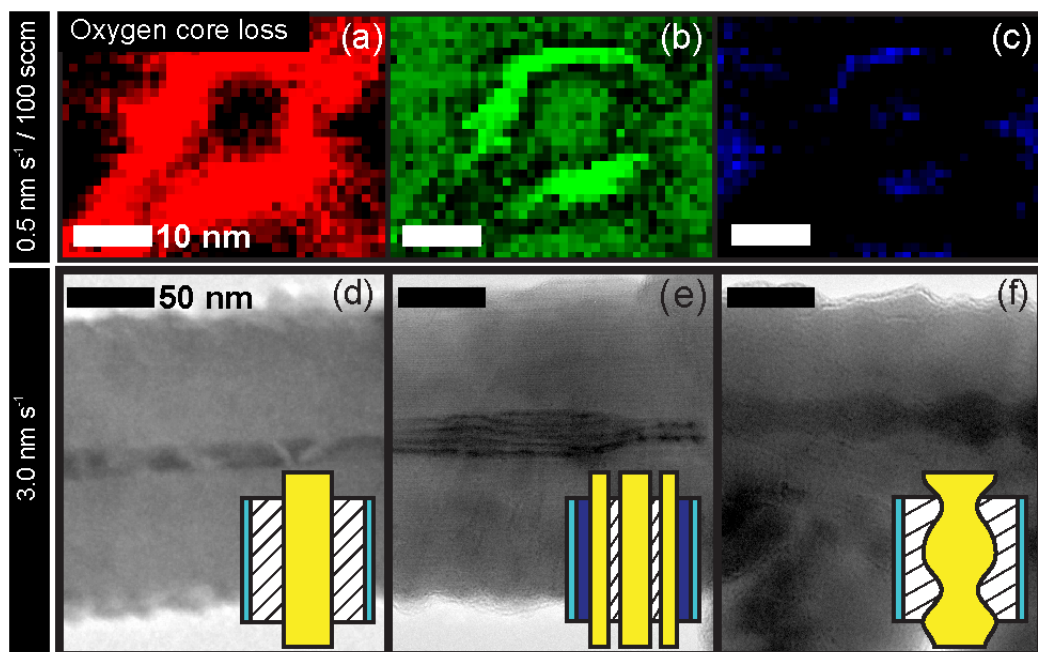


**Figure 6-11 Aperioidic cores as observed by EELs and TEM analysis.** Oxygen core-loss RGB (a,b,c) channels, where the scale matches that of previous EELs maps (see **Fig. 6-12 a**). Core-loss data presented using the ImageJ plugin Image5D (used to handle the time series of 3D-multichannel data stored in the .dm3 file). Edge view SEM of structures deposited at  $3.0 \text{ nm s}^{-1}$  (50 nm scale bar) for: (d) continuous core, (e) concentric core, and (f) rippled core; inset: schematic for various core-shell models.

The proceeding observations are consistent with the previously outlined chemical depletion mechanism with the depletion region extending into what is typically considered bulk. The pronounced metallic core is unlike the relatively uniform/flat elemental profile of the air-annealed NW isolated from device 3c211 (see **Appendix F** for air-only EELS temperature map). The above scale is presented in raw oxygen core-loss electron counts as the nature of the thickness correction required to further query the local oxygen bonding environment requires an updated conduction mechanism.

We reach the limits of our experiment when we consider the aperiodicity encountered along the  $z$ -axis (see **Fig. 6-11**). Separating the oxygen core-loss temperature map into its constituent RGB channels (where the scale is the same as **Fig. 6-10 b**) reveals an overlap between regions of minimum and maximum oxygen counts (**Fig. 6-11 a–c**,  $0.5 \text{ nm s}^{-1}$ ). The observed profile may be attributed to a rippled metallic core, and introduces the consideration of an aperiodicity and various core/shell configurations; similarly observed within films deposited at elevated rates (**Fig. 6-11 d–f**,  $3.0 \text{ nm s}^{-1}$ ). A challenge is assessing how this behaviour evolves for a NW array with a shifting degeneracy—operating near the 1-D limit may offer a physical reference point.

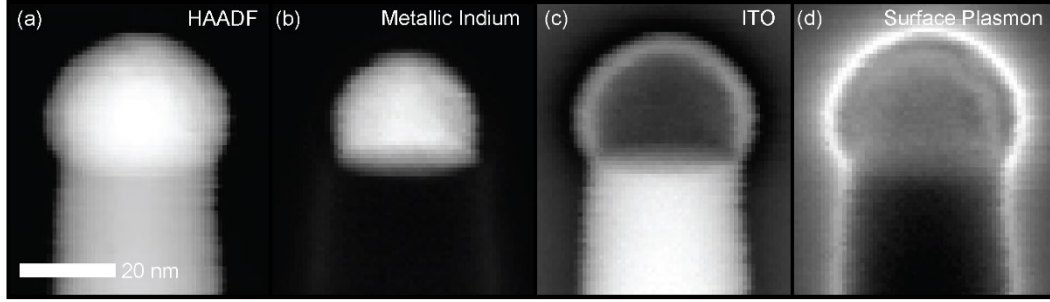


**Figure 6-12 EELS phase mapping of a side-contacted NW.** (a) High-angle annular dark-field (HAADF) image; isolated elemental phase map for (b) In, (c) ITO, and (d) the surface plasmon.

Of note, it has recently been demonstrated by others that for low-dimensional conduction within parallel arrays, excitations are of the type characterized by the 1-D phenomena of Tomonaga-Luttinger liquid theory result [204]. Similar features have been noted in recent study of confined carrier populations within ITO thin films [94], [136], [205]. Further, the fit electric field dependence outlined in **Table 6-2** is consistent with the power-law dependences on physical quantities, such as temperature, voltage, and frequency predicted by a such a conduction model [205], [206]. Of note, such a model implies that all NWs contribute and act in concert to define the device characteristics<sup>5</sup>.

Characteristic of a 1-D conduction model, the detection of a surface plasmon is possible through observation of resonance peaks in the energy-loss spectra [207]. Utilizing this, Kai Cui (National Institute of Nanotechnology—Edmonton, Alberta, Canada) separated the material phase contributions (i.e., In, ITO, and the surface plasmon, see **Fig. 6-12 a–d**).

## 6.3 Chapter Summary

Further effecting the distribution of  $V_0$  through post-processing anneals offers another degree of freedom to tune the conductivity of ITO NWs, measureable through relative shift in the electrical characteristics of CBKR devices with high temperature processing<sup>6</sup>.

<sup>5</sup>Entering the mesoscopic regime may explain the ‘loss of individuality’ at the macroscopic, device scale (see Sata et al., for the study of the turn-on of this effect [213]).

<sup>6</sup>For our updated conduction model—an incoming wave sees a thin barrier ( $\phi_b \lesssim 100$  meV) and a relevant transition at  $V_0 \sim 200$  meV below the CBM. We then observe  $q(\mu_2 - \mu_1) = qV_M (\gtrsim 300$  meV)  $= \Delta E_F$ , under testing conditions. Here, we operate near the 1-D limit—supported by the observed transverse dimensions—with the interfaces contributing negligibly (i.e., considering the as-

Devices are subject to an aperiodicity along the long-axis of the NW, which is believed to be the root cause of the observed multi-modal distribution. Here, as the variance within a given array increases (i.e., through formation of a dominant metallic core), fewer loops ( $\lesssim 10$ ) are required to saturate the observed resistance [179]. However, for our devices,  $30 \lesssim N_p \lesssim 1000$ ), and in **chapter 7**, future work is suggested to extend beyond this limit. Further analysis of this phenomena is difficult due to the consideration of the associated logarithmic band-edges [208][209], coalescence and/or ripening growth mechanisms [210], and other confounding factors such as the effect of hydrogen on conductivity [139].

In **chapter 5** we found as-deposited  $\text{ITO}_{\text{TF}}$  samples to be of similar electrical quality to as-deposited  $\text{ITO}_{\text{VLS85}}$  samples (see **Table 5-3**). In **chapter 6**, the non-normal distribution is found to be attributable to metallic NWs with device characteristics limited by the resulting channel constriction, supporting the theory that the core-shell architecture is responsible for the anomalous conductance behavior observed at the device level (and not device damage as was suggested in **chapter 5**). This work extends the 4-wire electrical characterization method to NW arrays, demonstrating the CBKR architecture as a useful tool to assess the atomic character of the arrays. The results of the present work require that we further address the core-shell architecture and the complex interaction between trunk and branch [136], [203], as well as the distribution of dopants as it applies to an individual NW [114], [211], subject to localized deposition conditions [94], [155]. Further work will be required to elucidate the behaviour of these VLS-grown NWs (including how they operate collectively); this requires an expanded toolkit and a more refined device architecture (see **chapter 7**, future work).

---

deposited condition, and the associated CBKR devices:  $\rho_c \sim 10^{-8} \Omega \text{ cm}^2$ , owing to the localized states at the interfaces).



## 7 Experimental conclusions

While most electrical characterization techniques provide either indirect measures of ITO NW thin films [94], [136], [151], or yield isolated measurements (i.e., single NWs) with low through-put [115]–[119], the 4-wire characterization of the ensemble electrical characteristics allows for measurement of nanometre-scale shifts, intrinsic to the NW arrays. Recent literature exploring the VLS growth mechanism suggests an intimate relationship between the bulk chemical depletion observed and chemical potential oscillations unique to sub-micron diameter NWs. Growth of these wires is expectedly sensitive to rate modulation and local geometric and atomic shadowing. In the case of metallic growth, only a few NWs with a metallic core would be needed to conduct the majority of the test current (owing to the large variance in conductivity between NWs [179]) and would explain the lack of dependence on the number of posts for the K-cluster analysis<sup>1</sup>. For this highly conductive subset of contacted NWs, the applied electric field would be the defining characteristic due to the dependence on the limiting

---

<sup>1</sup>One exception is samples processed at 10 sccm and 175 °C; this may be a potentially optimal processing range to minimize film variance (refer to **Appendix G**).



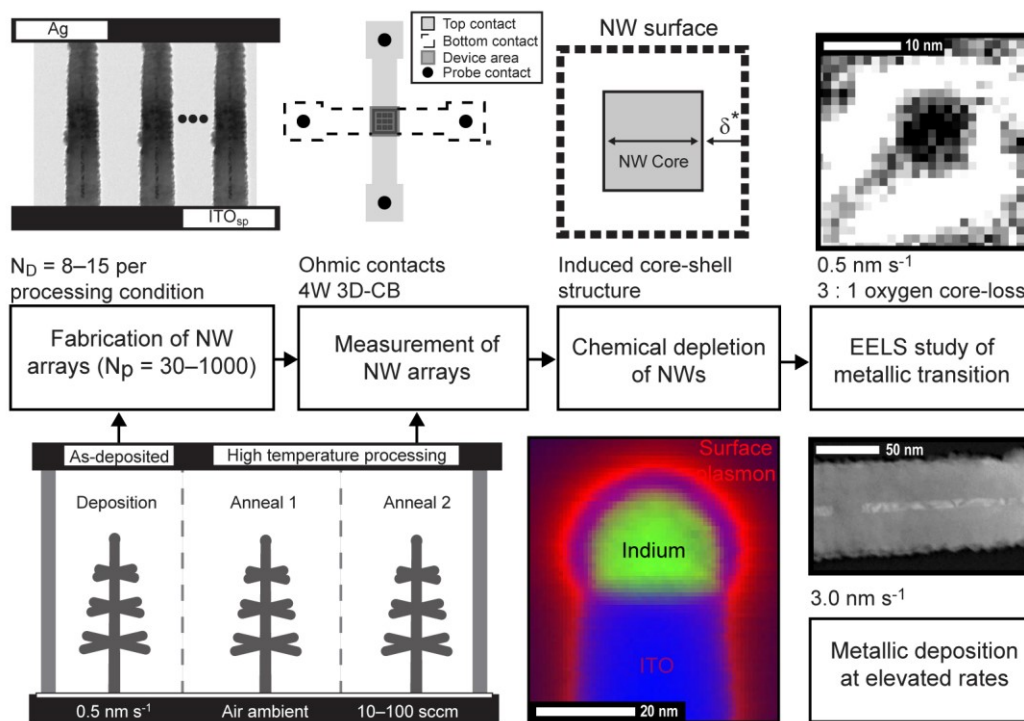


**Figure 7-1 Experimental schematic process flow.** Nanostructures processed under the indicated conditions are deposited between metallic contacts (outlined in **chapter 4** and **5**). Further characterization reveals an induced, aperiodic, core-shell structure (see the discussion of **chapter 6**). Inset: EELS mixed phase map (for ITO NW of **Fig. 6-14**) including In catalyst droplet, ITO and surface plasmon.

dimensions of the opening of the conductive channels; supporting the prediction that at nanometre-scale dimensions electrostatics play an increasingly dominate role [124].

By improving the conductivity of the nanostructures, the aim is to minimize internal resistances and enable the tuning of the opto-electronic response to affect the charge transfer characteristics within an OPV device. To meet this aim, from **chapter 1**, we outlined the following primary objectives:

1. *Validate electrical test structures fabricated within this work, understanding and eliminating defects to isolate an intrinsic measure of our nanostructures* — we have achieved this by using a 4-wire cross bridge architecture, which has afforded us a view of the intrinsic array properties.
2. *Use the above test structures to optimize the electrical properties of our material system through post deposition anneals*—Post-deposition anneals, particularly at the processing condition of 175 °C, 10 sccm may be a region of minimum variance in film properties (e.g., see **Appendix G**).

Addressing the above primary objectives enabled us to undertake our secondary objective, which was to:

3. *Interpret our results within the current understanding of GLAD and VLS growth mechanisms* — we must combine the relationship between: **i.** ‘leapfrog’ or a fast growth regime (characterized by rapid changes in NW length during growth) [158], **ii.** the decrease in oxygen incorporation at elevated rates [94], and **iii.** the effects of the local deposition environment particularly of  $V_O$ , as NWs ‘compete’ for their incorporation during growth [155].

My contributions to the efforts enclosed within this document include: **i.** integration of nanotree structures upon bottom contacts; **ii.** fabrication of high-quality electronic junctions; and **iii.** preliminary exploration of an induced core-shell structure (for a summary of the procedure see **Fig. 7-1**). The relevance of this work to nano-enhanced OPV devices stems from the ability to access the plasmonic behavior of the ITO NW (see **Fig. 7-1 inset** — EELS phase mapping for an ITO NW), as well as the ability to define the electronic properties of the NW near surface region (i.e., the surface dipole) together with the NW interior volume or ‘bulk’. These observations extend the technological feasibility of these nanostructures and present areas of potential improvement in future fabrication and design of TCEs.

## 7.1 Current OPV work

A suitable nanostructured TCE must provide maximum surface coverage, optimally dispersed current density, and have a sufficiently low resistance. Areas of improvement highlighted in the research of our collectively laboratories have been: the management of sub-5 nm dissociation interfaces, potential redistribution in the BHJ, vertical phase distribution within the OPV, and the ‘light trapping’/plasmonic response of the nanotree electrodes. The latter is highly dependent on the incorporation of oxygen vacancy states, and the eventual metallic transition observed in **chapter 6**. Further utilization of ITO NWs requires improved management of the ‘skin’ of the NW, as well as the distribution of metallic nanoparticles established at growth.

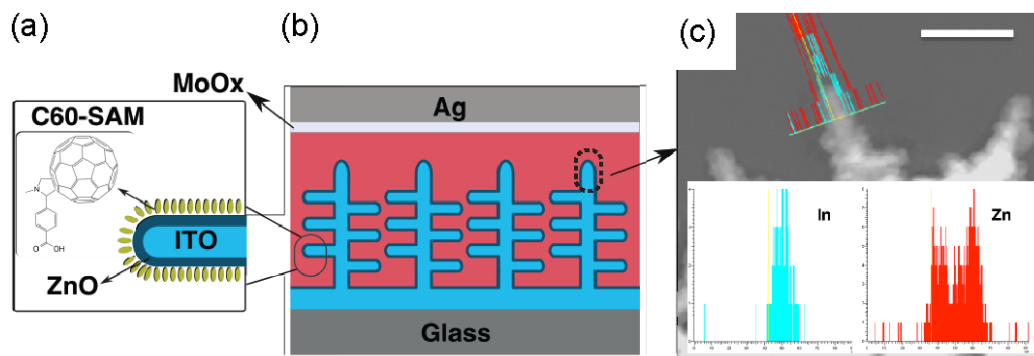


**Figure 7-2 Nanostructured OPV.** Explored by our collaborators in the Chemistry department, the (a) functionalization of the NW surface prepares it for (b) integration into a nano-enhanced OPV device; (c) A line scan elemental analysis indicates that strong indium signal from the inner the 'trunk', while the zinc signal is mainly from the outer skin, indicating that ZnO 'skin' surrounds the inner ITO 'core'. Figure credit: [212].

Bing Cao (Ph.D., Chemistry, U of A) studied the charge extraction behavior of ITO NW films (75–150 nm), and their effect on the solar cell performance [212]. In preparation for incorporation into the BHJ, structures were coated with ZnO (atomic layer deposition, 8 nm), followed by functionalization with a surface monolayer of C<sub>60</sub> (see **Fig. 7-2** for a schematic of the layers assembled by Cao). The former stabilizes the cathodic behavior of the NW, and the latter provides the excitonic dissociation interface required for separation of the photo-generated charge carriers. With variation of the height of ITO nanotree films, an optimum height of 75 nm was obtained (PCE ~ 5 %). Cao traced the low PCE values to charge recombination loss resulting from electric field redistribution near the nanotree surface.

It was assessed that the balance of charge extraction and bimolecular recombination reaches the optimum at this height, and leads to more balance electron/hole transport. For films >75 nm it was suggested that the pathway for holes may be blocked by the NWs, preventing their extraction at the anode. Assessment of the this requires a more refined device architecture; e.g., reduction of NW-NW variance (through the use of lattice matched substrates [96], and smaller devices, i.e.,  $1 \lesssim N_p \lesssim 10$ ) paired with probing at higher frequencies to study the internal electronic interfaces.

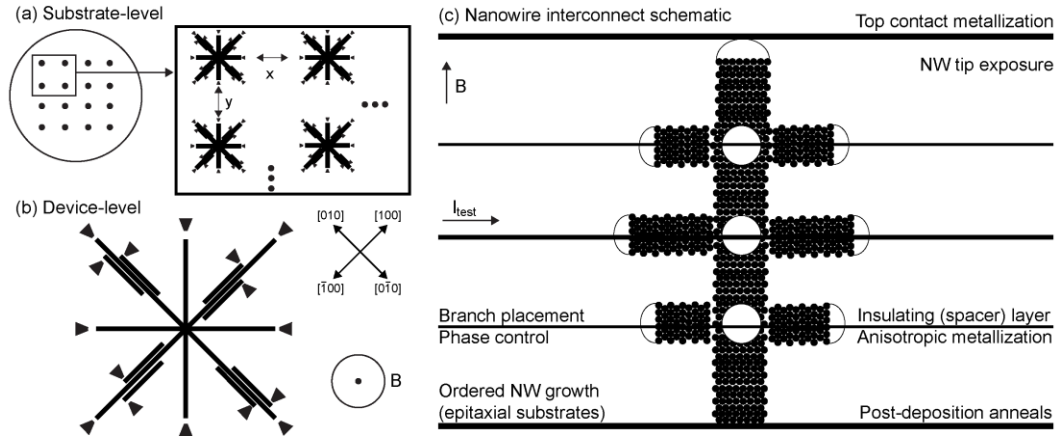


**Figure 7-3 Multi-gate CBKR architecture.** (a) Substrate-level layout; (b) Device-level layout; and (c) a schematic NW interconnect (deposition processes on the left and fabrication processes on the right).

## 7.2 A future nanotree array—hall mobility measurement

Towards a deeper understanding of the above, the CBKR architecture can be adapted to enable the measurement of the array hall mobility (see **Fig. 7-3 a and b**, for substrate- and device-level schematics, respectively). Fabrication of such a device begins with the ordered NW growth on epitaxial substrates (see **Fig. 7-3 b, inset** for branch alignment) [96], paired with branch placement [9], [196] and further refinement of the deposition parameters to implement controlled phase changes<sup>2</sup> [94], [99], [158]. Post-deposition anneals are followed by the repeated deposition of alternating insulating layers, paired with anisotropic metal deposition [8], enabling gate-control. The exposure of the NW tips and metallization proceed as previously outlined. The above fabrication methodology is outlined in **figure 7-3 c**.

In the above schematic, branches are aligned with the electrodes oriented along the diagonal axis through the use of lattice-matched substrates and epitaxial growth. The multiple electrodes should enable the isolation of branch and trunk ‘channels’ allowing for piece-wise diagnostic of the completed device. Here, the applied magnetic field ( $B$ ) is applied normal to the substrate [95], and the test current extracted through the

<sup>2</sup>Future study requires improving the resolution of branched-NW growth simulation [196], requiring now atomistic modelling to access the long time-scale molecular dynamics simulations of thin film growth [124], [233].

transverse contacts. By adjusting the spacing between the devices (see **Fig. 7-3 a, inset**, x and y dimensions) the turn-on of mesoscopic coupling effects should be observable [213]. Further, adjustment of the height of films and the number of branching layers, paired with the deposition of integration of vertically stacked, tandem polymeric domains [4], [5] may allow assessment of the balance of charge extraction and bimolecular recombination limitations observed by Cao.

## 7.3 Reflection

Throughout this work, a challenge was to consider a NW as a single unit, and later as a coherent device, collectively defined at growth. The focus remained to find a straight line through the work—it is interesting to note that the fit of **figure 6-12** implies that all NWs contribute and act in concert to define the device characteristics. Further understanding of the physical phenomena at play requires an expanded toolkit and a more refined device architecture. What remains is the pairing of the CBKR architecture and the ITO material system has proven to be an interesting way to make NWs and study their intrinsic properties.

Over the course of this thesis, additional developments in understanding the VLS growth mechanism [158] and low-dimensional conduction within parallel arrays [204] have been made, and together with this work represent an incremental step forward with respect to the field of advanced nanotechnology-based materials. Continued exploration pairing simulation and experimental work will likely enable a deeper appreciation of ballistic flux deposition, conduction and measurement, and the resulting low-dimensional crystalline structures.

# Bibliography

- [1] S. M. Sze and M. K. Lee, *Physics of Semiconductor Devices*, 3rd ed. John Wiley & Sons, 1969.
- [2] J. Jean, P. R. Brown, R. L. Jaffe, T. Buonassisi, and V. Bulovic, “Pathways for Solar Photovoltaics,” *Energy Environ. Sci.*, 2015.
- [3] M. M. Waldrop, “More than Moore,” *Nature*, vol. 530, pp. 144–147, 2016.
- [4] J. Paul, T. S. Small, E. New, T. Howells, P. Sullivan, and T. S. Jones, “Small molecule tandem organic photovoltaic cells incorporating an alpha -NPD optical spacer layer,” *Org. Electron.*, vol. 14, no. 9, pp. 2353–2359, 2013.
- [5] P. Sullivan, S. Schumann, R. Da Campo, T. Howells, A. Duraud, M. Shipman, R. A. Hatton, and T. S. Jones, “Ultra-High Voltage Multijunction Organic Solar Cells for Low-Power Electronic Applications,” *Adv. Energy Mater.*, vol. 3, pp. 239–244, 2013.
- [6] K. M. Krause, M. T. Taschuk, and M. J. Brett, “Glancing angle deposition on a roll: Towards high-throughput nanostructured thin films,” *J. Vac. Sci. Technol. A Vacuum, Surfaces, Film.*, vol. 31, no. 3, 2013.
- [7] F. C. Krebs, M. Hösel, M. Corazza, B. Roth, M. V. Madsen, S. A. Gevorgyan, R. R. Søndergaard, D. Karg, and M. Jørgensen, “Freely available OPV-The fast way to progress,” *Energy Technol.*, vol. 1, no. 7, pp. 378–381, 2013.
- [8] G. Larrieu and X.-L. Han, “Vertical nanowire array-based field effect transistors for ultimate scaling,” *Nanoscale*, vol. 5, pp. 2437–2441, 2013.
- [9] A. L. Beaudry, J. M. LaForge, R. T. Tucker, P. Li, M. T. Taschuk, and M. J. Brett, “Flux Engineering for Indium Tin Oxide Nanotree Crystal Alignment and Height-Dependent Branch Orientation,” *Cryst. Growth Des.*, vol. 13, no. 1, pp. 212–219, Jan. 2013.

- [10] “3D XPoint,” *Wikipedia*. p. 3D XPoint, 2016.
- [11] A. L. Beaudry, R. T. Tucker, J. M. LaForge, M. T. Taschuk, and M. J. Brett, “Indium tin oxide nanowhisker morphology control by vapour-liquid-solid glancing angle deposition,” *Nanotechnology*, vol. 23, no. 10, p. 105608, Mar. 2012.
- [12] A. I. Hochbaum and P. Yang, “Semiconductor nanowires for energy conversion,” *Chem. Rev.*, vol. 110, no. 1, pp. 527–546, Jan. 2010.
- [13] M. M. Hawkeye and M. J. Brett, “Glancing angle deposition: Fabrication, properties, and applications of micro- and nanostructured thin films,” *J. Vac. Sci. Technol. A Vacuum, Surfaces, Film.*, vol. 25, no. 5, p. 1317, 2007.
- [14] K. Robbie and M. J. Brett, “Sculptured thin films and glancing angle deposition: Growth mechanics and applications,” *J. Vac. Sci. Technol. A Vacuum, Surfaces, Film.*, vol. 15, no. 3, pp. 1460–1465, 1997.
- [15] K. Robbie, J. C. Sit, and M. J. Brett, “Advanced techniques for glancing angle deposition,” *J. Vac. Sci. Technol. B Microelectron. Nanom. Struct.*, vol. 16, no. 3, pp. 1115–1122, 1998.
- [16] J. J. Steele, M. T. Taschuk, and M. J. Brett, “Sensors and Actuators B : Chemical Response time of nanostructured relative humidity sensors,” *Sensors Actuators B Chem.*, vol. 140, pp. 610–615, 2009.
- [17] D. Chang, Y. J. Park, and C. K. Hwangbo, “Optical Humidity Sensor Using a Narrow Band-Pass Filter Prepared by Glancing Angle Deposition,” *J. Korean Phys. Soc.*, vol. 53, no. 5, pp. 2700–2704, 2008.
- [18] J. J. Steele, A. C. van Popta, M. M. Hawkeye, J. C. Sit, and M. J. Brett, “Nanostructured gradient index optical filter for high-speed humidity sensing,” *Sensors Actuators B Chem.*, vol. 120, no. 1, pp. 213–219, Dec. 2006.
- [19] A. Bonakdarpour, M. D. Fleischauer, M. J. Brett, and J. R. Dahn, “Columnar support structures for oxygen reduction electrocatalysts prepared by glancing

- angle deposition,” *Appl. Catal. A Gen.*, vol. 349, no. 1–2, pp. 110–115, Oct. 2008.
- [20] A. Bonakdarpour, R. T. Tucker, M. D. Fleischauer, N. A. Beckers, M. J. Brett, and D. P. Wilkinson, “Nanopillar Niobium Oxides as Support Structures for Oxygen Reduction Electrocatalysts,” *Electrochim. Acta*, vol. 85, pp. 492–500, Aug. 2012.
- [21] M. D. Gasda, R. Teki, T.-M. Lu, N. Koratkar, G. A. Eisman, and D. Gall, “Sputter-Deposited Pt PEM Fuel Cell Electrodes: Particles vs Layers,” *J. Electrochem. Soc.*, vol. 156, no. 5, pp. 614–619, 2009.
- [22] W. J. Khudhayer, N. N. Kariuki, X. Wang, D. J. Myers, A. U. Shaikh, and T. Karabacak, “Oxygen Reduction Reaction Electrocatalytic Activity of Glancing Angle Deposited Platinum Nanorod Arrays,” *J. Electrochem. Soc.*, vol. 158, no. 8, p. B1029, 2011.
- [23] S. A. Francis, R. T. Tucker, M. J. Brett, and S. H. Bergens, “Structural and activity comparison of self-limiting versus traditional Pt electro-depositions on nanopillar Ni films,” *J. Power Sources*, vol. 222, pp. 533–541, Jan. 2013.
- [24] C. Renault, C. P. Andrieux, R. T. Tucker, M. J. Brett, V. Balland, and B. Limoges, “Unraveling the mechanism of catalytic reduction of O<sub>2</sub> by microperoxidase-11 adsorbed within a transparent 3D-nanoporous ITO film,” *J. Am. Chem. Soc.*, vol. 134, no. 15, pp. 6834–6845, Apr. 2012.
- [25] G. K. Kiema, M. J. Colgan, and M. J. Brett, “Dye sensitized solar cells incorporating obliquely deposited titanium oxide layers,” *Sol. Energy Mater. Sol. Cells*, vol. 85, no. 3, pp. 321–331, Jan. 2005.
- [26] N. Li and S. R. Forrest, “Tilted bulk heterojunction organic photovoltaic cells grown by oblique angle deposition,” *Appl. Phys. Lett.*, vol. 95, no. 12, p. 123309, 2009.
- [27] D. a Rider, R. T. Tucker, B. J. Worfolk, K. M. Krause, A. Lalany, M. J. Brett, J. M. Buriak, and K. D. Harris, “Indium tin oxide nanopillar electrodes in



- polymer/fullerene solar cells,” *Nanotechnology*, vol. 22, no. 8, p. 85706, Feb. 2011.
- [28] H. K. Yu, “Three-Dimensional Nanobranched Solar Cells,” *ACS Nano*, no. 10, pp. 8026–8032, 2011.
- [29] B. C. Thompson and J. M. J. Fréchet, “Polymer-fullerene composite solar cells,” *Angew. Chemie - Int. Ed.*, vol. 47, pp. 58–77, 2008.
- [30] T. M. Clarke and J. R. Durrant, “Charge carrier photogeneration in organic solar cells,” *Chem. Rev.*, vol. 110, pp. 6736–6767, 2010.
- [31] F. Yang and S. R. Forrest, “Photocurrent Generation in Nanostructured Organic Solar Cells,” *ACS Nano*, vol. 2, no. 5, pp. 1022–1032, May 2008.
- [32] S. R. Forrest, “The Limits to Organic Photovoltaic Cell Efficiency,” *MRS Bull.*, vol. 30, no. January, pp. 28–32, 2005.
- [33] C. Breyer and A. Gerlach, “Global overview on grid-parity,” *Prog. Photovoltaics Res. Appl.*, vol. 21, no. 1, pp. 121–136, 2012.
- [34] I. Fraunhofer Institute for Solar Energy Systems, “Photovoltaics Report,” 2016.
- [35] H. Spanggaard and F. C. Krebs, “A brief history of the development of organic and polymeric photovoltaics,” *Sol. Energy Mater. Sol. Cells*, vol. 83, no. 2–3, pp. 125–146, Jun. 2004.
- [36] M. A. Green, K. Emery, Y. Hishikawa, and W. Warta, “Solar cell efficiency tables (version 36),” *Prog. Photovoltaics Res. Appl.*, vol. 18, no. 5, pp. 346–352, Jun. 2010.
- [37] M. A. Green, Y. Hishikawa, W. Warta, E. D. Dunlop, | Dean, H. Levi, J. Hohl-ebinger, and A. W. Y. Ho-baillie, “Solar cell efficiency tables (version 50).”
- [38] H. Hoppe and N. S. Sariciftci, “Organic solar cells: An overview,” *J. Mater. Res.*, vol. 19, no. 7, pp. 1924–1945, Mar. 2011.
- [39] C. J. Brabec, S. Gowrisanker, J. J. M. Halls, D. Laird, S. Jia, and S. P. Williams, “Polymer-fullerene bulk-heterojunction solar cells,” *Adv. Mater.*, vol. 22, pp.

3839–3856, 2010.

- [40] S. R. Forrest, “The path to ubiquitous and low-cost organic electronic appliances on plastic,” *Nature*, vol. 428, pp. 911–918, 2004.
- [41] F. Machui, M. Hosel, N. Li, G. D. Spyropoulos, T. Ameri, R. R. Sondergaard, M. Jorgensen, A. Scheel, D. Gaiser, K. Kreul, D. Lenssen, M. Legros, N. Lemaitre, M. Vilkman, M. Valimaki, S. Nordman, C. J. Brabec, and F. C. Krebs, “Cost analysis of roll-to-roll fabricated ITO free single and tandem organic solar modules based on data from manufacture,” *Energy Environ. Sci.*, p. , 2014.
- [42] B. A. Collins, J. R. Tumbleston, and H. Ade, “Miscibility, Crystallinity, and Phase Development in P3HT/PCBM Solar Cells: Toward an Enlightened Understanding of Device,” *J. Phys. Chem. Lett.*, vol. 2, pp. 3135–3145, 2011.
- [43] E. J. Lubber and J. M. Buriak, “Reporting performance in organic photovoltaic devices,” *ACS Nano*, vol. 7, no. 6, pp. 4708–4714, 2013.
- [44] D. Mühlbacher, M. Scharber, M. Morana, Z. Zhu, D. Waller, R. Gaudiana, and C. Brabec, “High Photovoltaic Performance of a Low-Bandgap Polymer,” *Adv. Mater.*, vol. 18, no. 21, pp. 2884–2889, Nov. 2006.
- [45] S.-S. Sun and N. S. Sariciftci, Eds., *Organic photovoltaics: Mechanisms, Materials, and Devices*. 2005.
- [46] F. Zhang, J. Bijleveld, E. Perzon, K. Tvingstedt, S. Barrau, O. Inganäs, and M. R. Andersson, “High photovoltage achieved in low band gap polymer solar cells by adjusting energy levels of a polymer with the LUMOs of fullerene derivatives,” *J. Mater. Chem.*, vol. 18, no. D, p. 5468, 2008.
- [47] B. Ray and M. A. Alam, “A compact physical model for morphology induced intrinsic degradation of organic bulk heterojunction solar cell,” *Appl. Phys. Lett.*, vol. 99, no. 2011, pp. 1–4, 2011.
- [48] B. Ray, P. R. Nair, and M. A. Alam, “Annealing dependent performance of

organic bulk-heterojunction solar cells: A theoretical perspective,” *Sol. Energy Mater. Sol. Cells*, vol. 95, no. 12, pp. 3287–3294, Dec. 2011.

- [49] J. Zhao, A. Swinnen, G. Van Assche, J. Manca, D. Vanderzande, and B. Van Mele, “Phase diagram of P3HT/PCBM blends and its implication for the stability of morphology,” *J. Phys. Chem. B*, vol. 113, no. 6, pp. 1587–91, Mar. 2009.
- [50] S. Honda, T. Nogami, H. Ohkita, H. Benten, and S. Ito, “Improvement of the light-harvesting efficiency in polymer/fullerene bulk heterojunction solar cells by interfacial dye modification,” *ACS Appl. Mater. Interfaces*, vol. 1, no. 4, pp. 804–10, May 2009.
- [51] D. A. Rider, B. J. Worfolk, K. D. Harris, A. Lalany, K. Shahbazi, M. D. Fleischauer, M. J. Brett, and J. M. Buriak, “Stable Inverted Polymer/Fullerene Solar Cells Using a Cationic Polythiophene Modified PEDOT:PSS Cathodic Interface,” *Adv. Funct. Mater.*, vol. 4, p. n/a-n/a, Jun. 2010.
- [52] M. Graetzel, R. A. J. Janssen, D. B. Mitzi, and E. H. Sargent, “Materials interface engineering for solution-processed photovoltaics,” *Nature*, vol. 488, pp. 304–312, 2012.
- [53] R. Steim, F. R. Kogler, and C. J. Brabec, “Interface materials for organic solar cells,” *J. Mater. Chem.*, vol. 20, p. 2499, 2010.
- [54] J. H. Lee, J.-H. Shin, J. Y. Song, W. Wang, R. Schlaf, K. J. Kim, and Y. Yi, “Interface Formation Between ZnO Nanorod Arrays and Polymers (PCBM and P3HT) for Organic Solar Cells,” *J. Phys. Chem. C*, vol. 116, no. 50, pp. 26342–26348, Dec. 2012.
- [55] B. Kannan, K. Castelino, and A. Majumdar, “Design of Nanostructured Heterojunction Polymer Photovoltaic Devices,” *Nano Lett.*, 2003.
- [56] P. Kohn, Z. Rong, K. H. Scherer, A. Sepe, M. Sommer, P. Mu, R. H. Friend, U. Steiner, and S. Hu, “Crystallization-induced 10-nm structure formation in

- P3HT/PCBM Blends,” *Macromolecules*, vol. 46, pp. 4002–4013, 2013.
- [57] “InfinityPV.pdf.” .
- [58] “Heliatek,” 2017. [Online]. Available: <http://www.heliatek.com/en/>.
- [59] N. Banerji, “Organic photovoltaics, pushing the knowledge of interfaces,” *Nat. Mater.*, vol. 16, pp. 503–505, 2017.
- [60] H. A. Atwater and A. Polman, “Plasmonics for improved photovoltaic devices,” *Nat. Mater.*, vol. 9, no. 3, pp. 205–13, Mar. 2010.
- [61] G. V. Naik, V. M. Shalae, and A. Boltasseva, “Alternative plasmonic materials: Beyond gold and silver,” *Adv. Mater.*, vol. 25, no. 24, pp. 3264–3294, 2013.
- [62] B. A. Gregg, “Coulomb forces in excitonic solar cells,” *Org. Photovoltaics Mech. Mater. Devices*, pp. 139–160, 2005.
- [63] X. Y. Zhao, Z. G. Li, T. J. Zhu, B. X. Mi, Z. Q. Gao, and W. Huang, “Structure optimization of organic planar heterojunction solar cells,” *J. Phys. D-Applied Phys.*, vol. 46, p. 9, 2013.
- [64] S. M. Mahpeykar, Q. Xiong, and X. Wang, “Resonance-induced absorption enhancement in colloidal quantum dot solar cells using nanostructured electrodes,” *Opt. Express*, vol. 22, no. S6, p. A1576, 2014.
- [65] B. A. Gregg and M. C. Hanna, “Comparing organic to inorganic photovoltaic cells: Theory, experiment, and simulation,” *J. Appl. Phys.*, vol. 93, no. 6, p. 3605, 2003.
- [66] W. Cai, X. Gong, and Y. Cao, “Polymer solar cells: Recent development and possible routes for improvement in the performance,” *Sol. Energy Mater. Sol. Cells*, vol. 94, no. 2, pp. 114–127, Feb. 2010.
- [67] M. T. Dang, L. Hirsch, and G. Wantz, “P3HT:PCBM, Best Seller in Polymer Photovoltaic Research,” *Adv. Mater.*, vol. 23, no. 31, pp. 3597–3602, Aug. 2011.

- [68] N. J. Gerein, M. D. Fleischauer, and M. J. Brett, "Effect of TiO<sub>2</sub> film porosity and thermal processing on TiO<sub>2</sub>-P3HT hybrid materials and photovoltaic device performance," *Sol. Energy Mater. Sol. Cells*, vol. 94, no. 12, pp. 2343–2350, Sep. 2010.
- [69] X. Yang, J. Loos, S. C. Veenstra, W. J. H. Verhees, M. M. Wienk, J. M. Kroon, M. A. J. Michels, and R. A. J. Janssen, "Nanoscale morphology of high-performance polymer solar cells," *Nano Lett.*, vol. 5, no. 4, pp. 579–83, Apr. 2005.
- [70] R. T. Tucker, A. L. Beaudry, J. M. Laforge, M. T. Taschuk, and M. J. Brett, "Branched nanowires and method of fabrication," 2014.
- [71] J. G. Van Dijken and M. J. Brett, "Nanopillar ITO electrodes via argon plasma etching," *J. Vac. Sci. Technol. A Vacuum, Surfaces, Film.*, vol. 30, no. 4, p. 40606, 2012.
- [72] J. G. Van Dijken, M. D. Fleischauer, and M. J. Brett, "Controlled nanostructuring of CuPc thin films via glancing angle deposition for idealized organic photovoltaic architectures," *J. Mater. Chem.*, vol. 21, no. 4, p. 1013, 2011.
- [73] M. Thomas, B. J. Worfolk, D. a Rider, M. T. Taschuk, J. M. Buriak, and M. J. Brett, "C60 fullerene nanocolumns -polythiophene heterojunctions for inverted organic photovoltaic cells," *ACS Appl. Mater. Interfaces*, vol. 3, no. 6, pp. 1887–94, Jun. 2011.
- [74] H. Kwon, J. Ham, D. Y. Kim, S. J. Oh, S. Lee, S. H. Oh, E. F. Schubert, K.-G. Lim, T.-W. Lee, S. Kim, J.-L. Lee, and J. K. Kim, "Three-Dimensional Nanostructured Indium-Tin-Oxide Electrodes for Enhanced Performance of Bulk Heterojunction Organic Solar Cells," *Adv. Energy Mater.*, Jan. 2014.
- [75] K. Ellmer, "Past achievements and future challenges in the development of optically transparent electrodes," *Nat. Photonics*, vol. 6, no. December, pp. 808–816, 2012.

- [76] F. Bonaccorso, Z. Sun, T. Hasan, and a. C. Ferrari, “Graphene Photonics and Optoelectronics,” vol. 4, no. August, pp. 611–622, 2010.
- [77] C. J. M. Emmott, A. Urbina, and J. Nelson, “Environmental and economic assessment of ITO-free electrodes for organic solar cells,” *Sol. Energy Mater. Sol. Cells*, vol. 97, pp. 14–21, 2012.
- [78] S. Calnan and A. N. Tiwari, “High mobility transparent conducting oxides for thin film solar cells,” *Thin Solid Films*, vol. 518, no. 7, pp. 1839–1849, 2010.
- [79] K. K. Kim, S. Niki, J. Y. Oh, J. O. Song, T. Y. Seong, S. J. Park, S. Fujita, and S. W. Kim, “High electron concentration and mobility in Al-doped n-ZnO epilayer achieved via dopant activation using rapid-thermal annealing,” *J. Appl. Phys.*, vol. 97, no. 6, 2005.
- [80] K. L. Chopra, S. Major, and D. K. Pandya, “Transparent Conductors - A Status Review,” *Thin Solid Films*, vol. 102, pp. 1–46, 1983.
- [81] R. Bel Hadj Tahar, T. Ban, Y. Ohya, and Y. Takahashi, “Tin doped indium oxide thin films: Electrical properties,” *J. Appl. Phys.*, vol. 83, no. 5, p. 2631, 1998.
- [82] G. J. Exarhos and X.-D. Zhou, “Discovery-based design of transparent conducting oxide films,” *Thin Solid Films*, vol. 515, no. 18, pp. 7025–7052, Jun. 2007.
- [83] C. G. Granqvist, *Handbook of Transparent Conductors*. Boston, MA: Springer US, 2011.
- [84] S. Choi, W. J. Potscavage, and B. Kippelen, “ITO-free large-area organic solar cells,” *Opt. Express*, vol. 18 Suppl 3, no. September, pp. A458–66, Oct. 2010.
- [85] A. Kumar and C. Zhou, “The race to replace tin-doped indium oxide: Which material will win?,” *ACS Nano*, vol. 4, no. 1, pp. 11–14, 2010.
- [86] G. Haacke, “New figure of merit for transparent conductors,” *J. Appl. Phys.*, vol. 47, no. 9, pp. 4086–4089, 1976.

- [87] Y. Shen, K. Li, N. Majumdar, J. C. Campbell, and M. C. Gupta, “Bulk and contact resistance in P3HT:PCBM heterojunction solar cells,” *Sol. Energy Mater. Sol. Cells*, vol. 95, no. 8, pp. 2314–2317, 2011.
- [88] G. Li, A. Luican, J. M. B. L. Dos Santos, A. H. C. Neto, A. Reina, J. Kong, and E. Y. Andrei, “Observation of Van Hove singularities in twisted graphene layers,” *Nat. Phys.*, vol. 6, no. 2, p. 21, 2009.
- [89] K. S. Novoselov, S. V. Morozov, T. M. G. Mohinddin, L. A. Ponomarenko, D. C. Elias, R. Yang, I. I. Barbolina, P. Blake, T. J. Booth, D. Jiang, J. Giesbers, E. W. Hill, and A. K. Geim, “Electronic properties of graphene,” *Phys. Status Solidi*, vol. 244, no. 11, pp. 4106–4111, 2007.
- [90] K. D. Harris, A. C. van Popta, J. C. Sit, D. J. Broer, and M. J. Brett, “A Birefringent and Transparent Electrical Conductor,” *Adv. Funct. Mater.*, vol. 18, no. 15, pp. 2147–2153, Aug. 2008.
- [91] S. I. Castañeda, F. Rueda, R. Diaz, J. M. Ripalda, and I. Montero, “Whiskers in indium tin oxide films obtained by electron beam evaporation,” *J. Appl. Phys.*, vol. 83, no. 4, pp. 1995–2002, 1998.
- [92] S. T. Takaki, Y. A. Oshima, R. S. Atoh, S. Takaki, Y. Aoshima, and R. Satoh, “Growth Mechanism of Indium Tin Oxide Whiskers Prepared by Sputtering,” *Jpn. J. Appl. Phys.*, vol. 46, no. 6A, pp. 3537–3544, Jun. 2007.
- [93] D. V. Shinde, D. Y. Ahn, V. V. Jadhav, D. Y. Lee, N. K. Shrestha, J. K. Lee, H. Y. Lee, R. S. Mane, and S.-H. Han, “A coordination chemistry approach for shape controlled synthesis of indium oxide nanostructures and their photoelectrochemical properties,” *J. Mater. Chem. A*, vol. 2, p. 5490, 2014.
- [94] J. M. Laforge, T. L. Cocker, A. L. Beaudry, K. Cui, R. T. Tucker, M. T. Taschuk, F. A. Hegmann, and M. J. Brett, “Conductivity control of as-grown branched indium tin oxide nanowire networks,” *Nanotechnology*, vol. 25, no. 3, p. 35701, Jan. 2014.

- [95] O. M. Berengue, R. A. Simon, E. R. Leite, and A. J. Chiquito, “The study of electron scattering mechanisms in single crystal oxide nanowires,” *J. Phys. D. Appl. Phys.*, vol. 44, p. 215405, 2011.
- [96] A. L. Beaudry, J. M. Laforge, R. T. Tucker, J. B. Sorge, N. L. Adamski, P. Li, M. T. Taschuk, and M. J. Brett, “Directed branch growth in aligned nanowire arrays,” *Nano Lett.*, vol. 14, pp. 1797–1803, 2014.
- [97] C. P. Sturmberg, K. B. Dossou, L. C. Botten, A. Asatryan, C. G. Poulton, R. C. Mcphedran, and M. De Sterke, “Absorption enhancing proximity effects in aperiodic nanowire arrays,” vol. 1060, pp. 307–312, 2013.
- [98] A. Klein, C. Körber, A. Wachau, F. Säuberlich, Y. Gassenbauer, S. P. Harvey, D. E. Proffit, and T. O. Mason, “Transparent Conducting Oxides for Photovoltaics: Manipulation of Fermi Level, Work Function and Energy Band Alignment,” *Materials (Basel)*, vol. 3, pp. 4892–4914, 2010.
- [99] R. T. Tucker, A. L. Beaudry, J. M. LaForge, M. T. Taschuk, and M. J. Brett, “A little ribbing: Flux starvation engineering for rippled indium tin oxide nanotree branches,” *Appl. Phys. Lett.*, vol. 101, no. 19, p. 193101, 2012.
- [100] O. Salehzadeh, M. X. Chen, K. L. Kavanagh, and S. P. Watkins, “Rectifying characteristics of Te-doped GaAs nanowires,” *Appl. Phys. Lett.*, vol. 99, no. 18, p. 182102, 2011.
- [101] R. A. Patil, R. S. Devan, J.-H. Lin, Y. Liou, and Y.-R. Ma, “An efficient methodology for measurement of the average electrical properties of single one-dimensional NiO nanorods,” *Sci. Rep.*, vol. 3, p. 3070, Jan. 2013.
- [102] A. Bid, A. Bora, and A. K. Raychaudhuri, “Temperature dependence of the resistance of metallic nanowires of diameter  $> 15$  nm: Applicability of Bloch-Grüneisen theorem,” *Phys. Rev.*, vol. 74, pp. 1–8, 2006.
- [103] L. B. Valdes, “Resistivity Measurements on Germanium for Transistors,” *Proc. IRE*, vol. 42, no. 2, pp. 420–427, 1954.



- [104] F. Smits, "Measurement of sheet resistivities with the four-point probe," *Bell Syst. Tech. J.*, 1958.
- [105] S. Zolfaghar Tehrani, W. L. Lim, and L. Lee, "Correction factors for films resistivity measurement," *Meas. J. Int. Meas. Confed.*, vol. 45, no. 3, pp. 219–225, 2012.
- [106] S. Smith, "Sheet Resistance and Electrical Linewidth Test Structures for Semiconductor Process Characterisation," The University of Edinburgh, 2003.
- [107] M. Levichkova, V. Mankov, N. Starbov, D. Karashanova, B. Mednikarov, and K. Starbova, "Structure and properties of nanosized electron beam deposited zirconia thin films," *Surf. Coatings Technol.*, vol. 141, no. 1, pp. 70–77, Jun. 2001.
- [108] J. Lintymer, N. Martin, J.-M. Chappé, P. Delobelle, and J. Takadoun, "Influence of zigzag microstructure on mechanical and electrical properties of chromium multilayered thin films," *Surf. Coatings Technol.*, vol. 180–181, pp. 26–32, Mar. 2004.
- [109] J. Lintymer, J. Gavaille, N. Martin, and J. Takadoun, "Glancing angle deposition to modify microstructure and properties of sputter deposited chromium thin films," *Surf. Coatings Technol.*, vol. 175, pp. 316–323, 2003.
- [110] A. Besnard, N. Martin, L. Carpentier, and B. Gallas, "A theoretical model for the electrical properties of chromium thin films sputter deposited at oblique incidence," *J. Phys. D. Appl. Phys.*, vol. 44, no. 21, p. 215301, Jun. 2011.
- [111] D. Vick and M. J. Brett, "Conduction anisotropy in porous thin films with chevron microstructures," *J. Vac. Sci. Technol. A Vacuum, Surfaces, Film.*, vol. 24, no. 1, p. 156, 2006.
- [112] T. Ishida, H. Kobayashi, and Y. Nakato, "Structures and properties of electron-beam-evaporated indium tin oxide films as studied by x-ray photoelectron spectroscopy and work-function measurements," *J. Appl. Phys.*, vol. 73, no. 9, pp. 4344–4350, 1993.

- [113] C. Durkan and M. E. Welland, “Size effects in the electrical resistivity of polycrystalline nanowires,” *Phys. Rev. B*, vol. 61, no. 20, pp. 14215–14218, 2000.
- [114] M. Gurvitch, “Ioffe-Regel criterion and resistivity of metals,” *Phys. Rev. B*, vol. 24, no. 12, pp. 7404–7407, 1981.
- [115] R. Gurwitz and I. Shalish, “Method for electrical characterization of nanowires,” *Nanotechnology*, vol. 22, no. 43, p. 435705, Oct. 2011.
- [116] Q. Wan, Z. T. Song, S. L. Feng, T. H. Wang, and S. In, “Single-crystalline tin-doped indium oxide whiskers: Synthesis and characterization,” *Appl. Phys. Lett.*, vol. 85, no. 20, pp. 4759–4761, 2004.
- [117] G. Meng, T. Yanagida, K. Nagashima, H. Yoshida, M. Kanai, A. Klamchuen, F. Zhuge, Y. He, S. Rahong, X. Fang, S. Takeda, and T. Kawai, “Impact of preferential indium nucleation on electrical conductivity of vapor-liquid-solid grown indium-tin oxide nanowires,” *J. Am. Chem. Soc.*, vol. 135, no. 18, pp. 7033–8, May 2013.
- [118] J. Gao, R. Chen, D. H. Li, L. Jiang, J. C. Ye, X. C. Ma, X. D. Chen, Q. H. Xiong, H. D. Sun, and T. Wu, “UV light emitting transparent conducting tin-doped indium oxide (ITO) nanowires,” *Nanotechnology*, vol. 22, no. 19, p. 195706, May 2011.
- [119] S.-P. Chiu, H.-F. Chung, Y.-H. Lin, J.-J. Kai, F.-R. Chen, and J.-J. Lin, “Four-probe electrical-transport measurements on single indium tin oxide nanowires between 1.5 and 300 K,” *Nanotechnology*, vol. 20, no. 10, p. 105203, Mar. 2009.
- [120] S. Enderling, C. L. Brown, S. Smith, M. H. Dicks, J. T. M. Stevenson, M. Mitkova, and M. N. Kozicki, “Sheet resistance measurement of non-standard cleanroom materials using suspended Greek cross test structures,” *IEEE Trans. Semicond. Manuf.*, vol. 19, no. 1, pp. 2–9, 2006.
- [121] M. Natan, “Geometrical effects in contact resistance measurements: Finite element modeling and experimental results,” *J. Appl. Phys.*, vol. 53, no. 8, pp.

5776–5782, 1982.

- [122] M. W. Cresswell, S. Member, N. M. P. Guillaume, W. E. Lee, R. A. Allen, W. F. Guthrie, R. N. Ghoshtagore, Z. E. Osborne, N. Sullivan, and L. W. Linholm, “Extraction of Sheet Resistance from Four-Terminal Sheet Resistors Replicated in Monocrystalline Films with Nonplanar Geometries,” *IEEE Trans. Semicond. Manuf.*, vol. 12, no. 2, pp. 154–165, 1999.
- [123] E. Stern, G. Cheng, M. P. Young, and M. a. Reed, “Specific contact resistivity of nanowire devices,” *Appl. Phys. Lett.*, vol. 88, no. 5, p. 53106, 2006.
- [124] F. Léonard and A. A. Talin, “Electrical contacts to one- and two-dimensional nanomaterials,” *Nat. Nanotechnol.*, vol. 6, no. 12, pp. 773–83, Dec. 2011.
- [125] W. M. Loh, K. Saraswat, and R. W. Dutton, “Analysis and scaling of Kelvin resistors for extraction of specific contact resistivity,” *IEEE Electron Device Lett.*, vol. 6, no. 3, pp. 105–108, Mar. 1985.
- [126] T. A. Schreyer and K. C. Saraswat, “A two-dimensional analytical model of the cross-bridge Kelvin resistor,” *IEEE Electron Device Lett.*, vol. 7, no. 12, pp. 661–663, 1986.
- [127] M. Natan, “Geometrical effects in contact resistance measurements: Finite element modeling and experimental results,” *J. Appl. Phys.*, vol. 53, no. 8, pp. 5776–5782, 1982.
- [128] R. J. Pedersen, “Effect of Film Resistance on Low-Impedance Tunneling Measurements,” *Appl. Phys. Lett.*, vol. 10, no. 1, pp. 29–31, 1967.
- [129] C. L. Bauer and A. G. Jordan, “Study of interfacial reactions in bimetallic thin-film couples by contact resistance measurements,” *Phys. Status Solidi*, vol. 47, no. 1, pp. 321–328, May 1978.
- [130] K. C. Saraswat, “Metal / Semiconductor Ohmic Contacts,” 1997.
- [131] A. L. Beaudry, “Flux Directed Branched Nanowire Growth via VLS-GLAD,”

2014.

- [132] H. C. Kim, T. L. Alford, and D. R. Allee, "Thickness dependence on the thermal stability of silver thin films," *Appl. Phys. Lett.*, vol. 81, no. 22, p. 4287, 2002.
- [133] J. Rosen and O. Warschkow, "Electronic structure of amorphous indium oxide transparent conductors," *Phys. Rev. B - Condens. Matter Mater. Phys.*, vol. 80, no. 11, p. 115215, Sep. 2009.
- [134] P. Reunchan, X. Zhou, S. Limpijumnong, A. Janotti, and C. G. Van de Walle, "Vacancy defects in indium oxide: An ab-initio study," *Curr. Appl. Phys.*, vol. 11, no. 3, pp. S296–S300, May 2011.
- [135] Z. Q. Li and J. J. Lin, "Electrical resistivities and thermopowers of transparent Sn-doped indium oxide films," *J. Appl. Phys.*, vol. 96, no. 10, pp. 5918–5920, 2004.
- [136] C. S. Yang, M. H. Lin, C. H. Chang, P. Yu, J. M. Shieh, C. H. Shen, O. Wada, and C. L. Pan, "Non-drude behavior in indium-tin-oxide nanowhiskers and thin films investigated by transmission and reflection thz time-domain spectroscopy," *IEEE J. Quantum Electron.*, vol. 49, no. 8, pp. 677–690, 2013.
- [137] H. Bruus and K. Flensberg, "Many-body quantum theory in condensed matter physics," no. August, pp. 10–11, 2006.
- [138] CRC Handbook, "Electron work function of the elements," *CRC Handb.*, p. (12-114), 2011.
- [139] S. Limpijumnong, P. Reunchan, A. Janotti, and C. G. Van De Walle, "Hydrogen doping in indium oxide: An ab initio study," *Phys. Rev. B - Condens. Matter Mater. Phys.*, vol. 80, pp. 1–4, 2009.
- [140] K. L. Chopra, S. Major, and D. K. Pandya, "Review Paper," *Thin Solid Films*, vol. 102, pp. 1–46, 1983.
- [141] E. Terzini, P. Thilakan, and C. Minarini, "Properties of ITO thin films deposited

- by RF magnetron sputtering at elevated substrate temperature,” *Mater. Sci. Eng. B*, vol. 77, no. 1, pp. 110–114, Aug. 2000.
- [142] J.-H. Kim, J.-H. Lee, Y.-W. Heo, J.-J. Kim, and J.-O. Park, “Effects of oxygen partial pressure on the preferential orientation and surface morphology of ITO films grown by RF magnetron sputtering,” *J. Electroceramics*, vol. 23, pp. 169–174, 2009.
  - [143] Q. Zhu, E. M. Hopper, B. J. Ingram, and T. O. Mason, “Combined Jonker and Ioffe analysis of oxide conductors and semiconductors,” *J. Am. Ceram. Soc.*, vol. 94, pp. 187–193, 2011.
  - [144] I. Hamberg, C. G. Granqvist, K.-F. Berggren, B. E. Sernelius, and L. Engstrom, “Band-gap widening in heavily Sn-doped  $\text{In}_2\text{O}_3$ ,” *Phys. Rev.*, vol. 30, no. 6, 1984.
  - [145] Y. Park, V. Choong, Y. Gao, B. R. Hsieh, and C. W. Tang, “Work function of indium tin oxide transparent conductor measured by photoelectron spectroscopy,” *Appl. Phys. Lett.*, vol. 19, no. 68, pp. 2699–2701, 1996.
  - [146] H. Kobayashi, T. Ishida, K. Nakamura, Y. Nakato, and H. Tsubomura, “Properties of indium tin oxide films prepared by the electron beam evaporation method in relation to characteristics of indium tin oxide/silicon oxide/silicon junction solar cells,” *J. Appl. Phys.*, vol. 72, no. 1992, pp. 5288–5293, 1992.
  - [147] D. C. Paine, T. Whitson, D. Janiac, R. Beresford, C. O. Yang, and B. Lewis, “A study of low temperature crystallization of amorphous thin film indium–tin–oxide,” *J. Appl. Phys.*, vol. 85, no. 12, p. 8445, 1999.
  - [148] H. Wulff, M. Quaas, H. Steffen, and R. Hippler, “In situ studies of diffusion and crystal growth in plasma deposited thin ITO films,” *Thin Solid Films*, vol. 377–378, pp. 418–424, Dec. 2000.
  - [149] I. Hamberg and C. G. Granqvist, “Evaporated Sn-doped  $\text{In}_2\text{O}_3$  films: Basic optical properties and applications to energy-efficient windows,” *J. Appl. Phys.*, vol. 60, no. December, pp. 123–159, 1986.

- [150] L. Gupta, A. Mansingh, and P. K. Srivastava, "Band gap narrowing and the band structure of tin-doped indium oxide films," *Thin Solid Films*, vol. 176, pp. 33–44, 1989.
- [151] C. G. Granqvist and A. Hultaker, "Transparent and conducting ITO films : new developments and applications," *Thin Solid Films*, vol. 411, pp. 1–5, 2002.
- [152] P. K. Chakraborty, G. C. Datta, and K. P. Ghatak, "The simple analysis of the Burstein-Moss shift in degenerate n-type semiconductors," *Phys. B Condens. Matter*, vol. 339, pp. 198–203, 2003.
- [153] L. Abelman and C. Lodder, "Oblique evaporation and surface diffusion," *Thin Solid Films*, vol. 305, no. 1–2, pp. 1–21, Aug. 1997.
- [154] M. Ohring, *Materials Science of Thin Films, Second Edition*. 2001.
- [155] R. Alvarez, C. Lopez-Santos, J. Parra-Barranco, V. Rico, A. Barranco, J. Cotrino, A. R. Gonzalez-Elipé, and A. Palmero, "Nanocolumnar growth of thin films deposited at oblique angles: Beyond the tangent rule," *J. Vac. Sci. Technol. B Microelectron. Nanom. Struct.*, vol. 32, no. 4, p. 41802, 2014.
- [156] C. Patzig and B. Rauschenbach, "Temperature effect on the glancing angle deposition of Si sculptured thin films," *J. Vac. Sci. Technol. A Vacuum, Surfaces, Film.*, vol. 26, no. 4, p. 881, 2008.
- [157] R. S. Wagner and W. C. Ellis, "Vapor-liquid-solid mechanism of single crystal growth," vol. 4, no. 5, p. 89, 1964.
- [158] H. Wang, J. Wang, Z. Cao, W. Zhang, C. Lee, and S. Lee, "A surface curvature oscillation model for vapour–liquid–solid growth of periodic one-dimensional nanostructures," *Nat. Commun.*, vol. 6, pp. 1–7, 2015.
- [159] V. Dubrovskii, N. Sibirev, G. Cirlin, J. Harmand, and V. Ustinov, "Theoretical analysis of the vapor-liquid-solid mechanism of nanowire growth during molecular beam epitaxy," *Phys. Rev. E*, vol. 73, no. 2, p. 21603, Feb. 2006.

- [160] R. Takaki, Satoru; Aoshima, Yuki; Satoh, “Growth Mechanism of Indium Tin Oxide Whiskers Prepared by Sputtering,” *Jpn. J. Appl. Phys.*, vol. 46, no. 6A, pp. 3537–3544, Jun. 2007.
- [161] S. P. Harvey, T. O. Mason, Y. Gassenbauer, R. Schafranek, and a Klein, “Surface versus bulk electronic/defect structures of transparent conducting oxides: I. Indium oxide and ITO,” *J. Phys. D. Appl. Phys.*, vol. 39, no. 18, pp. 3959–3968, Sep. 2006.
- [162] P. Nath and R. F. Bunshah, “Preparation of  $\text{In}_2\text{O}_3$  and Tin-doped  $\text{In}_2\text{O}_3$  films by a novel activated reactive evaporation technique,” *Thin Solid Films*, vol. 69, pp. 63–68, 1980.
- [163] N. Balasubramanian and a. Subrahmanyam, “Electrical and optical properties of reactively evaporated indium tin oxide (ITO) films- dependence on substrate temperature and tin concentration,” *J. Phys. D. Appl. Phys.*, vol. 22, pp. 206–209, 1989.
- [164] H. Kim, S. Park, C. Jin, and C. Lee, “Enhanced photoluminescence in Au-embedded ITO nanowires,” *ACS Appl. Mater. Interfaces*, vol. 3, pp. 4677–4681, 2011.
- [165] Y. Li, Y. Bando, and D. Golberg, “Single-Crystalline  $\text{In}_2\text{O}_3$  Nanotubes Filled with In,” *Adv. Mater.*, vol. 15, no. 78, pp. 581–585, Apr. 2003.
- [166] K. Fuchs, “The conductivity of thin metallic films according to the electron theory of metals,” vol. 157, no. 1936, pp. 100–108, 1937.
- [167] E. H. Sondheimer, *The mean free path of electrons in metals*, vol. 1, no. 1. 1952.
- [168] A. F. Mayadas and M. Shatzkes, “Electrical-Resistivity Model for Polycrystalline Films: the Case of Arbitrary Reflection at External Surfaces,” *Phys. Rev.*, vol. 1, no. February, 1970.
- [169] F. Léonard and a. A. Talin, “Size-dependent effects on electrical contacts to nanotubes and nanowires,” *Phys. Rev. Lett.*, vol. 97, no. 2, pp. 1–4, 2006.

- [170] Y. Sato, M. Taketomo, N. Ito, and Y. Shigesato, "Study on early stages of film growth for Sn doped  $\text{In}_2\text{O}_3$  films deposited at various substrate temperatures," *Thin Solid Films*, vol. 516, pp. 5868–5871, 2008.
- [171] K. Ellmer and R. Mientus, "Carrier transport in polycrystalline transparent conductive oxides: A comparative study of zinc oxide and indium oxide," *Thin Solid Films*, vol. 516, pp. 4620–4627, 2008.
- [172] A. K. Kulkarni, K. H. Schulz, T. S. Lim, and M. Khan, "Dependence of the sheet resistance of indium-tin-oxide thin films on grain size and grain orientation determined from X-ray diffraction techniques," vol. 345, pp. 273–277, 1999.
- [173] K. Zhang, F. Zhu, C. H. . Huan, and A. T. . Wee, "Indium tin oxide films prepared by radio frequency magnetron sputtering method at a low processing temperature," *Thin Solid Films*, vol. 376, no. 1–2, pp. 255–263, Nov. 2000.
- [174] K. Zhang, F. Zhu, C. H. A. Huan, and A. T. S. Wee, "Effect of hydrogen partial pressure on optoelectronic properties of indium tin oxide thin films deposited by radio frequency magnetron sputtering method," *J. Appl. Phys.*, vol. 86, no. 2, p. 974, 1999.
- [175] W. S. Rasband, "ImageJ," *ImageJ*. US National Institutes of Health, Bethesda, Maryland, USA, 1997.
- [176] Q. Wan, E. N. Dattoli, W. Y. Fung, W. Guo, Y. Chen, X. Pan, and W. Lu, "High-performance transparent conducting oxide nanowires," *Nano Lett.*, vol. 6, no. 12, pp. 2909–15, Dec. 2006.
- [177] S. Karim, K. Maaz, G. Ali, and W. Ensinger, "Diameter dependent failure current density of gold nanowires," *J. Phys. D: Appl. Phys.*, vol. 42, no. 18, p. 185403, Sep. 2009.
- [178] G. Sharma, M. V. Pishko, and C. a. Grimes, "Fabrication of metallic nanowire arrays by electrodeposition into nanoporous alumina membranes: Effect of barrier layer," *J. Mater. Sci.*, vol. 42, no. 13, pp. 4738–4744, 2007.



- [179] B. Denardo, "Experiments with electrical resistive networks," *Am. J. Phys.*, vol. 67, no. 1999, p. 981, 1999.
- [180] K. J. Dudeck, M. Couillard, S. Lazar, C. Dwyer, and G. A. Botton, "Quantitative statistical analysis, optimization and noise reduction of atomic resolved electron energy loss spectrum images," *Micron*, vol. 43, no. 1, pp. 57–67, 2012.
- [181] R. F. Egerton, "Electron energy-loss spectroscopy in the TEM," *Reports Prog. Phys.*, vol. 72, no. 1, p. 16502, 2008.
- [182] M. Seto, K. Westra, and M. Brett, "Arrays of self-sealed microchambers and channels," *J. Mater. Chem.*, vol. 12, no. 8, pp. 2348–2351, Jul. 2002.
- [183] D. A. Rider, R. T. Tucker, B. J. Worfolk, K. M. Krause, A. Lalany, M. J. Brett, J. M. Buriak, and K. D. Harris, "Indium tin oxide nanopillar electrodes in polymer/fullerene solar cells," *Nanotechnology*, vol. 22, no. 8, p. 85706, Feb. 2011.
- [184] M. M. Hawkeye and M. J. Brett, "Glancing angle deposition: Fabrication, properties, and applications of micro- and nanostructured thin films," *J. Vac. Sci. Technol. A Vacuum, Surfaces, Film.*, vol. 25, no. 5, pp. 1317–1335, 2007.
- [185] J. M. A. Siewert, J. M. Laforge, M. T. Taschuk, and M. J. Brett, "Disassembling glancing angle deposited films for high-throughput, single-post growth scaling measurements," *Microsc. Microanal.*, vol. 18, no. 5, pp. 1135–42, Oct. 2012.
- [186] M. T. Taschuk, K. M. Krause, J. J. Steele, M. A. Summers, and M. J. Brett, "Growth scaling of metal oxide columnar thin films deposited by glancing angle depositions," *J. Vac. Sci. Technol. B Microelectron. Nanom. Struct.*, vol. 27, no. 5, p. 2106, 2009.
- [187] H. A. Schafft, J. S. Suehle, and P. G. A. Mire, "Proc. IEEE 1989 Int. Conference," *IEEE 1989 Int. Conf. Microelec. Test Struct.*, vol. 2, no. 1, pp. 121–125, 1989.
- [188] Z. Huang, K. D. Harris, and M. J. Brett, "Morphology control of nanotube arrays," *Adv. Mater.*, vol. 21, pp. 2983–2987, 2009.

- [189] Z. Huang, M. M. Hawkeye, and M. J. Brett, "Enhancement in broadband and quasi-omnidirectional antireflection of nanopillar arrays by ion milling," *Nanotechnology*, vol. 23, p. 275703, 2012.
- [190] J. J. Steele, G. A. Fitzpatrick, and M. J. Brett, "Capacitive Humidity Sensors With High Sensitivity and Subsecond Response Times," *IEEE Sens. J.*, vol. 7, no. 6, pp. 955–956, Jun. 2007.
- [191] H. Overhof, "Fundamental concepts in the physics of amorphous semiconductors," *J. Non. Cryst. Solids*, vol. 227–230, pp. 15–22, May 1998.
- [192] D. Adler and E. Yoffa, "Electronic Structure of Amorphous Semiconductors," *Phys. Rev. Lett.*, vol. 36, no. 20, pp. 1197–1200, May 1976.
- [193] K. M. Krause, M. T. Taschuk, K. D. Harris, D. A. Rider, N. G. Wakefield, J. C. Sit, J. M. Buriak, M. Thommes, and M. J. Brett, "Surface area characterization of obliquely deposited metal oxide nanostructured thin films," *Langmuir*, vol. 26, no. 6, pp. 4368–76, 2010.
- [194] M. J. B. Matthew M. Hawkeye, Michael T. Taschuk, *Glancing Angle Deposition of Thin Films: Engineering the Nanoscale*. Wiley, 2014.
- [195] A. Klein, "Electronic properties of  $\text{In}_2\text{O}_3$  surfaces," *Appl. Phys. Lett.*, vol. 77, no. May 2014, p. 2009, 2000.
- [196] M. T. Taschuk, R. T. Tucker, J. M. Laforge, A. L. Beaudry, M. R. Kupsta, and M. J. Brett, "Towards engineered branch placement: Unreal??? match between vapour-liquid-solid glancing angle deposition nanowire growth and simulation," *J. Appl. Phys.*, vol. 114, no. 2013, 2013.
- [197] D. A. Rider, R. T. Tucker, B. J. Worfolk, K. M. Krause, and A. Lalany, "Indium tin oxide nanopillar electrodes in polymer / fullerene solar cells," pp. 1–5.
- [198] Y. Gassenbauer, R. Schafrank, A. Klein, S. Zafeiratos, M. Hävecker, A. Knop-Gericke, and R. Schlögl, "Surface states, surface potentials, and segregation at surfaces of tin-doped  $\text{In}_2\text{O}_3$ ," *Phys. Rev. B*, vol. 73, no. 24, p. 245312, Jun. 2006.

- [199] Y. Gassenbauer, R. Schafrank, a. Klein, S. Zafeiratos, M. Hävecker, a. Knop-Gericke, and R. Schlögl, “Surface potential changes of semiconducting oxides monitored by high-pressure photoelectron spectroscopy: Importance of electron concentration at the surface,” *Solid State Ionics*, vol. 177, pp. 3123–3127, 2006.
- [200] M. S. Aldenderfer and R. K. Blashfield, *Cluster analysis*. Beverly Hills: Sage Publications, 1984.
- [201] T. Bielz, H. Lorenz, W. Jochum, R. Kaindl, F. Klauser, B. Klötzer, and S. Penner, “Hydrogen on  $\text{In}_2\text{O}_3$ : Reducibility, Bonding, Defect Formation, and Reactivity,” *J. Phys. Chem. C*, vol. 114, no. 19, pp. 9022–9029, May 2010.
- [202] ISP Optics, “Fused Silica UV Grade,” <http://www.ispoptics.com/>, 2016. .
- [203] E. Prodan, C. Radloff, N. J. Halas, and P. Nordlander, “A hybridization model for the plasmon response of complex nanostructures,” *Science*, vol. 302, no. 5644, pp. 419–22, Oct. 2003.
- [204] M. Moreno, C. J. B. Ford, Y. Jin, J. P. Griffiths, I. Farrer, G. A. C. Jones, D. A. Ritchie, O. Tsyplatyev, and A. J. Schofield, “Nonlinear spectra of spinons and holons in short GaAs quantum wires,” *Nat. Commun.*, vol. 7, p. 17, 2016.
- [205] F. Liu, M. Bao, K. L. Wang, C. Li, B. Lei, and C. Zhou, “One-dimensional transport of indium oxide nanowires,” *Appl. Phys. Lett.*, vol. 86, no. 21, p. 213101, 2005.
- [206] C. L. Kane and M. P. A. Fisher, “Transmission through barriers and resonant tunneling in an interacting one-dimensional electron gas,” *Phys. Rev. B*, vol. 46, no. 23, pp. 15233–15262, 1992.
- [207] J. Nelayah, M. Kociak, O. Stéphan, F. J. García de Abajo, M. Tencé, L. Henrard, D. Taverna, I. Pastoriza-Santos, L. M. Liz-Marzán, and C. Colliex, “Mapping surface plasmons on a single metallic nanoparticle,” *Nat. Phys.*, vol. 3, no. 5, pp. 348–353, 2007.

- [208] J. Alstott, E. Bullmore, and D. Plenz, “Powerlaw: A python package for analysis of heavy-tailed distributions,” *PLoS One*, vol. 9, pp. 1–18, 2014.
- [209] L. B. Kiss, J. Söderlund, G. a Niklasson, and C. G. Granqvist, “New approach to the origin of lognormal size distributions of nanoparticles,” *Nanotechnology*, vol. 10, pp. 25–28, 1999.
- [210] R. B. Bergmann and A. Bill, “On the origin of logarithmic-normal distributions: An analytical derivation, and its application to nucleation and growth processes,” *J. Cryst. Growth*, vol. 310, pp. 3135–3138, 2008.
- [211] D. E. Perea, E. R. Hemesath, E. J. Schwalbach, J. L. Lensch-falk, P. W. Voorhees, and L. J. Lauhon, “Direct measurement of dopant distribution in an individual vapour – liquid – solid nanowire,” vol. 4, no. March, pp. 315–319, 2009.
- [212] B. Cao, “Materials Development and Architecture Engineering for High Efficiency Organic Solar Cells,” 2016.
- [213] N. Sata, K. Eberman, K. Eberl, and J. Maier, “Mesoscopic fast ion conduction in nanometre-scale planar heterostructures,” *Nature*, vol. 408, no. December, pp. 946–949, 2000.
- [214] K. M. Coakley, Y. Liu, M. D. McGehee, K. L. Frindell, and G. D. Stucky, “Infiltrating Semiconducting Polymers into Self-Assembled Mesoporous Titania Films for Photovoltaic Applications,” *Adv. Funct. Mater.*, vol. 13, no. 4, pp. 301–306, Apr. 2003.
- [215] K. M. Coakley, B. S. Srinivasan, J. M. Ziebarth, C. Goh, Y. Liu, and M. D. McGehee, “Enhanced Hole Mobility in Regioregular Polythiophene Infiltrated in Straight Nanopores,” *Adv. Funct. Mater.*, vol. 15, no. 12, pp. 1927–1932, Dec. 2005.
- [216] P. Meakin, *Fractals, scaling and growth far from equilibrium*. Cambridge University Press, 1998.

- [217] IBM, “IBM SPSS Statistics for Windows.” IBM Corporation, Armonk, NY, 2013.
- [218] S. O. Kasap, *Optoelectronics and Photonics : Principles and Practices*. Pearson, 2013.
- [219] J. S. Moon, C. J. Takacs, Y. Sun, and A. J. Heeger, “Spontaneous Formation of Bulk Heterojunction Nanostructures : Multiple Routes to Equivalent Morphologies,” pp. 1036–1039, 2011.
- [220] K. I. Bolotin, K. J. Sikes, Z. Jiang, M. Klima, G. Fudenberg, J. Hone, P. Kim, and H. L. Stormer, “Ultrahigh electron mobility in suspended graphene,” *Solid State Commun.*, vol. 146, no. 9–10, pp. 351–355, 2008.
- [221] Q. Zhang, C. S. Dandeneau, X. Zhou, and G. Cao, “ZnO Nanostructures for Dye-Sensitized Solar Cells,” *Adv. Mater.*, vol. 21, no. 41, pp. 4087–4108, 2009.
- [222] T. T. Heikkilä, *The Physics of Nanoelectronics: Transport and Fluctuation Phenomena at Low Temperatures*. Oxford University Press, 2013.
- [223] K. Kim, H. Song, J. T. Park, and J. Kwak, “C<sub>60</sub> Self-Assembled Monolayer Using Diamine as a Prelayer,” *Chem. Lett.*, pp. 958–959, 2000.
- [224] S. H. Kim, J. Jang, and J. Y. Lee, “Relationship between indium tin oxide surface treatment and hole injection in C<sub>60</sub> modified devices,” *Appl. Phys. Lett.*, vol. 89, pp. 2006–2008, 2006.
- [225] E. Matveeva, “Electrochemistry of the Indium-Tin Oxide Electrode in 1 M NaOH Electrolyte,” *J. Electrochem. Soc.*, vol. 152, p. H138, 2005.
- [226] S. A. Bashar, “Study of Indium Tin Oxide (ITO) for Novel Optoelectronic Devices,” 1998.
- [227] A. Lalany, R. T. Tucker, M. T. Taschuk, M. D. Fleischauer, and M. J. Brett, “Axial resistivity measurement of a nanopillar ensemble using a cross-bridge Kelvin architecture,” *J. Vac. Sci. Technol. A Vacuum, Surfaces, Film.*, vol. 31, no. 3, p. 31502, 2013.

- [228] A. S. S. Shapiro and M. B. Wilk, “An Analysis of Variance Test for Normality (Complete Samples),” *Biometrika*, vol. 52, no. 3, pp. 591–611, 1965.
- [229] M. Mendoza, N. A. M. Araújo, S. Succi, and H. J. Herrmann, “Transition in the Equilibrium Distribution Function of Relativistic Particles,” *Sci. Rep.*, vol. 2, 2012.
- [230] N. Fukata, T. Oshima, N. Okada, T. Kizuka, T. Tsurui, S. Ito, and K. Murakami, “Phonon confinement in silicon nanowires synthesized by laser ablation,” *Phys. B Condens. Matter*, vol. 376–377, pp. 864–867, 2006.
- [231] H. I. Liu, D. K. Biegelsen, F. A. Ponce, N. M. Johnson, and R. F. W. Pease, “Self-limiting oxidation for fabricating sub-5 nm silicon nanowires,” *Appl. Phys. Lett.*, vol. 64, no. 11, pp. 1383–1385, 1994.
- [232] H. Cui, C. X. Wang, and G. W. Yang, “Origin of self-limiting oxidation of Si nanowires,” *Nano Lett.*, vol. 8, no. 9, pp. 2731–2737, 2008.
- [233] A. Khorshidi and A. A. Peterson, “Amp: A modular approach to machine learning in atomistic simulations,” *Comput. Phys. Commun.*, vol. 207, pp. 310–324, 2016.

# A Case-study: GLAD-OPV

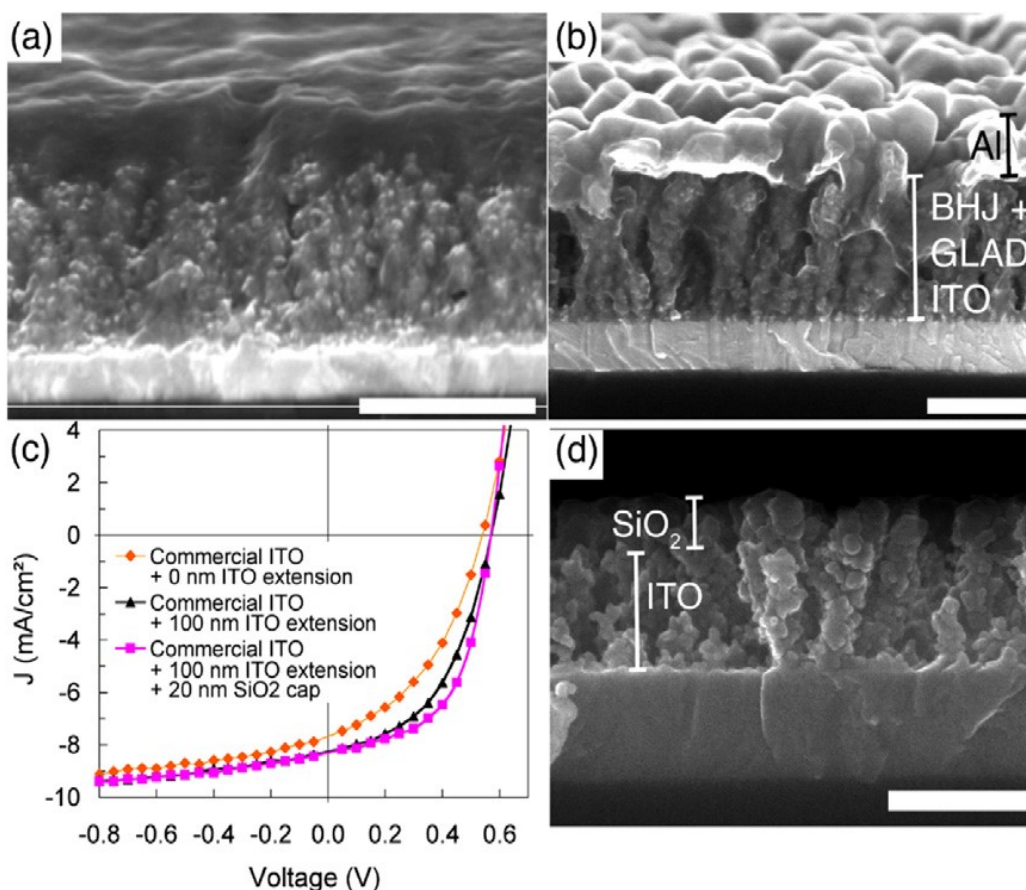


**Figure A-1 GLAD-ITO OPV.** (a) GLAD-ITO ( $\alpha = 83^\circ$ ) structures integrated into a P3HT : PCBM BHJ; (b) capped with  $\sim 80$  nm of Al. (c) The resulting illuminated current density-voltage plots<sup>1</sup> fabricated with commercial ITO (orange diamonds), GLAD ITO (black triangles) and silica-capped GLAD ITO (magenta squares) anodes. (500 nm scale bar); (d) Scanning electron micrograph of 150 nm GLAD ITO capped with 50 nm silica to prevent electrical shorts between electrode and cathode (200 nm scale bar). Figure credit: [51].

Often, the complex interaction between the photoactive matrix (the mixture of donor and acceptor) and the non-uniform nanostructures results in PCE improvements that do not scale with parameters such as surface area. However, nanostructures offer an added degree of control by influencing the alignment of polymers within the confining nanoporous films [27], [68], [214]. In our initial 2011 study, a structured ITO film was grown via the GLAD technique, producing a high surface area electrode upon which an

<sup>1</sup>Optical properties were obtained using a Perkin-Elmer Lambda 900 UV/VIS/NIR spectrometer, with films grown on commercial ITO substrates (Delta Technologies  $8\sim 12 \Omega/\square$ ). Series resistance values were derived from I-V characteristics of the completed OPV devices. I-V curves were measured with a Keithley 2400 source meter.

industry-standard Poly(3-hexylthiophene) (P3HT)/[6,6]-phenyl C61-butyric acid methyl ester (PCBM) BHJ was deposited (see **Fig. A-1 a** and **b**) [27]. There was a demonstrated improvement in  $R_S$  and subsequent improvements in FF with 100 nm ITO extensions into the BHJ (see **Fig. A-1 c**).

Novel contributions from this study included the fabrication of nanostructured ITO<sub>GLAD</sub> coated with an electro-deposited layer of poly(3,4-ethylenedioxythiophene):poly(p-styrenesulfonate) (PEDOT:PSS), as well as a novel silica capping technique. PEDOT:PSS-modified ITO acts to enhance hole collection by improving electrical uniformity, reducing the contact resistance within the photo-junction and increasing  $V_{OC}$  [27]. Typically, PEDOT:PSS is applied to ITO electrodes by spin-coating, but this technique results in poor infiltration of the nano-electrode array, diminishing the useful surface-area enhancement. An alternative, the deposition technique, uses a hydrolyzed layer of triethoxy-2-thiensiylsilane to provide nucleation sites for the electrochemical polymerization of ethylenedioxythiophene (EDOT) from an aqueous sodium polystyrenesulfonates (PSSNa) electrolyte, resulting in a conformal coating and leading to improved device performance [27]. By capping with an insulating silica cap, we can further improve  $R_S$  and better prevent shorting from the cathode to the nanostructures (see **Fig. A-1 d**).

Since then internal efforts<sup>2</sup> utilizing GLAD structures in OPV devices have included structuring of the and acceptor phase [73], and donor phase [72]. In the former, Thomas et al., thermally evaporated C<sub>60</sub> nano-columns (0.05–0.1 nm s<sup>-1</sup>) via GLAD, with inter-column spacing tuned to better match the expected polymeric exciton diffusion length while simultaneously increasing the hetero-interface area. In the latter, Van Dijken et al. utilized periodically seeded substrates to deposit copper phthalocyanine (CuPc) nanostructures, with the further process refinement of utilizing the  $\phi$ -sweep technique to mitigate column-broadening enabling fabrication of uniform columnar films. In this sub-class of GLAD, as opposed to the continuous rotation in  $\phi$  used to create vertical post, the  $\phi$ -sweep technique involves periodically and discretely

---

<sup>2</sup>External to our lab, several attempts have been directed at structuring the transparent conducting oxide (TCO) electrode using single crystal ITO NWs [28], [74] however it has been difficult to achieve commercially relevant device efficiencies.



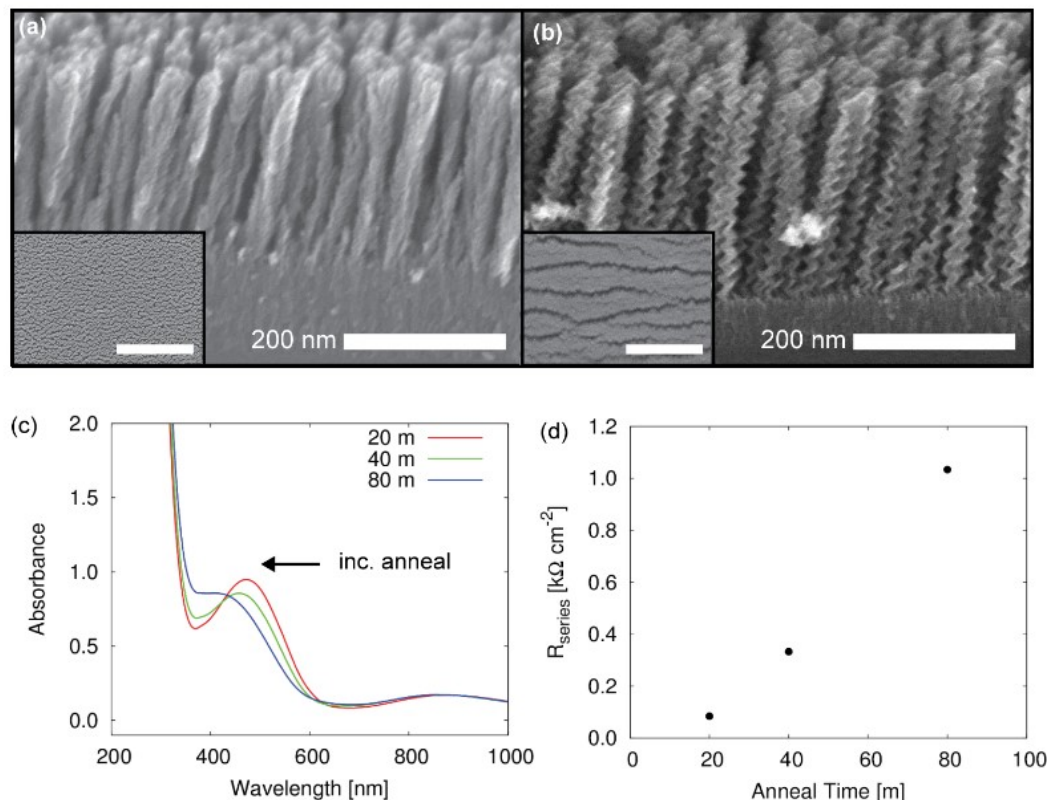


**Figure A-2 Polymer pore confinement.** (a) edge tilt (10°) SEM images of GLAD-SBD TiO<sub>2</sub> film, with 3 nm growth intervals, 1 nm transition period, inset: top-down view of same (1 μm scale bar) (b) 11 nm growth interval, 1 nm transition period. (c) absorption spectra for annealed GLAD-SBD TiO<sub>2</sub> devices (175 °C, 20–80 mins) (d) R<sub>s</sub> measurements for same.

rotating the substrate back and forth about the substrate normal as the film grows. Periodic shifts in  $\phi$  by an angle of  $\pm\gamma$  breaks the anisotropy of shadowing [72]. In its extreme ( $\gamma = 90^\circ$ ), this technique results in posts that are completely erect/vertical and is a special case referred to serial bi-deposition (SBD), and can results in refined control of the morphology of individual structures.

Progress of the above research was hampered by a lack of characterization of the internal structure and composition of our GLAD films, and a lack of understanding of the complex interaction between the photoactive matrix and the non-uniform nanostructures. To explore the latter, GLAD structures were fabricated with features approximately 10 nm in dimension (see **Fig. A-2 a and b**). Films were in-filled with a polymer matrix, and annealed at 175 °C for 20–80 mins. We observed an increase in R<sub>s</sub> and a blue-shift in the absorption curves, indicating that the degree of polymer chain

coiling increased with anneal time (see **Fig. A-2 c** and **d**). This was attributed to disrupted  $\pi$ -stacking of polymer chains resulting from increased polymer coiling, occurring as the features of nanostructured thin-films that approached the scale of the radius of gyration of the polymer, which induced polymer-backbone alignment due to pore confinement [214], [215]. This observed behaviour influenced the selection of ITO<sub>VLS</sub> films deposited at moderate rates, where NW and branch spacing are considered near-ideal.

## B 2-wire measurement of GLAD-ITO

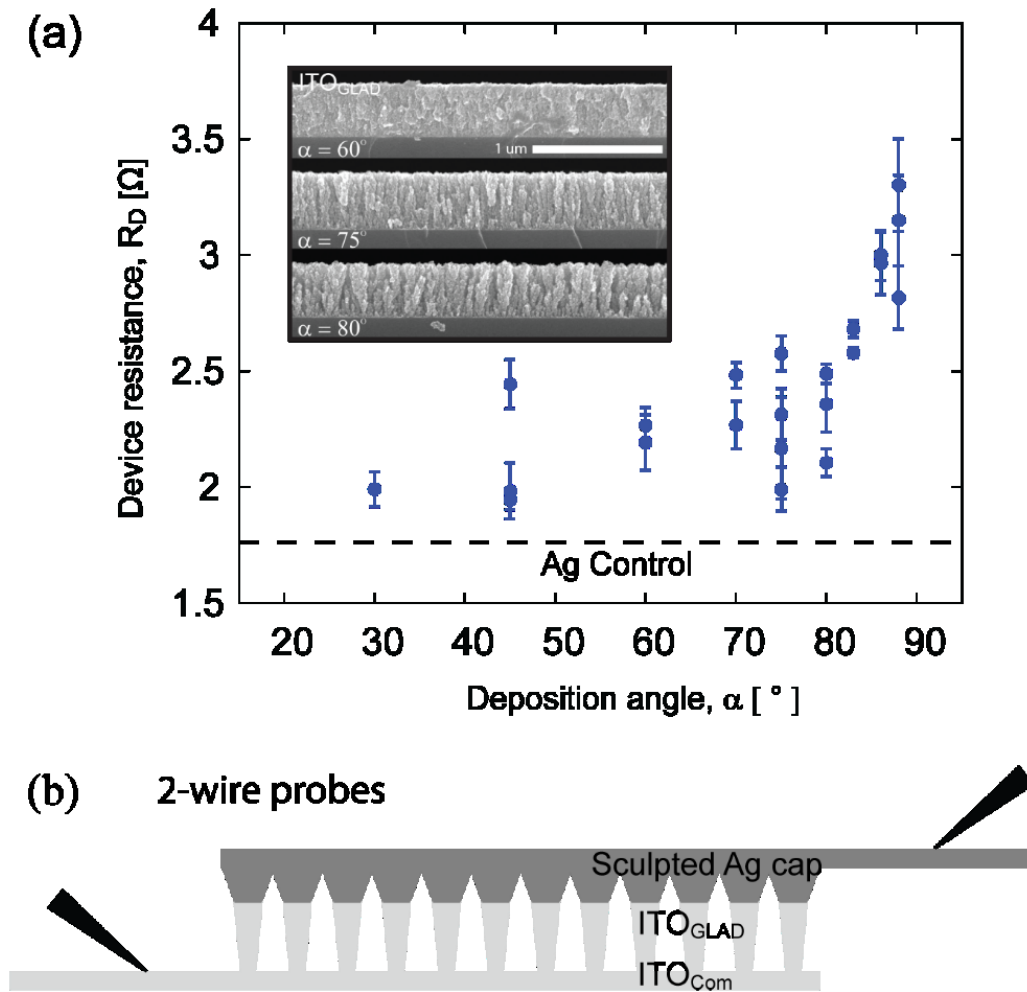


**Figure B-1  $\alpha$  sweep and 2-wire measurement.** (a) 2-wire measure of the axial resistance revealed a factor of  $\sim 2$  increase in  $R_D$  for high- $\alpha$  films (relative to our planar Ag control), inset: evolving laterally-isolated  $\text{ITO}_{\text{GLAD}}$  films; (b) schematic device architecture of nanostructures isolated between sculpted Ag cap and commercial ITO substrates.

**Figure B-1** outlines an initial study investigating the formation of a planar top contact with sufficient lateral conductivity to probe the thin film. The observations from this initial work influenced the design and microfabrication parameters of our subsequent 4-wire van der Pauw-type test structures, particularly the maximum transition thickness from conformal to planar deposition (refer to **chapter 4** for details).

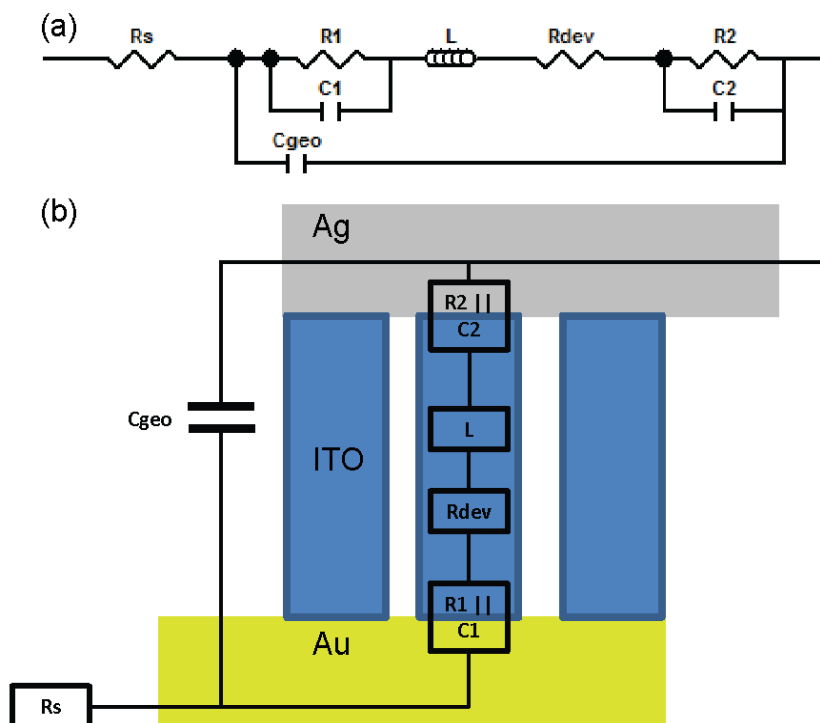


**Figure B-2 Equivalent circuit model and schematic.** (a) The series contribution from the electrodes is removed with 4-wire measurement; included are the interface contributions and the geometrical contribution due to the parallel plate contribution of the electrodes. A series inductance was supposed during these initial experiments; (b) schematic of same.

An equivalent circuit model (see **Fig. B-2 a**), where the 4-wire methodology minimizes the contribution from the electrodes, we are then left with the contribution from the interfaces (Ag/ITO and ITO/Au), the nanostructure array and any geometric contribution (see **Fig. B-2 b** for schematic). An initial attempt was made to explore the AC characteristics for GLAD-ITO devices, probing into the MHz range, but yielded purely resistive samples ( $C_{\text{geo.}} = 0$  implies no interface information is available in this configuration). This could be due to the formation of nearly ideal ohmic contacts, or alternatively due to the low driving voltages (i.e., not enough carriers to see the capacitance). Initial estimates indicate that a power supply with a GHz probing range and/or the inclusion of a blocking layer is required for further measurement.

# C Film deposition details

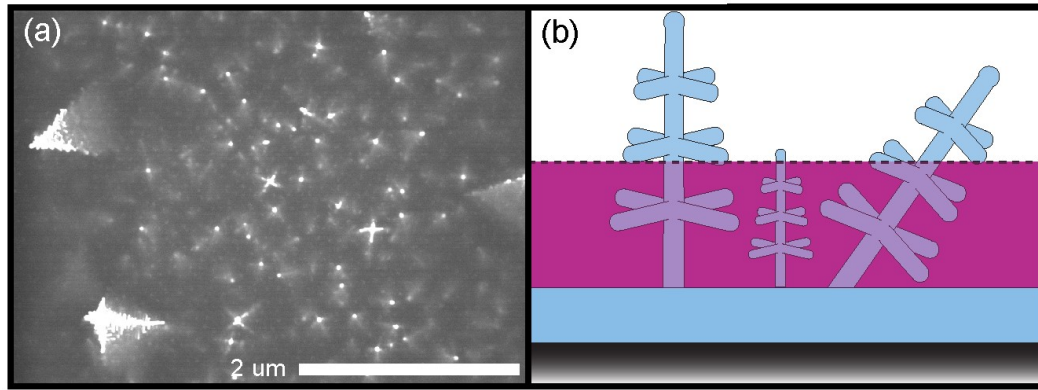


**Figure C-1 Film-level defects.** (a) Top-down SEM showing NWs that are ideally plasma-ashed, those with exposed branches, and large film level defects; (b) schematic illustration depicting the latter.

## Film level defects

Film-level defects occurring in a limited number of frames include larger structures that are believed to result from the interplay between positive feedback and competitive growth dynamics characteristic of GLAD thin-films (shown in **Fig. C-1 a** and schematically in **b**; see **Fig. C-2** for extreme examples of film-scale defects) [216]. Here, potential issues include:

- i. Defects identified as multiple structures during image analysis; and
- ii. Larger diameter NWs resulting in the asymmetrical conduction of  $I_{\text{test}}$  (due to device damage or preferential current paths).

The former required that we examine all SEM frames used during analysis, and remove spurious contributions, while the latter required that we address device performance at the experiment-level, assessing all devices and processing conditions as well as the interpretation of our devices operating as a uniform parallel array.

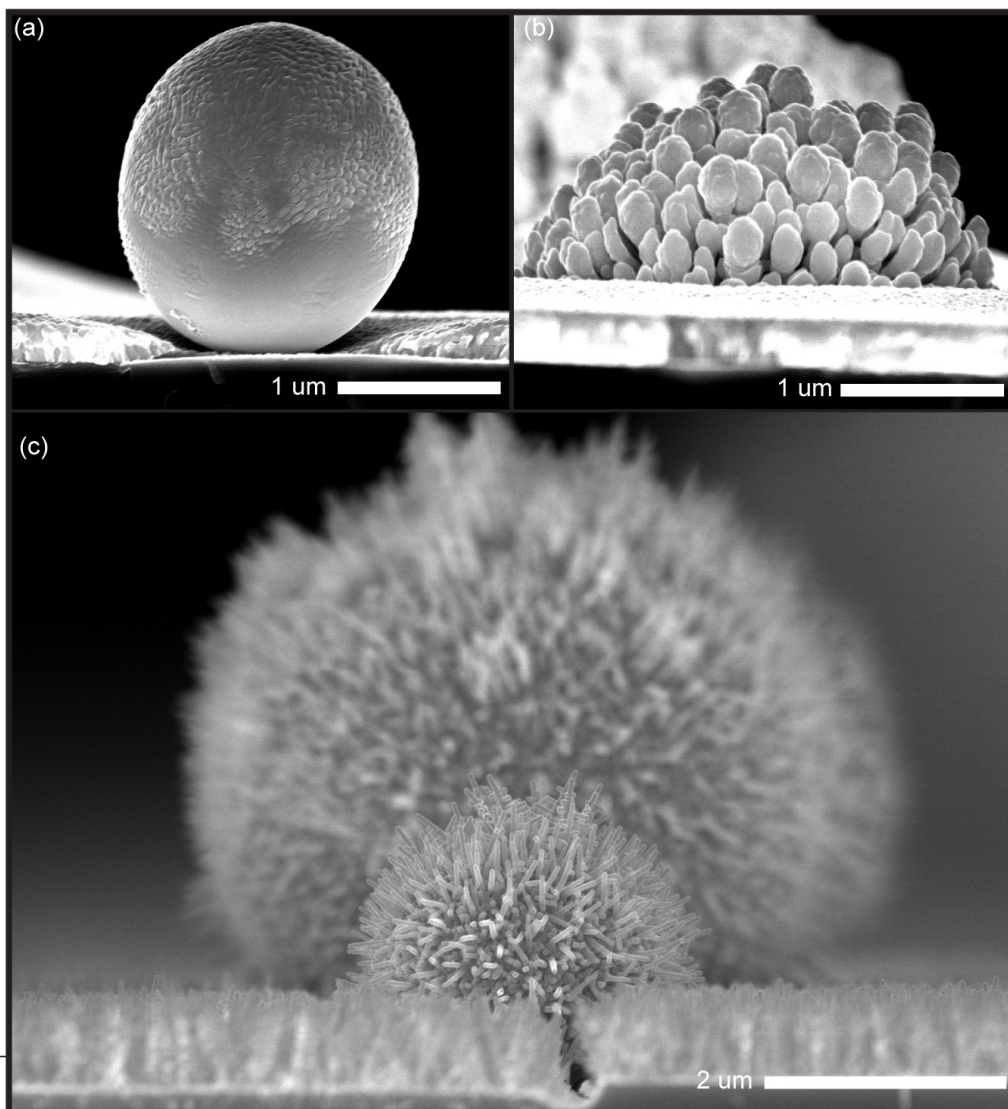


**Figure C-2 Device-scale defects.** Isolated defects observed during (a) Ag deposition; (b) Ag + VLS-GLAD-ITO deposition; and (c) VLS-GLAD-ITO deposition.

## C.1 GLAD-ITO deposition details

### *GLAD Deposition*

#### General Info

<b>Date</b>	March 10 /2013		
<b>Material</b>	Indium-tin-oxide	<b>System</b>	Soundwave
<b>Film Name</b>	AL3-134		
<b>Film Description</b>	Planar ITO		

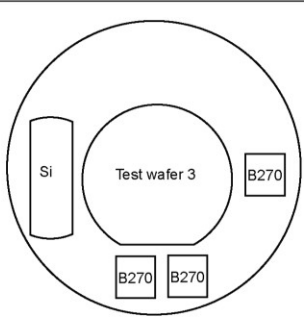
#### Vacuum System

<b>Rough Time</b>	5 min
<b>Hi-Vac Time</b>	Overnight (multiple)
<b>Base Pressure</b>	$2 \times 10^{-8}$ Torr
<b>Dep. Pressure</b>	$9 \times 10^{-6}$ Torr

#### Deposition

<b>Structure</b>	Planar (embedded contact study)		
<b>Angle</b>	$\alpha = 20^\circ$	<b>Thickness</b>	~ 380 nm
<b>Pitch</b>	25 nm	<b>Turns</b>	16
<b>Density</b>	$7.16 \text{ g / cm}^3$	<b>Z-factor</b>	1
<b>CTM Ratio</b>		<b>Tooling</b>	-
<b>Beam Pattern</b>	Circle	<b>Power Profile</b>	1
<b>Sweep Amp.</b>	1.6		
<b>Voltage</b>	5.10 kV	<b>Current</b>	30 mA
<b>CTM Rate</b>	$0.1 \text{ nm s}^{-1}$ (nominal)	<b>Condition Time</b>	9 min
<b>CTM Thickness</b>	365 nm	<b>Deposition Time</b>	30 min
<b>Gas Info</b>			

#### Comments

Motion file:	AL3-134_2013.05.10	
Ratio file:	AL3-134_2013.05.10	
Minor variations while adjusting rate.		

## C.2 VLS-GLAD-ITO deposition details

### ***GLAD Deposition***

#### General Info

<b>Date</b>	November 2 /2013		
<b>Material</b>	Indium-tin-oxide	<b>System</b>	Soundwave
<b>Film Name</b>	AL4-007B		
<b>Film Description</b>	Nanotrees		

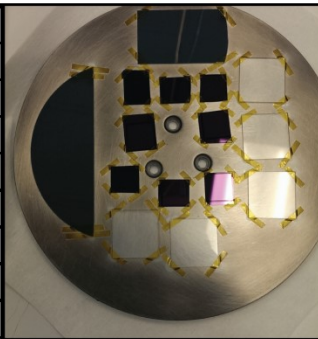
#### Vacuum System

<b>Rough Time</b>	5 min
<b>Hi-Vac Time</b>	1.5 hr
<b>Base Pressure</b>	$4 \times 10^{-7}$ Torr
<b>Dep. Pressure</b>	$1 \times 10^{-6}$ Torr (increasing to $4 \times 10^{-5}$ Torr)

#### Deposition

<b>Structure</b>	VLS - nanowires		
<b>Angle</b>	$\alpha = 85^\circ$	<b>Thickness</b>	300 nm (nominal)
<b>Pitch</b>	20 nm	<b>Turns</b>	15
<b>Density</b>	$7.16 \text{ g / cm}^3$	<b>Z-factor</b>	1
<b>CTM Ratio</b>		<b>Tooling</b>	-
<b>Beam Pattern</b>	Circle	<b>Power Profile</b>	1
<b>Sweep Amp.</b>	1.5		
<b>Voltage</b>	5.1 kV	<b>Current</b>	80-85 mA
<b>CTM Rate</b>	$0.5 \text{ nm s}^{-1}$	<b>Condition Time</b>	12 min
<b>CTM Thickness</b>	300 nm	<b>Deposition Time</b>	15 min
<b>Gas Info</b>			

#### Comments

<b>Motion file:</b>	AL4-007B_2013.11.02	
<b>Ratio file:</b>	AL4-007B_2013.11.02	
<b>Start at 238°C, stable at 247°C</b>		

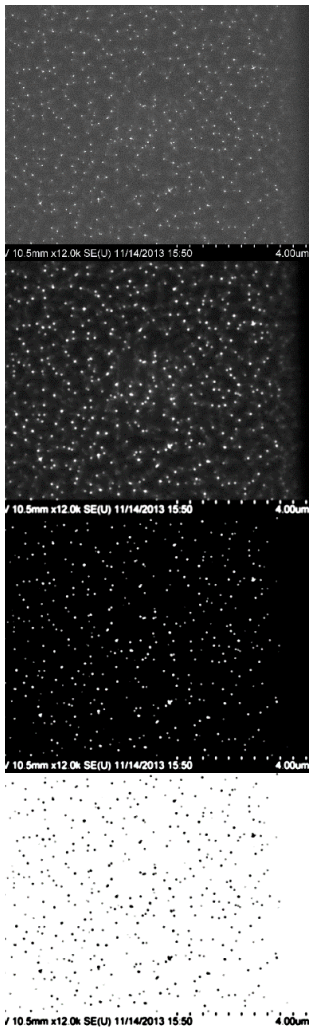


# D Determination of $N_p$

An image analysis was conducted using imageJ software. To gauge the suitability of the minimum threshold routine, a manual threshold was conducted from 1-200 (0-255 scale). When calibrating for low end noise (i.e., "ghosting" of unexposed posts). It was found that the minimum threshold routine was a fair means of determining the  $N_p$ .

**Table D-1 Manual/minimum imageJ threshold routine.**

Threshold (0-255):	N [posts]:	Post density [posts/ $\mu\text{m}^2$ ]:
1	75	5.1
50	116	7.9
100	133	9.0
150	145	9.8
200	166	11.3
Minimum	150	10.2



**Note:** Original image cropped to include device area only (not shown)

```
run("Enhance Contrast", "saturated=0.4");
```

```
run("Smooth");
```

**Note:** This step was omitted when determining post cross-sectional area.

```
run("Auto Threshold",  
"method=Minimum white");
```

```
run("Invert");  
run("AnalyzeParticles...", "size=25-Infinity  
circularity=0.00-1.00 show=outlines");
```

**Note:** the output of this sequence is a .csv file from which the number of elements (line items) is used in the subsequent device analysis.

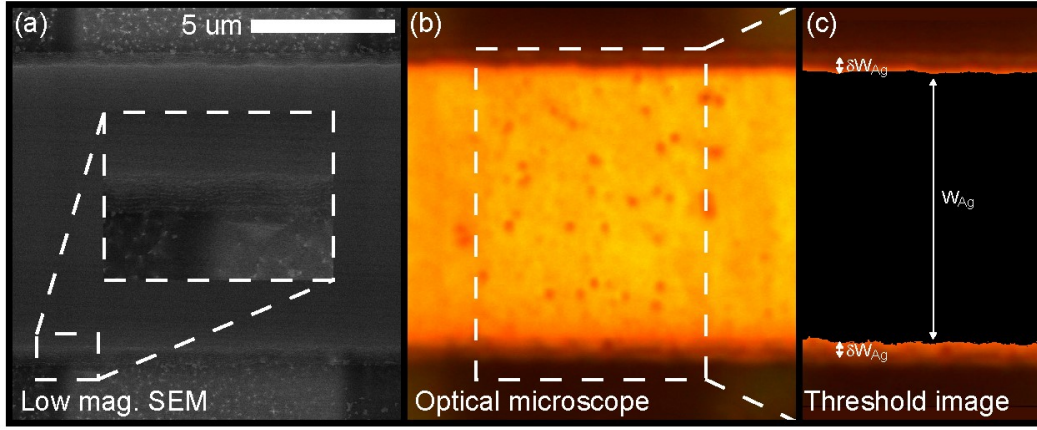


**Figure D-1 Estimated Ag trace dimensions.** (a) Top-down SEM of a device with PR overhang; inset: ‘terracing’ at the edge of PR photo-mask (1  $\mu\text{m}$  scale bar); (b) Top-down optical microscopy of the same; (c) Top-down threshold image of optical frame, depicting estimated error region ( $\delta W_{\text{Ag}}$ ) and Ag linewidth ( $W_{\text{Ag}}$ ).

## D.1 Device-level defects: Undercutting of Ag contact

Our previous discussion of  $W_{\text{Ag}}$  centered upon the estimated degree of undercutting, with uncertainty stemming from shadowing and tapering at the Ag contact edge. ( $W_{\text{Ag}}$  is estimated as a percentage of the total PR trace width, and is complicated by what can be considered as a defect near the edge of the trace.) The challenge is then identifying the edge of the trace, deviations from nominal dimensions, and the associated uncertainty. Shown in **Fig. D-1 a** and **b** is an ideally etched device where the uncertainty is estimated as one half of the PR ‘over-hang’ region for all devices ( $\delta W_{\text{Ag}} \sim 230 \text{ nm}$ , depicted in **Fig. D-1 c**). The uncertainty in  $N_{\text{p}}$  with respect to  $W_{\text{Ag}}$  is discussed further in terms a more pronounced defect — the under-cutting and subsequent narrowing of the top-contact trace during wet etching (discussed in **section 5.4.2**), and in extreme cases of under-cutting, top contact degradation potentially through the width of a trace (discussed here). The latter is another class of device-level defect which was first observed at a cleaved trace edge during FIB isolation and is further discernable with optical microscopy (see **Fig. D-2 a** and **b**). In extreme cases of under-cutting (potentially through the width of a trace), contact degradation results in the formation of ‘micro-channels’ (see **Fig. D-2 c** and **d**). The formation of these channels severely undermines our confidence in the determined  $N_{\text{p}}$ , however in the limited cases where this class of defect was observed, devices failed open circuit and were therefore not included in the final dataset.

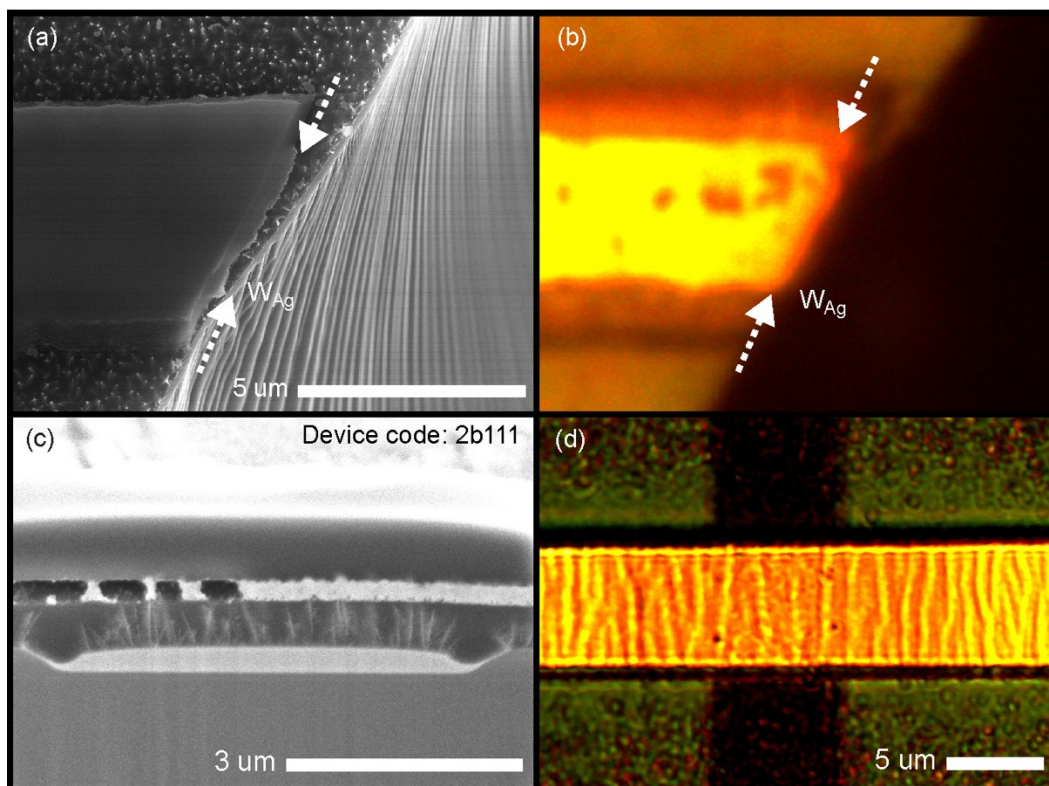


**Figure D-2 Determination of  $W_{Ag}$  and device damage.** (a) oblique SEM, and (b) optical micrograph view of cleaved top contact section allowing us to observed the PR coated Ag contact directly; (c) edge-view SEM of device 2b111 and (d) top-view optical micrograph of same. Undercutting is believed to be responsible for contact degradation and deviation of device performance. Note: device 2b111 failed open circuit and therefore is not included in the final dataset.

# E Crystallographic details

Table E-2 Process legend.

	Process condition	Process code
A	As-deposited	111
B	Ox-only/ 1.5 ox	211
C	24 ox	311
D	24-175-10	322
E	275-10	232
F	375-10	242
G	24-425-10	352
H	375-30	243
I	375-100	244

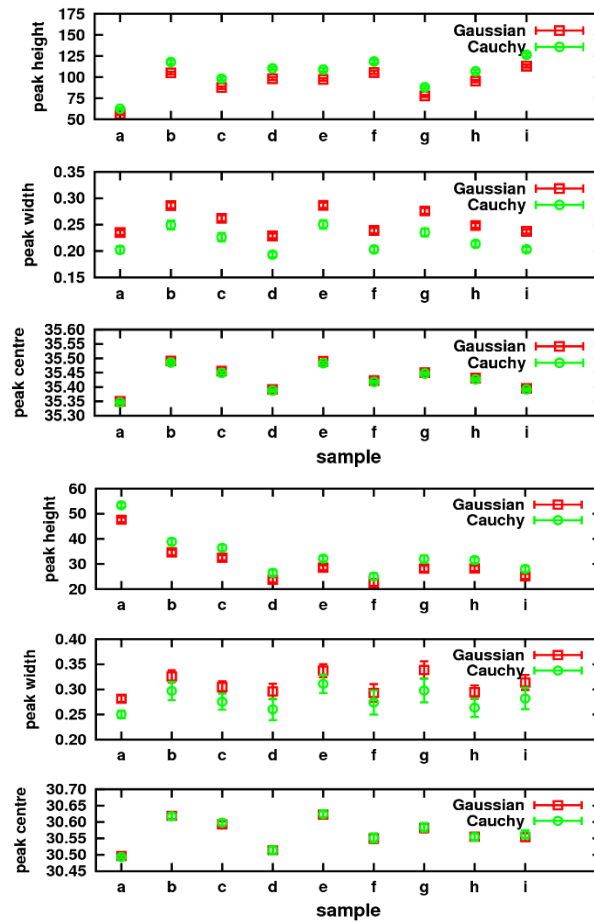


**Figure E-1 Peak width, centre and width for (400) and (222) peaks of interest.** Error bars represent instrument error (calibrated against LaB6 standard ( $I_{111}/I_{110}$ ), and with varying goniometer angle). Maximum intensity ratio between  $I_{400}/I_{222} \sim 88-92^\circ$  for (400), and  $118-122^\circ$  for (222). An alternative Cauchy fit gives, (400):  $(75 \pm 16)$  nm, (222):  $(30 \pm 5)$  nm. Here, the uncertainty represents the standard deviation of the range of observed grain sizes for the given orientation (across all processing conditions). For a detailed consideration of the progression of film texture with rate see ref: [94] and [9].

# F EELS sample preparation and processing

The FIB NW isolation procedure is as follows:

- a. A device is selected (in this case a nominally  $100\ \mu\text{m}^2$  device) and coated with tungsten to protect the device cross-sectional area of interest during excavation (see **Fig. 6-9 a**).
- b. The sample is held with its z-plane perpendicular to the FIB and thinned from the top (removing the catalyst droplet) and bottom (removing the undergrowth) to isolate a mid-body section of NW ‘torsos’ suspended in the PR matrix (see **Fig. 6-9 b**, as well see **Fig. 3-3** for a schematic representation of the isolated section).
- c. See **figure 6-9 c** for a magnified view of the same.
- d. A selected NW is shown in **figure 6-9 d** (top down view). The corresponding energy loss spectra (inset) is collected at a scan rate of  $1.2\ \text{s/pixel}$  — limiting dwell times to avoid damaging the crystal with the high-energy beam<sup>1</sup>.

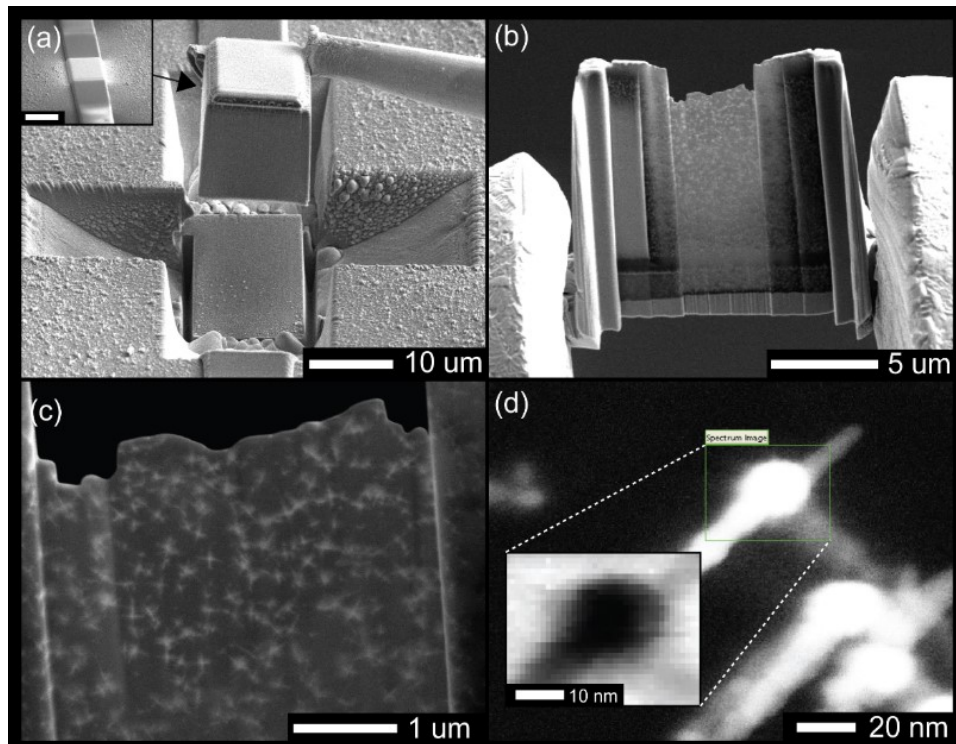


**Figure F-13 EELS sample preparation and data collection.** (a) Oblique-view SEM of a 100 sccm device being excavated using a FIB; (b) plan-view SEM of sample after being thinned from top and bottom with the FIB; (c) top-down TEM of branched NW film suspended within the polymer in-fill region; (d) isolated NW; inset: corresponding core-loss EELS spectrum map.

<sup>1</sup>Isolation of samples using the FIB technique is time intensive, taking  $\sim 3$  hours to isolate a sample, with a full EELS map taking a further  $\sim 45$  mins to collect.



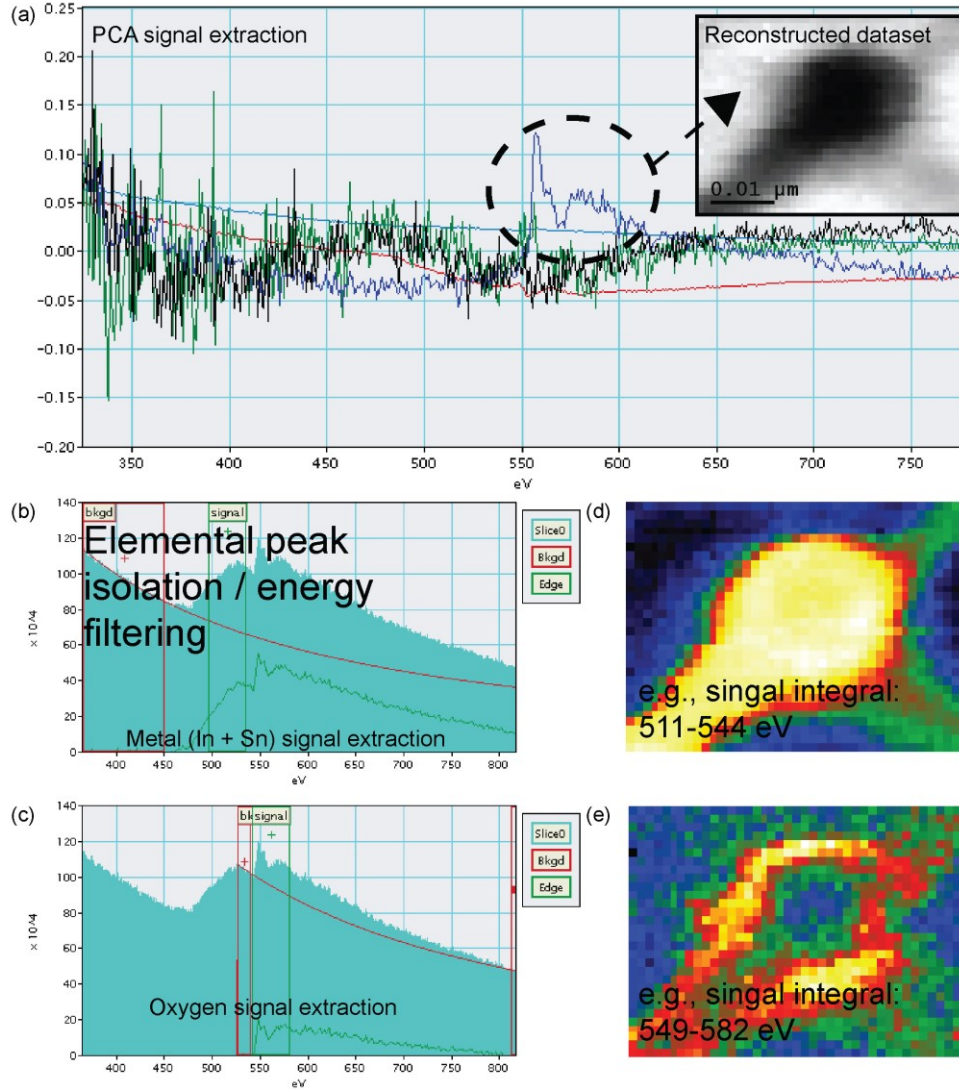


**Figure F-2 EELS spectrum collection process.** (a) During EELS characterization, an incident transmission beam ( $\sim 1.1$  eV) scans the cross-section of an isolated NW mid-section ( $\sim 150$  nm thick), and the resulting elemental peaks are resolved using principle component analysis (PCA). PCA is a statistical technique that considers the variance in contrast of a spectrum image; inset: the data set is then reconstructed using only those principal components, eliminating those that represent noise<sup>2</sup> [180]; (b) this analysis produces a dataset (.dm3 file) that can be manipulated and analyzed digitally. The resulting dataset can be considered as a three-dimensional data cube whose x-y dimensions (real-space imaging dimensions) and z dimension (energy loss in the spectra) contain spectroscopic information related to the local bonding environment. Energy filtering allows us to select the metal components and (c) oxygen component in the collected spectrum image, by isolating the associated energy range characteristic of In, Sn, and O; from this analysis we can generate the core-loss temperature map for metal spectra and oxygen (d and e, respectively).

<sup>2</sup>Fit over a pre-edge energy range, and then extrapolated into the indicated edge integration range [180].

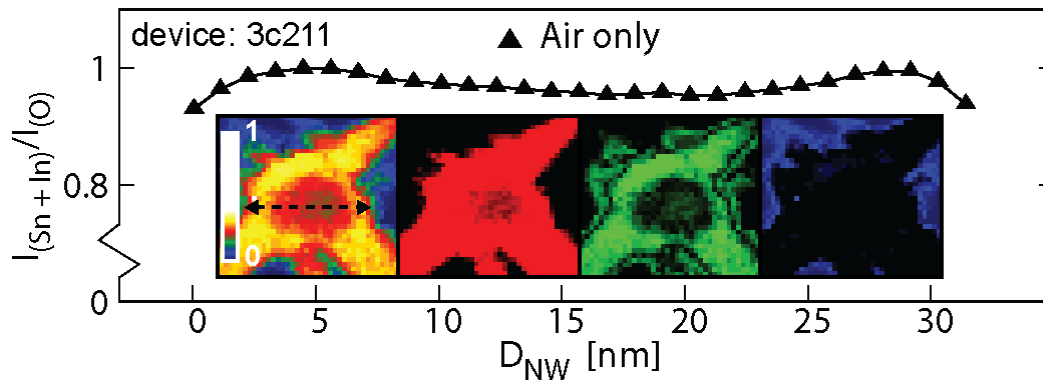


**Figure F-3 Air-annealed EELS core-loss temperature map.** (a) oxygen normalized metal profile for the ‘air-only’ sample (taken along  $\sim 30$  nm dashed line); the relatively uniform/flat elemental profile of the air-annealed NW isolated from device 3c211 (unlike the pronounced metallic core of **Fig. 6-10**). Inset: the RGB channels are separated using the ImageJ plugin Image5D (used to handle the time series of 3D-multichannel data stored in the .dm3 file). Compare with **Fig. 6-12 a–c**.

# G K-cluster analysis

A K-means Cluster analysis [200] was undertaken for classification of the data into two (user selected) clusters for each processing condition; this statistical analysis technique was utilized to validate the interpretation of a bi- or multi-modal distribution. The purpose of the K-means clustering analysis is to address the dominant variable describing the observed clustering of  $R_D$ , as it progresses with processing and varies with  $N_P$ . Said another way, this analysis is meant to answer the question: is the observed clustering due to the processing condition,  $N_P$ ,  $E$ , or some combination thereof? Here, we test the null hypothesis that the cluster means are equal, and further explore the dataset [217]. Results from the analysis of normalized variance (ANOVA), reveal that relative to  $E$ ,  $N_P$  and processing condition are not the dominant variables that explain the clustering of our device data (summarized in **Fig. G-2**).

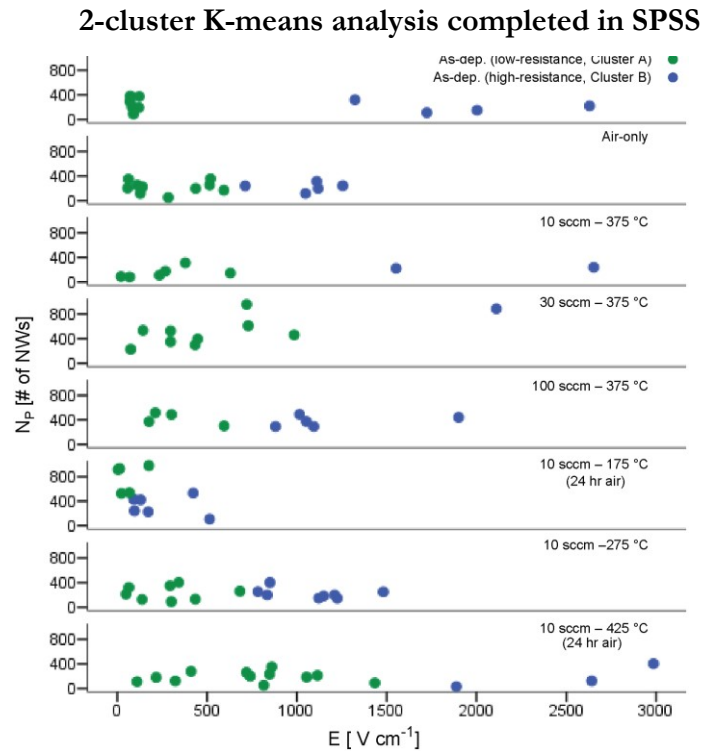


**Figure G-1 K-means cluster assignment for all conditions.** SPSS output for 2 cluster, 'K-means clustering' analysis. Results from the analysis of normalized variance (ANOVA), reveal that relative to the electric-field [ $F(1, 92) = 165.57$ ,  $p < 0.05$ ], the number of posts [ $F(1, 92) = 0.987$ ,  $p = 0.323$ ] and processing condition [ $F(1, 92) = 0.990$ ,  $p = 0.322$ ] are not the dominant variables that explain the clustering of our device data; a notable exception is samples processed at 10 sccm and 175 °C for which the number of posts is the dominant variable need to explain the multi-modal clustering.